EUROPEAN ORGANIZATION FOR NUCLEAR RESEARCH

CERN-SPSC-2004-009
SPSC-P-284 Add. 4
21 April 2004

LIFETIME MEASUREMENT OF $\pi^+\pi^-$ AND $\pi^\pm K^\mp$ ATOMS TO TEST LOW ENERGY QCD

Addendum to the DIRAC Proposal

B. Adeva[o], L. Afanasyev[l], Z. Berka[b], V. Brekhovskikh[n], G. Caragheorgheopol[k], T. Cechak[b], M. Chiba[j], S. Constantinescu[k], C.C. Detraz[a], A. Dudarev[l], D. Drijard[a], I. Evangelou[d], M.V. Gallas[ao], J. Gerndt[b], R. Giacomich[f], P. Gianotti[e], D. Goldin[p], F. Gomez[o], A. Gorin[n], O. Gortchakov[l], C. Guaraldo[e], M. Hansroul[a], R. Hosek[b], M. Iliescu[ek], V. Karpukhin[l], J. Kluson[b], M. Kobayashi[g], P. Kokkas[d], V. Komarov[l], A. Kulikov[l], A. Kuptsov[l], V. Kruglov[l], L. Kruglova[l], K.-I. Kuroda[l], A. Lamberto[f], A. Lanaro[e], V. Lapshin[n], R. Lednicky[c], P. Levi Sandri[e], V. Lucherini[e], N. Manthos[d], L. Nemenov[l], M. Nikitin[l], K. Okada[h], V. Olchevskii[l], L. Penescu[k], M. Pentia[k], A. Penzo[f], C. Petrascu[ek], M. Plo[o], Zh. Pustylnik[l], G.F. Rappazzo[f], A. Ryazantsev[n], A. Romero[o], V. Rykalin[n], C. Santamarina[a], J. Saborido[o], J. Schacher[q], C. Schuetz[p], A. Sidorov[n], D. Sirghi[e], F. Sirghi[e], J. Smolik[c], F. Takeutchi[h], A. Tarasov[l], L. Tauscher[p], F. Triantis[d], S. Trusov[m], O. Vázquez Doce[o], P. Vázquez[o], S. Vlachos[p], V. Yazkov[m], Y. Yoshimura[g], M. Zhabitsky[l], P. Zrelov[l]

[a] CERN, Geneva, Switzerland
[b] Czech Technical University, Prague, Czech Republic
[c] Institute of Physics ASCR, Prague, Czech Republic
[d] Ioannina University, Greece
[e] INFN - Laboratori Nazionali di Frascati, Frascati, Italy
[f] Trieste University and INFN-Trieste, Italy
[g] KEK, Tsukuba, Japan
[h] Kyoto Sangyou University, Japan
[i] UOEH-Kyushu, Japan
[j] Tokyo Metropolitan University, Japan
[k] National Institute for Physics and Nuclear Engineering IFIN-HH, Bucharest, Romania
[l] JINR Dubna, Russia
[m] Skobeltsyn Institute for Nuclear Physics of Moscow State University
[n] IHEP Protvino, Russia
[o] Santiago de Compostela University, Spain
[p] Basel University, Switzerland
[q] Bern University, Switzerland

GENEVA
2004

Abstract

The proposed experiment is the further development of the DIRAC experiment already running at CERN PS. Up to now more than 15000 $\pi^+\pi^-$ pairs originated from the $A_{2\pi}$ breakup were identified and the expected statistical accuracy of the lifetime is about 10% in accordance with the DIRAC proposal.

The new experiment aims to measure simultaneously the lifetime of $\pi^+\pi^-$ atoms ($A_{2\pi}$), to observe πK atoms ($A_{\pi K}$) and to measure their lifetime using 24 GeV proton beam. The precise measurement of these quantities will enable us to determine the combination of s-wave pion-pion $|a_0 - a_2|$ and pion-kaon $|a_{1/2} - a_{3/2}|$ scattering lengths (with isospin 0, 2 and 1/2, 3/2, respectively) in a model-independent way. The precision of $A_{2\pi}$ lifetime measurement will be better than 6% and the difference $|a_0 - a_2|$ will be determined within 3% or better. The accuracy of $A_{\pi K}$ lifetime measurement will be at the level of 20% and the difference $|a_{1/2} - a_{3/2}|$ will be determined at the level of 10%. Low energy QCD predicts these values with an accuracy about 2% for the pion-pion scattering lengths and about 10% for the πK-scattering lengths. These results have been obtained assuming a strong condensation of quark-antiquark pairs in vacuum. The pion-pion and pion-kaon scattering lengths have never been verified with experimental data with the same level of precision. For this reason the proposed measurements will be a crucial check of the low energy QCD predictions and our understanding of the nature of the QCD vacuum.

The observation of the long-lived (metastable) $A_{2\pi}$ states is also considered with the same setup. This allows one to measure the energy difference between ns and np states and to determine the value of $2a_0 + a_2$ in a model-independent way.

A by-product of the experiment is the measurement of two-pion, pion-kaon and kaon-proton correlation functions with unprecedented accuracy of less than 1 MeV/c in the relative momentum Q and high statistics even in the region of Q's less than some tens of MeV/c. This will allow for a detailed femtoscopy of particle production, particularly for a measurement of the large-distance behavior of the distribution of the relative distances of the particle emitters.

Contents

Introduction

The goal of the DIRAC experiment at CERN was to measure with high precision the lifetime of the $\pi^+\pi^-$ atom ($A_{2\pi}$), which is of order 3×10^{-15} s, and thus to determine the S-wave $\pi\pi$-scattering lengths difference $|a_0 - a_2|$. $A_{2\pi}$ atoms are detected through the characteristic features of $\pi^+\pi^-$ pairs from the atom breakup (ionization) in the target. Up until now more than 15000 $\pi^+\pi^-$ pairs originated from the $A_{2\pi}$ breakup were identified and the expected statistical accuracy of the lifetime is about 10% in accordance with the DIRAC proposal.

The new proposed experiment aims to measure simultaneously the lifetime of $\pi^+\pi^-$ atoms ($A_{2\pi}$), to observe πK atoms ($A_{\pi K}$) and to measure their lifetime using 24 GeV proton beam PS CERN and the upgraded DIRAC setup.

The precise measurement of $A_{2\pi}$ and $A_{\pi K}$ lifetime will enable us to determine the combination of s-wave pion-pion $|a_0 - a_2|$ and pion-kaon $|a_{1/2} - a_{3/2}|$ scattering lengths (with isospin 0, 2 and 1/2, 3/2, respectively) in a model-independent way. The precision of $A_{2\pi}$ lifetime measurement will be better than 6% and the difference $|a_0 - a_2|$ will be determined within 3% or better. The accuracy of $A_{\pi K}$ lifetime measurement will be at the level of 20% and the difference $|a_{1/2} - a_{3/2}|$ will be estimated at the level of 10%.

Scattering amplitudes of the $\pi\pi$ and πK systems at low energies are usually expressed in terms of scattering lengths. To evaluate the scattering lengths in the framework of QCD the effective Lagrangians or lattice calculations may be used. The effective Lagrangian can be constructed using the chiral symmetry breaking mechanism and other well established symmetries. The effective Lagrangian of Chiral Perturbation Theory (ChPT) allows to calculate S-wave $\pi\pi$ and πK scattering lengths with $\sim 2\%$ and $\sim 10\%$ accuracy, respectively. These results have been obtained assuming a strong condensation of quark-antiquark pairs in vacuum.

For the $\pi\pi$ system these calculations have not yet been tested at this level of accuracy, but different experiments (DIRAC at CERN, E865 at Brookhaven, KLOE at DAΦNE) are attempting to measure $\pi\pi$ scattering lengths with a precision of $\sim 5\%$.

For πK scattering, experimental model-independent data at low energy are not available, but a clean way to achieve this goal would be to measure the lifetime τ of atoms formed by π^+ and K^- ($A_{\pi K}$) and by K^+ and π^- ($A_{K\pi}$).

In fact, there exists a precise relationship between the decay probability of the πK atom in the ground state into $\pi^0\overline{K^0}$ and the s-wave πK scattering lengths, valid at leading order in isospin breaking:

$$W(A_{\pi^+K^-} \to \pi^0\overline{K^0}) = C(a_{1/2} - a_{3/2})^2 \tag{1}$$

where $a_{1/2}$ and $a_{3/2}$ are the scattering lengths for the isospin 1/2 and 3/2 states, and C is known at leading order in isospin breaking. Because the decay channel in Eq. (1) is the dominant one, ChPT can predict a value for τ by taking into account only this strong decay: $\tau \approx 5 \cdot 10^{-15}$ s.

In the $\pi\pi$ case, a precise measurement of scattering lengths provides a crucial test of the modern concept of chiral symmetry breaking in processes, where only *u* and *d* quarks are involved. A measurement of πK scattering lengths will extend this test to processes including the *s* quark as well.

The observation of the long-lived (metastable) $A_{2\pi}$ states is also considered with the same setup. This allows one to measure the energy difference between ns and np states and to determine the value of $2a_0 + a_2$ in a model-independent way.

A by-product of the experiment is the measurement of two-pion, pion-kaon and kaon-proton correlation functions with unprecedented accuracy of less than 1 MeV/c in the relative momentum Q and high statistics even in the region of Q's less than some tens of MeV/c. This will allow for a detailed femtoscopy of particle production, particularly for a measurement of the large-distance behavior of the distribution of the relative distances of the particle emitters.

In order to detect the atoms $A_{\pi^+K^-}$ and $A_{K^+\pi^-}$ and to measure their lifetime, we plan to use the PS extracted proton beam and the DIRAC setup, which was used for taking data to measure the $A_{2\pi}$ lifetime. The present setup has to be upgraded in order to achieve optimal conditions for detecting πK pairs from $A_{\pi K}$ ionization without affecting the $\pi^+\pi^-$ data taking. The setup upgrading comprises:

- ◇ Measurements with single and multilayer targets (two-target method). This method allows to decrease systematic errors by 6 times.
- ◇ Additional iron shielding (shielding 1) near the target station with collimators for the primary and secondary beams instead of existing wide tube common for the both beams. The existing iron shielding between the target station and the spectrometer magnet we will call as shielding 2. The additional shielding will allow essentially to decrease counting rates of upstream and downstream detectors.
- ◇ A permanent magnet installation in the secondary particle channel between the target station and the first shielding to improve close track separation in the Scintillation Fiber Detector (SFD).
- ◇ Installation of a new detector, Microdrift Chambers (MDC), in the air gap of the secondary particle channel instead of existing Microstrip Gas Chambers (MSGC). The MDC measures particle coordinates using 18 identical planes: X, Y and U. The sensitive area of the MDC is close to $80 \times 80\,\mathrm{mm}^2$ and the space resolution for single hits is about 25 μm.
- ◇ A new front-end electronics implementation for the existing Scintillation Fiber Detector (SFD). The new electronics will allow to measure time and amplitude for every SFD column. As a result the SFD efficiency will be increased up to 98% and a close hit detection will be much better. Production of the new detector with the fiber diameter 0.28 mm instead of 0.5 mm in the existing detector.
- ◇ Updating of electronics for the existing Drift Chambers (DC) downstream of the spectrometer magnet. The new electronics will allow to decrease threshold and, consequently, to decrease high voltage. This will allow to work at higher intensities with the high efficiency.
- ◇ Two Aerogel Cherenkov counters installation in the right arm of the downstream detectors for kaon and proton separation.
- ◇ New gas Cherenkov detectors installation in both arms of the spectrometer for pion and kaon separation. These counters will be filled by sulfur hexafluoride (SF_6) or by perfluorobutane (C_4F_{10}). The existing gas Cherenkov counters filled by nitrogen (N_2) after a small modification will be still in use for electron suppression.
- ◇ New scintillation counters installation in both arms as an extension to the existing Vertical Hodoscopes (VH) and Preshowers (PSh). These counters will allow to increase aperture of the setup and essentially increase the $A_{\pi K}$ detection efficiency.
- ◇ Additional fast hardware processors for on-line selection of πK pairs with small relative velocities.

Chapter 1

Theoretical motivation

1.1 QCD at high and low energy

Quantum chromodynamics (QCD) describes strong interactions at high as well as low energies. In the region of high energy and large momentum transfer the interaction of quarks (q) and gluons (g) gets weak (asymptotic freedom) and, hence, strong interaction can be treated perturbatively: $pertQCD$. In the absence of quark masses the QCD Lagrangian splits into the left-handed (L) and right-handed (R) quark terms, corresponding to a chiral symmetry $SU(2)_L \times SU(2)_R$ (L_{sym}) in the case of only u and d quarks. In the presence of quark masses there is an additional quark term breaking chiral symmetry explicitly ($L_{\mathrm{break-sym}}$):

$$L_{QCD}(\mathrm{q},\mathrm{g}) = L_{\mathrm{sym}} + L_{\mathrm{break-sym}}. \tag{1}$$

It is known, that processes with large momentum transfer or at small distances are not sensitive to $L_{\mathrm{break-sym}}$. Chiral symmetry is a direct consequence of QCD. This symmetry also plays a fundamental role in the description of strong interaction phenomena governed by the confinement regime of QCD. In this regime — at low energy and large distances — the spontaneous breakdown of chiral symmetry (non-zero vacuum expectation value or quark condensate) allows to write down an effective Lagrangian of the same form as above (1), but replacing the q (here u and d) degrees of freedom by the hadron (π) ones:

$$L_{\mathrm{eff}}(\pi) = L_{\mathrm{sym}} + L_{\mathrm{break-sym}}. \tag{2}$$

In the framework of chiral perturbation theory (ChPT), by performing an expansion in momentum (p) and mass (and not in the coupling as in $pertQCD$), precise prediction for low energy hadronic (pionic) processes can be obtained from $L_{\mathrm{eff}}(\pi)$. For instance, the $\pi\pi$ scattering amplitude, calculated in ChPT including mass corrections, is given by

$$A = \frac{s - M_\pi^2}{F_\pi^2} + \mathcal{O}(p^4) + \ldots, \tag{3}$$

where the term $\frac{M_\pi^2}{F_\pi^2}$ accounts for $L_{\mathrm{break-sym}}$.

It should be emphasized, that pionic processes at low energy check both parts (L_{sym} and $L_{\mathrm{break-sym}}$) of the effective Lagrangian (2). ChPT allows to compute higher order corrections (1- and 2-loop) in a systematic way.

1.2 $\pi\pi$ scattering

The most precise predictions by ChPT have been achieved for the s-wave $\pi\pi$ scattering lengths (in units $M_{\pi^+}^{-1}$) [COLA01B]:

$$a_0 = 0.220 \pm 0.005\,, \quad a_2 = 0.0444 \pm 0.0010\,, \quad a_0 - a_2 = 0.265 \pm 0.004\,. \tag{4}$$

These values will be compared with those determined in the K_{e4} decay ($K \to \pi^+\pi^- e\nu_e$) as well as in the decay of the $\pi^+\pi^-$ atom ($A_{2\pi} \to \pi^0\pi^0$).

Another quantity of interest is the mass of the lightest hadron, the pion mass. Its chiral expansion starts with

$$M_\pi^2 = (m_u + m_d)B + \mathcal{O}(m^2), \tag{5}$$

where m are the corresponding quark masses, $B = |\langle 0|\overline{u}u|0\rangle|/F_\pi^2$, F_π the pion decay constant and $\langle 0|\overline{u}u|0\rangle$ is the quark condensate, an QCD order parameter. Eq.(5) corresponds the famous Gell-Mann–Oakes–Renner relation [GOR68].

Going further, the correction term in Eq.(5) at first non-leading order and in the isospin limit $m_u = m_d = \hat{m}$ is determined by one of the low-energy coupling constants (LEC), $\overline{l_3}$ [COLA01A]:

$$M_\pi^2 = M^2 - \frac{1}{2}M^2\left(\frac{M}{4\pi F}\right)^2 \overline{l_3} + \mathcal{O}(M^6) \;\; and \;\; M^2 \equiv 2\hat{m}B \tag{6}$$

with the pion decay constant F and the coefficient B in the chiral limit ($m_u, m_d \to 0$ at physical $m_s \neq 0$). Eq.(6) exhibits a relation between $\overline{l_3}$ and, via B, the quark condensate, a crucial quantity, reflecting a property of the QCD vacuum. Crude estimates from standard ChPT [GASS84] indicate a $\overline{l_3}$ range from 0 to 5, supporting the hypothesis of a large quark condensate.

This result needs an independent check. Since s-wave $\pi\pi$ scattering lengths also depend on this same coupling constant $\overline{l_3}$ (see Figure1.1[1]), measurements of scattering lengths or combinations of them allow to extract values for $\overline{l_3}$. At present time, there are three model-independent methods to experimentally investigate $\pi\pi$ scattering lengths, the K_{e4} decay, the decay of the $\pi^+\pi^-$ atom and the atomic level shift in the $\pi^+\pi^-$ atom. In practice only the first two methods have been realized.

1.2.1 K_{e4} decay

Since around 40 years ago it is known, that the rare K_{e4} decay, $K \to \pi^+\pi^- e\nu_e$, is a clean source of information about strong interaction in the form of $\pi\pi$ scattering at low energy. The final state interaction can be studied by analyzing the difference between the s- and p-wave scattering phases. In 1977, when the Geneva-Saclay experiment [ROSS77] collected around 30000 events, the s-wave isospin 0 scattering length could be measured with a precision of 20%. From the phase analysis in the effective mass region $280\ \mathrm{MeV} < M_{\pi\pi} < 380$ MeV the Geneva-Saclay collaboration obtained $a_0 = 0.28 \pm 0.05$. A more sophisticated analysis, taking advantage of the Roy equations together with peripheral $\pi N \to \pi\pi N$ data at high energy (above 0.8 GeV), led to the presently still quoted value $a_0 = 0.26 \pm 0.05$ [NAGE79]. The most recent results from K_{e4}, explored in the experiment E865 at Brookhaven, are the following ones [PISL03]. If a_0 and a_2 are regarded as independent, then a result outside the universal band in the (a_0, a_2) plane is found: $a_0 = 0.203 \pm 0.033$ and $a_2 = -0.055 \pm 0.023$. Using the Roy equations and a relation between a_0 and a_2 in ChPT (low-energy theorem, $\overline{l_3}$ unconstrained) E865 quotes as final result:

$$a_0 = 0.216 \pm 0.013(\mathrm{stat}) \pm 0.004(\mathrm{syst}) \pm 0.002(\mathrm{th}) \tag{7}$$

$$a_2 = -0.0454 \pm 0.0031(\mathrm{stat}) \pm 0.0010(\mathrm{syst}) \pm 0.0008(\mathrm{th}) \tag{8}$$

[1] We thank Gilberto Colangelo for providing us with this figure.

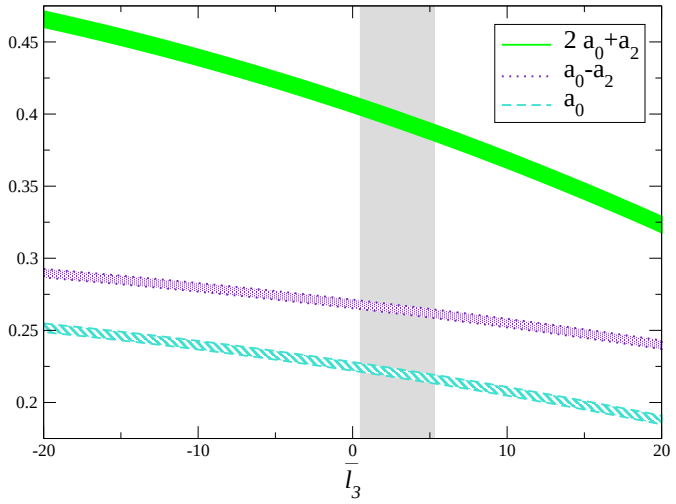

Figure 1.1: *s-wave scattering lengths as functions of the low-energy constant* $\overline{l_3}$*. The* $A_{2\pi}$ *lifetime measurement (see sect. 1.2.2) provides a value for the combination* $a_0 - a_2$*, whereas the determination of the energy level splitting* ΔE_{2s-2p} *in* $A_{2\pi}$ *leads to a value for* $2a_0 + a_2$*. The grey vertical bar indicates the range relevant in standard ChPT (see sect. 1.2.3).*

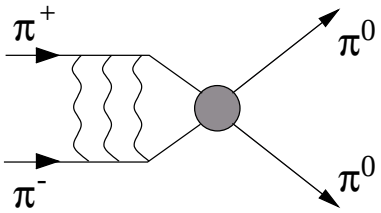

Figure 1.2: *The dominant decay channel of* $A_{2\pi}$ *or pionium.*

According to Colangelo, Gasser and Leutwyler [COLA01A] the above result of a_0 can be used to state an upper limit for the LEC $\left|\overline{l_3}\right| \leq 16$. This conservative limit, implemented into Eq.(6), implies that the bulk part of the pion mass originates from the first term in Eq.(6), i.e. from the term determined by the quark condensate: the correction term only contributes less than 6% to the pion mass. In comparison with the generalized ChPT [KNEC95] with unconstrained quark condensate and arbitrarily large $\overline{l_3}$, this result suggests that the quark condensate acts as leading order parameter of the spontaneously broken chiral symmetry.

1.2.2 Decay of the $\pi^+\pi^-$ atom

In the case of hadronic atoms a measurement of the lifetime τ allows to determine a combination of s-wave scattering lengths of the particles, which constitute the atom [DESE54]. Using the framework of low energy QCD the decay $A_{2\pi}(\text{ground state}) \rightarrow \pi^0\pi^0$ (Fig.1.2) is described by the decay rate or inverse lifetime [URET61, BILE69, JALL98, IVAN98, GASS01, GASH02]

$$\Gamma_{2\pi^0} = \frac{1}{\tau} = \frac{2}{9}\,\alpha^3\,p\,|a_0 - a_2|^2\;(1+\delta). \tag{9}$$

Here α is the fine structure constant, $p = \left(M_{\pi^+}^2 - M_{\pi^0}^2 - \frac{1}{4}M_{\pi^+}^2\alpha^2\right)^{1/2}$ is the π^0 momentum in the pionium system, M_{π^+} and M_{π^0} are the masses of π^+ and π^0, and a_0 and a_2 are the s-wave $\pi\pi$ scattering

lengths for isospin $I = 0$ and 2, respectively. The correction term $\delta = (5.8 \pm 1.2) \cdot 10^{-2}$ accounts for corrections of order α as well as for those due to $m_u \neq m_d$. This term δ is known and provides an accuracy level of 1% for Eq.(9) [GASS01]. As demonstrated in (9) a measurement of the lifetime τ allows to obtain in a model-independent way a value of $|a_0 - a_2|$.

Using Eqs.(9),(4) the lifetime of $A_{2\pi}$ in the ground state is predicted to be [COLA01B]

$$\tau = (2.9 \pm 0.1) \cdot 10^{-15}\,\mathrm{s}\,. \tag{10}$$

This result is based on the assumption that the spontaneous chiral symmetry breaking is due to a strong quark condensate [COLA01A].

The method to observe $A_{2\pi}$ and to measure its lifetime has been proposed in [NEME85]. Pairs of $\pi^+\pi^-$ are produced mainly as unbound ("free") pairs, but rarely also as $A_{2\pi}$. The latter may either annihilate into $2\pi^0$ or break up into $\pi^+\pi^-$ pairs ("atomic" pairs) after interaction with target atoms. For thin targets ($10^{-3}X_0$) the observable relative momentum Q in the atomic pair system is $Q \leq 3$ MeV/c. The atomic pair yield is $10 \div 20$ of the number of free pairs in the same Q interval. The number of atomic pairs is a function of the atom momentum and depends on the dynamics of the $A_{2\pi}$ interaction with the target atoms and particularly on the $A_{2\pi}$ lifetime [AFAN96]. For a given target thickness, the theoretical ionization probability for $A_{2\pi}$ is precise at the 1% level and uniquely linked to the lifetime of the atom.

The first observation of $A_{2\pi}$ [AFAN93] has been achieved in the interaction of 70 GeV/c protons with Tantalum at the Serpukhov U-70 synchroton. In that experiment the atoms were produced in an $8\,\mu$m thick Ta target, inserted into the internal proton beam. With only 270 ± 50 observed atomic pairs, it was already possible to set a lower limit on the $A_{2\pi}$ lifetime [AFAN94, AFAN97]: $\tau > 1.8 \times 10^{-15}$ s $(90\%\ CL)$.

In the DIRAC experiment [ADEV95] the expected statistical accuracy of the $|a_0 - a_2|$ determination will be about 5%. This value is more than 3 times larger than the corresponding theoretical accuracy in Eq.(4).

1.2.3 Atomic level shift in the $\pi^+\pi^-$ atom

Strong interaction and electromagnetic vacuum polarization effects lead to a splitting of $A_{2\pi}$ energy levels and hence to a difference ΔE_{ns-np} between ns and np energy levels:

$$\Delta E_{ns-np} = E_{ns} - E_{np} \approx \Delta E_n^s + \Delta E_n^{vac} \tag{11}$$

The term ΔE_n^s, resulting from strong interaction, constitutes the main contribution to ΔE_{ns-np} and is proportional to the sum $(2a_0 + a_2)$ of $\pi\pi$ scattering lengths. By measuring ΔE_{ns-np} accurately, $(2a_0 + a_2)$ can be determined, as the rest in Eq.(11) is calculable [NEME85, NEME01, NEME02]. Thus, the simultaneous measurement of the $A_{2\pi}$ lifetime and level shift enables to extract a_0 as well as a_2 in a model-independent way.

1.3 πK scattering

The chiral 2-flavour $SU(2)$ perturbation theory describes very successful the interaction of the lightest hadrons, the pions, which are interpreted as the corresponding Goldstone bosons. The study of processes with u and d quarks, however, tests only the $SU(2)_L \times SU(2)_R$ chiral symmetry breaking of the QCD and the effective Lagrangian. Investigating processes including also the s together with the u and d quarks means to extend the 2-flavour space to the 3-flavour space (u, d and s with $m_s \gg m_u, m_d$), leading to a chiral $SU(3)$ perturbation theory. To check our understanding of the $SU(3)_L \times SU(3)_R$ symmetry breaking of the same Lagrangians, the simplest and ideal process involving strange quarks is πK scattering [KNEC93]. A basic question, which arises here, is: can the K with a mass $M_K \gg M_\pi$

still act as a Goldstone boson. While the above process is interesting by itself, a detailed knowledge of πK scattering also helps to disentangle the flavour dependence of the order parameter (condensate) of ChPT.

The measurement of πK scattering lengths permits to perform direct comparisons between experiment and prediction from the 3-flavour $SU(3)_L \times SU(3)_R$ ChPT. Alternatively, such a measurement can be exploited utilizing dispersion relation techniques to generate a wealth of other constraints for ChPT.

In the following let us concentrate on the s-wave scattering lengths with isospin 1/2 and 3/2, $a_0^{1/2}$ and $a_0^{3/2}$, and in particular on $a_0^{1/2} - a_0^{3/2}$. This difference can be determined from the measurement of the πK atom *lifetime* and be compared with predictions from ChPT. For the mentioned πK scattering lengths the following values in units of $M_{\pi^+}^{-1}$ have been predicted in the framework of ChPT in 1-loop approximation [BERN91]:

$$a_0^{1/2} = 0.19 \pm 0.02; \qquad a_0^{3/2} = -0.05 \pm 0.02. \tag{12}$$

The errors in Eq.(12) are due to the uncertainties of the low-energy constants and to higher order corrections.

An alternative approach in ChPT [ROES99, FRIN02], assuming the s quark as a heavy partner particle, yields for the difference [ROES99]

$$a_0^{1/2} - a_0^{3/2} = 0.23 \pm 0.01, \tag{13}$$

in good agreement with the previous ones.

Recently a new investigation of πK scattering, applying dispersion techniques, has been performed [BUTT03B]. In this context a system of Roy and Steiner type equations has been analyzed and new solutions obtained. According to Ref. [BUTT03B] the scattering length combination, relevant for the πK atom lifetime, is found to be

$$a_0^{1/2} - a_0^{3/2} \simeq 0.269 \pm 0.015. \tag{14}$$

Precise values of the s-wave scattering lengths can be used as inputs to these equations from which one can obtain a precise determination of the πK scattering amplitude, in particular in the unphysical region, which is optimal for matching with ChPT expansions. This matching can provide detailed information on the currently poorly known next-to-leading order coupling constants.

At present there is no model-independent measurement of low energy πK scattering available. Therefore, we propose a study program for the πK atom: 1) Observation of πK atoms and 2) measurement of the πK atom lifetime, followed by extraction of the difference $a_0^{1/2} - a_0^{3/2}$ of πK scattering lengths.

1.3.1 Decay of the πK atom

The dominant decay process for the $A_{\pi K}$ atom is

$$A_{\pi^+ K^-} \to \pi^0 \overline{K^0} \quad (A_{K^+ \pi^-} \to \pi^0 K^0). \tag{15}$$

For $A_{\pi K}$ in the ground state the decay width is given by the following relation [BILE69, SCHW04]:

$$\Gamma(\pi^0 \overline{K^0}) = \frac{1}{\tau} = 8\alpha^3 \mu_+^2 p^* (a_0^-)^2 \, (1 + \delta) \, . \tag{16}$$

The s-wave isospin-odd πK scattering length $a_0^- = 1/3(a_0^{1/2} - a_0^{3/2})$ (a_0^I for isospin I) is defined in QCD for $m_u = m_d$ and $M_\pi \doteq M_{\pi^+}$, $M_K \doteq M_{K^+}$. Here $\mu_+ = \dfrac{M_\pi M_K}{M_\pi + M_K}$ and p^* is the outgoing

π^0 or K^0 momentum (including the ground state binding energy) in the πK atom system. The term δ, which accounts for corrections of order α and $m_u - m_d$, is known and thus providing a 1% accuracy in Eq.(16). Corrections from isospin violation have been calulated [NEHM02, KUBI01] and found to be rather small. As can be seen from (16), a measurement of the lifetime τ enables to derive a value for the πK scattering length a_0^- in a model-independent way.

Introducing the scattering length $a_0^- = (0.090 \pm 0.005) M_{\pi^+}^{-1}$ [BUTT03B] and the correction term $\delta = 0.040 \pm 0.022$ [SCHW04] in Eq.(16), the following $A_{\pi K}$ lifetime is found:

$$\tau = (3.7 \pm 0.4) \cdot 10^{-15} \text{ s}. \tag{17}$$

Therefore, if τ is measured with a precision of 20%, the πK scattering length a_0^- will be known with a 10% accuracy.

1.3.2 πK scattering, experimental results

In the 60's and 70's set of experiments were performed to measure πK scattering amplitudes. Most of them were done studying the scattering of kaons on protons or neutrons, and later also on deuterons. The kaon beams used in these experiments had energies ranging from 2 to 13 GeV.

The main idea of those experiments was to determine the contribution of the One Pion Exchange (OPE) mechanism. This allows to obtain the πK scattering amplitude. Due to kinematic restrictions it is not possible to have an on mass shell propagated pion ($t \neq M_\pi^2$, $t < 0$). Therefore, one has to determine the scattering amplitude for $t < 0$, and then extrapolate the results to $t = M_\pi^2$. Some of the processes studied are listed in Table 1.1:

Table 1.1:

Processes	References
$K^+p \to K^+\pi^-\Delta^{++}$	[TRIP68, MERC71, BING72, MATI74]
$K^+p \to K^0\pi^0\Delta^{++}$	[CHLI75, DUNW77, BRAN77, ESTA78]
$K^+p \to K^+\pi^+\Delta^0$	[DEBA69]
$K^+p \to K^0\pi^+p$	[BAKE75, BALD76, BALD78, MART78]
$K^+p \to K^+\pi^+n$	[DUNW77, ESTA78, BRAN77]
$K^-p \to K^-\pi^-\Delta^{++}$	[KIRS71, JONG73, LING73, BRAN77, DUNW77, ESTA78]
$K^-p \to K^-\pi^+n$	[YUTA71, AGUI73, FOX74, LAUS75, GRAE77, SPIR77] [DUNW77, BRAN77, ESTA78]
$K^-p \to K^-\pi^0p$	[AGUI73, GRAE77, SPIR77]
$K^-p \to \overline{K}^0\pi^-p$	[AGUI73, GRAE77, SPIR77, BALD78, MART78]
$K^+n \to K^+\pi^-p$	[FIRE72, FOX74, BAKE75]
$K^+n \to K^0\pi^+n$	[BAKE75]
$K^-n \to K^-\pi^+p$	[BAKK70, CHO70, ANTI71]

Table 1.2: *Measured πK s-wave scattering lengths for the isospin $I = 1/2$ state.*

reference	[BING72]	[MATI74]	[FOX74]	[ESTA78]
$a_{1/2}$	0.168	0.220 ± 0.035	0.280 ± 0.056	0.335 ± 0.006

Analysis of experiments gave the phases of πK-scattering in the region of $0.7 \leq m(\pi K) \leq 2.5$ GeV. The most reliable data on the phases belong to the region $1 \leq m(\pi K) \leq 2.5$ GeV [BUTT03B].

Table 1.3: *Measured πK s-wave scattering lengths for the isospin $I = 3/2$ state.*

reference	[BAKK70]	[CHO70]	[ANTI71]	[KIRS71]	[JONG73]	[ESTA78]
$a_{3/2}$	-0.085	-0.092	-0.078	-0.096	-0.072	-0.14 ± 0.07

Table 1.4: *πK scattering lengths determined by using dispersion relations.*

reference	[LANG77]	[JOHA78]	[KARA80]
$a_{1/2}$	0.237	0.240 ± 0.002	0.13 ± 0.09
$a_{3/2}$	-0.074	-0.05 ± 0.06	-0.13 ± 0.03

Since the energy regions, where the πK-amplitudes were measured, were not very close to threshold, the method described in [LANG78, KARA80] to obtain predictions for the low energy parameters, had to be used. Tables 1.2, 1.3 and 1.4 show the results for s-wave scattering lengths obtained by different analysis. Large fluctuations in these results and some inconsistency are evident.

The most precise values of πK scattering lengths [BUTT03B] were obtained only recently and presented above (14). At present time the experimental data on πK scattering at low energy are absent and the model-independent measurement of $|a_{1/2} - a_{3/2}|$ from the $A_{\pi K}$ lifetime will give the first experimental information on this important parameters.

Chapter 2

$A_{2\pi}$ and $A_{\pi K}$ production in p-nucleus interactions at 24 GeV

The relations to calculate the production probabilities for $A_{2\pi}$, $A_{\pi K}$ and any other hydrogen-like atoms, starting from the inclusive production cross-sections of the particles forming these atomic states, can be found in [NEME85]. In the same paper a method to observe these atoms and to measure their lifetime is proposed. Estimates are given for the yields of atoms produced in pp-collisions at a beam energy of 70 GeV and an atom emission angle of 8.4° in the lab system. The more detailed calculations of the $A_{2\pi}$ [GORC96] and $A_{\pi^+K^-}$, A_{pK^-}, $A_{p\pi^-}$ [GORC00] yields in proton-nucleus interactions have been made as a function of the atom angle in the proton energy range from 24 GeV/c to 1000 GeV/c.

The existence of $A_{2\pi}$ has been experimentally demonstrated at the U-70 accelerator [AFAN93] at Serpukhov in p-Ta collisions at $E_p = 70$ GeV and at emission angle of 8.4° in the lab system. This experiment allowed to estimate the $A_{2\pi}$ lifetime [AFAN94]. At present a precise determination (10%) of this lifetime is carried out by the DIRAC experiment at CERN.

2.1 Basic relations

The cross-section of atom production is proportional to the double inclusive production cross-section for the two constituents with small relative momentum. Atomic states can only be formed by two particles arising from short-lived sources (ρ, ω, $\Delta\ldots$), since their decay lengths are much smaller than the Bohr radius of the atom. In general, the differential production cross-section for such pairs is enhanced at small relative momenta, due to their Coulomb interaction in the final state. Therefore, they are called "Coulomb" pairs.

There exists another category of pairs, which contain at least one particle from long-lived sources (η, η', Λ, K^0_s, $\Sigma^\pm\ldots$) with decay lengths much larger than the Bohr atomic radius. Hence they are not sensitive to the Coulomb and also not to strong interaction in the final state, and are called "non-Coulomb" pairs.

The differential inclusive cross-section for $A_{\pi K}$ atom production can be written analogously to $A_{2\pi}$ production in the form [NEME85]:

$$\frac{d\sigma_n^A}{d\vec{p}_A} = (2\pi)^3 \frac{E_A}{M_A} |\Psi_n(0)|^2 \left. \frac{d\sigma_s^0}{d\vec{p}_1 d\vec{p}_2} \right|_{\vec{p}_1 \approx \frac{M_\pi}{M_A}\vec{p}_A ; \vec{p}_2 \approx \frac{M_K}{M_A}\vec{p}_A}, \tag{1}$$

where $\vec{p}_A$, E_A and M_A are the momentum, energy and mass of the atom in the lab system, respectively; $|\Psi_n(0)|^2 = p_B^3/\pi n^3$ is the square of the atomic wave function (without taking into account strong interaction between the particles forming the atom, i.e. pure Coulomb wave function), calculated at the origin for an atom of principal quantum number n and orbital angular momentum $l = 0$; p_B is the Bohr

momentum of the particles forming the atom; $d\sigma_s^0/d\vec{p}_1 d\vec{p}_2$ is the double inclusive production cross-section for pairs from short-lived sources not considering the Coulomb final state interaction; $\vec{p}_1$ and $\vec{p}_2$ are pion and kaon momenta in the lab system, respectively. The momenta must obey with a very good approximation the relations: $\vec{p}_1 = \vec{p}_A M_\pi/M_A$ and $\vec{p}_2 = \vec{p}_A M_K/M_A$ (M_π and M_K are the masses of the two mesons). According to the n^{-3} behaviour of $|\Psi_n(0)|^2$, the atomic populations of the levels are: $W_{n=1} = 83.2\%$, $W_{n=2} = 10.4\%$, $W_{n=3} = 3.1\%$, $W_{n\geq 4} = 3.3\%$ and $\Sigma_{n=1}^{\infty}|\Psi_n(0)|^2 = 1.202|\Psi_1(0)|^2$ ([NEME85, AMIR99]).

Neglecting Coulomb interaction in the final state, the double inclusive cross-section has the form [GRIS82]:

$$\frac{d\sigma^0}{d\vec{p}_1 d\vec{p}_2} = \frac{1}{\sigma_{in}} \frac{d\sigma}{d\vec{p}_1} \frac{d\sigma}{d\vec{p}_2} R(\vec{p_1}, \vec{p_2}), \tag{2}$$

where $d\sigma/d\vec{p}_1$ and $d\sigma/d\vec{p}_2$ are the pion and kaon inclusive cross-sections, σ_{in} is the inelastic cross-section of hadron production, R is a correlation function due to strong interactions in the final state.

The probability to produce a particle in the interaction (yield) can be obtained from the differential cross-section:

$$\frac{dN}{d\vec{p}} = \frac{d\sigma}{d\vec{p}} \frac{1}{\sigma_{in}}. \tag{3}$$

From Eqs.(1), (2) and (3), after substituting the expression for $|\Psi_n(0)|^2$ and summing over n, one obtains an expression for the inclusive yield of atoms in all S–states from the inclusive yields of pions and kaons:

$$\frac{d^2N_A}{dp_A d\Omega} = 1.202 \cdot 8\pi^2(\mu\alpha)^3 \frac{E_A}{M_A} \frac{p_A^2}{p_1^2\, p_2^2} \frac{d^2N_1}{dp_1 d\Omega} \frac{d^2N_2}{dp_2 d\Omega} R, \tag{4}$$

where $\mu = M_\pi M_K/(M_\pi + M_K)$ is the reduced mass of the $A_{\pi K}$, α is the fine structure constant, and Ω is the solid angle.

2.2 Calculated particle yields

We have used the program FRITIOF 6.0 [NILS87] to obtain the yields of π and K mesons. FRITIOF is a generator for hadron-hadron, hadron-nucleus and nucleus-nucleus collisions, and it makes use of JETSET 7.3 code [SJOS87] based on the Lund string fragmentation model.

A detailed test of the FRITIOF 6.0 results at the energy of 24 GeV has been made [GORC96] by comparing the calculated and the experimental yields of p, π^+, π^-, K^+ and K^-, reported in paper [EICH72], in the range of emission angles and momenta of our setup. The comparison shows that the deviation of the calculated yields from the data is less than 20%. Thus, the precision of the calculated yields of $A_{2\pi}$ and $A_{\pi K}$ is better than 40%.

Similar calculations performed with FRITIOF 7.02, the latest version of FRITIOF, show big disagreements for K^+, K^- and p yields. The p yield is the worst case, and since FRITIOF 6.0 fits well the experimental p data, we decided to use it for our calculations. This difference in the behaviour of the two programs can probably be explained by the fact, that FRITIOF 7.02 was developed for higher energies and higher $p_\perp$.

2.3 Comparison of two methods of atom yield calculations

The atom yield can be calculated directly using double inclusive cross-section Eq. (1) or using its expression through the product of single inclusive cross-sections Eq. (2) containing uncertain correlation function R. The two approaches were compared calculating $A_{2\pi}$ and $A_{\pi K}$ yields. The results for $A_{\pi^- K^+}$ and $A_{\pi^+ K^-}$ yields into unit solid angle are shown in figs. 2.1 and 2.2. In the Eq. (2) we have put $R = 1$. The yields (per one interaction) are calculated for the reaction $p + \mathrm{Ni} \rightarrow A_{2\pi}(A_{\pi K}) + X$ at the angle

5.7° and the proton energy of 24 GeV as a function of the atom momentum. The crossed distributions were obtained with Eq. (1), the dashed ones with Eq. (2). There is a small difference between two approaches. The crossed distributions show in average lower momenta because in this case conservation laws work in FRITIOF 6.0. For $A_{2\pi}$ the analogous results were obtained. So below we use in the atom yield calculations only double inclusive cross-sections Eq. (1).

2.4 $A_{\pi^+\pi^-}$, $A_{\pi^-K^+}$ and $A_{\pi^+K^-}$ yields

Using the double particle yields calculated by FRITIOF 6.0 for the short-lived sources, we have obtained the distributions of the atom yields versus the atom momentum into the DIRAC angular and momentum acceptance. The yield for $A_{\pi K}$ in the DIRAC setup is suppressed by the geometry of the spectrometer, which is optimized to detect particles with equal masses.

For the $A_{\pi K}$ identification and $A_{\pi K}$ yield increasing the DIRAC setup will be modified (see Chapter 9). After the setup modification the $A_{\pi K}$ detection efficiency will be increased by $\sim$3 times, and the $A_{2\pi}$ detection efficiency will be increased by $\sim$10% only. The all simulation results are done for modified setup except for $A_{2\pi}$ yields. For $A_{2\pi}$ atoms the results are shown for the present and modified setups.

The results of the simulations of $A_{2\pi}$ yields for the present setup are shown in figs. 2.3 and 2.4. In fig. 2.3 the yields of $A_{2\pi}$ are shown into the secondary particle channel (continuous line) and into downstream detectors (dashed line). In both cases the $\pi^{\pm}$ decay up to the Cherenkov detectors is taken into account. The number of $A_{2\pi}$ into the channel per one p-Ni interaction is $0.346 \cdot 10^{-8}$. In fig. 2.4 the atoms detected by the downstream detectors are shown as a function of kaon momentum. The number of $A_{2\pi}$ detected per one p-Ni interaction is $0.963 \cdot 10^{-9}$. The detection efficiency is 28%.

The results of the simulations of $A_{2\pi}$ yields for the upgraded setup are shown in figs. 2.5 and 2.6. The number of $A_{2\pi}$ into the channel per one p-Ni interaction is $0.346 \cdot 10^{-8}$. The number of $A_{2\pi}$ detected per one p-Ni interaction is $0.110 \cdot 10^{-9}$. The detection efficiency is 32%. For $A_{2\pi}$ the upgraded setup efficiency of detection becomes by 11% higher in comparison with the present setup.

In figs. 2.7 and 2.8 the $A_{\pi^-K^+}$ yields are shown into the secondary particle channel and into downstream detectors. In both cases the π and K decays up to the Cherenkov detectors are taken into account. The number of $A_{\pi^-K^+}$ into the channel per one p-Ni interaction is $0.327 \cdot 10^{-9}$. The number of $A_{\pi^-K^+}$ detected per one p-Ni interaction is $0.521 \cdot 10^{-10}$. The detection efficiency is 16%.

In figs. 2.9 and 2.10 the $A_{\pi^+K^-}$ yields are shown into the secondary particle channel and into downstream detectors. In both cases the π and K decays up to the Cherenkov detectors are taken into account. The number of $A_{\pi^+K^-}$ into the channel per one p-Ni interaction is $0.188 \cdot 10^{-9}$. The number of $A_{\pi^+K^-}$ detected per one p-Ni interaction is $0.294 \cdot 10^{-10}$. The detection efficiency is 16%.

Occupancy of the Scintillation Fiber Detector by $A_{\pi^-K^+}$ (dashed line), $A_{\pi^+K^-}$ (dotted line) and by sum (continuous line) is shown in fig. 2.11.

The integrated yields of $A_{2\pi}$, $A_{\pi^-K^+}$ and $A_{\pi^+K^-}$ are shown in the Table 2.1. From the Table the ratio of $A_{\pi K}$ detected by the upgraded setup to $A_{2\pi}$ atoms detected by the present setup is

$$N(A_{\pi-K^+} + A_{\pi^+K^-})/N(A_{2\pi}) = 0.084. \tag{5}$$

The ratio of $A_{\pi K}$ to $A_{2\pi}$ atoms both detected by the upgraded setup is

$$N(A_{\pi-K^+} + A_{\pi^+K^-})/N(A_{2\pi}) = 0.074. \tag{6}$$

It should be stressed that the ratios (5) (8.4%) and (6) (7.4%) are calculated with relatively high precision because they depend mainly from the ratio of the inclusive cross-sections of π and K generation (2) described well by FRITIOF 6.0.

In the Table 2.2 the minimum and maximum atom and particle momenta detected by the setup are shown.

Table 2.1: *Yields of detected $A_{2\pi}$, $A_{\pi^-K^+}$ and $A_{\pi^+K^-}$ (N_A per one $p-$Ni interaction).*

Atoms	Setup	Yields
$A_{2\pi}$	present	$9.63 \cdot 10^{-10}$
$A_{2\pi}$	upgraded	$11.0 \cdot 10^{-10}$
$A_{\pi^-K^+}$	upgraded	$0.52 \cdot 10^{-10}$
$A_{\pi^+K^-}$	upgraded	$0.29 \cdot 10^{-10}$
$A_{\pi^-K^+}$+$A_{\pi^+K^-}$	upgraded	$0.81 \cdot 10^{-10}$

Table 2.2: *Minimum and maximum atom and particle momenta detected by the setup are shown.*

Atoms	p_A min	p_A max	p_π min	p_π max	p_K min	p_K max
$A_{2\pi}$	2.6	8.6	1.3	4.3		
$A_{\pi K}$	5.0	11.4	1.1	2.5	3.9	8.9

2.5 Required particle separation coefficients

Detecting K^+ from $A_{\pi^-K^+}$ atoms we should discriminate them from pions and protons. In order to estimate the particle separation coefficients we use the experimental data on the inclusive positive pion, kaon and proton yields [EICH72] at the proton energy of 24 GeV/c in the angular and momentum range of interest. In the Table 2.3 the π^+, K^+ and p yields (in relative units) are shown for p-Cu interactions at the angles 87 mrd (5.0°) and 127 mrad (7.3°) and at the particle momenta 4 and 6 GeV/c. Remember that we study the atom production in p-Ni interactions at the angle 100 mrd (5.7°). So the experimental conditions are practically the same. From the Table we can see that the suppression pions and protons required should be approximately by 10 times.

Table 2.3: *Yields of π^+, K^+ and p at the proton energy of 24 GeV/c, in arbitrary units.*

Target	θ, mrd	GeV/c	π^+	K^+	p	π/K^+	p/K^+
Cu	87	4	52.90	6.25	24.80	8.5	4.0
Cu	87	6	18.60	2.82	20.20	6.6	7.2
Cu	127	4	27.80	4.02	17.90	6.9	4.5
Cu	127	6	6.38	1.20	9.30	5.3	7.7

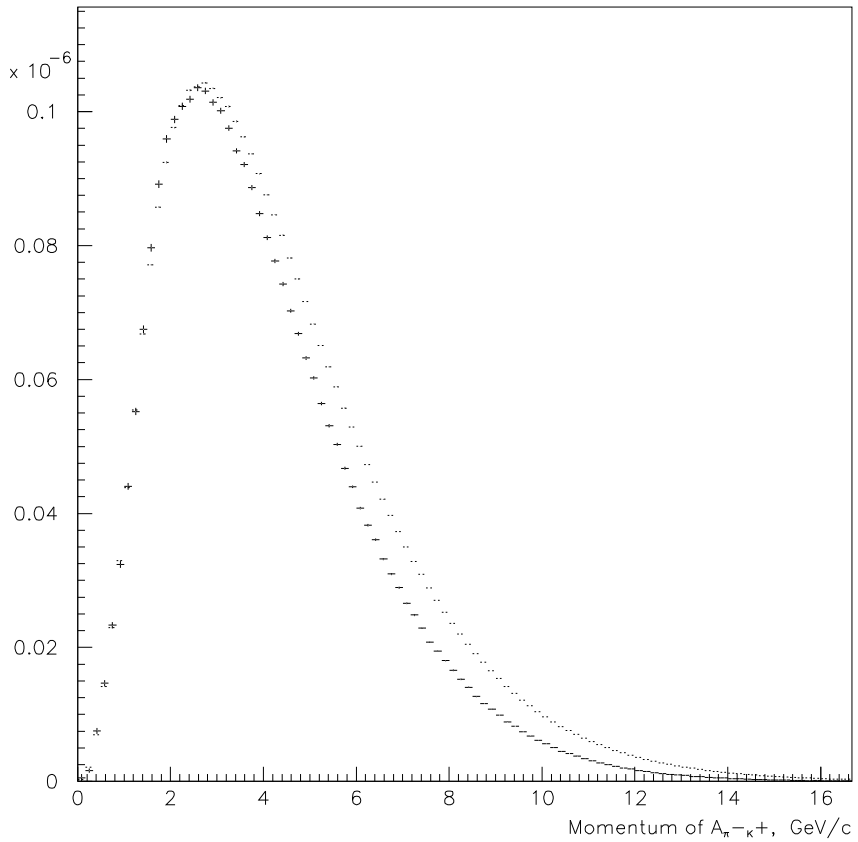

Figure 2.1: *Yields of $A_{\pi^- K^+}$ into unit solid angle calculated using Eqs. (1) (crossed distribution) and (2) (dashed distribution). The yields are calculated for the reaction $p + \mathrm{Ni} \to A_{\pi K} + X$ at the angle 5.7° and the proton energy 24 GeV as a function of the atom momentum.*

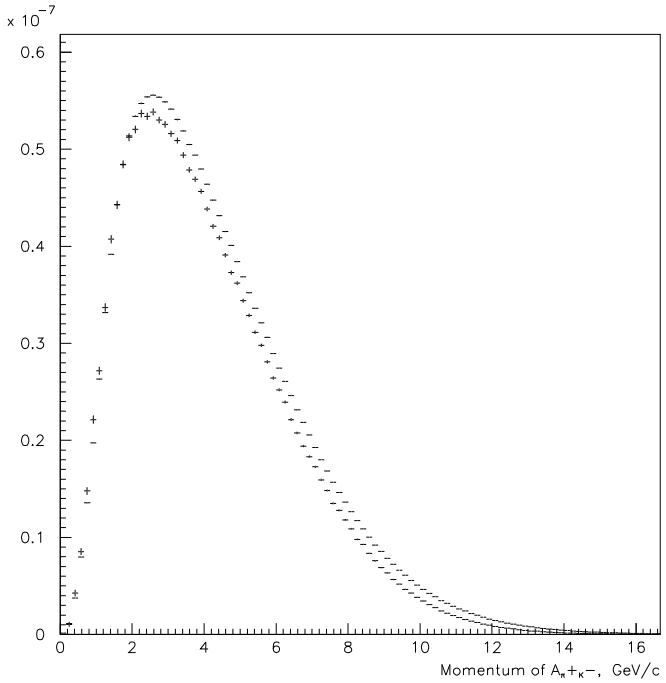

Figure 2.2: *Yields of $A_{\pi^+K^-}$ into unit solid angle calculted using Eqs. (1) (crossed distribution) and (2) (dashed distribution). The yields are calculated for the reaction $p + \mathrm{Ni} \to A_{\pi K} + X$ at the angle 5.7° and the proton energy 24 GeV as a function of the atom momentum.*

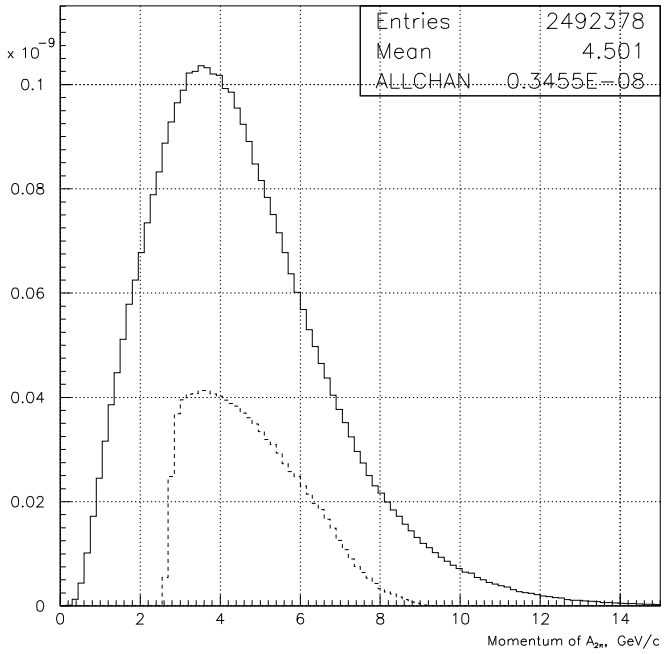

Figure 2.3: *Yield of $A_{2\pi}$ in the present setup for the reaction $p + \mathrm{Ni} \to A_{2\pi} + X$ at the proton energy $E_p = 24$ GeV as a function of the atom momentum. Continuous line shows $A_{2\pi}$ emitted into the angular aperture of the secondary channel with $\pi^\pm$ decay up to the Cherenkov counter. Dashed line refers to atoms detected by the DIRAC setup (all atoms ionised).*

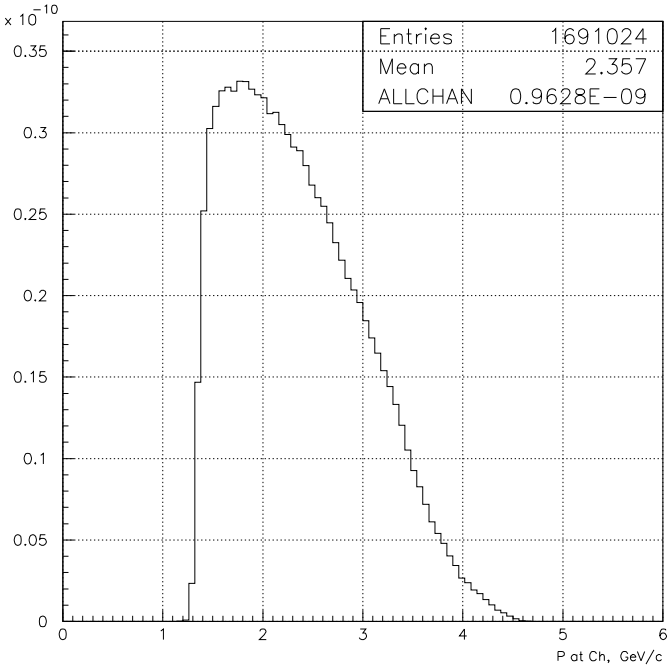

Figure 2.4: *Yield of $A_{2\pi}$ in the present setup for the reaction $p + \mathrm{Ni} \to A_{2\pi} + X$ at the proton energy $E_p = 24$ GeV as a function of the π momentum. Atoms are detected by the DIRAC setup (all atoms ionised). $\pi^{\pm}$ decay up to the Cherenkov detectors is taken into account.*

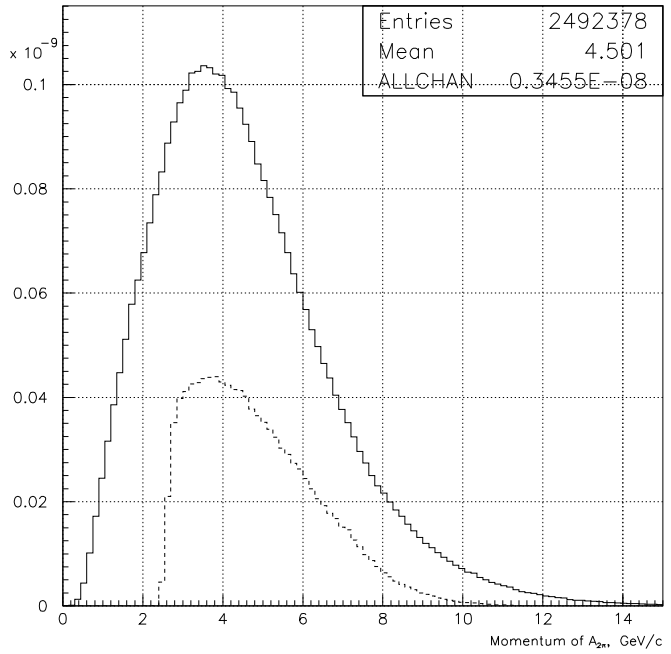

Figure 2.5: *Yield of $A_{2\pi}$ in the upgraded setup for the reaction $p + \mathrm{Ni} \to A_{2\pi} + X$ at the proton energy $E_p = 24$ GeV as a function of the atom momentum. Continuous line shows $A_{2\pi}$ emitted into the angular aperture of the secondary channel with $\pi^{\pm}$ decay up to the Cherenkov counter. Dashed line refers to atoms detected by the DIRAC setup (all atoms ionised).*

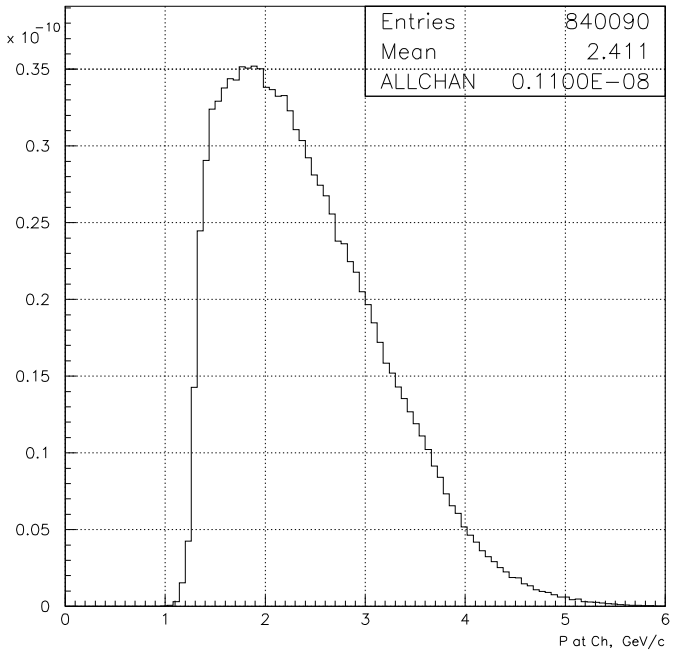

Figure 2.6: *Yield of $A_{2\pi}$ in the upgraded setup for the reaction $p + \mathrm{Ni} \rightarrow A_{2\pi} + X$ at the proton energy $E_p = 24$ GeV as a function of the π momentum. Atoms are detected by the DIRAC setup (all atoms ionised). $\pi^{\pm}$ decay up to the Cherenkov detectors is taken into account.*

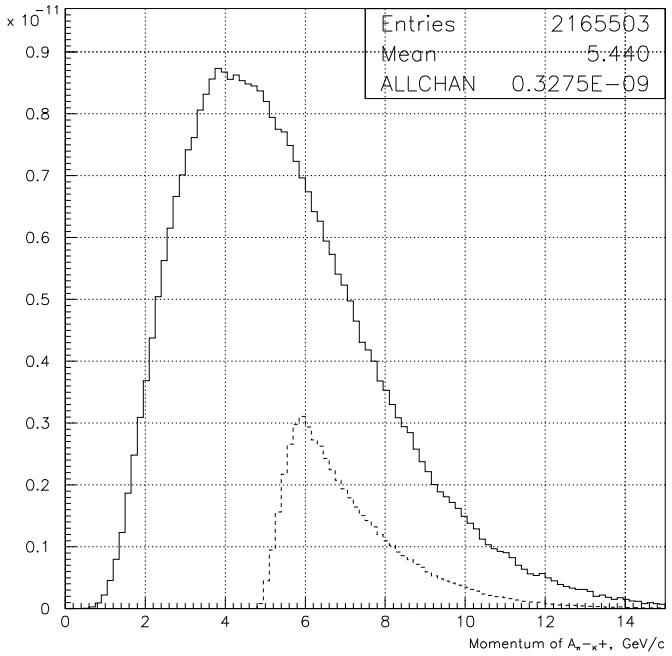

Figure 2.7: *Yield of $A_{\pi^- K^+}$ for the reaction $p + \mathrm{Ni} \rightarrow A_{\pi^- K^+} + X$ at the proton energy $E_p = 24$ GeV as a function of the atom momentum. Continuous line shows $A_{\pi^- K^+}$ emitted into the angular aperture of the secondary channel. Dashed line refers to the atoms detected by the DIRAC setup (all atoms ionised). In both cases the π^- and K^+ decay up to the Cherenkov counters is taken into account.*

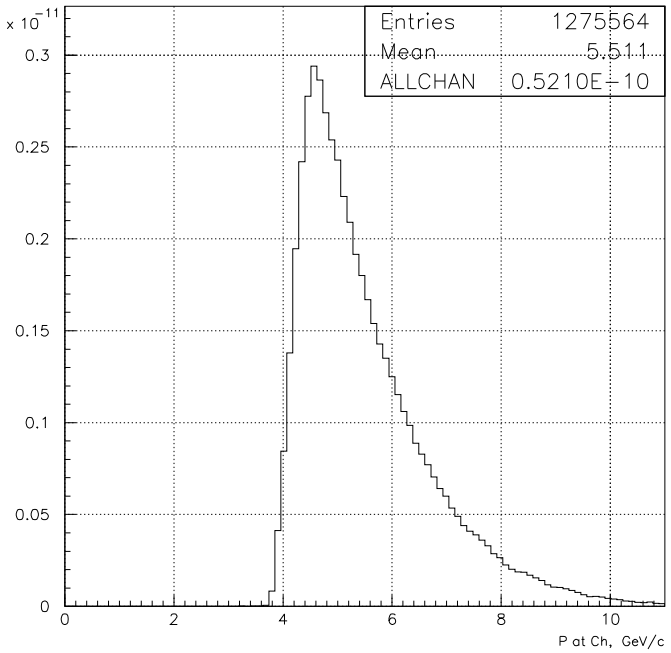

Figure 2.8: *Yield of $A_{\pi^-K^+}$ for the reaction $p + \mathrm{Ni} \rightarrow A_{\pi^-K^+} + X$ at the proton energy $E_p = 24$ GeV as a function of the K^+ momentum. Atoms are detected by the DIRAC setup (all atoms ionised). The π^- and K^+ decay up to the Cherenkov counters is taken into account.*

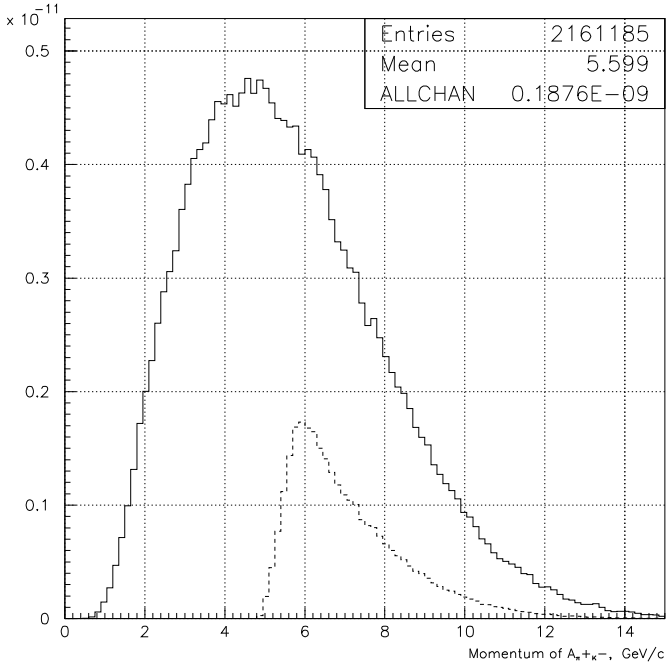

Figure 2.9: *Yield of $A_{\pi^+K^-}$ for the reaction $p + \mathrm{Ni} \rightarrow A_{\pi^+K^-} + X$ at the proton energy $E_p = 24$ GeV as a function of the atom momentum. Continuous line shows $A_{\pi^+K^-}$ emitted into the angular aperture of the secondary channel. Dashed line refers to the atoms detected by the DIRAC setup (all atoms ionised). In both cases the π^+ and K^- decay up to the Cherenkov counters is taken into account.*

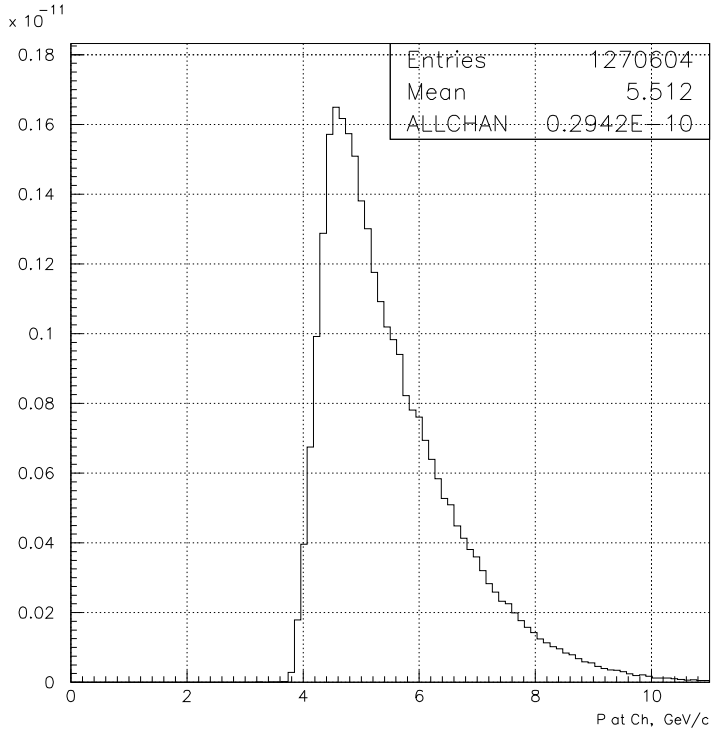

Figure 2.10: *Yield of $A_{\pi^+K^-}$ for the reaction $p + \mathrm{Ni} \rightarrow A_{\pi^+K^-} + X$ at the proton energy $E_p = 24$ GeV as a function of the K^- momentum. Atoms are detected by the DIRAC setup (all atoms ionised). The π^+ and K^- decay up to the Cherenkov counters is taken into account.*

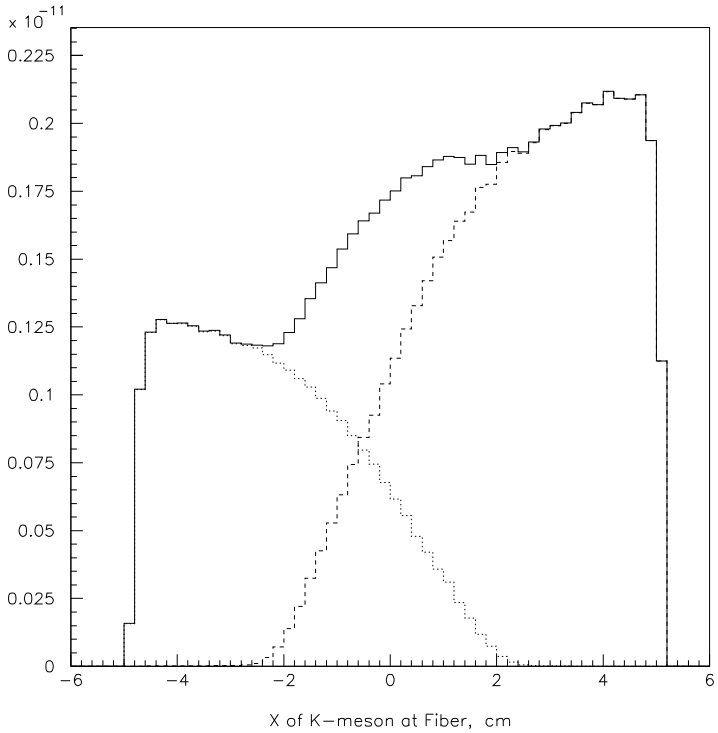

Figure 2.11: *Occupancy of the Scintillation Fiber Detector by $A_{\pi^-K^+}$ (dotted line), $A_{\pi^+K^-}$ (dashed line) and by sum (continuous line).*

Chapter 3

Interaction of relativistic πK atoms with matter

The interaction of the hydrogen-like relativistic atoms, formed by elementary particles, with the material of the production target is the key point for the observation and lifetime measurement of these atoms. In the approach proposed by Nemenov [NEME85], the atoms are detected via the low relative momentum pairs, produced from atom breakup (ionizations). To obtain the atom lifetime one has to measure the ratio between the number of "ionized" atoms and the number of produced atoms (called the atom breakup probability) and then to use the calculated dependence of $P_{\rm br}$ on the lifetime. In order to get a precise evaluation of the atom lifetime it is crucial to perform an accurate calculation of the atom breakup probability in target materials.

The theory of the $A_{2\pi}$ interaction with ordinary atoms allows to calculate the relevant cross-sections [AFAN96, DULI83, MROW86, HALA99, TARA91, VOSK98, AFAN99, IVAN99A, HEIM00, HEIM01, SCHU02, AFAN02, SANT03].

The method to relate the breakup probability with the atom lifetime was originally developed for $\pi^+\pi^-$ atoms [AFAN93A, AFAN96, ADEV95] and consists of two main steps:
— calculation of the interaction cross-sections of the relativistic hydrogen-like atoms with ordinary atoms;
— description of the evolution of the atom state population, as it traverses the target to evaluate the breakup probability.

In this Chapter we describe the application of this method to πK atom. The results on the breakup probability allow to select the optimal target for the $A_{\pi K}$ observation and lifetime measurement.

3.1 $A_{\pi K}$ interactions with target atoms

After production in hadron-nucleus interactions, $A_{\pi K}$ atoms interact with the atoms of the target material, in which they are traveling. The electromagnetic cross-sections of the $A_{\pi K}$ ground state with target atoms are of the order of 10^{-21} cm^2 (1 kbarn). Strong interaction cross-sections are much smaller and can be neglected.

Since the electromagnetic interaction depends on the charge as Z^2, the cross-section with the atom electrons is Z times smaller than with nuclei. Indeed exact calculations, performed for interactions of πK atoms with different materials [AFAN91], show that the precision of this simple estimation is sufficient. For target materials with Z about 30, which are considered below, the correction due to $A_{\pi K}$ electromagnetic interaction with electrons (the so-called incoherent scattering) leads to a cross-section increase of $\sim$2%. In the following we do not take into account this contribution, but for more precise calculations it should be considered (see also the following remark about Hartree–Fock calculations).

The projectile atom interacts dominantly with the electric field of the target atoms (Coulomb interaction). The interaction via the magnetic field arising due to the Lorentz boost is small enough. In refs. [MROW87, DENI87] it has been shown that for the interaction of relativistic $A_{\pi K}$ with Cu the total cross-section of the magnetic interaction compared with the electric one is 0.8% only, and hence is not considered here.

To describe the Coulomb interaction of the $A_{\pi K}$ with the target atoms, we use the first Born approximation [AFAN96], considering only single photon exchange. For these calculations the form factors of arbitrary discrete-discrete transitions of a hydrogen-like atom have been derived in a closed analytical form [AFAN93A, AFAN96]. The precision of this approach is of the order $(Z\alpha)^2$. Hence, this leads to an accuracy of 4% for target materials with Z about 30. For $A_{2\pi}$ the total cross-sections have been calculated more accurately using the Coulomb-modified Glauber approximation [TARA91, AFAN99, IVAN99A]. This allows to take into account all multi-photon exchanges and provides a much higher accuracy. It has been shown [AFAN99], that following this approach, all the computed cross-sections are smaller than those evaluated in the Born approximation. The difference ranges from 1.5% for titanium ($Z = 22$) up to 14% for tantalum ($Z = 73$). Thus, the accuracy of the first Born approximation is sufficient for low-Z target materials, discussed below. Nevertheless, additional calculations, using the Glauber approach, are in progress.

The calculation accuracy of the electromagnetic cross-sections depends also on the precision the form factors of target atoms. In our calculation [AFAN96] we use the Moliere parametrization of the Thomas–Fermi potential (TFM) [MOLI47]. However, more accurate representations of these form factors, based on the self-consistent field method of Hartree–Fock [HUBB75, HUBB79, SALV87], are available. Calculations of $A_{\pi K}$ interaction with various materials, performed using both methods [AFAN91], have shown that the cross-sections, calculated with the TFM parametrization, are larger by $\sim 1\%$ for the $A_{\pi K}$ ground state and slightly more for the excited states than those obtained using the Hartree–Fock approach. On the other hand, since we neglect the incoherent part of the interactions, which is of the same order of magnitude, the total uncertainty of the calculated cross-section does not exceed $1 \div 2\%$, at least for the low lying states of $A_{\pi K}$.

In the paper [HALA99] cross-sections for $\pi^+\pi^-$ atoms have been calculated using Hartree–Fock form factors at first-order of perturbation theory. For a Ni target, the difference between these cross-sections and our calculations [AFAN96] varies from -1%, for the ground state, up to 15% for states with principal quantum number $n = 10$. In spite of such large difference (see [HALA99] for discussion), the $A_{2\pi}$ breakup probability, calculated with both sets of cross-sections [AFAN00], differs only by 0.6%. Therefore, one can conclude that only the cross-section accuracy for low lying atomic states is significant for a precise determination of the atom breakup probability. For the detailed analysis of accuracy of the atom breakup probabilities one can refer to [SANT03].

3.2 Passage of $A_{\pi K}$ through the target material and target choice

In this section we describe the procedure to calculate the $A_{\pi K}$ breakup probability, using the method developed for $A_{2\pi}$ [AFAN96]. There will be given some numerical results in order to select the target material.

Using the calculated total and excitation cross-sections, the evolution of the atomic state populations during πK atom passage through the target can be described by a set of differential equations. The lifetime and momentum of $A_{\pi K}$ are parameters of this set of equations. Since the atom can get excited or deexcited in the interaction, an exact solution for any state may only be obtained as a solution of the infinite set of equations. However, since the most probable transitions are between nearest states, we can establish an upper limit to the number of equations without affecting significantly the accuracy of the result. Thus we have considered only states with principal quantum number $n \leq 10$. In this limit the

number of states, having a non-zero population (in the first Born approximation), is 220. The populations of all states, with principal quantum number $n \leq 10$, as a function of the target thickness have been found by solving the set of differential equations. These quantities takes into account $A_{\pi K}$ interaction with the target atoms and $A_{\pi K}$ annihilations.

The sum of these populations gives the probability for $A_{\pi K}$ to survive in one of the finite states with $n \leq 10$, $P_{\rm fin}$. The total populations of all other atomic states with $n > 10$, $P_{\rm tail}$, has been estimated extrapolating from the populations calculated for $n \leq 10$. Since πK atoms annihilate dominantly from 1S state [NEME85] and the population of the first few states is known with high accuracy, the probability of $A_{\pi K}$ annihilation $P_{\rm anh}$ is known very precisely. Having calculated the probabilities for $A_{\pi K}$ to survive or to annihilate, the remainder is the $A_{\pi K}$ breakup probability $P_{\rm br}$:

$$P_{\rm br} = 1 - P_{\rm fin} - P_{\rm tail} - P_{\rm anh}. \tag{1}$$

The accuracy of the $P_{\rm br}$ calculation is estimated to be not worst than 0.5%. In this way, the $A_{\pi K}$ breakup probability can be calculated in any target as a function of the atom momentum and lifetime. All the results presented below are obtained with this procedure. For a detailed discussion about the procedure accuracy, see [ADEV95, AFAN96].

In all calculations the $A_{\pi K}$ momentum has been fixed to the value 6.5 GeV/c, which corresponds to the mean momentum of the atoms, entering the experimental setup. The calculations have been performed for the set of targets, already used by the DIRAC experiment. Their thickness was selected in order to provide the same multiple scattering contribution.

In fig. 3.1 the $A_{\pi K}$ breakup probability is shown as a function of the atom lifetime for several targets. Fig. 3.2 shows the lifetime dependence of the relative uncertainty, $\Delta P_{\rm br}/P_{\rm br}$, corresponding to a 20% accuracy in the determination of the $A_{\pi K}$ lifetime. The number of produced $A_{\pi K}$, which can provide the required accuracy, can be roughly estimated to be proportional to $(\Delta P_{\rm br}/P_{\rm br})^{-2}$. Fig. 3.3 shows the lifetime dependence on the number of produced πK atoms, necessary to get the same accuracy in the lifetime measurement for all targets. It can be used to select the most adequate target for the lifetime measurement.

The $P_{\rm br}$ dependence on the atom momentum shown in fig. 3.4 illustrates that all above results will not change significantly if the average $A_{\pi K}$ momentum will differ from the value used in the above calculation.

Table 3.1 shows some numerical results. For different target materials with nucleus charge Z and for the $A_{\pi K}$ ground state the total cross-sections $\sigma_{\rm 1S}^{tot}$ and the corresponding interaction lengths $\lambda_{\rm int}$ are given. The calculations have been done assuming the $A_{\pi K}$ lifetime $4.7 \cdot 10^{-15}$ s and the $A_{\pi K}$ momentum of 6.5 GeV/c, corresponding to an annihilation length $\lambda_{\rm anh} = 15.1$ μm. For a given target thickness S, the following numbers are reported: the total population $P_{\rm fin}$ of all states with $n \leq 10$, the "tail" population $P_{\rm tail}$, the $A_{\pi K}$ annihilation $P_{\rm anh}$ and breakup $P_{\rm br}$ probabilities, and the relative uncertainty $\Delta P_{\rm br}/P_{\rm br}$ to obtain the lifetime with 20% accuracy.

Table 3.1:

	Z	$\sigma_{\rm 1S}^{tot}$ cm^2	$\lambda_{\rm int}$ μm	S μm	$P_{\rm fin}$	$P_{\rm tail}$	$P_{\rm anh}$	$P_{\rm br}$	$\Delta P_{\rm br}/P_{\rm br}$
Be	04	$6.14 \cdot 10^{-23}$	1307	2042	0.020	$3.8 \cdot 10^{-4}$	0.885	0.095	$6.4 \cdot 10^{-2}$
Al	13	$5.94 \cdot 10^{-22}$	278	560	0.041	$4.9 \cdot 10^{-4}$	0.801	0.157	$6.2 \cdot 10^{-2}$
Ti	22	$1.63 \cdot 10^{-21}$	107	251	0.067	$5.8 \cdot 10^{-4}$	0.713	0.219	$7.2 \cdot 10^{-2}$
Ni	28	$2.59 \cdot 10^{-21}$	41.9	95	0.131	$8.3 \cdot 10^{-4}$	0.559	0.310	$7.3 \cdot 10^{-2}$
Mo	42	$5.63 \cdot 10^{-21}$	27.4	85	0.125	$7.3 \cdot 10^{-4}$	0.493	0.381	$7.2 \cdot 10^{-2}$
Pt	78	$1.84 \cdot 10^{-20}$	8.14	28	0.199	$1.0 \cdot 10^{-3}$	0.249	0.551	$4.1 \cdot 10^{-3}$

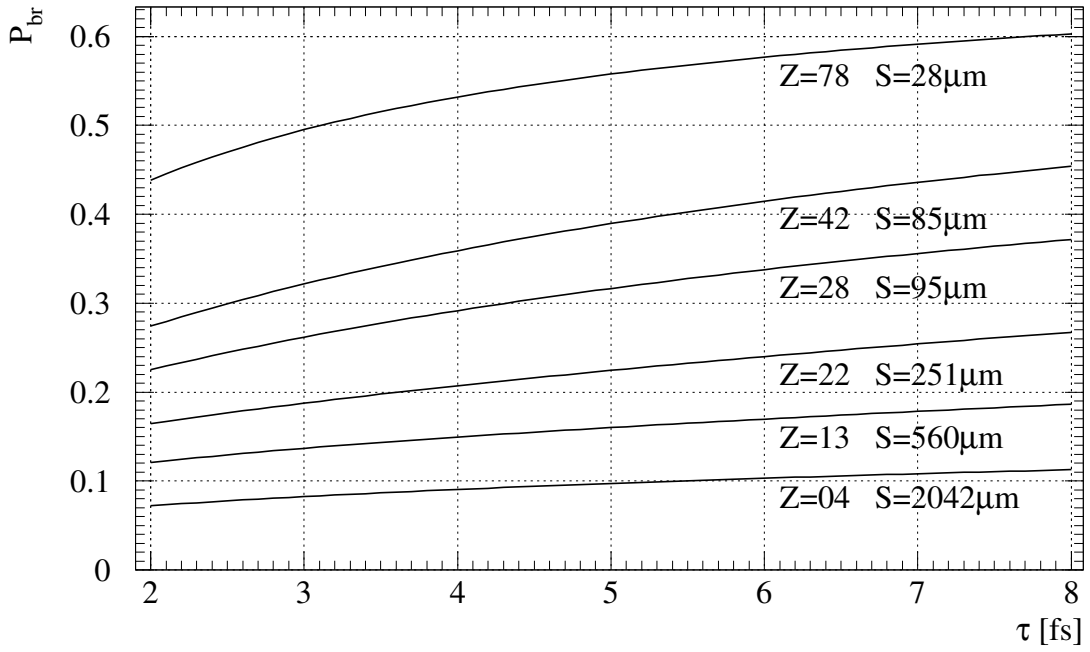

Figure 3.1: *$A_{\pi K}$ breakup probability as a function of the atom lifetime for different targets with the nucleus charge Z and the target thickness S.*

From fig. 3.1 one can conclude, that the Pt target seems to be most suitable for the $A_{\pi K}$ observation, since it provides the highest yield of "atomic" pairs. Figures 3.2 and 3.3 show, that for the expected value of the $A_{\pi K}$ lifetime around $5 \cdot 10^{-15}$ s, the Ti, Ni and Mo targets provide almost equal sensitivities for the lifetime measurement. Moreover, with these three targets, a comparable statistics is required to measure the $A_{\pi K}$ lifetime with the desired accuracy in a range of the lifetimes much wider than the theoretically estimated uncertainty.

The sensitivities for the lifetime measurement are almost the same for $A_{2\pi}$ and $A_{\pi K}$: the value $\Delta P_{\rm br}/P_{\rm br} = 7 \cdot 10^{-2}$, obtained for $A_{2\pi}$ produced in Ni target, can be compared to the corresponding value, shown in the last column of table 3.1 for $A_{\pi K}$.

3.3 Distributions of $\pi\pi$ and πK "atomic" pairs on relative momentum

The precise knowledge of the relative momentum distribution for the pairs, originating from the atom breakup ("atomic" pairs) is crucial in order to determine the overall number of produced πK atoms in the target. Fig. 3.5 shows distributions for $1s$ and $2s$ states for $A_{2\pi}$ and $A_{\pi K}$, calculated in a dipole approximation. These distributions reflect the momentum distributions before the atom breakup. Those from excited states are narrower than those from the ground one, and the $A_{\pi K}$ spectra are wider than the corresponding $A_{2\pi}$ ones, because of the higher Bohr momentum for $A_{\pi K}$.

However, the initial distributions are significantly modified by multiple scattering inside the target. Results of a simulation for $A_{2\pi}$ show, that only the $1s$ distribution contributes to the width of the final distribution, whereas the effect of the other states is completely invisible. For $A_{\pi K}$ the final momentum distribution will be wider.

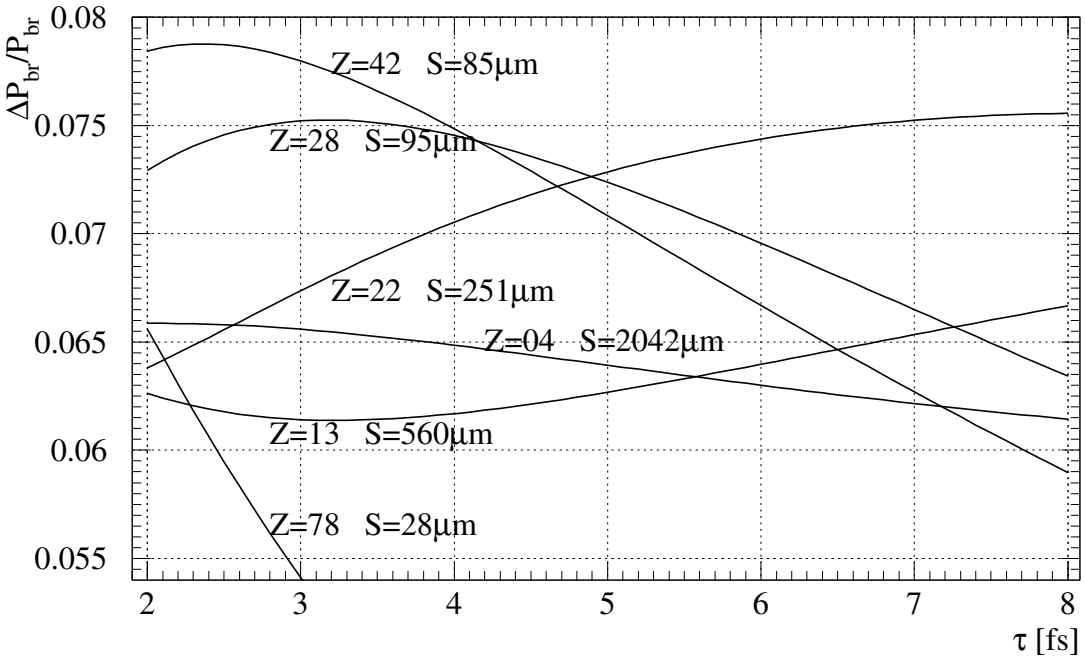

Figure 3.2: *Relative accuracy, necessary for the breakup probability, $\Delta P_{\rm br}/P_{\rm br}$, to obtain the $A_{\pi K}$ lifetime with a precision of 20%, versus the atom lifetime, for different targets.*

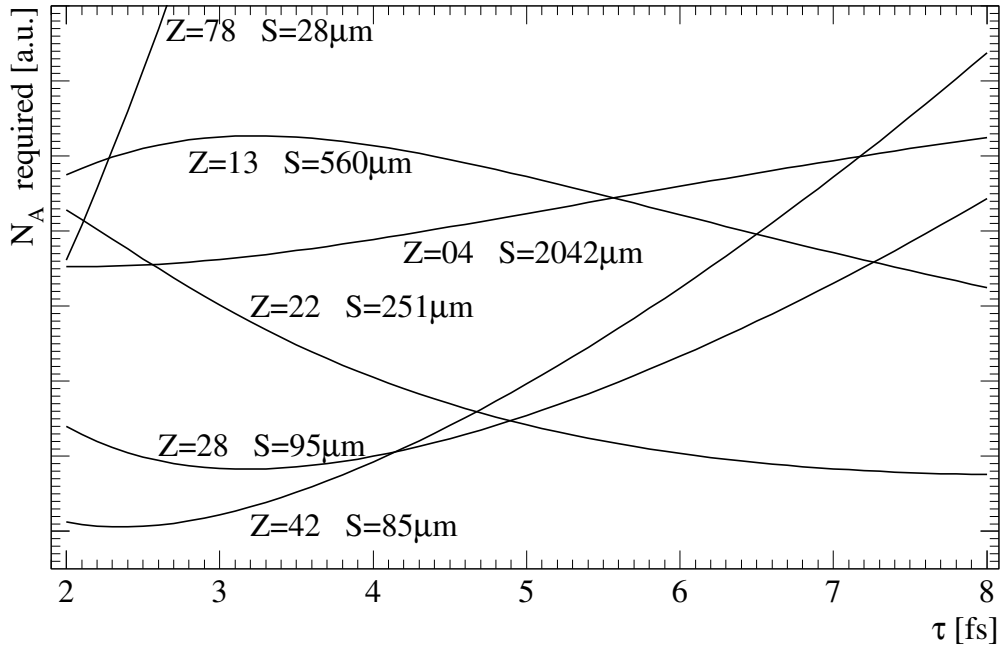

Figure 3.3: *Number of $A_{\pi K}$, versus the atom lifetime, necessary to provide the same accuracy in the lifetime measurements, for different targets.*

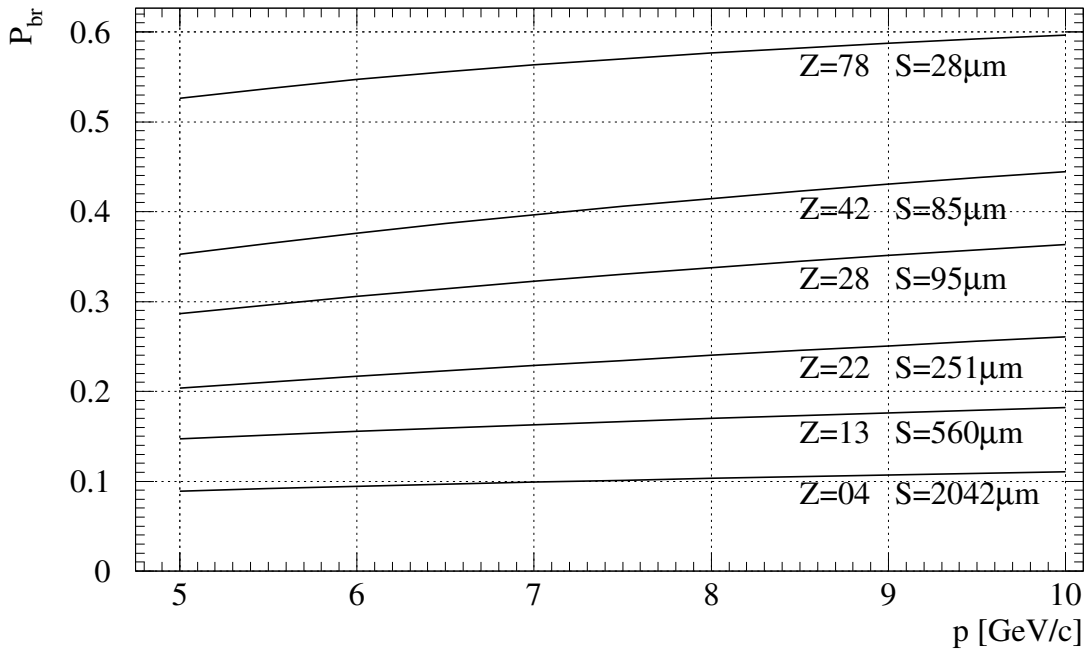

Figure 3.4: *$A_{\pi K}$ breakup probability as a function of the atom momentum for the $A_{\pi K}$ lifetime fixed to $4.7 \cdot 10^{-15}$ s.*

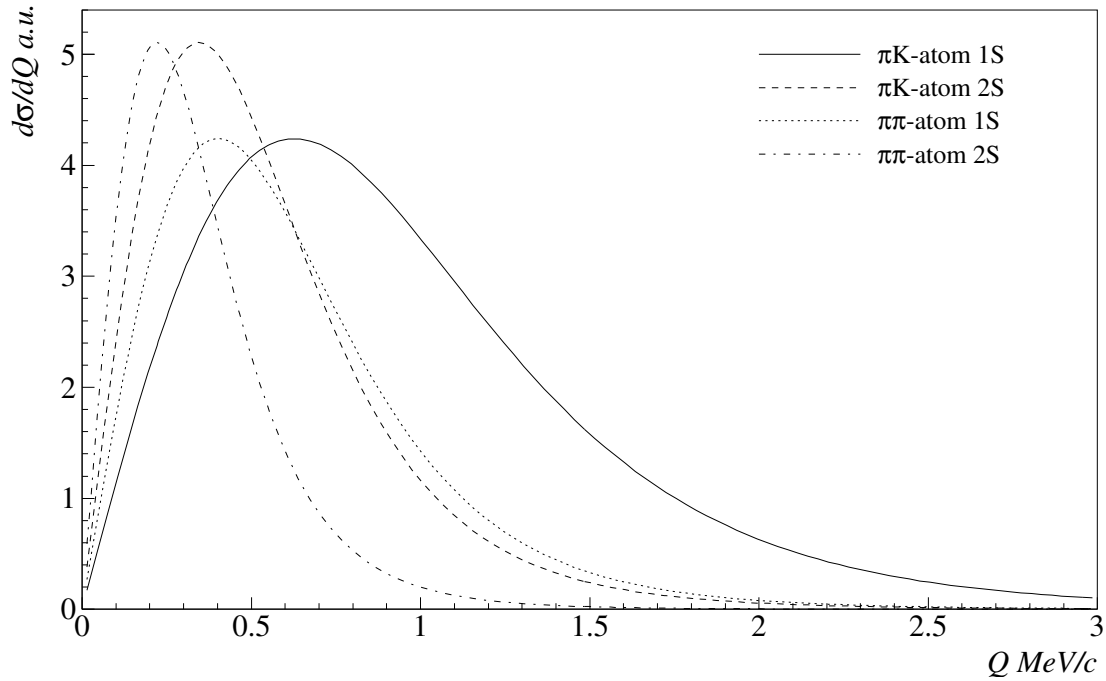

Figure 3.5: *Relative momentum distributions for pairs from atom breakup for $\pi^+\pi^-$ and πK-atoms, being initially in $1s$ and $2s$ states.*

Chapter 4

Detection of relativistic $A_{2\pi}$ and $A_{\pi K}$ and their lifetime measurement

4.1 Measurements with single target

The method for detecting $A_{2\pi}$ ($A_{\pi K}$) is based on the observation of $\pi\pi$ (πK) pairs from the atom breakup (ionization) which occurs in the production target. The main feature of these "atomic" pairs is their low relative momentum in the center of mass system ($Q < 4$ MeV/c). For a given target thickness and $A_{2\pi}$ ($A_{\pi K}$) momentum, the breakup probability of the $\pi\pi$ (πK) atom is a unique function of the lifetime in the ground state τ, [AFAN96] (see Chapter 3). Therefore, the measurement of this breakup probability allows to investigate the atom lifetime [NEME85].

The breakup probability is the ratio between the number (n_A) of ionized and the number (N_A) of produced $A_{2\pi}$ ($A_{\pi K}$) atoms:

$$P_{\rm br} = n_A/N_A\,. \tag{1}$$

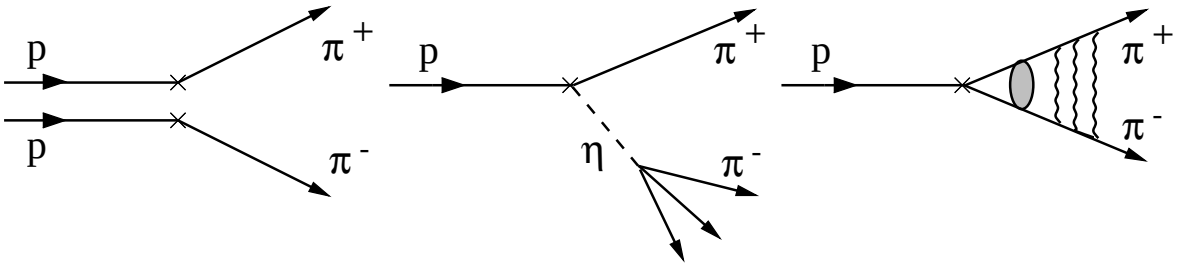

$\frac{dN_{\rm acc}}{dQ} \sim \Phi(Q)$ (a)

$\frac{dN_{\rm nC}}{dQ} \sim \Phi(Q)$ (b)

$\frac{dN_{\rm C}}{dQ} \sim \Phi(Q)(1+kQ)A_C(Q)$ (c)

Figure 4.1: *Production diagrams ($\pi\pi$): (a) accidental pairs, (b) pairs from long-lived sources, (c) pairs from short-lived sources. Accidental pairs and pairs originating from long-lived sources have the same Q distribution in the region of low Q, at least for $Q \leq 30$ MeV/c.*

All detected $\pi\pi$ (πK) pairs produced in the target include pairs of real and accidental coincidences (Figs. 4.1, 4.2):

$$N = N_{\rm real} + N_{\rm acc}\,. \tag{2}$$

"Real" pairs consist of pairs produced in the free states and "atomic" pairs:

$$N_{\rm real} = N_{\rm free} + n_A\,. \tag{3}$$

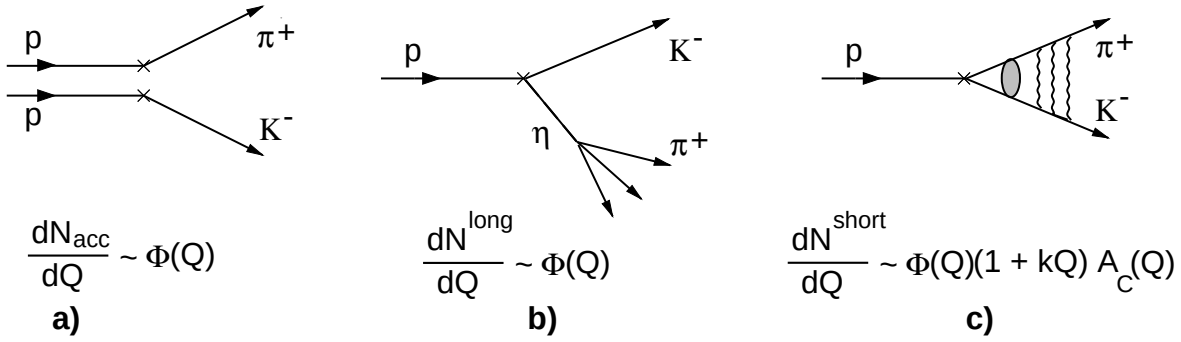

Figure 4.2: *Production diagrams (πK) of accidental pairs a), of pairs from long-lived sources b) and of pairs from short-lived sources c). Accidental pairs and pairs originating from long-lived sources have the same relative Q distribution.*

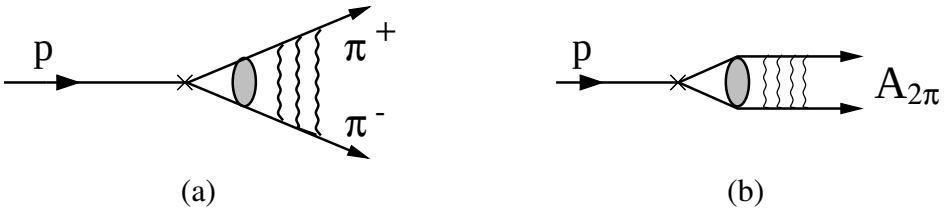

Figure 4.3: *Diagrams of "Coulomb" $\pi\pi$ pairs (a) and $A_{2\pi}$ (b) production. Both have the same strong production vertex.*

"Free" pairs can be separated with respect to the size of their production region:

$$N_{\rm free} = N_{\rm C} + N_{\rm nC}\,. \tag{4}$$

Here $N_{\rm C}$ is the number of so called "Coulomb" pairs originating from short-lived sources (ρ, K^*, ϕ, fragmentation, ..., Figs. 4.1c, 4.2c) and affected by the strong and – more significantly – Coulomb interaction in the final state. $N_{\rm nC}$ is the number of $\pi\pi$, (πK) pairs with at least one particle originating from long-lived sources (η, η',..., Figs. 4.1b, 4.2b), hence, they are named "non-Coulomb" pairs.

The value of n_A can be extracted from the analysis of the experimental Q-distribution of all free and atomic $\pi\pi$ (πK) pairs, whereas the value of N_A is related to the number of free pairs with low relative momentum.

The Q distribution of all $\pi\pi$ (πK) pairs produced in proton-nucleus interactions is described in the form:

$$\begin{aligned} dN/dQ &= dN_{\rm real}/dQ + dn_A/dQ, \\ dN_{\rm real}/dQ &= dN_{\rm nC}/dQ + dN_{\rm C}/dQ \end{aligned} \tag{5}$$

where Q is the relative momentum in the $\pi\pi$ (πK) center of mass system.

Accidental $\pi\pi$ (πK) pairs are uncorrelated in time (Figs. 4.1a, 4.2a), i.e. they are neither affected by Coulomb nor strong interaction in the final state. We use them to describe the distribution of free $\pi\pi$ (πK) pairs. If we denote the Q distribution of accidental pairs as $dN_{\rm acc}/dQ \equiv \Phi(Q)$, then the distribution of real $\pi\pi$ (πK) pairs $dN_{\rm free}/dQ$ can be approximated as follows:

$$\begin{aligned} dN_{\rm free}/dQ &= \underbrace{A\Phi(Q)}_{\rm long} + \underbrace{B\Phi(Q)(1+aQ)A_C(Q)}_{\rm short} = \\ &= B\Phi(Q)\left[(1+aQ)A_C(Q) + f\right], \qquad f = A/B \end{aligned} \tag{6}$$

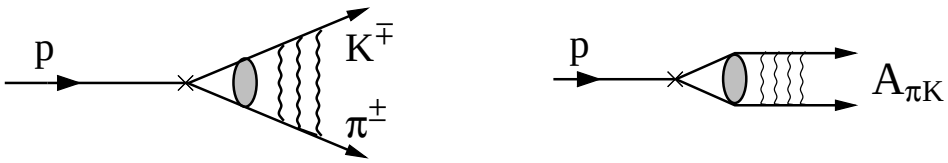

(a) (b)

Figure 4.4: *Diagrams of "Coulomb" πK pairs (a) and $A_{\pi K}$(b). Both have the same strong production vertex.*

where the terms $(1 + aQ)$ and $A_C(Q)$ take into account strong and Coulomb final-state interactions, respectively [SAKH48]. The Coulomb correlation function, $A_C(Q)$, is known from theory with a precision of $\sim 0.5\%$ [BAYE69], whereas B, a, f are free parameters, and $\Phi(Q)$ is the measured accidentals spectrum.

The experimental distribution $dN_{\rm real}/dQ$ of real $\pi\pi$ (πK) pairs is fitted by the function (6) for values $Q > 4$ MeV/c, where no "atomic" pairs are expected. The values of the fit parameters B, a and f are then used to determine the total number of free pairs ($N_{\rm real}$) in the region $0 \leq Q \leq 3$ MeV/c. Finally, the number of "atomic" pairs n_A in the interval $Q \leq 3$ MeV/c is obtained by subtracting $N_{\rm free}$ from the total number of $\pi\pi$ (πK) pairs collected in this interval. The Q distribution of atomic pairs can be theoretically predicted and can be used to determine the total number of atomic pairs for any value of Q:

$$n_A = n_A(Q \leq 3 \text{ MeV}/c) + n_A(Q > 3 \text{ MeV}/c). \tag{7}$$

From the best values of the fit parameters B, a and f we can also determine the total number of "Coulomb" pairs ($N_{\rm C}$) in the region $Q \leq 3$ MeV/c. The strong interaction part in the production of the "Coulomb" pairs with $Q \leq 3$ MeV/c as well as in the production of $A_{2\pi}$ ($A_{\pi K}$) is the same and, thus, cancels out in the ratio $N_A/N_{\rm C}$. Therefore, the number of produced $A_{2\pi}$ ($A_{\pi K}$), N_A, can be determined in the model-independent way [AFAN97, AFAN99A], *i.e.* via the relationship:

$$N_A = kN_{\rm C} = 0.615 N_{\rm C}(Q \leq 2 \text{ MeV}/c) \tag{8}$$

This procedure was used in our previous experiment, where the first experimental evidence for $A_{2\pi}$ was found and a lifetime estimation was made [AFAN93], and then later in DIRAC [ADEV95].

The lifetime dependence of the $A_{2\pi}$ ($A_{\pi K}$) breakup probability $P_{\rm br}^{\rm th}(\tau)$ can be calculated with a precision $\sim 1\%$ for any target [HALA99, AFAN99, HEIM00, HEIM01, SCHU02, AFAN02]. The $A_{2\pi}$ ($A_{\pi K}$) lifetime, τ, can be determined by comparing the measured value, $P_{\rm br}^{\rm exp} = n_A/N_A$, with the theoretical curve $P_{\rm br}^{\rm th}(\tau)$ (see Fig. 4.5).

4.2 Two-target method

The method is based on measurements with two different target types: 1) single-layer target and 2) multi-layer target of the same total thickness, but consisting of a few layers with 1 mm gaps in between. The main idea is to provide a "pure" experimental observation of $\pi\pi$ (πK) pairs from $A_{2\pi}$ ($A_{\pi K}$) breakup in the target.

Production of all types of $\pi\pi$ (πK) pairs in these two targets will be the same excluding "atomic" pairs. The probability of $A_{2\pi}$ breakup in the multi-layer targets is lower and its dependence on the lifetime is much weaker than for the single-layer target (see Fig. 4.5). Thus, the difference between the observed distributions obtained with these two targets should only contain "atomic" pairs and their number depends on the atomic lifetime τ.

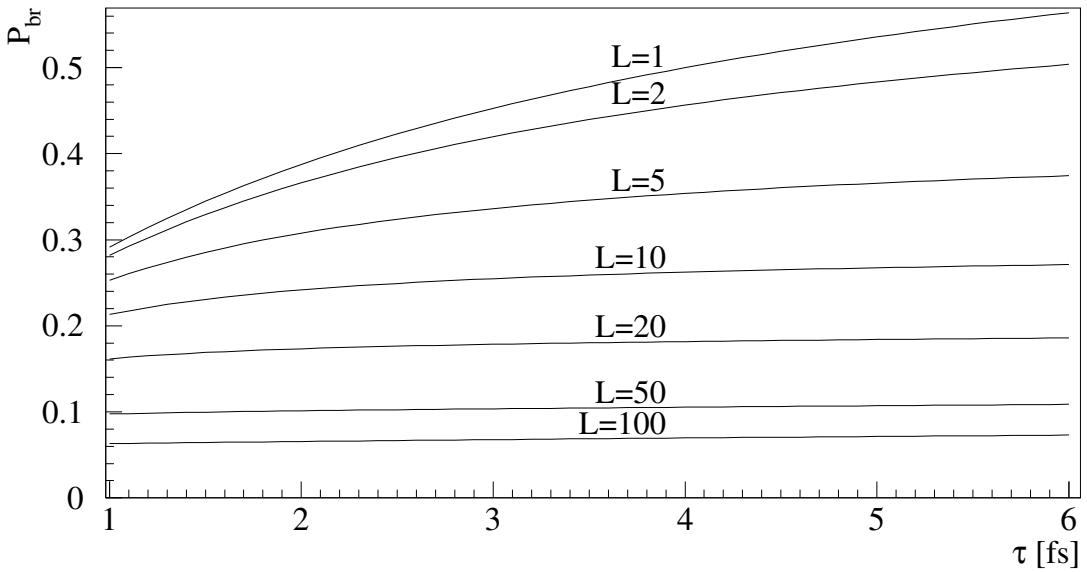

Figure 4.5: *The probability of $A_{2\pi}$ breakup in the Nickel targets consisting of the different number of layers (L) with 1 mm gap between and having a total thickness of 100 μm as a function of lifetime τ.*

Let us consider the following relationship for the numbers of "real" events (see Eq.3) in the range of small relative momentum for these two targets, assuming the same number of the proton interactions in both targets:

$$V(\tau) = \frac{N^s_{\rm real} - N^m_{\rm real}}{N_{\rm C}} = \frac{n^s_A - n^m_A}{N_A/k} = \frac{kN_A(P^s_{\rm br} - P^m_{\rm br})}{N_A} = k(P^s_{\rm br}(\tau) - P^m_{\rm br}(\tau)) \; . \qquad (9)$$

Here indices s and m denote values corresponding to the single- and multi-layer targets; $N_{\rm C}$ is number of "Coulomb" pairs extracted from the fit procedure described above in Sect. 4.1 and k comes from the relation $N_A = kN_{\rm C}$ (see Eq. 8). The dependences of the function $V(\tau)$ on the lifetime τ are shown in Fig. 4.6.

To compare two methods of the lifetime measurement the theoretical values of $P_{\rm br}(\tau)$ and a part of the data collected in 2001 with the Nickel target have been used: $N_{\rm real} = 17696 \pm 135$, $N_{\rm C} = 13763 \pm 250$ and $n_A = 3265 \pm 259$. To simulate n_A for multi-layer target the measured value have been corrected according to $P_{\rm br}$ values. Summarized values are given in the Table 4.1. The first column contains information for the single-target method, and the rest for the two-target method with different numbers of layers of the multi-layer target. The nomenclature of the row labels is the following: "Layers" stands for number of layers in the target; "Thickness" is the thickness of one layer in μm; "$P_{\rm br}$" is the theoretical probabilities of the atomic breakup in each target at the predicted value of $\tau = (2.9 \pm 0.1) \cdot 10^{-15}$ s (10), V is the function defined in Eq.9; "Relative derivative" is $(dP_{\rm br}/d\tau)/P_{\rm br}$ for the first column and $(dV/d\tau)/V$ for all other; "Statistics" is the multiplication factor for the required raw data to have the same statistical accuracy of the lifetime measurement as for the single-target method. For the two-target method it was assumed that total statistics were divided into equal parts for measurements with the single- and multi-layer targets.

From the Table 4.1 it can be seen that the required amount of raw data with respect to the statistical accuracy for the two-target method (with the multi-layer target having the number of layers between 10 and 20) is almost the same or even less as compared to the single-target method. This is due to two

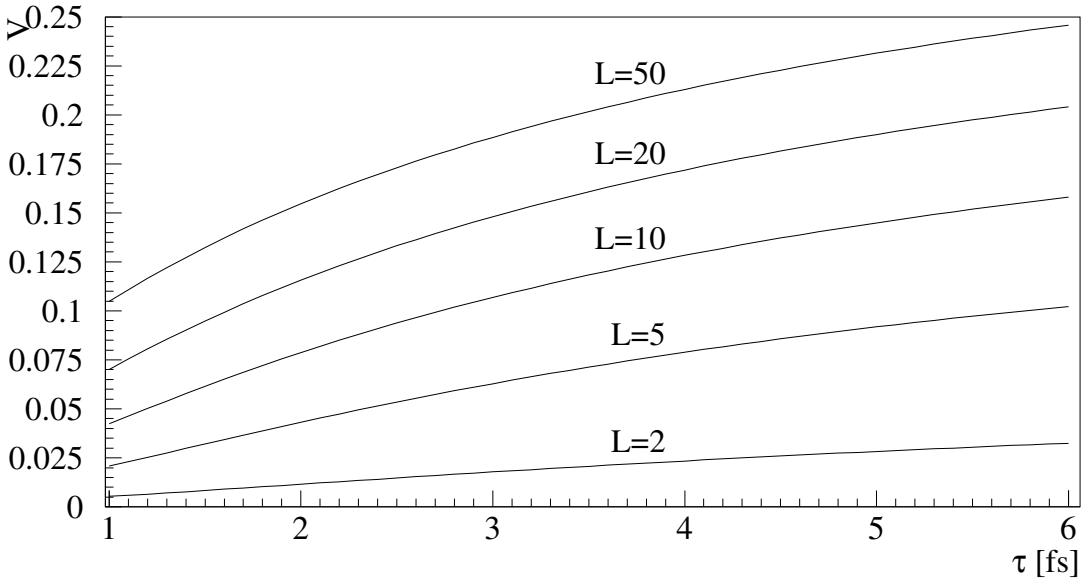

Figure 4.6: *Variable V defined in Eq.9 as a function of the $A_{2\pi}$ lifetime τ for different number of layers (L).*

Table 4.1:

Layers	1	5	10	20
Thickness (μm)	100	20	10	5
$P_{\rm br}$	0.447	0.334	0.254	0.178
V		0.061	0.104	0.145
Relative derivative	0.126	0.298	0.241	0.195
Statistics	1.0	2.1	1.1	0.84

reasons. First, $V(\tau)$ function has much high sensitivity to the lifetime τ compared to $P_{\rm br}(\tau)$ which is evidenced by the higher relative derivative. Second, the statistical accuracy of $V(\tau)$ increases with the increasing difference in the numerator. Thus with the smaller total number of observed $A_{2\pi}$ we can measure the lifetime with the same or better accuracy.

Moreover, the results of the fitting procedure described above in Sect. 4.1, which is one of the main sources of the systematic error for the lifetime measurement, enters only in the denominator of $V(\tau)$. It can be shown that in this case its contribution to the systematic error of lifetime is at about 6 times smaller than for the case of the single-target method.

Thus, the two-target method with the number of layers in the multi-layer target between 10 and 20 will be used for the lifetime measurement.

The target with 12 layers have already been produced and data using it was collected in the 2002 and 2003 runs. For demonstration of the two target method the difference (without any fit procedure) of the experimental distributions collected with single and multi-layer targets containing the pure "atomic" pair signal is shown in Fig. 4.7.

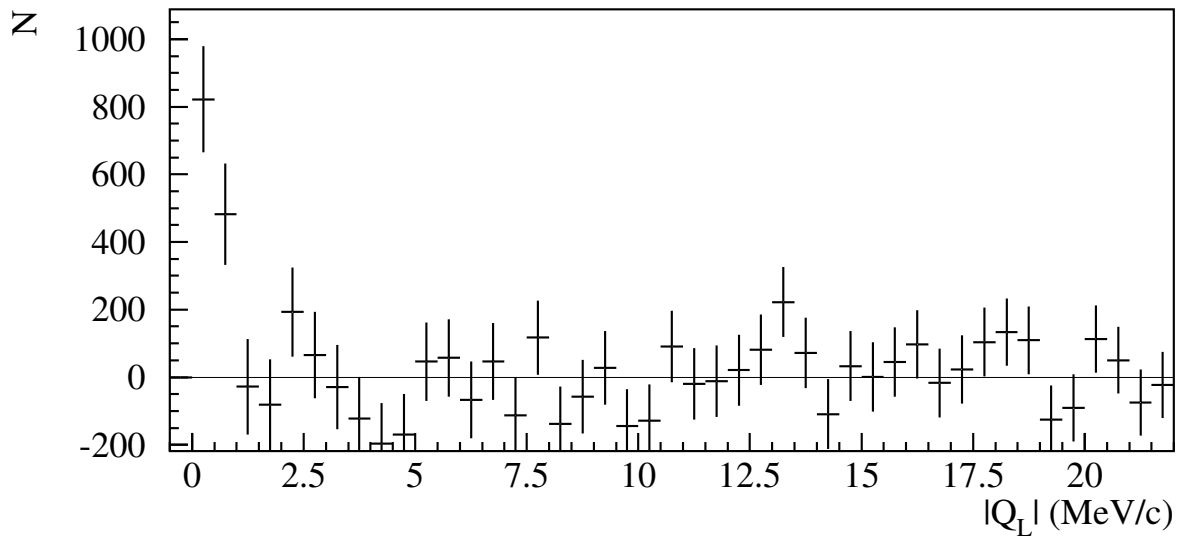

Figure 4.7: *Difference of the experimental distributions over Q_L of the data collected with single and multi-layer targets shows the pure "atomic" pair signal with $Q_L < 1.5$ MeV/c.*

Chapter 5

Observation of $A_{2\pi}$ and $A_{\pi K}$ long-lived states

5.1 Observation of $A_{2\pi}$ long-lived states, physical motivation

The lifetime of $A_{2\pi}$ for annihilation in the process $A_{2\pi} \to \pi^0 + \pi^0$ depends on the difference between the s-wave $\pi\pi$ scattering lengths a_0 and a_2 with isospins zero and two [URET61, BILE69, JALL98, IVAN98, GASS01].

$$\frac{1}{\tau} \sim (a_0 - a_2)^2. \tag{1}$$

To get the values of a_0 and a_2 separately basing on the $\pi^+\pi^-$ atom data, one may use the fact that the energy splitting between levels ns and np, $\Delta E_n = E_{ns} - E_{np}$, depends on the the another combination of scattering lengths: $2a_0 + a_2$. The dependence of the atomic level shift on the value of the πN- scattering length in the s-state has been derived in [DESE54]. The influence of the strong and electromagnetic interactions on the $A_{2\pi}$ energy structure was studied in [KARI79, AUST83, EFIM86, GASH98, EIRA00, RUSETS]. The difference ΔE_n between the energies of atomic states ns and np is

$$\Delta E_n = E_{ns} - E_{np} = \Delta E_n^{\rm s} + \Delta E_n^{\rm vac} + E_n^{\rm rel} + E_n^{\pi} \approx \Delta E_n^{\rm s} + \Delta E_n^{\rm vac} \tag{2}$$

where $\Delta E_n^{\rm s}$, $\Delta E_n^{\rm vac}$, $E_n^{\rm rel}$, E_n^{π} determine the contribution into ΔE_n of strong interaction, vacuum polarization, relativistic corrections and electromagnetic structure of pion. By measuring the value of ΔE_n we can determine the numerical value of $\Delta E_n^{\rm s}$, as the rest of the terms in Eq. (2) have been calculated with high accuracy. For the $n = 2$ state $E_2^{\rm vac} = -0.107$ eV is known from the QED calculations [KARI79, GASH98, RUSETS]. Since the value of $\Delta E_n^{\rm s}$ obeys the relation [EFIM86, GASH98]

$$\Delta E_n^{\rm s} \sim (2a_0 + a_2)\ , \tag{3}$$

an accurate measurement of ΔE_n allows to determine the value of $2a_0 + a_2$. For a_0 and a_2 from [COLA00] the values of the energy shifts are: $\Delta E_2^{\rm s} \approx -0.45$ eV and $\Delta E_2 \approx -0.56$ eV.

Thus measurements of the lifetime τ and ΔE_n make possible to obtain the values of a_0 and a_2 separately in a model-independent way.

The method of measuring ΔE_n was qualitatively discussed in [NEME85]. In order to measure ΔE_{ns-np}, the dependence of the lifetime for long-lived $A_{2\pi}$ states ($l \geq 1$) on the applied electric field can be studied [NEME85, NEME01, NEME02].

In inclusive processes $A_{2\pi}$ are produced in s-states and their distribution over the principal quantum number n is proportional to n^{-3}. When moving inside the target, the relativistic $A_{2\pi}$ interacts with the electric field of target atoms and may come out of the target with orbital momentum $l \neq 0$. Calculations show that up to $\sim 10\%$ of the atoms, generated in the thin target, reach the vacuum region as long-lived

states [AFAN97A]. The main part of these atoms will be in $2p$-states. For $A_{2\pi}$ in a p-state the decay into two π^0-mesons is forbidden by the conservation low for the angular momentum and the process $A_{2\pi} \to \pi^0 + \gamma$ is also strongly suppressed. Therefore, the main mechanism of annihilation is the $2p - 1s$ radiative transition with a subsequent annihilation from $1s$-state into two π^0-mesons within the lifetime of $\tau_{1s} \approx 3 \times 10^{-15}$ s. Thus, the lifetime of the atom in $2p$-state is determined by the radiation transition probability and equals to $\tau_{2p} = 1.17 \times 10^{-11}$ s [NEME85]. For the average $A_{2\pi}$ momentum in DIRAC of 4.5 GeV/c ($\gamma = 16.6$) the corresponding decay length for $2p$-state is 5.7 cm, for $3p$ — 35 cm and for $4p$ — 138 cm.

The $A_{2\pi}$ decay from ns-states is allowed with the corresponding lifetimes $\tau_{ns} = \tau_{1s} n^3$. Since the lifetime in np-states is about 10^3 of the lifetime in the ns-state, the possibility exists to measure the energy difference of these levels by exerting an electrical field on the atom and measuring the dependence on the field of the decay probability due to mixing of ns- and np-state in the external electrical field.

In [NEME01] the dc field effect on the $A_{2\pi}$ atom life-time is studied and the possibility is demonstrated for measuring the splitting between $2s$- and $2p$-levels with the use of relativistic atomic beams produced in existing accelerators.

The transverse magnetic field B_0 in the lab reference frame increases its amplitude in the atom reference frame and equals $B = \gamma B_0$ (γ is Lorentz factor). The corresponding electric field has nearly the same amplitude $F = \beta B$ (β is atom velocity in the lab frame) and perpendicular to the atom momentum.

In the electric field a small admixture of the $2s$-state to the $2p$ wave function arises and this admixture may cause significant acceleration of the decay for atoms being initially in $2p$-states. At $B_0 = 4$ T and $\gamma = 20$ the decay rate increases more than twice.

5.2 Observation of $A_{\pi K}$ long-lived states, physical motivation

The energy difference between the πK atomic levels $2s$ and $2p$ consists of an electromagnetic component, $\Delta E^{em}_{2s-2p} = -0.29$ eV [KARI86] and a strong component $\Delta E^{\rm s}_{2s-2p} \propto 2a_0^{1/2} + a_0^{3/2}$. By taking the πK scattering lengths from (12), we get $\Delta E^{\rm s}_{2s-2p} = -0.9$ eV [EFIM87]. This difference, in principle, can be measured experimentally [NEME85]. The ChPT expression for $2a_0^{1/2} + a_0^{3/2}$ involves combination of constants $L_8 + 2L_6$ providing information on the value of quark condensate and the ratio of the strange to non-strange quark masses [DESC03].

5.3 Yields of $A_{2\pi}$ long-lived states

To obtain the numerical value of the long-lived state production we have use the approach describing evolution of the atomic states population in terms of probabilities, used for all above calculations of the atom breakup probabilities. For the all values below the $A_{2\pi}$ ground state lifetime was fixed to 3.0×10^{-15} s and the momentum to 4.5 GeV/c. It should be mentioned that the results are essentially independent on these values.

Production of $\pi^+\pi^-$ atoms in the np states have been considered for different target materials and thicknesses with the intent to optimize the experimental conditions for their observation. It have been shown that for the DIRAC experiment usage of thiner targets with smaller Z provides increase of yield of np states and a better ratio to the atom breakup. In Table 5.1 a set of targets providing the highest yield of the long-live states with the orbital quantum number $l \geq 1$ are shown. The yields of p-states with the magnetic quantum numbers $m = 0$ ($2p_0$, $3p_0$, $4p_0$) which are can be mixed with s-states in the electrical field and thus suitable for the energy shift measurement are shown also.

Table 5.1: *For different target material with atomic number Z the following values are shown: the probabilities of $A_{2\pi}$ breakup, the total yield of the long-live states $\sum(l \geq 1)$ including states with $n \leq 7$, yields of p-states with the magnetic quantum numbers $m = 0$ $2p_0$, $3p_0$, $4p_0$ and their sum up to $n = 7$ $\sum(l = 1, m = 0)$. The target thicknesses were chosen to provide the maximum yield of the long-live states.*

Target		Thickness	Breakup	$\sum(l \geq 1)$	$2p_0$	$3p_0$	$4p_0$	$\sum(l = 1, m = 0)$
	Z	μm						
Be	04	100	4.45%	6.01%	1.18%	0.46%	0.15%	1.90%
C	06	50	5.00%	6.92%	1.46%	0.51%	0.16%	2.52%
Al	13	20	5.28%	7.84%	1.75%	0.57%	0.18%	2.63%
Ni	28	5	9.42%	9.69%	2.40%	0.58%	0.18%	3.29%
Pt	78	2	18.8%	10.5%	2.70%	0.55%	0.16%	3.53%

5.4 Methods of observation of $A_{2\pi}$ and $A_{\pi K}$ long-lived states

The atoms in metastable states may be observed in the DIRAC setup without any change and the results can demonstrate the feasibility of ΔE_{ns-np} measurement.

5.4.1 Detection of long-lived states with breaking foil

For that it is necessary to put a retractable Platinum foil in the secondary particle channel downstream of the target to break up metastable states. Measurements with and without the foil and subtraction of distributions at low relative momenta give an effect which is due to presence of long-lived states. It is necessary to avoid the proton beam interaction with the foil. For this reason the shortest distance between the target and foil can be of order of 10 cm (see Fig.5.1).

Usage of the permanent magnet (see appendix. B) installed in the channel between the target and the foil will destroy the peak in the relative momentum distribution for all "atomic" pairs produced in the target and thus will provide significantly better background conditions for observation of "atomic" pairs produced in the foil.

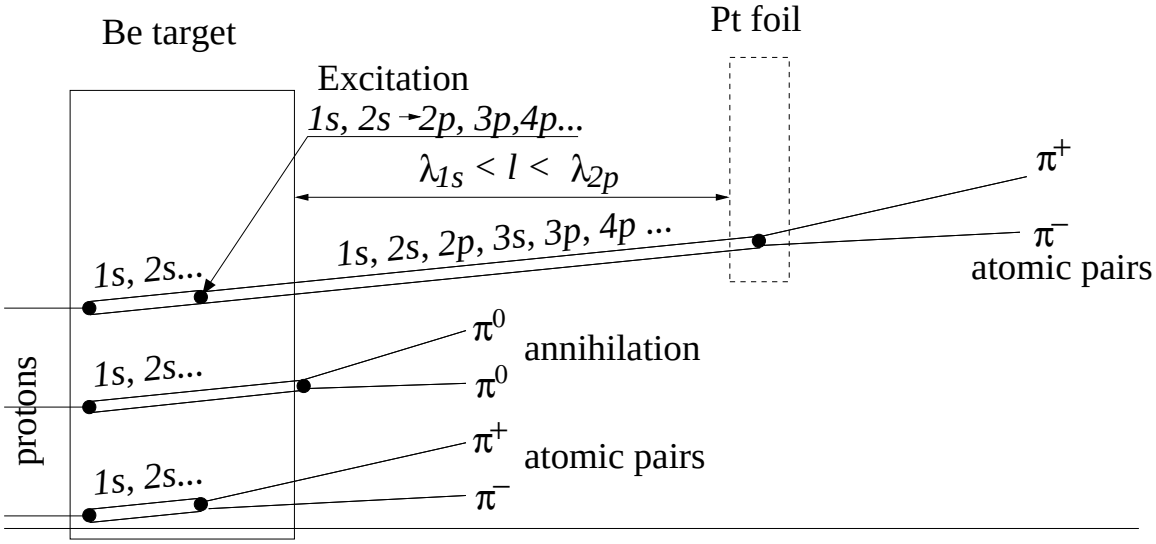

Figure 5.1: Illustration for observation of the $A_{2\pi}$ long-lived states with breaking foil.

5.4.2 Detection of long-lived states with two layer target

The foil insertion in the secondary channel changes experimental conditions (γ conversion and so on) and a part of long-lived states will annihilate before the foil. We can circumvent these shortcomings using a two layer target.

Let us consider the combination of foils of two materials — Beryllium and Platinum — inserted in the beam with the gap of 1 mm between. Calculation shows that the best observable effect can be obtain with 100 μm Be and 2 μm Pt foils. The nuclear efficiencies of these targets are 2.5×10^{-4} and 2.3×10^{-5} respectively. So the Beryllium foil will serve as the main source of $A_{2\pi}$ which will break up inside with the probability of 4.5% and dominantly escape the foil. The ns states will annihilate at the distance of tens micron. If the Platinum foil will be placed behind at the distance of 1 mm it will break up the long-live states increasing the total probability of $A_{2\pi}$ breakup in the two foils up to 10.9%. However placing the Platinum foil ahead of the Beryllium one we will not observe this increasing and the total probability of $A_{2\pi}$ for this case will be 6.2%. The difference between two last numbers can be observed to prove the existence of the log-lived states of $A_{2\pi}$.

Chapter 6

Present DIRAC setup

6.1 General description

The aim of the DIRAC experiment is to detect $\pi^+\pi^-$ pairs with very small opening angles and therefore it is designed to measure their relative c.m. momentum Q with high precision $\sim$1 MeV/c. To accomplish this task a double arm magnetic spectrometer was commissioned during October – November 1998 at the T8 experimental area of the CERN PS East Hall (fig. 6.1).

The entire DIRAC apparatus is surrounded by radiation shielding to protect the outside area against radiation. A detailed description of the DIRAC setup may be found in [ADEV03]. A view of the DIRAC setup inside the radiation shielding is shown in fig. 6.2. A top view of the setup with indication of the different components is shown in fig. 6.3. The side and isometric views of the DIRAC setup are shown in figs. 6.4 and 6.5.

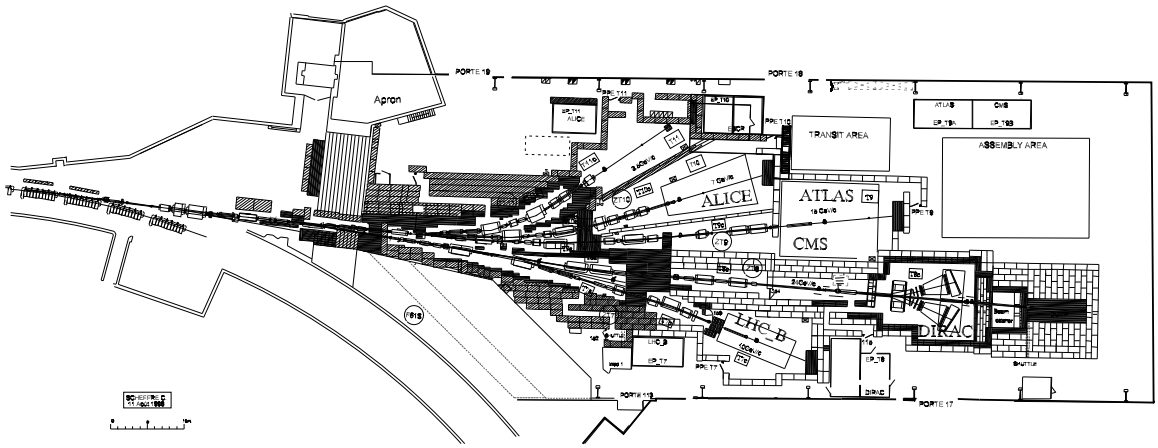

Figure 6.1: *East Hall general view.*

The DIRAC setup consists of a proton beam line, target station, secondary particle channel, spectrometer magnet and upstream and downstream detectors.

The 24 GeV/c PS proton beam entering the DIRAC experimental setup encounters the target station. Several target materials (Be, Al, Ti, Ni, Mo, Pt and Pb) have been installed and can be placed alternatively across the beam by rotating a remotely controlled support device.

The proton beam intensity during data taking was $0.9 \cdot 10^{11}$ per spill with a spill duration of $400 \div 450$ ms. The beam-line was designed to decrease the beam halo to a negligible level [ADEV95], [FERR97]. The horizontal and vertical widths of the beam spot were $\sigma_{\rm hor} = (0.80 \pm 0.08)$ mm and $\sigma_{\rm vert} = (1.60 \pm 0.07)$ mm, respectively [LANA02].

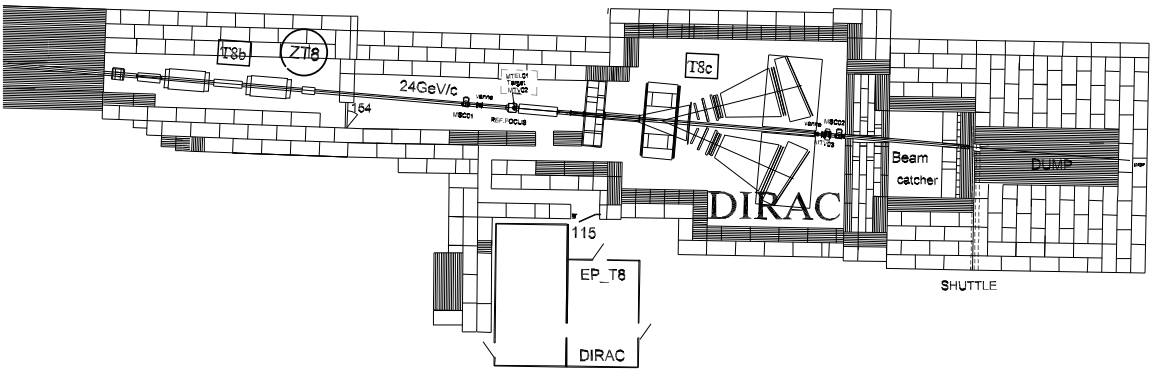

Figure 6.2: *The DIRAC setup and the radiation shielding.*

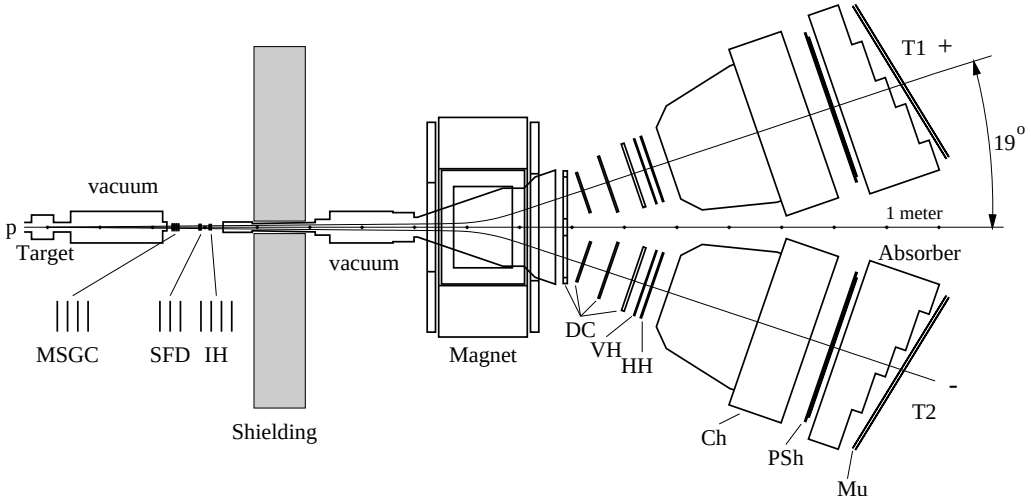

Figure 6.3: *Schematic top view of the DIRAC spectrometer. Upstream of the magnet: microstrip gas chambers (MSGC), scintillating fiber detectors (SFD), ionization hodoscopes (IH) and shielding of iron. Downstream of the magnet, in each arm of the spectrometer: drift chambers (DC), vertical and horizontal scintillation hodoscopes (VH, HH), gas Cherenkov counter (Ch), preshower detector (PSh) and, behind the iron absorber, muon detector (Mu).*

Data were collected with the Ni targets of 94 and 98 μm thicknesses, corresponding to $\sim 6.4 \times 10^{-4}$ nuclear interaction probability [PDG002].

The spectrometer axis is inclined upward by 5.7° with respect to the proton beam (fig. 6.4). Particles produced in the target propagate in vacuum up to the upstream (with respect to the spectrometer magnet) detectors and then re-enter into a vacuum channel which ends with a flat vacuum chamber placed between the spectrometer magnet poles. The vacuum exit window is made of a 0.68 mm thick Al foil. The secondary particle channel angular aperture is defined by a square collimator and is 1.2 msr ($\pm 1^{\circ}$ in both directions). The dipole magnet properties are $B = 1.65$ T and $BL = 2.2$ Tm. The upstream detectors are located in an air gap of the secondary channel.

The momentum range covered by the spectrometer is $1.2 \div 8$ GeV/c. The relative resolution on the particle lab momentum is $3 \cdot 10^{-3}$. The resolutions on the relative c.m.-momentum of a $\pi^+\pi^-$ pair from atomic breakup, $\vec{Q} = (Q_x, Q_y, Q_L)$, are in the transverse plane (with respect to the total momentum $\vec{p}^{\,Lab}_{\pi^+\pi^-}$ in the laboratory frame) $\sigma_{Q_x} \approx \sigma_{Q_y} \leq 0.49$ MeV/c and longitudinally $\sigma_{Q_L} = 0.50$ MeV/c, here Q_L is a projection on the total lab momentum of pair.

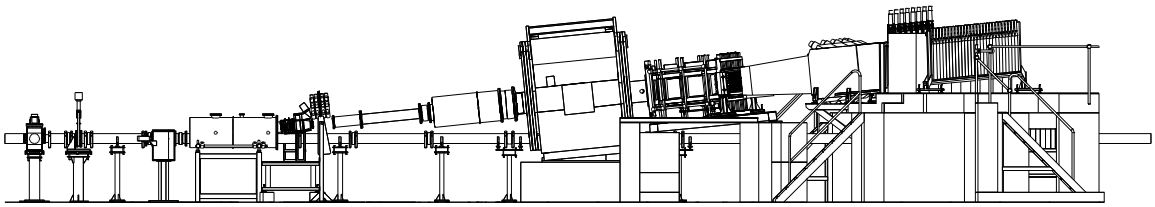

Figure 6.4: *Setup side view.*

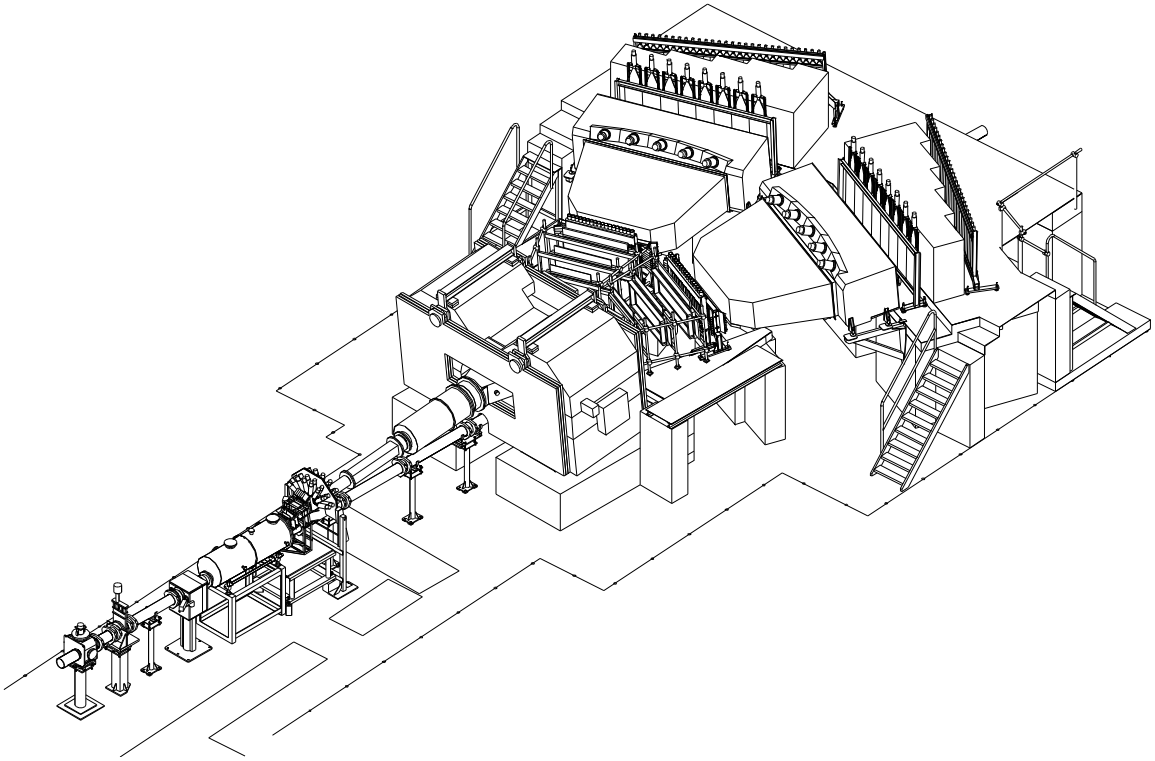

Figure 6.5: *DIRAC setup isometric view. The radiation shielding boundaries are drawn on the floor.*

The setup allows to identify electrons (positrons), protons with $p \leq 4$ GeV/c (by time-of-flight) and muons. It cannot distinguish π- from K-mesons, but kaons constitute a negligible contamination [GORC00, ADEV02].

To track the produced pion pairs, a first set of detectors is placed upstream of the spectrometer magnet:
— 4 planes of Micro Strip Gas Chambers (MSGC) with Gas Electron Multiplier (GEM);
— Scintillating Fibre Detector (SFD);
— Ionization Hodoscope (IH).

Downstream of the magnet two identical detector arms are located both including the following detectors:
— 4 modules of Drift Chambers (DC1–DC4);
— Vertical Hodoscope (VH);
— Horizontal Hodoscope (HH);
— Threshold gas Cherenkov counter (Ch);

— Preshower counter (PSh);
— Muon identification system (Mu).

6.2 Detectors upstream of the magnet

The upstream detectors are 2.5 to 3 m away from the target and cover an area of roughly $10 \times 10\,\mathrm{cm}^2$. The detectors perform tracking before the magnet. They comprise the microstrip gas chambers (MSGC), the scintillating fiber detector (SFD) and the ionization hodoscopes (IH). The total thickness of all upstream detectors, including the vacuum channel windows, is $6.0 \times 10^{-2} X_0$.

6.2.1 Microstrip Gas Chambers

The microstrip gas chambers (MSGC) measure particle coordinates using 4 identical planes: X, Y, U and V, with rotation angles of $0°$, $90°$, $5°$, $85°$ with respect to the X-plane perpendicular to the secondary beam axis.

Each chamber has a gas gap of 6 mm divided into two 3 mm regions by means of a GEM foil with a 140 μm pitch pattern of holes with 50/70 μm (internal/external) hole diameters. Each plane has 512 anode strips with a pitch of 0.2 mm made of Chromium on a bare Desag D263 glass, with 9 μm and 100 μm anode and cathode widths, respectively. The gas employed is a mixture of Ar–DME. The front-end electronics used is the APC64 [HORI93, GOME97] with analog readout.

The number of detector dead channels is around 1% and no significant deterioration due to radiation has been observed since their installation. The average efficiency for a standard detector is around 93%. Clustering results in a space resolution for single tracks of 54 μm.

6.2.2 Scintillating Fiber Detector

The three planes (X, Y and U) of the scintillating fiber detector (SFD) provide both coordinate and timing information and it is used also for triggering. Each X and Y plane has the size of $104 \times 104\ \mathrm{mm}^2$ and contains 240 fiber columns (0.44 mm pitch). Each column consisting of 5 scintillation fibers of 0.5 mm in diameter. Each column is mapped to one channel of the 16 channel position sensitive photomultiplier (PSPM) Hamamatsu H6568. The plane U is rotated by 45 degrees and has 5 sections of different fiber lengths to cover roughly the same area like the X- and Y-planes. The plane U contains 320 3-fibers columns with fiber diameter of 0.57 mm.

An analog signal processor produces information for the appropriate TDC channel. The space and time resolutions of the SFD are 130μm (rms) and 0.8 ns (rms), respectively.

6.2.3 Ionization Hodoscope

The Ionization Hodoscope (IH) is optimized to separate ionization signals produced by otherwise unresolved double tracks from ionization signals produced by a single particle. It consists of two vertical (X) and two horizontal (Y) layers, each with 16 slabs of plastic scintillator ($1 \times 7 \times 110\ \mathrm{mm}^3$). The sensitive area of the IH is $11 \times 11\,\mathrm{cm}^2$. It suppresses the background from single track events by a factor 50 while keeping more than 80% of double track events.

The detector provides both time (TDC) and amplitude (ADC) measurements. Signals from both X-planes are used by the neural network trigger DNA.

6.3 Detectors downstream of the magnet

The two arms of the spectrometer are identically equipped with detectors. These are drift chambers (DC), vertical scintillation hodoscopes (VH), horizontal scintillation hodoscopes (HH), gas Cherenkov detectors (Ch), preshowers (PSh) and muon detectors (Mu).

6.3.1 Drift Chambers

The drift chambers are used to perform particle tracking after the magnet. The signals from the DC hit wires are also used to implement the fourth level topological trigger, which selects track pairs with small relative momentum.

The DC system consists of four chamber modules per arm including 6 sensitive planes in X and Y projection.

— The first module (DC1) has a frame common to both arms; it has two active regions of 80×40 cm^2 housing 6 planes of signal wires (X, Y, W, X$'$, Y$'$, W$'$). The W-wires are inclined at 11.3° with respect to the X-wires.

Three modules are then placed on each spectrometer arm:

— DC2 with an active area of 80×40 cm^2 and 2 wire planes (X, Y);

— DC3 with an active area of 112×40cm^2 and 2 wire planes (X, Y);

— DC4 with an active area of 128×40 cm^2 and 4 wire planes (X, Y, X$'$, Y$'$).

The drift cell layout, common to all chambers, consists of a sensitive region of 10×10 mm^2 around the anode wire (copper-beryllium of 50 μm in diameter, step of signal wires is 10 mm) limited by cathode planes (carbon-coated Mylar foils 20 μm thick) and potential wires (copper-beryllium of 100 μm in diameter).

The chambers are operated with an $\mathrm{Ar}(\sim 50\%) + i\mathrm{C_4H_{10}}(\sim 50\%) + \mathrm{H_2O}(0.5\%)$ gas mixture and the anode wire HV is 3.8 kV.

The accuracy of coordinate measurements in the DC is better than 90 μm. The efficiency of each chamber is around 97% which corresponds to a reconstruction efficiency for one track of 99% with requirement of 4 hits per projection.

6.3.2 Vertical Hodoscopes

These detectors are used to perform fast coincidences between the two arms of the spectrometer at first level trigger, and also to select low Q_L pairs at higher level trigger. The VH supply time-of-flight information.

Each VH covers an area of 40×130 cm^2 (H$\times$W) with an array of 18 scintillator slabs ($7 \times 40 \times 2.2$ cm^3, W$\times$H$\times$T) arranged vertically. All the slabs (Bicron BC420) are connected at both ends to photomultipliers (Hamamatsu R1828-01) by means of fish tail light guides. The PM's are equipped with voltage dividers, which allow to operate the detector at high counting rates. Each slab can work with a particle flux up to 1.2 MHz, with additional HV applied to the last four dynode stages.

Time resolution of a single vertical hodoscope is 127 ps which corresponds to 174 ps resolution for the time difference between the signals in the positive and negative arms. The VH efficiency is 99.5% for the positive, and 98.8% for the negative hodoscope arm.

6.3.3 Horizontal Hodoscopes

The main purpose of the HH is the trigger level selection of pairs with a small difference in hit slab numbers ("coplanarity cut") typical for the pairs from the breakup of pionic atoms ($\Delta y \leq 7.5$ cm).

Each HH consists of 16 horizontal scintillator slabs of the dimensions of $130 \times 2.5 \times 2.5\,\mathrm{cm}^3$ (W×H×T) covering an area of 130×40 cm^2 (W×H). The slabs are connected at both ends to photomultipliers. Each PM (Philips XP2008) is equipped, as for VH, with a voltage divider allowing high counting rates.

The efficiency of HH is $> 96.6\%$ (both arms), and the time resolution is 320 ps (rms).

6.3.4 Cherenkov Counters

The Cherenkov counters are used at first level trigger for rejecting e^+ and e^-. The counters have a total length of 285 cm. Their entrance windows have dimensions 143×56 cm^2 and the exit ones 336×96 cm^2. The gas radiator used is nitrogen (N_2) at normal temperature and pressure.

Each counter is provided with 20 mirrors, and 10 photomultipliers on two rows. Cherenkov light reflected by pairs of adjacent mirrors is focused onto the same PM (Hamamatsu R1587 with UV-glass window). Mirrors are spherically formed rectangles, with average dimensions 30×35 cm^2 and 6 mm thick.

The average number of photoelectrons for particles with $\beta = 1$ is over 16. Both counters have an efficiency $> 99.8\%$ and the pion contamination above the detection threshold is less than 1.5%. Such contamination arises from pion with momenta above the Cherenkov threshold and from accidental coincidences occurring within the gate window.

6.3.5 Preshower Detectors

The Preshowers are used to construct first level trigger and to improve the electron rejection power in the off-line analysis.

The PSh detector consist of 8 elements per arm and cover an area of 280×75 cm^2. Each PSh element comprises a Pb converter and a scintillation counter placed behind it. The first two converter elements (farthest from the proton beam line) have a thickness of 1 cm, whereas the others have a thickness of 2.5 cm. The scintillator slabs (Bicron BC408) have lateral dimensions 35×75 cm^2 and thickness 1 cm. EMI 9954-B photomultipliers are connected to the top of each slab by means of light guides. Since the maximal particle flux on each PSh counter is as high as $\sim$ 2 MHz, an additional 800 V supply is connected to the last dynodes of the photomultipliers.

The efficiency of the detector is $\sim 99.5\%$ (both arms). Off-line analysis of the amplitudes from PSh provides an additional e/π separation.

6.3.6 Muon Hodoscopes

These detectors are used to reject muons in the off-line analysis.

Each muon detector consists of a thick iron absorber followed by scintillation hodoscopes. Each hodoscope is made of two layers of 28 scintillator slabs having the same area 75×12 cm^2 and 0.5 cm thicknesses. The muon detector data are read out only if simultaneous signals from a pair of corresponding counters in the two layers are detected. This essentially reduces the background counting rate induced by a particle flux from the beam dump. Using of meantimers as coincidence units allow us to obtain good reduction of background together with high time resolution ($\sigma \approx 1$ ns).

6.4 Trigger and Readout system

The present scheme of the DIRAC trigger is shown in fig. 6.6.

Pion pairs are produced in the target mainly in a free state with a broad distribution over their relative momentum Q. For the purposes of data analysis the accidental coincidences of particles in the two arms

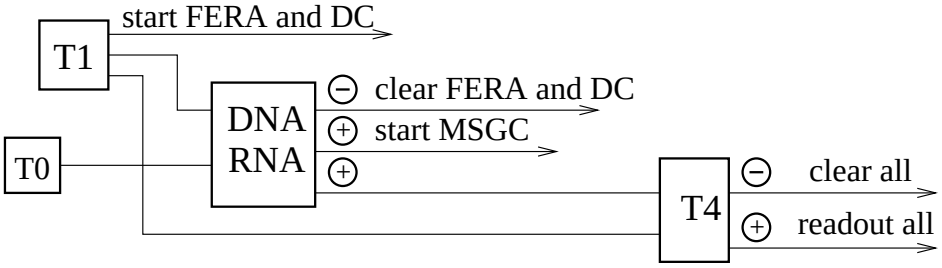

⊕ and ⊖ denote positive and negative decisions of the corresponding trigger level

Figure 6.6: *DIRAC trigger scheme.*

are also detected. Thus, the trigger is made to accept the accidental particles in the time window ± 20 ns with respect to the positive arm as well.

The trigger logic provides a reduction of the event rate up to the level acceptable for the data acquisition system. The trigger system [AFAN02M] comprises a fast first level trigger [AFAN021] and higher level trigger processors which apply selection criteria to different components of the relative momentum of pion pairs. All hardware cuts in the trigger processors affect equally real and accidental coincidences.

In the first level trigger [AFAN021] a simple coincidence of VH, HH and PSh signals and anticoincidence with Ch signal in both arms is treated as a pion-pair event. Coincidence of pion signals in both arms, with simultaneously applied at the hardware level the complanarity cut, initiates the first level trigger. The complanarity cut puts a limitation to the vertical component Q_y of the relative momentum for the accepted pairs using the difference of hit slab numbers in two arms of the horizontal hodoscopes.

Since the pion pairs from the $A_{2\pi}$ atom breakup have small relative momenta Q, the higher level triggers suppress pairs with large relative momentum. Two fast hardware processors [AFAN02M, GALL02, KOKK01, VLAC00] are used to decrease the first level trigger rate by a factor 5.5, selecting pairs with low Q values.

One of them is based on a neural network algorithm [AFAN02M, KOKK01] which employs the hit maps of the IH, SFD and VH detectors. The neural trigger system takes decision in 250 ns, the reduction rate coefficient is around 2.

Another processor (trigger T4) [AFAN02M] makes use the drift chamber data to select $\pi^+\pi^-$ pairs from atom decays. It reconstructs tracks (by wire numbers) and rejects the events with high components of relative momentum Q_L or Q_x basing on the preloaded lookup tables. Decision time depends on the complexity of the event, on the average this time is 3.5 μs. The reduction rate coefficient is 2.5 with respect to the neural trigger. The trigger T4 provides the strongest cut on Q. The data readout is started if T4 has asserted the positive decision and the "good event" flag has been set.

The on-line event selection keeps almost all events with $Q_X < 4$ MeV/c, $Q_Y < 4$ MeV/c and $Q_L < 22$ MeV/c and rejects events with higher Q progressively [VLAC03].

In the DIRAC experiment the total trigger provided a rate reduction around 5.5 with respect to the first level trigger (or more than 1000 with respect to single rates of the downstream detectors), while preserving a high efficiency of 96% in the low Q region of interest. The trigger rate for the standard conditions was around 700 per spill.

The trigger system provides parallel accumulation of events from several other processes needed for calibration such as e^+e^- pairs, $\Lambda \to p\pi^-$ and $K^\pm \to \pi^\pm\pi^+\pi^-$.

Muon detector data are analyzed only off-line.

6.5 Data Acquisition System

The detailed scheme of the DIRAC data acquisition system (DAQ) is described in [OLSH00, OLSH00A]. The data collected during the PS accelerator burst are transferred to VME memory modules (via the FERA bus) or stored inside other dedicated electronic modules without any software intervention. When data for the current burst are accepted, the DAQ software performs readout as well as event building and transfers events to the central data recorder and on-line monitoring hosts.

The DIRAC DAQ is able to accept data from 3 consecutive bursts per PS supercycle, each containing up to 2 MB of data. With the event size (about 1.2 kB at intensity of 10^{11} p/burst) the data acquisition [OLSH01, KARP03] is capable to accept up to 2000 events per spill of 450 ms, with an interval between the spills as short as 1 s.

The DAQ [OLSH01, KARP03] is configured from dedicated and commercial readout branches running in a parallel hardware-controlled mode. The readout process is controlled by the trigger processors which may decide to reject an event during its acquisition. The system design provides a small dead time resulting in a sufficiently high rate capability.

6.6 Experimental conditions

The present experimental conditions in the DIRAC runs are reported in table 6.1. Here, the counting rate information for each trigger detector is shown at beam intensity of $\sim 0.9 \cdot 10^{11}$ protons per spill ($t_{spill} \approx 0.4$ s). The initial 11 kHz rate of T1 trigger is reduced by the higher level triggers. This enables us to collect up to 2000 triggers per spill in the actual experimental conditions with mixed trigger (pion trigger including DNA and T4, plus additional 10% of T1 electron trigger and 10% of Λ triggers). The average number of accepted events was 700 per spill.

Table 6.1: *Counting rate and multiplicity for triggering detectors at an average intensity* $I_P = 0.9 \cdot 10^{11}$ *protons/spill (*$t_{spill} \approx 0.4$ *s).*

Detectors	Counts per spill, 10^3	Counts per second, 10^3	Counts max. per channel & spill, 10^3	Counts max. per channel & second, 10^3	Average multiplicity per event
IH	2450	6125	153	382	3.35
VH left	790	1760	83	184	1.20
VH right	530	1170	44	98	1.28
HH left	720	1600	70	156	1.28
HH right	500	1110	43	96	1.36
PSh left	790	1750	176	391	1.26
PSh right	540	1190	113	251	1.32
Mu left	84	187	3	7	0.114
Mu right	57	127	2	50	0.097

The full setup, including detectors, detector responses, read-outs, triggers and magnet has been implemented into DIRAC-GEANT [GEANT] and into the DIRAC analysis package ARIANE [ARIAN] such that simulated data can be treated in the same way as real measurements.

Chapter 7

Data processing and calibration

7.1 Track reconstruction

The off-line analysis of the experimental data aims to reconstruct the $\pi\pi$ pairs originating from the target. Events of interest consist of two particles of opposite charge with very low Q, resulting in two close lying tracks upstream that are separated downstream into the two arms of the spectrometer.

The magnetic field was carefully mapped and fine-tuned to a relative precision of 10^{-4}. The final field map is used in the Monte Carlo GEANT simulation of the experiment [GEANT]. For tracking, the field is summarized by a transfer function that uses the position, direction and momentum of a track in a reference plane at the exit of the magnet as input and calculates the position and direction of that track in a reference plane five meters upstream of the magnet. The transfer function consists of 4 polynomials with 5 parameters each.

Track reconstruction starts from the downstream part exploiting DC data. At first, only hit wires are used to achieve a fast pattern recognition. A track candidate is searched for in the horizontal and vertical planes of the drift chambers separately. A "horizontal" candidate must have a hit wire in one of the horizontal planes of the first (DC1) and last (DC4) chamber, as well as corresponding hits in the HH-detectors. They define a straight line. Hits close to that line are looked for in the other four horizontal planes of DC1 to DC4. Based on an acceptance window, a candidate is accepted if at least two more hits are found. The "vertical" candidates are found analogously. Then the recorded drift times are used to refine the pattern recognition and to solve left/right ambiguities, inherent to such detectors. Finally candidates from horizontal and vertical wires are matched using the inclined planes. Only candidates are retained which point into the magnet aperture. To associate a rough momentum estimate with each track candidate (crucial for error estimates in the precision tracking), the spatial track parameters are, by means of the magnetic field polynomials, projected to the center of the beam spot at the target.

Using the precise position measurements deduced from drift-times an overall track-fit is made for each candidate using a standard modified least-squares method. Bad candidates are rejected on the basis of a confidence level ceiling. The downstream track candidates are thus defined spatially with high precision.

Every track is again projected through the magnet onto the beam spot by adjusting the momentum. This defines a line along which to search for hit candidates in the upstream detectors, within spatial windows defined mainly by multiple scattering and within time windows defined by the time-of-flight from the upstream detectors to the vertical hodoscopes downstream and their time resolutions.

Horizontal and vertical SFD hit candidates to be associated with a track must have times within a window of ± 4 ns (corresponding to $\pm 5\sigma$) with respect to the associated VH slab. Moreover, the hit candidates must be found in a spatial window of $\pm(0.2 + 4.8/p\ [\mathrm{GeV}/c])$ cm (corresponding to $\pm 6\sigma$) with respect to the point of intersection of the track candidate with the SFD plane. This window is given

by the multiple scattering in the downstream material when backward-extrapolating the track. At least one hit candidate is required. If there are more than four, the four closest to the window center are kept.

Using all identified upstream information, a track-fit is made for each track-candidate by means of the Kalman-filter method [KALM79], starting from the first downstream hit and ending at the exit window of the vacuum tube upstream of the MSGC detector. All measurements associated with a track are used in this fit. After the first stage of Kalman filtering, only events are kept with at least one track candidate per arm with a confidence level better than 1% and a distance to the beam spot in the target smaller than 1.5 cm in x and y.

With the hypothesis that the track originates from the target, the target itself provides another measurement point for the Kalman filter, whose uncertainty is given by the measured intensity distribution of the proton beam across the target [SCHU02B].

With the hypothesis that a track pair originates from the same interaction, each pair of candidates with opposite charges may be fitted with the constraint that both tracks intersect in the central plane of the target ("vertex fit"). The complete 5×5 uncertainty matrices of the two tracks are used. A threshold confidence level is applied to reject events with tracks originating far from each other.

These two alternative procedures require exactly one track per arm and do not use the MSGC's, for reasons of optimum efficiency for atomic track pairs.

The full tracking method uses MSGC and SFD to connect all upstream hits by a straight line and match these track candidates with the downstream candidates. A vertex probability is calculated for each track pair, corresponding to the hypothesis that both tracks intersect at a common point lying on the target central plane. Correlations from the estimated errors from multiple scattering are fully taken into account [PENT96]. Both tracks are re-fitted at the end, under the constraint of having a common vertex [ADEV03].

To illustrate that the reconstructed events do in fact originate from the target, the distances between two tracks at the target are shown in Fig. 7.1. No vertex fit was done for these data.

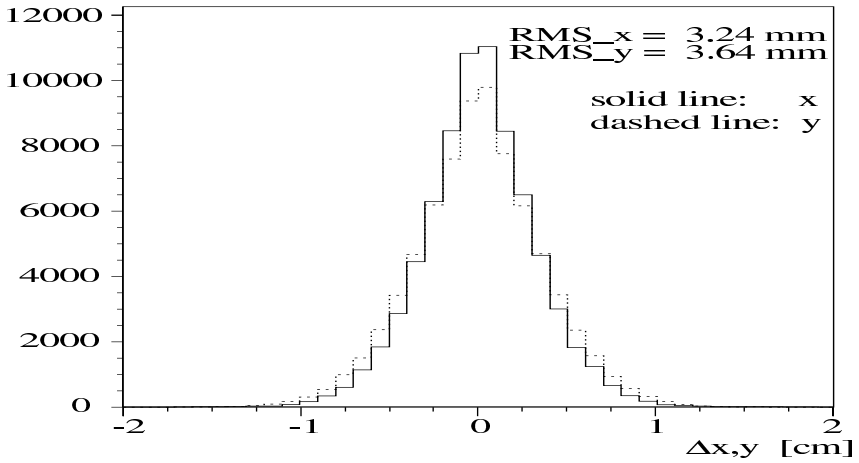

Figure 7.1: *Distances Δx and Δy between two reconstructed tracks at the target in the transverse plane.*

7.2 Selection criteria

An event is rejected if more than two downstream tracks in either of the two arms are reconstructed. In the case of two tracks in one arm the earlier in time is taken for further analysis.

For such tracks, the SFD hits are re-determined in a narrower ($\pm$1cm) window around the new track intersect. Events with less than five hits in the window per SFD plane and not more than six in both planes

are retained. Finally, all track pairs with $|Q_x| < 6\,\text{MeV}/c$, $|Q_y| < 6\,\text{MeV}/c$ and $|Q_L| < 45$ MeV/c are selected for further analysis.

This pre-selection procedure retains 6.2% of the $\pi\pi$ data obtained with the Ni target in 2001. The time difference measured by the VH's between the positive and the negative arm for events that passed the pre-selection criteria is shown in Fig. 7.2.

For the final analysis further cuts and conditions are applied:
— "prompt" events are defined by a time difference (corrected for the flight path assuming pions) measured by the VH's between the positive and the negative arm, $|\Delta t| \leq 0.5$ ns, corresponding to a $\pm 2.7\sigma$ cut (Δt_2 in Fig. 7.2);
— "accidental" events are defined by time intervals Δt_1 and Δt_3 far away from the prompt peak (see Fig. 7.2), protons from prompt events are rejected by requiring momenta of the positive particle to be $p_+ \leq 5$ GeV/c.
— $e^{\pm}$ and $\mu^{\pm}$ are rejected through appropriate cuts on the Cherenkovs, the Preshower and the Muon counters [BREK01].
— $\sqrt{Q_x^2 + Q_y^2} = Q_T \leq 4\,\text{MeV}/c$ and $|Q_L| < 22\,\text{MeV}/c$.
— only one vertex-fit is considered, the best one based on confidence levels from track fits and subsequent vertex fits.
— only events with at most two pre-selected hits per SFD plane are accepted. This provides the cleanest possible event pattern.

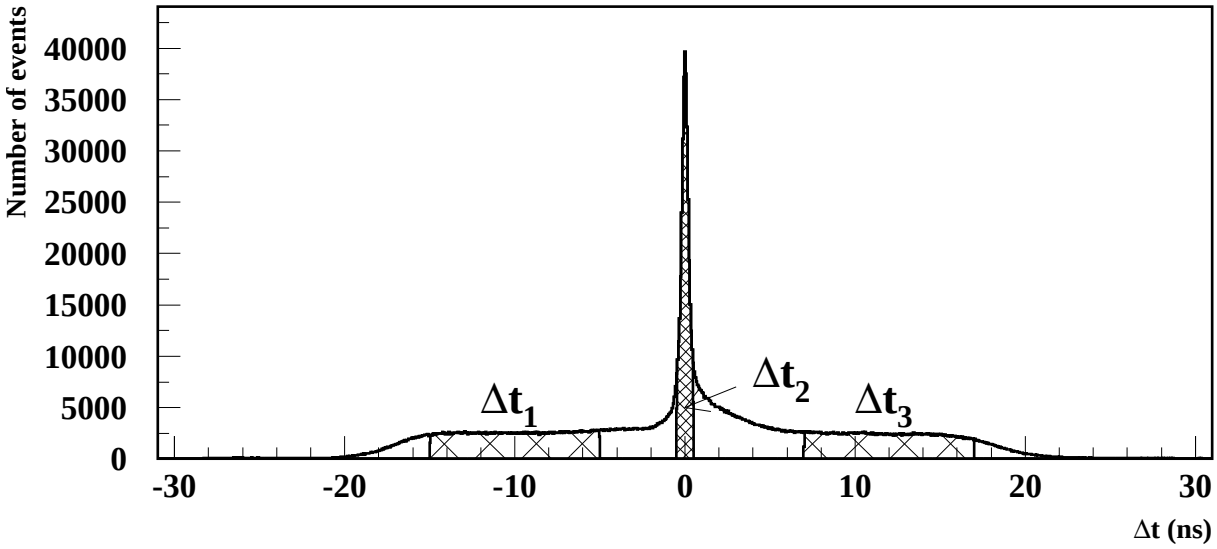

Figure 7.2: *Time difference between positive and negative vertical hodoscope slabs associated with the selected tracks. The asymmetry for positive differences is due to protons.*

7.3 Calibrations

7.3.1 Calibration with Coulomb peak

The reconstruction of Coulomb-correlated $\pi^+\pi^-$ pairs is sensitive to the precision of the setup alignment. Any misalignment of the tracking system in one arm relative to the other arm would generate asymmetrical errors on the reconstructed momenta. This would lead to a systematic shift and additional spread of the Coulomb peak in the Q_L distribution (see fig. 7.3). The mean value of the Coulomb peak is close to zero, well within the accepted tolerances.

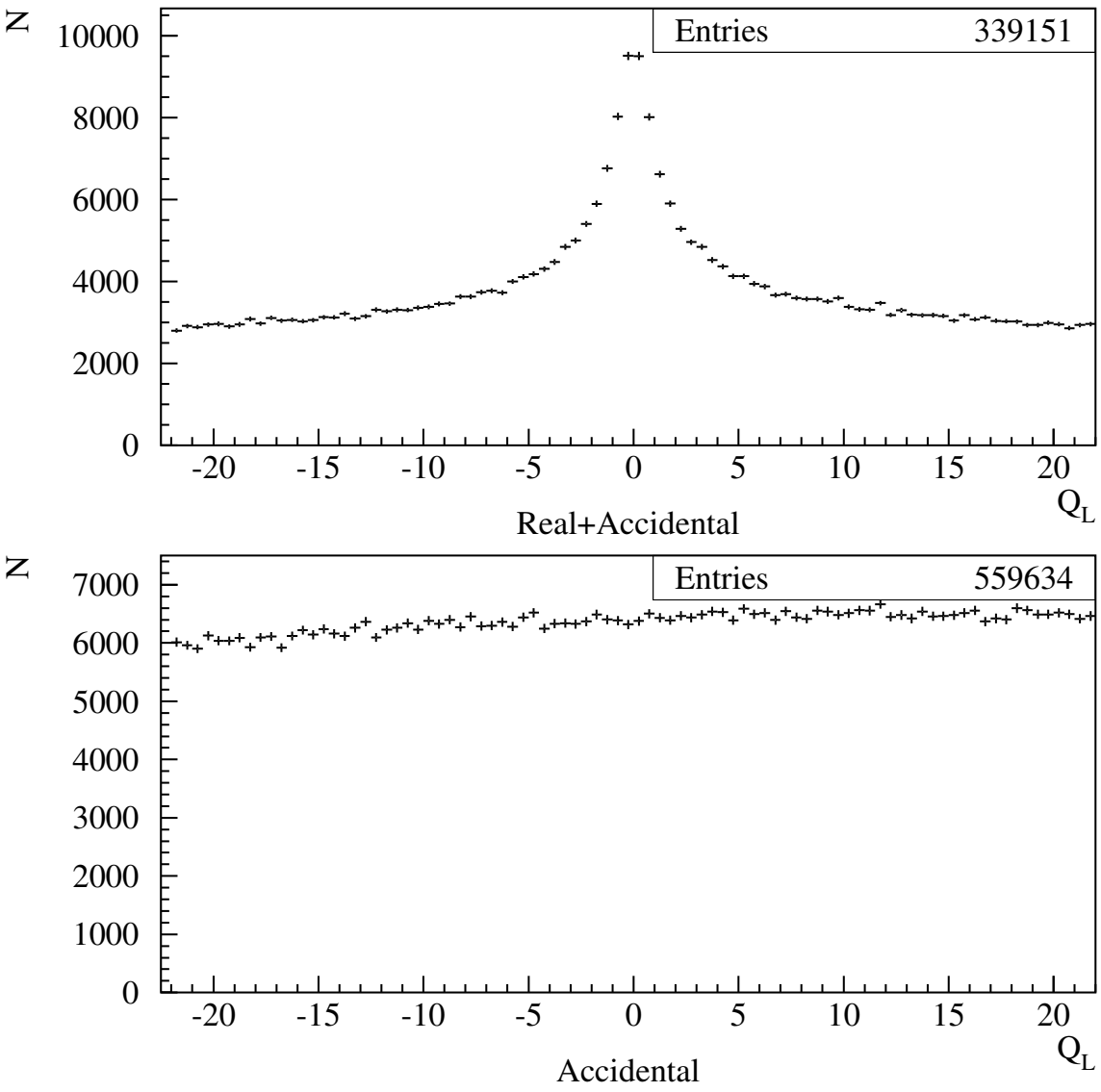

Figure 7.3: *The event distribution of Q_L for "real" and "accidental" pairs (upper); for pure "accidental" pairs (lower). Selction cut $Q_T < 3$ Mev/c.*

7.3.2 Calibration with e^+e^- pairs

Accurate time measurement is a crucial point for DIRAC data analysis. Precise timing information is provided by the VH. Time measurements calibration is performed using the data sample collected with the T1 electron-positron trigger. This trigger selects mainly e^+e^- pairs from γ conversions which are almost synchronous in time, as the time of flight for e^+e^- pair does not depend on the momentum in the region of the setup acceptance. In addition, they can be strictly selected with Cherenkov counters. Therefore the e^+e^- pair distribution as a function of time difference between positive and negative arms of the hodoscopes contains only one peak of real coincidence (see fig. 7.4a).

7.3.3 Mass identification of time correlated pairs

Vertical Hodoscope is also used to identify $K^+\pi^-$ and $p^+\pi^-$ pairs which contaminate time correlated $\pi^+\pi^-$ pairs. The distribution of the time difference of the hits in the positive and negative arms is

shown in fig. 7.4b for hadron pairs collected with the main DIRAC trigger. Here, one can observe the peak of time correlated particles over the flat plateau of accidental coincidences. The peak is asymmetric, the right side excess is due to the presence of slower protons and kaons hitting the positive arm. The plateau, on both sides of the peak, provides the data sample of accidental pairs needed for the analysis.

To identify $\pi^+\pi^-$, $K^+\pi^-$ and $p^+\pi^-$ pairs we can measure the time-of-flight difference between negative and positive particles coming from the target. Assuming the negative particle to be π^- we can reconstruct the mass of the positive particle. The squared mass spectrum of positive particles is shown in fig. 7.4c. Three peaks can be identified corresponding to π^+, K^+ and p^+ particles correlated to the π^-.

7.3.4 Calibration with Λ decays

It was proposed [ADEV95] to use the $\Lambda \to p\pi^-$ decay for the telescope position tuning. So the correctness of the alignment and magnetic field description was verified by studying the decay of Λ particles.

The analyzed data samples consist of events with one downstream track per spectrometer arm and a time-of-flight difference between the positive and negative particle between 0 and 1.3 ns (VH's). The Λ mass reconstruction using full tracking method is presented in Fig. 7.5. Fig. 7.5 shows, for a typical control data sample, the invariant mass distribution from the two tracks under the hypothesis proton-π^-.

A Gaussian fit over a linear background yields $M_\Lambda = (1115.570 \pm 0.031)$ MeV/c^2 with $\sigma_{M_\Lambda} = (0.395 \pm 0.007)$ MeV/c^2, where only statistical errors are given. The measured width is entirely due to track reconstruction.

This standard deviation is better than in the experiment by Hartouni [HART94], where the most precise measurement of M_Λ with the standard deviation $\sigma_\Lambda = 0.49$ MeV$/c^2$ was performed.

The difference $(M_{p\pi^-} - M_\Lambda(PDG))$ in units of the reconstruction error provides a measure of the correctness of the error estimation. The resulting distribution is fitted by a Gaussian with $\sigma = 1.028 \pm 0.006$, showing that the reconstruction errors are underestimated by about 3%. The same ratio was studied as a function of the pion momentum and found to be independent of it. The long term stability of the apparatus has been controlled using the Λ mass and the corresponding widths.

7.3.5 Setup momentum resolution

The relative resolution on the particle lab momentum is $3 \cdot 10^{-3}$. The resolutions on the relative c.m.-momentum of a $\pi^+\pi^-$ pair from atomic breakup, $\vec{Q} = (Q_x, Q_y, Q_L)$ are in the transverse plane (with respect to the total momentum $\vec{p}^{\,Lab}_{\pi^+\pi^-}$ in the laboratory frame) $\sigma_{Q_x} \approx \sigma_{Q_y} \leq 0.49$ MeV/c and longitudinally $\sigma_{Q_L} = 0.50$ MeV/c, here Q_L is a projection on the total lab momentum of pair.

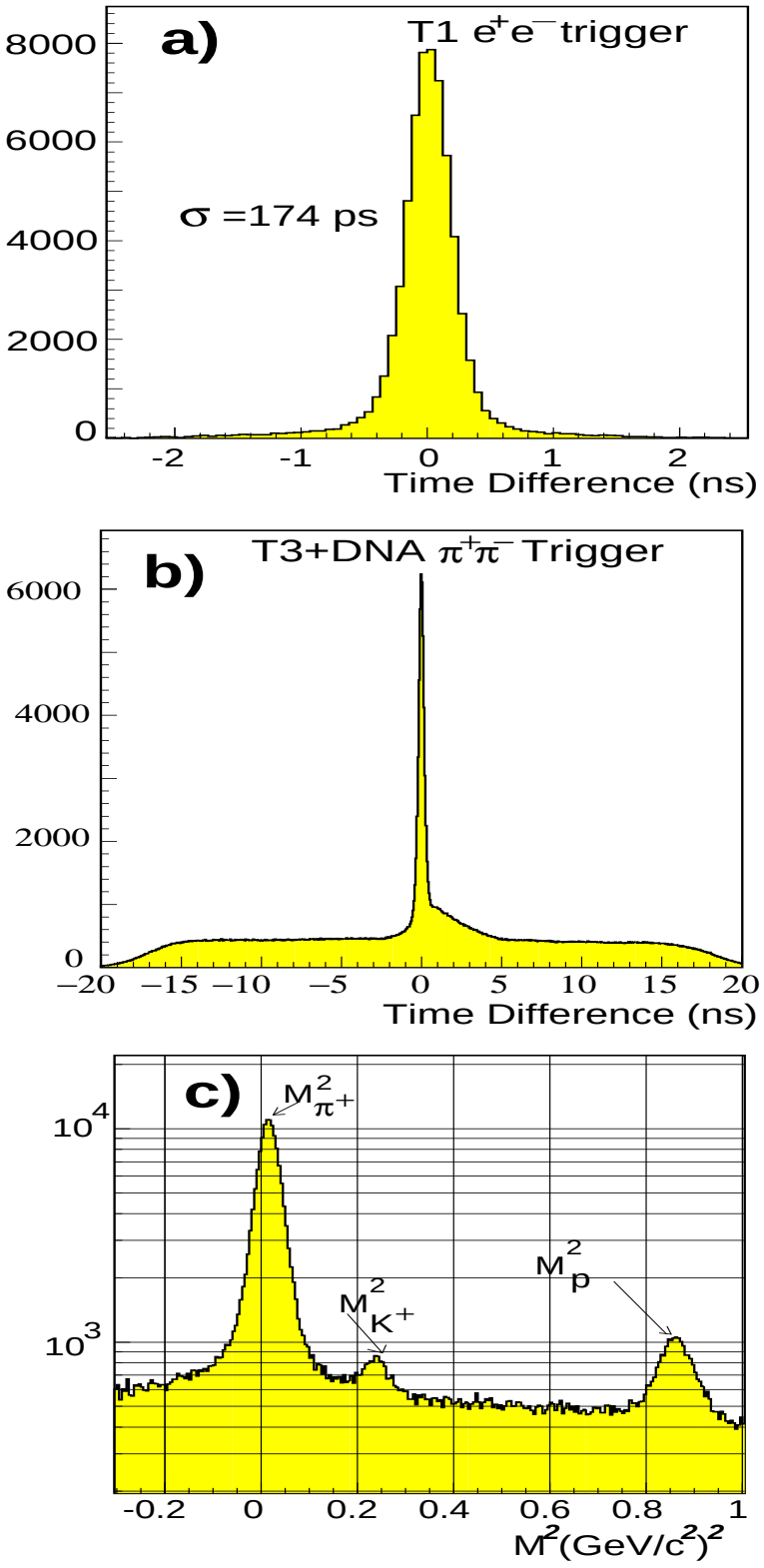

Figure 7.4: *a) VH time difference spectrum for electron-positron T1 trigger. b) Time difference spectrum from events collected with the standard DIRAC trigger. c) Mass spectrum of positive particles recorded with the standard DIRAC trigger.*

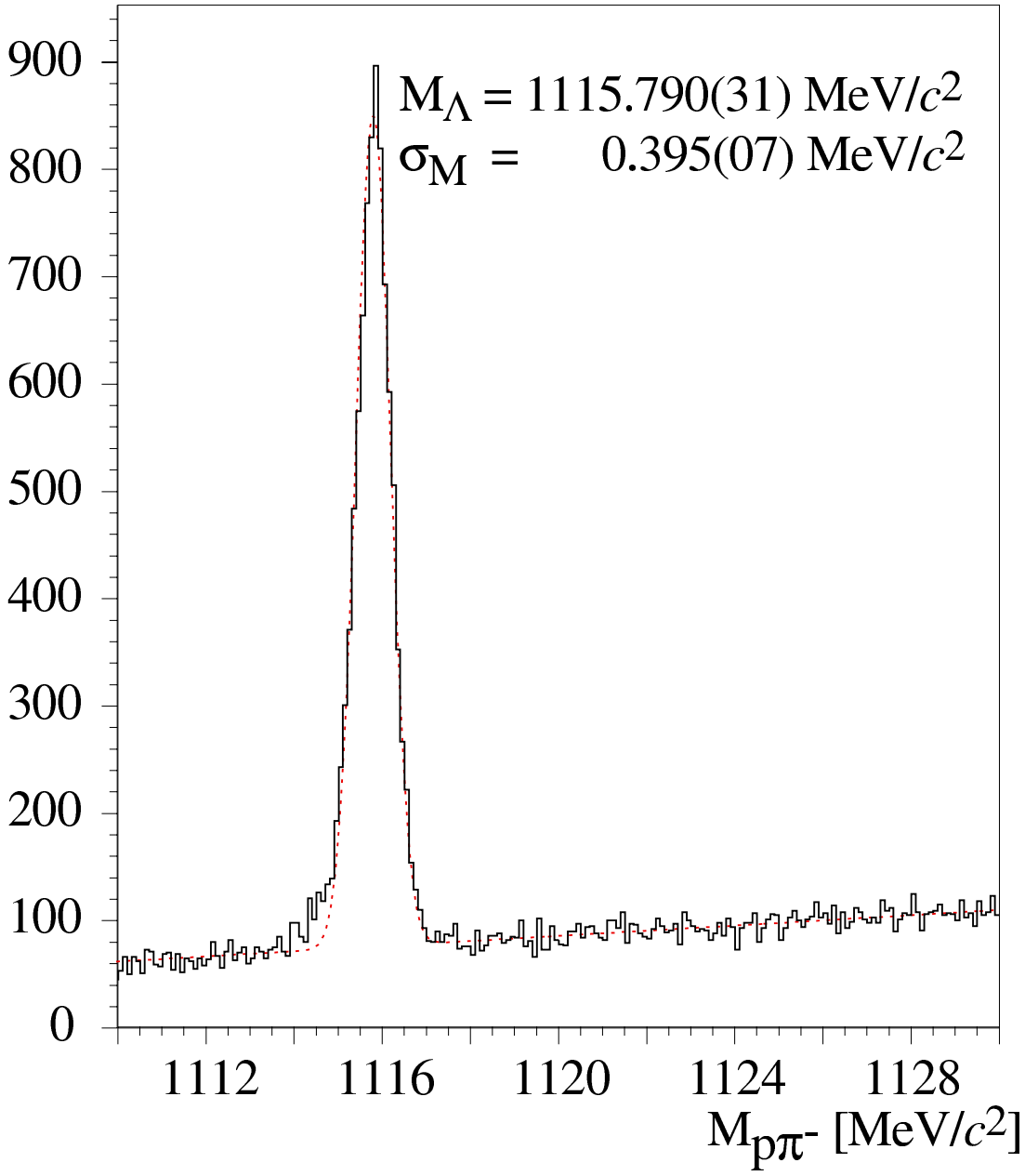

Figure 7.5: *Invariant proton-pion mass ($M_{p\pi^-}$) distribution. The dashed line represents a fit of a Gaussian plus a straight line.*

Chapter 8

Preliminary results

8.1 Signal and background in $\pi^+\pi^-$ atom detection

Once produced in a proton-nucleus interaction, all $A_{2\pi}$ atoms will annihilate if they propagate in vacuum. In a finite target they will, however, interact electro-magnetically with the target atoms and partly break up. A Monte Carlo simulation of $\pi^+\pi^-$ pairs from $A_{2\pi}$ break-up yields Q and Q_L distributions as shown in Fig. 8.1. At the exit of the target, multiple scattering has caused a considerable broadening of the Q-distribution while the Q_L distribution has remained unchanged. The Q_L distribution at breakup is already much narrower than the Q-distribution because the breakup mechanism itself affects mostly Q_T. These features lead us to consider in the analysis Q as well as Q_L distributions.

The atomic pairs are accompanied by a large background. The Q distribution of all $\pi^+\pi^-$ pairs produced in single proton-nucleus interactions in the target is described by:

$$dN/dQ = dN_{\rm C}/dQ + dN_{\rm nC}/dQ + dn_A/dQ, \tag{1}$$

$N_{\rm C}$ is the number of $\pi^+\pi^-$ pairs originating from short-lived sources (fragmentation, rescattering, mesons and excited baryons that decay strongly). These pairs undergo Coulomb interaction in the final state (Coulomb pairs). $N_{\rm nC}$ is the number of $\pi^+\pi^-$ pairs with at least one particle originating from long-lived sources (mesons and baryons that decay electromagnetically or weakly). They do not exhibit Coulomb final state interaction (non-Coulomb pairs). Finally, n_A is the number of $\pi^+\pi^-$ pairs from $A_{2\pi}$ breakup.

Accidental $\pi^+\pi^-$ pairs ($dN_{\rm acc}/dQ$) originate from different proton-nucleus interactions and are uncorrelated in time, i.e. they are neither affected by Coulomb nor strong interaction in the final state. Such events may also belong to the time window that defines prompt events (see section 7.2).

These backgrounds, as they are measured and reconstructed, are needed for subtraction from the measured data in order to obtain the excess produced by the atomic signal. The backgrounds may be obtained in different ways.

One method is based on a Monte Carlo modelling of the background shapes using special generators for the non-Coulomb (nC) and Coulomb (C) backgrounds and accidental pairs [SANT03]. Uniformity in phase space is assumed for the backgrounds, modified by the theoretical Coulomb correlation function $A_{\rm C}^{\rm theo}(Q)$ [SAKH48] for C-background. Effects of the strong final state interaction and the finite size of the pion production region [LEDN82] on the Coulomb correlation function are small and neglected here. The differences in phase space for the different origins of $\pi^+\pi^-$ pairs are implemented (cf. [LANA01, SANT03]). The generated events are propagated through the detector using GEANT package [GEANT]. Simulating the detectors and triggers and analyzing the events using the ARIANE analysis package of DIRAC [ARIAN] results in the high statistics distributions (cf. Eq. 1) $dN_{\rm C}/dQ$, $dN_{\rm nC}/dQ$, and $dN_{\rm acc}/dQ$. These distributions are used later to analyze the measured distributions. Though not

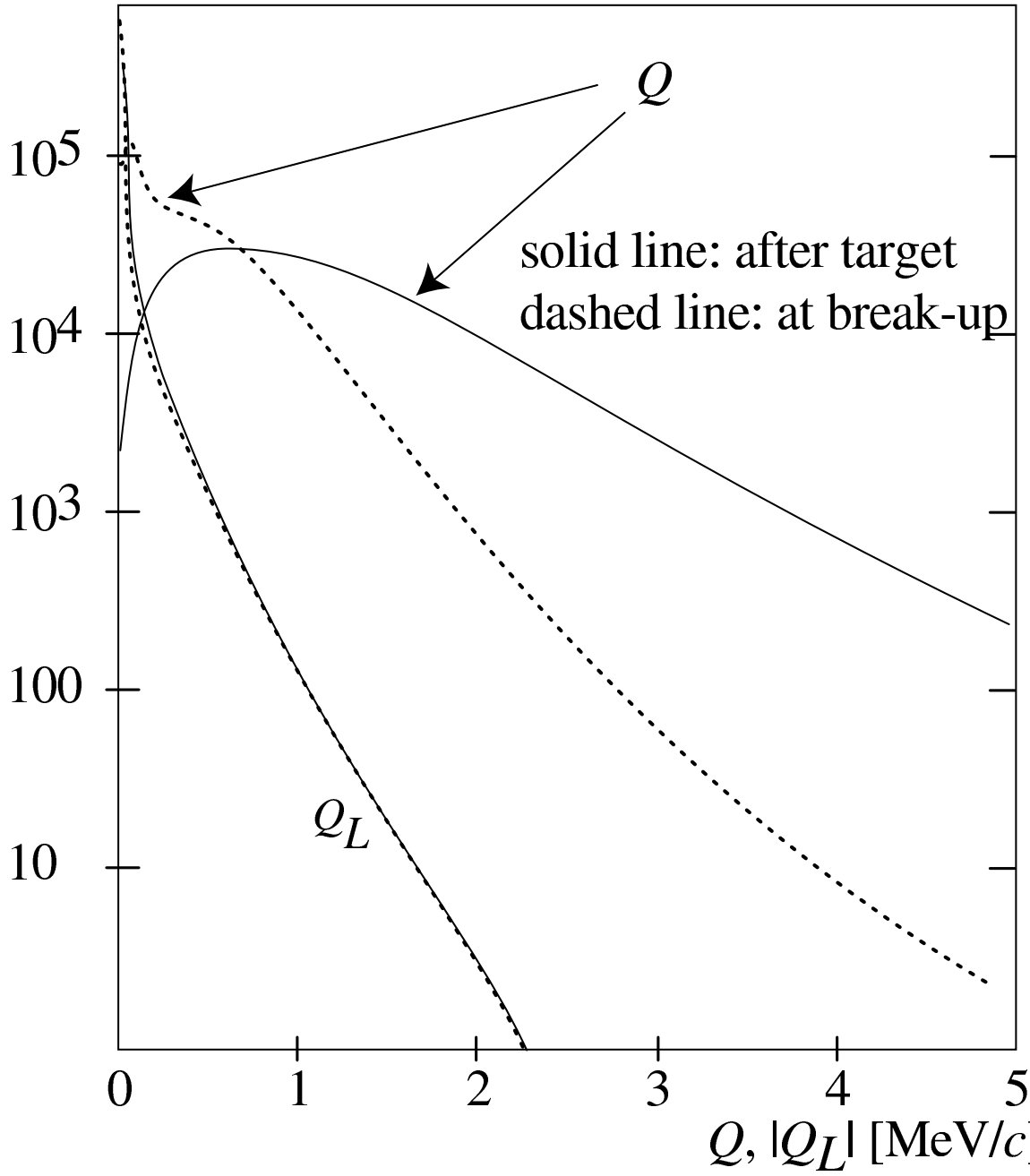

Figure 8.1: *Relative momentum distributions (Q, Q_L) for atomic $\pi^+\pi^-$ pairs at breakup and at the exit of the target (Monte Carlo simulation). Notice that Q_L is almost not affected by multiple scattering in the target.*

necessary for the signal extraction, the $A_{2\pi}$ signal was simulated in an analogous way and dn_A/dQ was obtained. Intrinsic uncertainties in such simulations originate from unrecognized effects.

The second method circumvents the Monte Carlo background simulation and its uncertainties by relating the backgrounds to the measured accidental background. The assumption is that accidentals can be used to describe the distribution of free $\pi^+\pi^-$ pairs, which then must be corrected for final state interactions. By denoting $\Phi(Q) \equiv dN_{\rm acc}^{meas.}/dQ$, the experimental "correlation" function $R(Q)$ is given by:

$$R(Q) = \frac{1}{\Phi(Q)} \left(\frac{dN_{\mathrm{nC}}}{dQ} + \frac{dN_{\mathrm{C}}}{dQ} \right) = N \times [f + A_{\mathrm{C}}(Q)] \tag{2}$$

Here $A_C(Q)$ is the Coulomb enhancement function [SAKH48] smeared by multiple scattering in the target and the finite setup resolution. It is obtained from Monte Carlo simulation. N and f are free parameters, and $\Phi(Q)$ is the measured spectrum of accidentals, properly normalized and corrected for the differences between prompt and accidental momentum distributions [LANA01].

8.2 Experimental data and atomic signal extraction

DIRAC began data taking in autumn 1998. Here we present data taken in 2001 using 94 μm and 98 μm thick Nickel targets. The integrated proton flux through the target for these data is 8.6×10^{16}, corresponding to 5.5×10^{13} p-Ni interactions and to 6.4×10^{8} recorded $\pi\pi$ triggers. The reconstructed accidental and prompt $\pi\pi$ pairs (see Section 7.2 for the cuts) are shown in Fig. 8.2 (Q distribution) and Fig. 8.3 (Q_L distribution).

The Monte Carlo backgrounds or the "correlation" function $R(Q)$ (cf. Section 8.1) are fitted to the measured prompt spectra in Q and Q_L intervals which exclude the atomic signal (typically $Q > 4$ MeV/c and $Q_L > 2$ MeV/c). The amount of time-uncorrelated events in the prompt region was determined to be 6.5% of all prompt events by extrapolating the accidental Δt distribution to zero and was subtracted from the prompt distributions (cf. Fig. 7.2). The fits provide the relative amounts of non-Coulomb and Coulomb backgrounds and the parameters N and f of Eq. 2. As a constraint, these background components must be the same for Q and Q_L.

The analysis using Monte Carlo backgrounds is summarized in Fig. 8.4 and Fig. 8.5. The background composition and the excess at low Q and Q_L are clearly seen. Subtraction provides the residuals, also shown in Fig. 8.4 and Fig. 8.5, which represent the atomic signals. As expected from Fig. 8.1, the signal is narrower in Q_L than in Q. The simulated shape is in agreement with the data. Irrespective of statistics, the signal strength has to be the same in Q and Q_L if the background is properly reconstructed. The observed difference of ~ 10 events demonstrates that the backgrounds are consistent at the per-mille level or even better.

The results of the analysis using the accidentals as a basis for background modelling is shown in Fig. 8.6 and Fig. 8.7. The clear deviation of $R(Q)$ at low Q from unity is due to the attractive Coulomb interaction in the final state. There is good agreement between the experimental and fitted "correlation" function R for $Q > 2.5$ MeV/c, whereas for $Q < 2.5$ MeV/c the experimental correlation function (left hand side of Eq. 2) shows significantly higher values, due to the presence of atomic pairs. In order to extract the number of atomic pairs the fit function (right hand side of Eq. 2) has been multiplied by the accidental distribution $\Phi(Q)$. The subtraction of the latter from the full measured spectrum leads to the atomic pair signal in Fig. 8.6 and Fig. 8.7.

In order to check the procedure of reconstructing two close lying tracks in the upstream detectors, the data have also been processed using only the information from the downstream detectors. Here the particles were assumed to be emitted from the center of the beam spot at the target.

The higher number of events (see Table 8.1) is expected because of reconstruction cuts and inefficiencies of the upstream detectors. For this analysis only the Q_L distribution shows a signal since the multiple scattering in the upstream detectors does not so much distort Q_L but destroys Q_T and hence Q. The larger signal is, however, accompanied by an even larger background.

The results are summarized in Table 8.1. The column "Full" shows the yet preliminary results obtained with the full tracking (cf. section 7.1) and backround from Monte Carlo. The column "MC" shows the result from reconstruction using Monte Carlo backgrounds and no vertex fit. The column "ACC" shows the result of reconstruction using the measured accidentals and vertex fit. The column "3

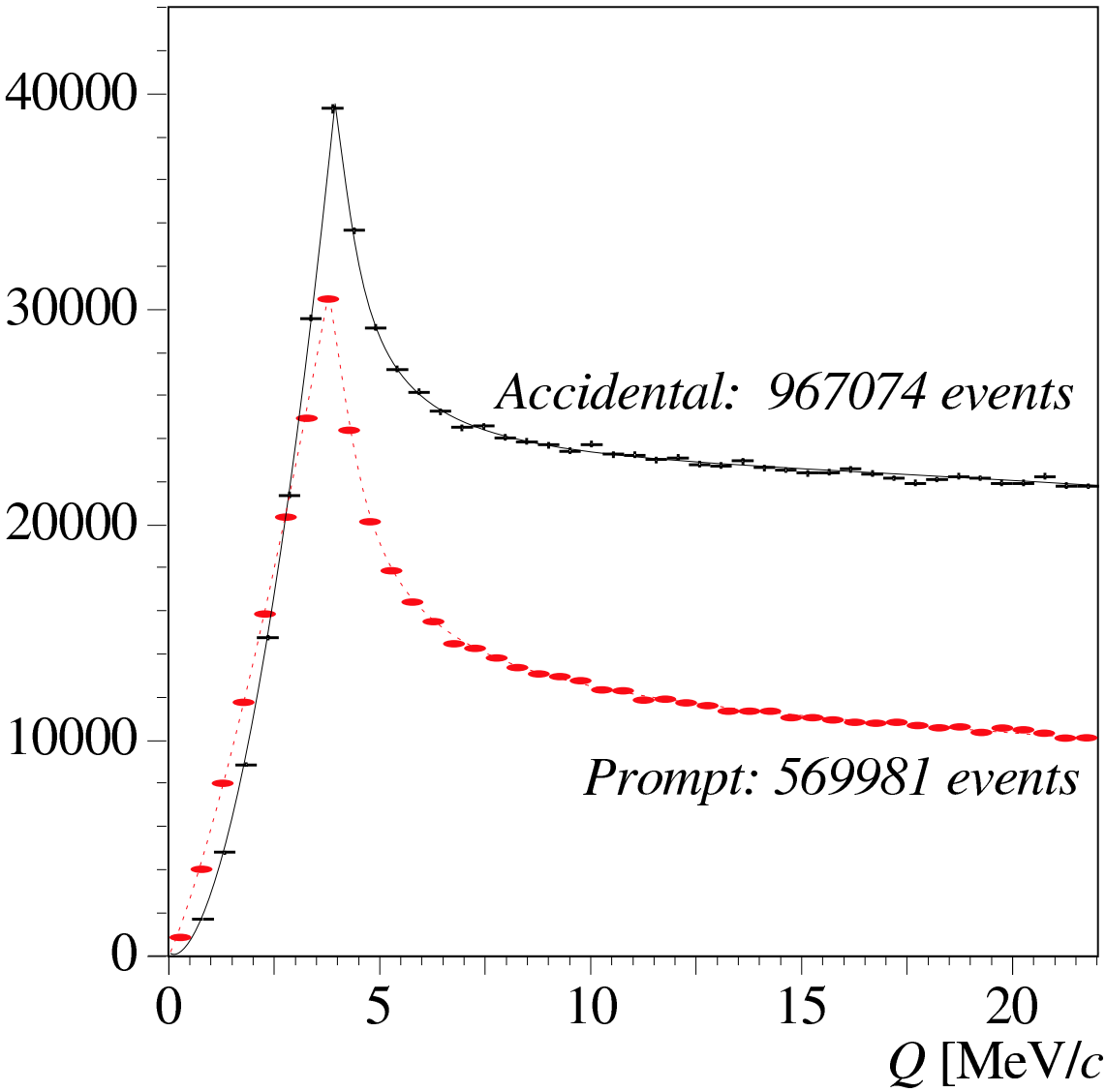

Figure 8.2: *Experimental Q distributions for prompt and accidental $\pi\pi$ events. Continuous lines serve as guides for the eye. The sharp peak at $Q = 4$ MeV/c is due to the cut $Q_T \leq 4$ MeV/c. The number of events is given for the displayed momentum window, the bin-width is 0.5 MeV/c.*

hits" is analogous to column "MC" but allowing for 3 hits in the SFD planes instead of two (cf. section 7.2). The column "Down" shows the result of using only the downstream detectors and the background reconstruction based on accidentals.

The consistency of the signal, especially in Q_L, is satisfactory. The large errors of column "ACC" are due to the limited statistics of the measured accidentals. The difference in signal strength for Q and Q_L in column "ACC" is due to the fact that here the constraint of equal background proportions in Q and Q_L was not applied. Allowing for three hits instead of two in the SFD's yields 25% more atomic pairs, but the relative accuracy of the signal stays unchanged, i.e. the background increases by about 50%. On the other hand allowing for three hits enables to reconstruct almost all ($\approx 90\%$) of the events which are also found without using any upstream detector. This indicates that the main source of inefficiency is due to physics background and related complications in the reconstruction.

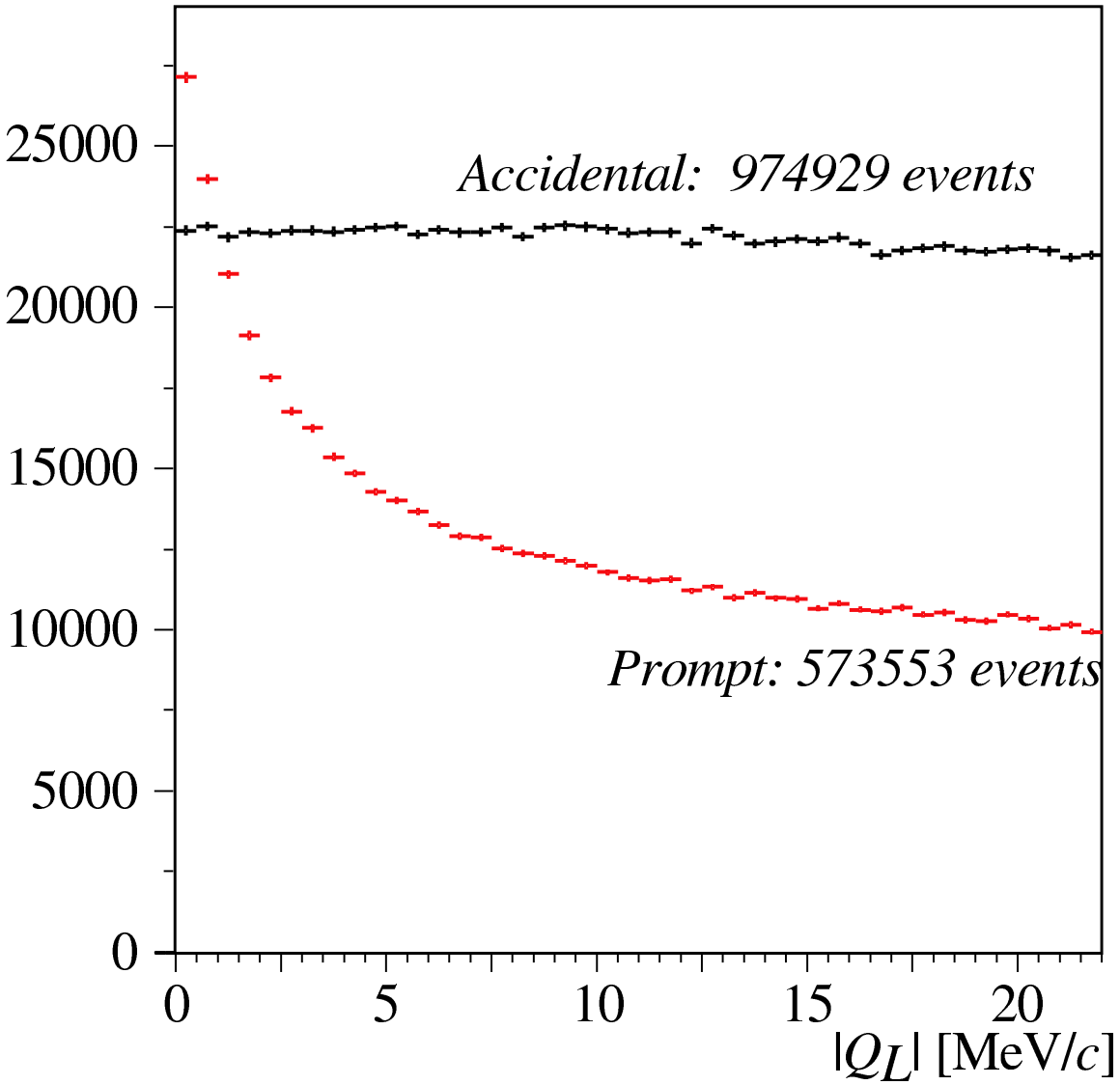

Figure 8.3: *Experimental Q_L distributions for prompt and accidental $\pi\pi$ events. Continuous lines serve as guides for the eye. The number of events is given for the displayed momentum window, the bin-width is 0.5 MeV/c. Note the strong Coulomb enhancement in the Q_L distribution for prompt events.*

8.3 Conclusion

For the first time a large statistics sample of $\pi^+\pi^-$ pairs from atom breakup has been detected. Independent tracking procedures and complementary background reconstruction strategies lead to compatible results.

The processing of all statistics collected in 2000÷2003 with Ni and Ti targets now in progress. The full number of "atomic" pairs selected with and without the upstream detectors are ∼14000 and ∼24000, respectively. The higher number of events selected without upstream detectors is because of reconstruction cuts and inefficiencies of the upstream detectors.

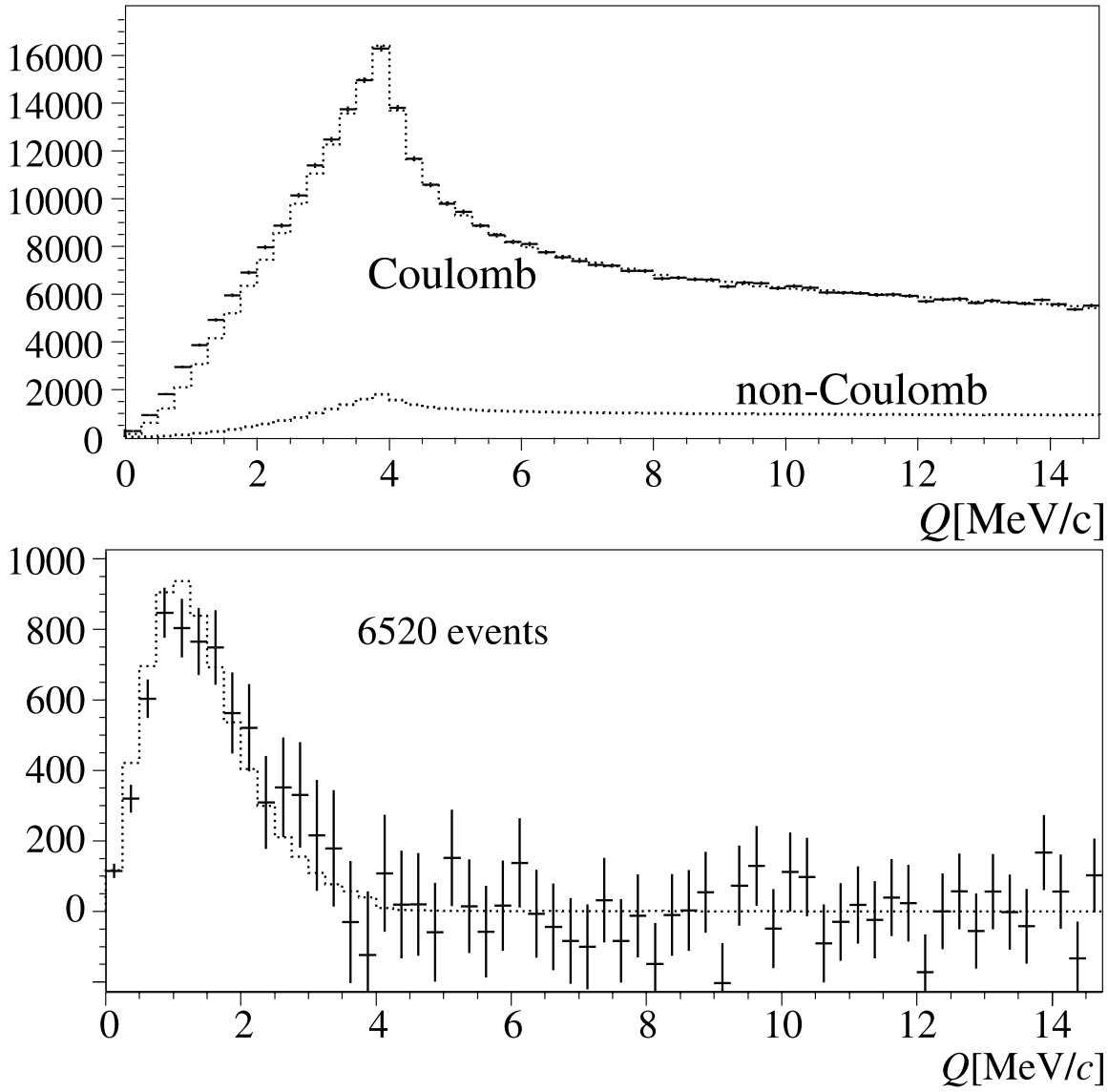

Figure 8.4: *Top: Experimental Q distributions after subtraction of the time uncorrelated background, approximated with Monte Carlo backgrounds (dashed lines). Bottom: Residuals after background subtraction. The dashed lines represent the expected atomic signal shape. The bin-width is 0.25 MeV/c.*

Table 8.1: *Reconstructed atomic pair events using full tracking and Monte Carlo background (Full), no vertex fit and Monte Carlo background (MC), vertex fit and background reconstruction from accidentals (ACC), 3 hits (instead of two) in the SFD acceptance, and reconstruction only with downstream detectors (Down).*

	Full	MC	ACC	3 hits	Down
Q	5530 ± 380	6520 ± 370	4670 ± 930	8230±440	-
Q_L	5320 ± 350	6510 ± 330	5730 ± 580	8050±380	9280 ± 970

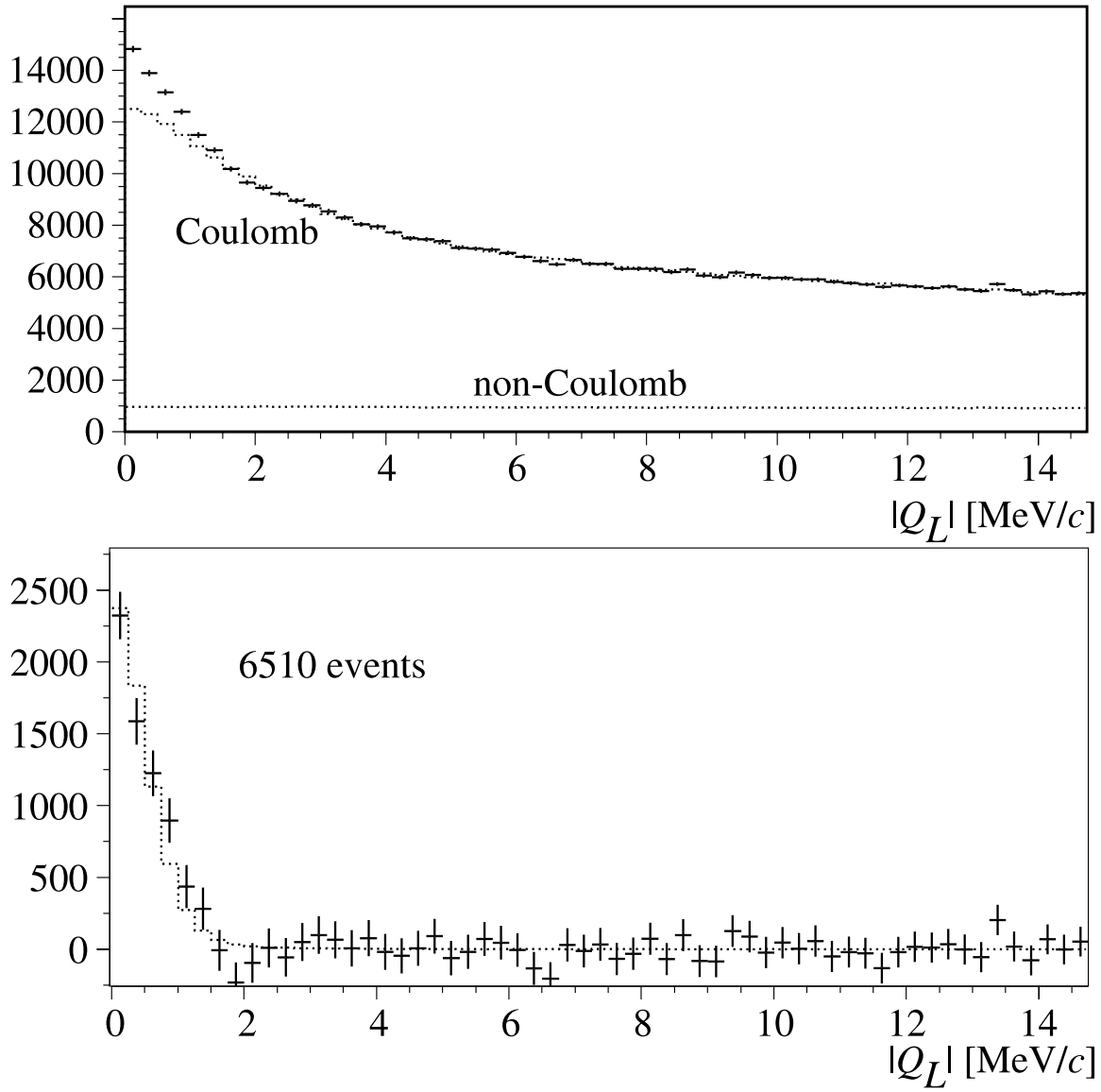

Figure 8.5: *Top: Experimental Q_L distributions after subtraction of the time uncorrelated background, approximated with Monte Carlo backgrounds (dashed lines). Bottom: Residuals after background subtraction. The dashed lines represent the expected atomic signal shape. Notice that the signal strengths in Q and* Q_L *are about the same. The bin-width is 0.25 MeV/c.*

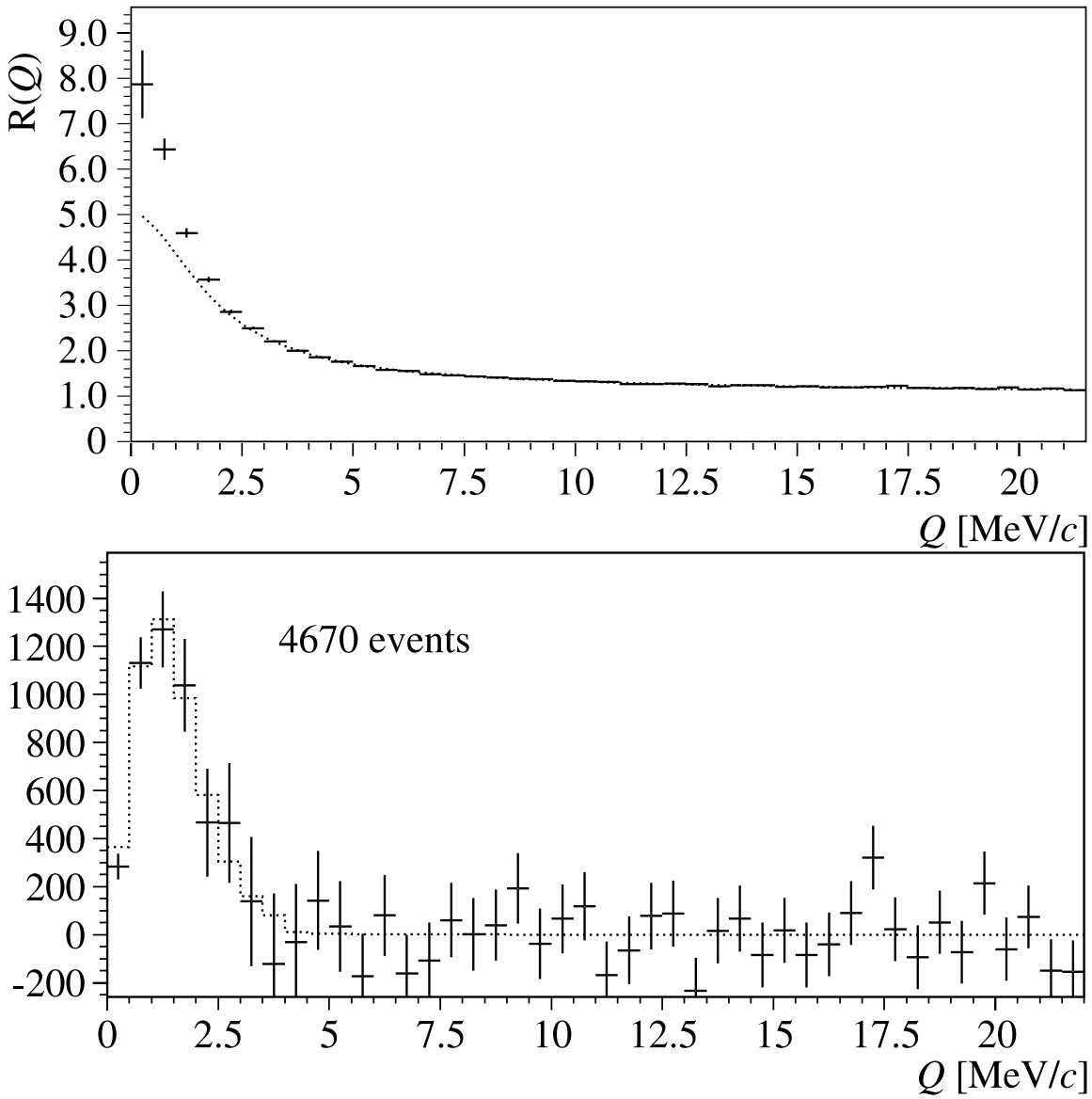

Figure 8.6: *Top: Experimental Q correlation functions (experimental points). The background correlation function is shown as a smooth curve. Bottom: Residuals after background subtraction. The dashed lines represent the expected atomic signal shape. The bin-width is 0.5 MeV/c.*

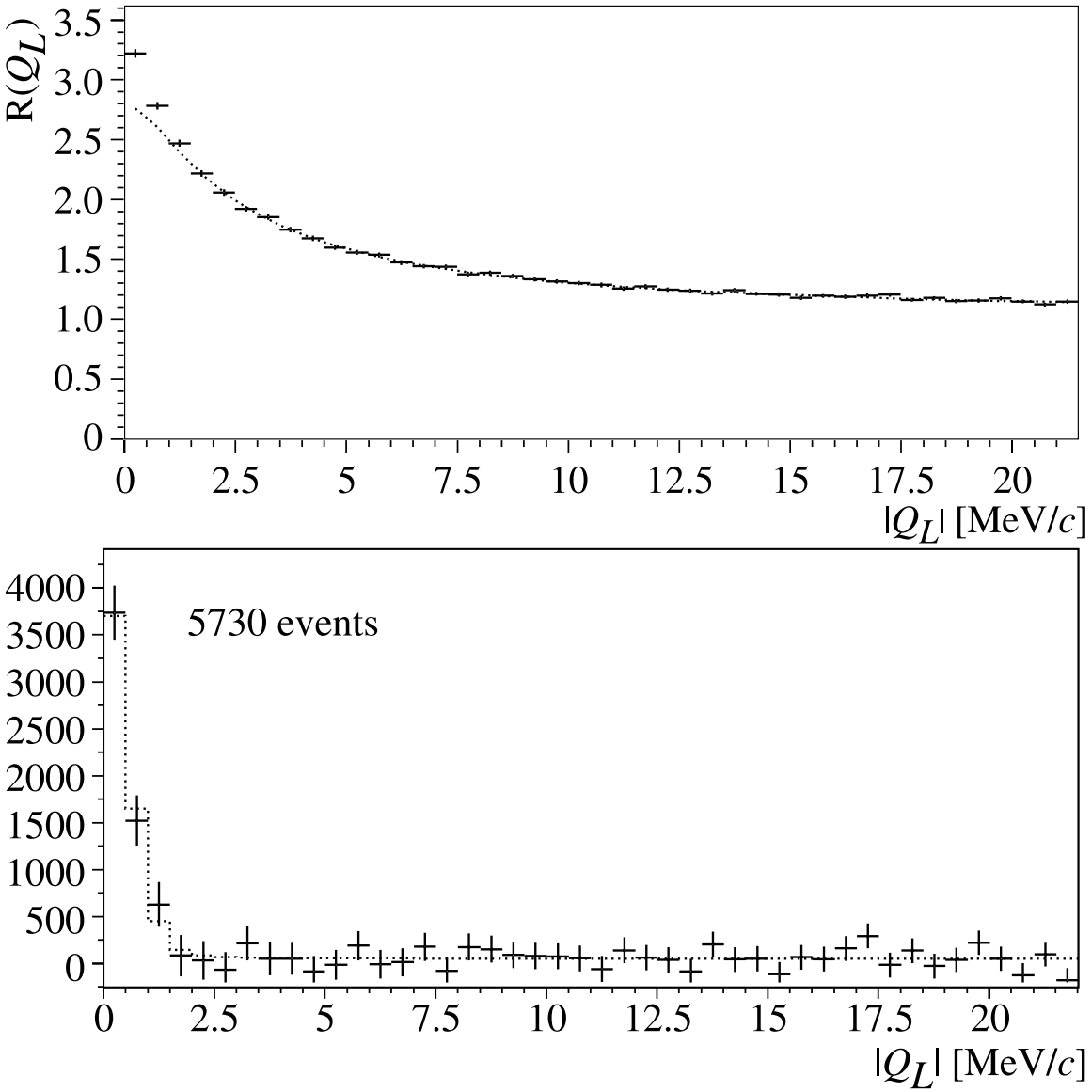

Figure 8.7: *Top: Experimental Q_L correlation functions (experimental points). The background correlation function is shown as a smooth curve. Bottom: Residuals after background subtraction. The dashed lines represent the expected atomic signal shape. The bin-width is 0.5 MeV/c.*

Chapter 9

Modification of the DIRAC setup for $A_{\pi^+K^-}$ and $A_{\pi^-K^+}$ detection

9.1 Introduction

For the continuation of $A_{2\pi}$ lifetime measurement and for observation and lifetime measurement of $A_{\pi K}$ we are planning to update the the DIRAC experimental setup retaining symmetric geometry. In the symmetric geometry we will detect simultaneously πK "atomic" pairs of both signs with acceptable efficiency. Only modifications are discussed in this section.

Contrary to $\pi\pi$ pairs the πK pairs from $A_{\pi^+K^-}$ and $A_{K^+\pi^-}$ breakup have momenta, that differ by a factor 3.5. Only $A_{\pi K}$ with momenta higher than ~ 5.4 GeV$/c$ will breakup into detectable πK pairs, namely pairs entering the apparatus acceptance. The pions from $A_{\pi K}$ pairs have momentum range between 1.2 and 2.1 GeV$/c$, whereas the kaons have momenta between 4.2 GeV$/c$ and $\sim$ 7.3 GeV$/c$.

In order to detect π^+K^- "atomic" pairs one needs to discriminate pions from kaons in the negative arm. The detection of π^-K^+ pairs is somehow more complex as in this case, in addition to π^+, a large admixture of protons to positive kaons is also expected.

The present setup has to be upgraded in order to detect πK pairs from $A_{\pi K}$. The implementation of new detectors and trigger schemes should, however, not affect the detection efficiency of $\pi^+\pi^-$ atomic pairs, as this class of events will still constitute the bulk of our collected data.

The setup upgrading comprises:

◇ Measurements with single and multilayer targets (two-target method). This method allows to decrease systematic errors by 4 times.

◇ Additional iron shielding (shielding 1) near the target station with collimators for the primary and secondary beams instead of existing wide tube common for the both beams. The existing iron shielding between the target station and the spectrometer magnet we will call as shielding 2. The additional shielding will allow essentially to decrease counting rates of upstream detectors.

◇ A permanent magnet installation in the secondary particle channel between the target station and the first shielding to improve close track separation in the Scintillation Fiber Detector (SFD).

◇ A new detector — Microdrift Chambers (MDC) — installation in the air gap of the secondary particle channel instead of existing Microstrip Gas Chambers (MSGC). The MDC measures particle coordinates using 18 identical planes: X, Y and U. The sensitive area of the MDC is close to $80 \times 80\,\text{mm}^2$ and the space resolution for single hits is about 25 μm.

◇ A new front-end electronics implementation for SFD. The new electronics will allow to measure time and amplitude for every SFD column. As a result the SFD efficiency will be increased up to 98%

and a close hit separation will be much better. Production of the new detector with the fiber diameter 0.28 mm instead of 0.5 mm in the existing detector.

◇ Front-end electronics modification for the existing Drift Chambers (DC) downstream of the spectrometer magnet. The modified electronics will allow to decrease threshold and, consequently, to decrease high voltage. This will allow to work at higher intensities with the high efficiency.

◇ Two aerogel Cherenkov counters installation in the left arm of the downstream detectors for kaon and proton separation.

◇ New gas Cherenkov detectors installation in both arms of the spectrometer for pion and kaon separation. These counters will be filled by sulfur hexafluoride (SF_6) or by perfluorobutane (C_4F_{10}). The existing gas Cherenkov counters filled by nitrogen (N_2) after a modification will be still in use for electron suppression.

◇ New scintillation counters installation in both arms as an extension to the existing Vertical Hodoscopes (VH) and Preshowers (PSh). These counters will allow to increase the setup aperture and essentially to increase the $A_{\pi K}$ detection efficiency.

◇ Implementation of additional fast hardware processors for on-line selection of π^+K^- and π^-K^+ pairs with small relative velocities.

The updated experimental setup is shown in Fig.9.1. The topology of π^-K^+ pairs from π^-K^+ atom breakup is shown in fig. 9.2. The kaon trajectories are close to the setup symmetry axis, whereas the correlated pions are away from the axis.

Kaons from π^-K^+ atoms are detectable in the K^+ momentum range from ~ 3.9 to ~ 8.9 GeV/c when the π^-K^+ atoms are emitted along the left side of the collimator. When the π^-K^+ atoms are emitted along the secondary particle axis the kaons are practically at the edge of detection (somewhere at the momenta 4.5÷5 GeV/c. For π^+K^- atoms the particle trajectories should be mirrored relative to the symmetry axis (proton beam). Of course the kaons and pions should be detected in coincidence.

9.2 Accelerator

For continuation of the experiment we need the slow extracted proton beam with a good time structure during a spill in order to have flat distribution of triggers. To improve beam structure we intend to implement feedback from the existing device which detects secondary emission electrons from the target or using the first level trigger intensity. The spot radius of the beam on the target should be about 1 mm.

9.3 Secondary particle channel modification

9.3.1 Existing target station

The target station configuration provides insertion different types of targets into the beam. Data will be collected with single and multilayer Ni targets. The target thicknesses are the same ($\approx 100\,\mu$m) and the nuclear interaction probability $\varepsilon_{nucl} = 6.5 \cdot 10^{-4}$. The targets will be inserted in the proton beam alternatively, for example, one data taking run with the single layer target, one run with the multilayer target.

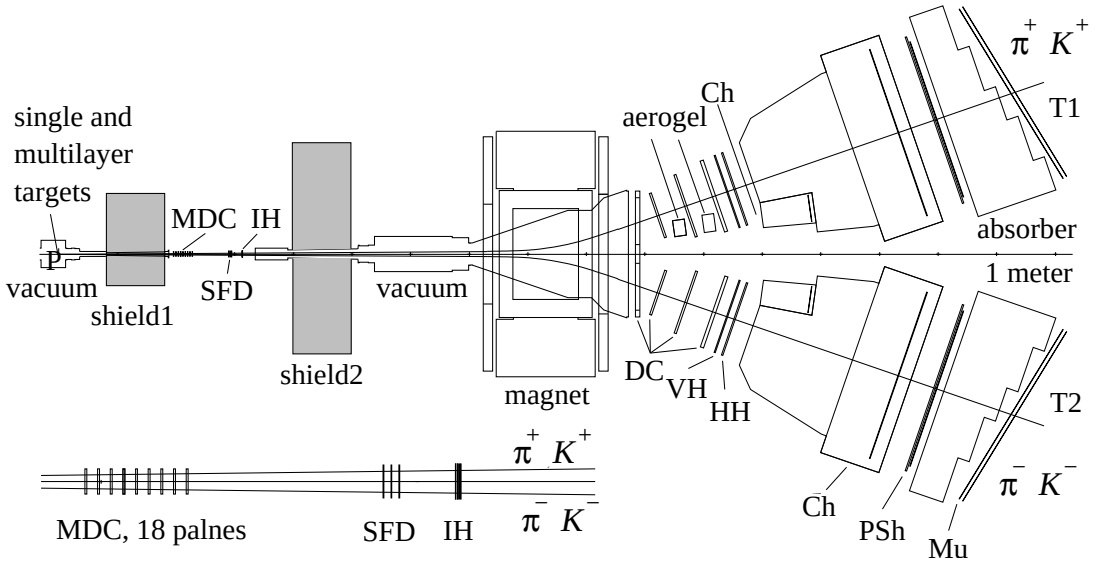

Figure 9.1: *Schematic top view of the updated DIRAC spectrometer. Upstream of the spectrometer magnet: microdrift chambers (MDC), scintillating fiber detectors (SFD), ionization hodoscopes (IH). Downstream of the magnet, in each arm of the spectrometer: drift chambers (DC), vertical and horizontal scintillation hodoscopes (VH, HH), gas Cherenkov counters (Ch), preshower detector (PSh) and, behind the iron absorber, muon detector (Mu). In the left arm: Aerogel Cherenkov counters.*

9.3.2 Shielding near the target station

In the existing setup after the target station the common for the proton and secondary beams wide tube is installed. We plan to install instead of the wide tube a shielding (shielding 1) with collimators for the proton and secondary beams. A simulation shows that after installation of such shielding the background counting rates of upstream and downstream detectors will be suppressed by factor ~ 1.8. For details see Appendix A.

9.3.3 Available permanent magnet

In the present setup we have some problems with measurement of the opening angle of two tracks that hit the same fiber of the SFD. A way to overcome this problem is the installation of a small permanent magnet (PMG) close to the target to recover the close track separation [CHIB01].

The permanent magnet with BL = 0.01 Tm deflects charged particles with 3 GeV/c momentum by 1 mrad. It means that the magnet separates π^+ and π^- with $Q_x = 0$ ($Q_x \sim 0$ are most likely coming from $A_{2\pi}$) into the distance of 4.7 mm at SFD. So two close separated particles ("atomic" pairs) will be detected by SFD unambiguously.

The size of the PMG is $150 \times 40 \times 50$ mm^3 (W×L×H) with the weight of 1 kg. The permanent magnet poles are made of Nd-Fe-B which is the strongest type of permanent magnet. The pole size is $70 \times 40 \times 5$ mm (W×L×H). The two poles are set with the gap of 30 mm at the soft iron yoke.

The position of this magnet will be at the distance of 55 cm from the target. In this position the transverse dimensions of the secondary particle beam is equal to $\sim 20 \times 20$ mm^2. The proton beam passes under the magnet. For details see Appendix B.

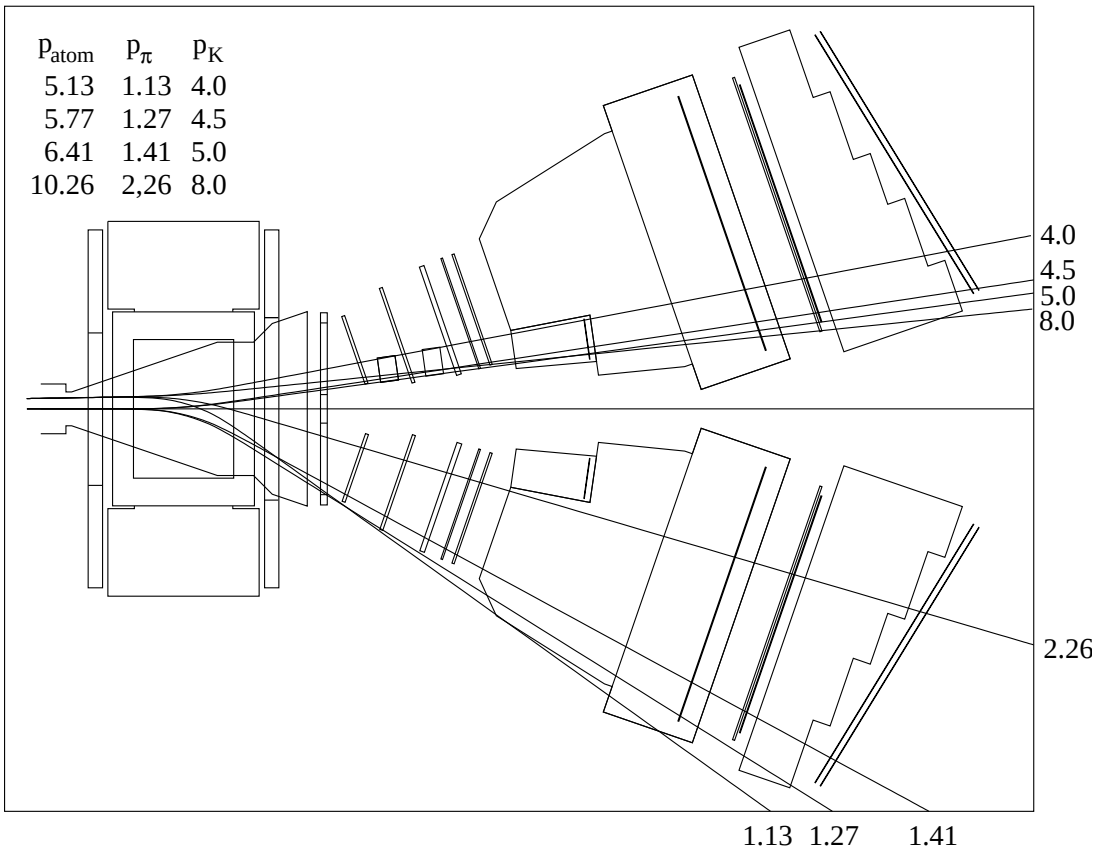

Figure 9.2: *Trajectories of π^- and K^+ from the $A_{\pi^-K^+}$ breakup. The numbers on the trajectory lines are the π^- and K^+ momenta in GeV/c. The $A_{\pi^+K^-}$, π^- and K^+ momenta are shown in the table in the left upper corner.*

9.3.4 Secondary particle channel and spectrometer magnet

The updated first vacuum part of the channel (between the target station and the upstream detectors) contains the permanent magnet and the collimator inside the shielding 1 (see Appendix A). It is necessary to foresee an access into the channel for the foil installation to ionize metastable atoms. This part of the channel is ended with Mylar vacuum window.

The secondary particle channel behind of the upstream detectors will be retained without changes. This concerns the spectrometer magnet also.

9.4 Upstream detectors modification

The upstream detectors are located in the air gaps of the secondary particle vacuum channel. They include the microdrift chambers (MDC), the scintillating fiber detector (SFD) and the scintillation ionization detector (IH).

9.4.1 Microdrift Chambers

We plan to implement in the upstream setup region a new detector — Micro Drift Chambers (MDC) with small gap ($\sim$ 3 mm) — a detector with high coordinate precision. The MDC is a new detector replacing the MSGC. The MDC measure particle coordinates using 18 identical planes: X, Y and U with 32 wires in each plane. The sensitive area of MDC is close to $80 \times 80\,\mathrm{mm}^2$, the space resolution for

single hits is about 25 μm and the efficiency per plane is close to 100%. The MDC will be installed behind the first shielding wall. The full scale detector with the full set of electronics is existing and was tested in summer 2003 and a new test is planed for autumn 2004. For details see Appendix C.

9.4.2 Scintillation Fiber Detector

The detector will be retained without changes. Only new ADC and TDC will be implemented. The new electronics will allow to suppress the cross-talk effect, improve the spacial resolution and increase detection efficiency up to 98%. The new TDC-ADC module for SFD readout is developed now. The new SFD with the fiber diameter of 0.28 mm, instead of 0.5 mm in the existing detector, was successfully tested in 2003. For details see Appendix D. Production of the new detector of such type to upgrade the present SFD is foreseen.

9.4.3 Ionization Hodoscope

The detector will be retained without changes. For detection of highly ionizing particles (nuclei) the signals from the last dynodes will be used.

A Si detector instead of the IH may also be used for double ionization measurements. For details see Appendix E.

9.5 Downstream detectors modification

The upgrade of the downstream detectors comprises:
— Modification of front-end electronics for Drift Chambers.
— Modification of the existing gas Cherenkov counters filled with nitrogen (N_2).
— Implementation of Aerogel Cherenkov counters.
— Implementation of new Gas Cherenkov counters filled with sulfur hexafluoride (SF_6) or perfluorobutane (C_4F_{10}).

9.5.1 Drift Chambers

Mechanically the Drift Chambers will be without changes. We plan to modify the front-end electronics to decrease the threshold. This will allow to decrease high voltage and to increase intensity. Implementation of the new code for more effective track reconstruction at high counting rates is foreseen also.

9.5.2 Vertical Hodoscopes

To the Vertical Hodoscopes the additional scintillation slabs will be added to increase aperture. These counters will allow to increase essentially the $A_{\pi K}$ detection efficiency. We plan also to implement a new front-end electronics with ADC and TDC for each photomultiplier of the VH.

9.5.3 Horizontal Hodoscopes

The Horizontal Hodoscopes will be without changes.

9.5.4 Aerogel Cherenkov detectors

The two aerogel Cherenkov counters installed in the left (positive) arm will be used for kaons detection and suppression of protons in the kinematic range of accepted $A_{\pi K}$. The aerogel detectors will be placed between the second (DC2) and the fourth (DC4) drift chamber modules.

The dimensions of the first and second aerogel radiator $300 \times 400 \times 90$ mm^2 (W×H×L) will be sufficient to intersect all trajectories of K^+ from $A_{\pi K}$ breakup. The each module is viewed by four 5-inches photomultipliers (Hamamatsu R1587) attached to the top and bottom sides. For details see Appendix H.

9.5.5 Existing gas Cherenkov counters

To suppress electrons and positrons we will use the existing gas Cherenkov counters filled with nitrogen (N_2). But these counters should be modified to clear a space for the new gas Cherenkov counters dedicated for pion and kaon separation. See Appendix I.

9.5.6 New gas Cherenkov Counters

For π and K separation we will use new gas Cherenkov counters filled with sulfur hexafluoride (SF_6) or perfluorobutane (C_4F_{10}). Sulfur hexafluoride and perfluorobutane are gases in normal atmospheric conditions, nontoxic, nonflammabable, chemically inert, noncorrosive, previously used as radiator.

SF_6 and C_4F_{10} are known to have excellent transparency to light with wavelength above $160 \div 190$ nm [GARW71], comparable to that of N_2. Indices of refraction of SF_6 and C_4F_{10} are 1.00072 and 1.0014, respectively. For details see Appendix J.

9.5.7 Preshower detectors

To the Preshower detectors the additional scintillation slabs will be added. These counters will allow to increase essentially the $A_{\pi K}$ detection efficiency.

9.5.8 Muon detectors

The Muon detectors will be without changes.

9.6 Trigger, Readout system and DAQ

The trigger logic will provide a reduction of the event rate up to a level acceptable to the data acquisition system. The trigger logic will be modified to collect both $\pi\pi$ and πK pairs with the low relative momentum Q. We will implement three hardware processors [AFAN02M] (of already used type), which use DC information, to select independently the $\pi^+\pi^-$, π^+K^- and π^-K^+ pairs from $A_{2\pi}$ and $A_{\pi K}$ decays.

The trigger system [AFAN02M] comprises a fast first level trigger [AFAN021] and higher level trigger processors which apply selection criteria to different components of the relative momentum of $\pi\pi$ and πK pairs.

The logic of T1 trigger level will remain the same. In the first level trigger a simple coincidence of VH, HH and PSh signals in both arms with a simultaneously applied "coplanarity cut" (at the hardware level) will be used for selecting $\pi\pi$ and πK pairs. The "coplanarity cut" limits the vertical component Q_y of the relative momentum of the accepted pairs.

Hardware processors are subsequently used to select pairs with low Q values. One is based on a neural network algorithm [KOKK01] which relies on the hit maps of the SFD, IH and VH detectors.

The neural (DNA) trigger will be upgraded in order to select π^+K^- and π^-K^+ candidates with a small relative momentum. In fact, it will be necessary to implement a new logic according to the new correlation maps among the VH slabs due to the new event topology. This means that for the DNA trigger a new training of the neuronal network will be necessary in order to select π^+K^- and π^-K^+ candidates. This can be done using Monte Carlo data and real data collected with T1 trigger.

Other three processors (for $\pi^+\pi^-$, π^+K^- and π^-K^+ pairs) will make use of the drift chamber data. They reconstruct tracks (by wire numbers) and reject the events with high components of relative momentum Q_L or Q_x. For these processors the look-up tables of the track analyzer will be modified to take into account the specific track correlations for the πK pairs.

We don't plan any particular modification in the on-line software (DAQ). The present DAQ architecture will be able to manage the volume of data foreseen for the new experiment.

9.7 Advantages of the modified setup for detection of $A_{2\pi}$ and $A_{\pi K}$

Below we summarize advantages of the modified setup with respect to the existing experimental setup.

Measurements with single and multilayer targets will allow to decrease the systematic uncertainty in the value of the $A_{2\pi}$ lifetime by 6 times.

Improved particle identification (Cherenkov counters with SF_6 or C_4F_{10}, Aerogel detector) and additional hardware processors will allow to detect $\pi^+\pi^-$, π^+K^- and π^-K^+ "atomic" pairs simultaneously.

The additional shielding together with the existing one will decrease background rates in the detectors and will allow us to increase the intensity of the primary proton beam by a factor two. Together with all other modification, which includes a better time structure of spills, implementation of MCD, modification of SFD, the aperture increasing, it will increase the total efficiency of the data collection by factor of 4.

Chapter 10

Other physics subjects

10.1 Study of charged particle production dynamics using Coulomb and Bose-Einstein correlations

The DIRAC setup may also be used to study other physics topics simultaneously with hadronic atoms detection.

The study of the $\pi^+\pi^-$ Coulomb correlation enables to measure the fraction of pion pairs generated by short-lived (ρ, ω, $\Delta\ldots$) or by long-lived sources (η, $\eta\prime\ldots$) [AFAN91, AFAN97A]. This relation can be measured as a function of the pair energy in the lab system at the few percent level. The identification of K^-, K^+ and p allows one to perform the same analysis for further combinations of charged particles. The Coulomb correlations for K^+K^- and K^-p are sensitive to the size of their production region. Therefore the correlation study allows to obtain a picture of the particle production dynamics in coordinate space for light and heavy nuclei.

A study of the Bose-Einstein correlations in $\pi^-\pi^-$ and $\pi^+\pi^+$ requires the consideration of Coulomb corrections for those pairs, which originate from short-lived sources [LEDN82]. Exploiting the high relative momentum resolution of our spectrometer, it is possible to extract these corrections from the measurements ($\pi^-\pi^-$, $\pi^+\pi^+$ and $\pi^+\pi^-$) themselves. The data for like-sign particles are taken as a by-product during normal data acquisition.

The momentum correlations of particles at small relative velocities are widely used to study space-time characteristics of the production processes, thereby serving as a correlation femtoscope. In particular, in the case of non-interacting identical particles, like photons or, to some extent, pions, these correlations result from the interference of the two-particle amplitudes due to the symmetrization requirement of quantum statistics (QS) [GOLD60, KOPY72].

The momentum correlations of particles emitted at nuclear distances are also influenced by the effect of final state interaction (FSI) [KOON77, LEDN82]. Thus the effect of the Coulomb interaction dominates the correlations of charged particles at very small relative momenta (of the order of the inverse Bohr radius of the two-particle system), respectively suppressing or enhancing the production of particles with like or unlike charges. Though the FSI effect complicates the correlation analysis, it is an important source of information allowing for the coalescence femtoscopy (see, e.g., [SATO81, LYUB88, MROW92, SCHE99]), the correlation femtoscopy with unlike particles [LEDN82, BOAL86] including the access to the relative space–time asymmetries in particle production [LEDN96] and a study of strong particle interaction.

For the collisions involving nuclei, the effective radius r_0 of the emission region can be considered much larger than the range of the strong interaction potential. The FSI contribution to the correlation function is then independent of the actual form of the potential [LEDN82, GMIT86]. At small $Q = 2k^*$, it is determined by the s-wave scattering amplitudes $f(k^*)$ [LEDN82]. In the case of $|f| > r_0$, this

contribution is of the order of $|f/r_0|^2$ and dominates over the effect of QS. In the opposite case, the sensitivity of the correlation function to the scattering amplitude is determined by the linear term f/r_0.

The possibility of the correlation measurement of scattering amplitudes has been demonstrated [LEDN99] in a recent analysis of the NA49 $\pi^+\pi^-$ correlation data within the RQMD transport model. The fitted s-wave $\pi^+\pi^-$ scattering length $(2a_0+a_2)/3$ appeared to be $\sim 35\%$ lower than the input value of 0.23 fm. The recent BNL data on K_{l4} decays [PISL03] also point to a similar shift ($\sim 20\%$ in a_0). Clearly, the correlation measurement of the two-pion scattering amplitudes can serve as an important additional information to the pionium lifetime measurements. Besides, this measurement can also be performed for other two-particle systems like $\pi^\pm K^\pm$, K^+K^- $K^\pm p$.

The correlation function of two non–identical particles, compared with the identical ones, contains a radically new piece of information on the relative space-time asymmetries in particle emission [LEDN96]. It can be accessed by studying the correlation functions $\mathcal{R}_{+i}$ and $\mathcal{R}_{-i}$ with positive and negative projection k_i^* onto a given direction $\mathbf{i}$ or the ratio $\mathcal{R}_{+i}/\mathcal{R}_{-i}$. Particularly, $\mathbf{i}$ can be chosen as the direction of the pair velocity — a natural choice in the geometry of the experiment DIRAC. Being sensitive to relative time delays and collective flows, the correlation asymmetries proved to be a useful tool for a study of the space-time evolution of particle production in heavy ion collisions (see a review [LEDN04] and references therein). Clearly, they can give a valuable information about the dynamics of proton-nucleus collisions as a by-product of the experiments with hadronic atoms.

10.2 Study of Coulomb correlations in 3π system

It is well-known that the presence of the coherent pions (or pions emitted in the same quantum state) manifests itself as a suppression of the BE correlations of two or more identical pions [GUIL79, FOWL77, LEDN83, LYUB91]. Unfortunately, there are also other reasons leading to the suppression of particle correlations. Besides the experimental effects like finite resolution and particle misidentification (that can be corrected for), presumably the most important one is the contribution of the particles emitted by long-lived sources [LEDN79], leading to the appearance of the parameter $\lambda < 1$ suppressing the correlation. Also the usual Gaussian parameterizations of the QS correlation functions may be inadequate and lead to $\lambda < 1$ in the presence of the sources with moderate but very different space-time characteristics [LEDN79, LEDN92, CSOR96].

In principle, the effect of long-lived sources can be eliminated in a combined analysis of two–pion and three–pion correlation functions. The measured quantity is the genuine three–pion correlation normalized with the help of the three two–pion contributions - its intercept measures the chaotic or coherent fraction [HEIN97]. First such measurements have been done only recently in heavy ion experiments at CERN SPS [BEAR99, AGGA00] and RHIC [ADAM03] and, in e^+e^- collisions at LEP [ACHA02]. The most accurate ones at RHIC and LEP indicate a dominant chaotic fraction though the systematic errors allow for a substantial coherent component. Some sources of the systematic errors, *e.g.*, the simplified treatment of the two-body Coulomb and strong FSI, can be overcome. However others, *e.g.*, the approximate (factorization) treatment of the multiparticle FSI (see, e.g. [MERC97]) or the insufficiently differential analysis of the three-pion correlation function, can hardly be avoided at present computational and experimental possibilities.

The proposed experiment has a chance to clarify the situation since it can study the Coulomb three-body forces with extremely high statistics just in the region of interest - at small relative momenta for all three pairs in the three-pion system in various charge states.

10.3 Decay $\pi^0 \to \mathrm{e^+e^-e^+e^-}$

The high resolution on the pair relative momentum and a use of thin targets (less than $10^{-3}X_0$) raise a possibility to study Dalitz and double Dalitz decays of π^0 on the DIRAC experimental setup in parallel

with the observation of metastable atoms. These decays are of interest because they can be exploited to perform a measurement of the electromagnetic form factor of the decaying pion.

The tree-level rate for double Dalitz decay were obtained by Kroll and Wada [KROL55]. Recently, radiative corrections to double Dalitz decays have been derived [BARK03]. The first experimental observation of a double Dalitz decay was published in 1962 [PLAN59, SAMI62]. A total of 206 examples of the decay $\pi^0 \to \mathrm{e}^+\mathrm{e}^-\mathrm{e}^+\mathrm{e}^-$ were observed by Samios in a sample of some 800000 bubble chamber photographs. Based on the observed angular correlations, Samios was able to exclude the possibility that the the π^0 was a scalar particle at the 3.6σ confidence level. His measurement of the branching ratio was of the 10% precision and remains the only one published to date.

In order to estimate the feasibility of detection of the double Dalitz π^0 decay by the current DIRAC setup the dedicated trigger, which selected events with two simultaneous electron-positron pairs, was introduced in June 2003 [KULI03]. The detected yield of the double Dalitz process is one event per $2 \cdot 10^6$ main $\pi\pi$ triggers.

Chapter 11

Cost estimation for $A_{\pi K}$ experiment

11.1 Cost of the existing DIRAC setup

We intend to reuse a major part of the existing detectors so let us estimate the cost basing on the existing setup.

Cost of the existing DIRAC setup	
(detectors, electronics, vacuum system and computers):	3.5 MCHF.
Cost of the electronics rentals from the CERN pool:	0.4 MCHF.
Total cost:	3.9 MCHF.

11.2 Cost of new vacuum channel and shielding

Cost of new vacuum channel and shielding:	20 kCHF.

11.3 Cost of upstream detectors upgrade

11.3.1 Micro Drift Chambers

Front-end electronics “D411” (40 units):	8 kCHF.
Other expenses:	10 kCHF.
Total cost:	18 kCHF.

11.3.2 Scintillation Fiber Detector

New electronics for SFD (480 channels):	210 kCHF.

11.4 Cost of downstream detectors upgrade

11.4.1 Drift Chambers

Front-end electronics “D411” (130 units):	26 kCHF.
Other expenses:	4 kCHF.
Total cost:	30 kCHF.

11.4.2 Verical Hodoscopes

New electronics for VH (72 channels): 20 kCHF.

11.4.3 Additional scintillation counters

8 scintillation counters: 20 kCHF.

11.4.4 Aerogel detectors

Two aerogel detectors: 48 kCHF.

11.4.5 Present gas Cherenkov counters

Upgrade of the existing Cherenkov counters: 20 kCHF.

11.4.6 New gas Cherenkov counters with heavy gas

2 new gas Cherenkov counters: 52 kCHF.

11.4.7 Preshower detector

4 new scintillation counters: 10 kCHF.
New electronics for Preshower: 20 kCHF.
Total sum: 30 kCHF.

11.5 Trigger and Readout system

Trigger (processors): 50 kCHF.
Readout system: 50 kCHF.

11.6 Overal cost

The overall cost of the DIRAC setup upgraded: 568 kCHF.

Time scale for the $A_{2\pi}$ and $A_{\pi K}$ experiment

After approval of the Addendum, we estimate that the construction of the detectors and the electronics manufacture will take 18 months. The installation of the new detectors can be done within 3 months.

The upgraded setup test and calibration will require 4 months of beam time in 2006. In this run we are planning to observe $A_{2\pi}$ in long-lived states.

The measurement of $A_{2\pi}$ lifetime will continue within 14 months of beam time (2007–2008 or 2007–2009). In this time ∼66000 $\pi\pi$ atomic pairs will be collected with the single and multilayer targets. The $A_{2\pi}$ lifetime and the difference of the s-wave scattering lengths $a_0 - a_2$ will be estimated with a precision:

$$\frac{\sigma_\tau}{\tau} = 6\% \,, \qquad \frac{\sigma(a_0 - a_2)}{a_0 - a_2} = 3\% \,. \tag{1}$$

During the same time we plan also to detect ∼5000 πK atomic pairs to estimate the $A_{\pi K}$ lifetime and the difference of the s-wave scattering lengths $a_{1/2} - a_{3/2}$ with a precison:

$$\frac{\sigma_\tau}{\tau} = 20\% \,, \qquad \frac{\sigma(a_{1/2} - a_{3/2})}{a_{1/2} - a_{3/2}} = 10\% \,. \tag{2}$$

This estimation of the beam time is based on the $A_{2\pi}$ statistics collected in 2001–2003 and on the assumption that we will use 2.5 spills from supercycle during 20 hours per day.

Beam request in 2004

In 2004 we need two weeks of the accelerator time to test the Microdrift Chambes at the beam line T8.

The proton beam intensity is $(1 \div 2) \cdot 10^{11}$ protons per spill.

Preferable time is September-October.

Time schedule:

Beam — one week.

Pause — three days.

Beam — one week.

The full DIRAC setup will be switched on, spectrometer magnet including.

Information about collaboration

Responsibilities

The authors of this Addendum are the members of the DIRAC collaboration at CERN (PS212). As we are going to reuse a major part of the existing setup, the responsibilities of participants will be kept:

- Microdrift Chambers with readout electronics — JINR Dubna, Bazel;
- Scintillating Fiber Detector — Japanese group, INFN–Trieste, IHEP Protvino;
- Ionization Hodoscope — IHEP Protvino;
- Drift Chambers with readout electronics — JINR Dubna;
- Vertical Hodoscope — Santiago de Compostela University;
- Horizontal Hodoscope — IHEP Protvino;
- Preshower Detector — IFIN–HH Bucharest;
- Cherenkov Counters — INFN Frascati;
- Muon Counters — IHEP Protvino;
- Trigger and DAQ — JINR Dubna with support of collaboration.

Acknowledgements

We are grateful to J. Gasser and G. Colangelo, (Bern University) for their invaluable help in writing the theoretical part of our Addendum. For many interesting and stimulating discussions about status and future of the underlying theory (especially pion-kaon scattering) we also thank P. Büttiker, S. Descotes-Genon, T. Heim, K. Hencken, H. Leutwyler, U. Meißner, B. Moussallam, A. Rusetsky, H. Sazdjian, J. Stern, and D. Trautmann.

We acknowledge R. Steerenberg for the helpfull discussion of the DIRAC beam quality.

Appendix A

Shielding

A.1 Present initial part of the secondary channel

In the existing setup the common for the proton and secondary beams the wide tube is installed. Side and isometric views of the target station and the wide tube are shown in Figs. A.1, A.2 and A.3.

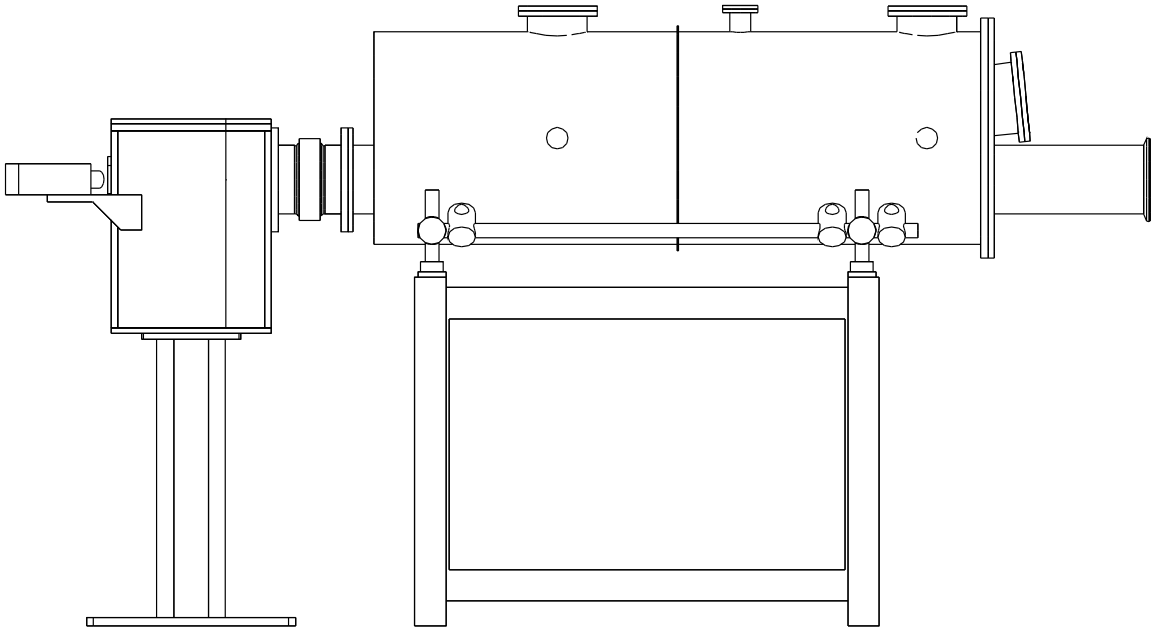

Figure A.1: *Side view of the target station (on the left) and the wide tube (on the right).*

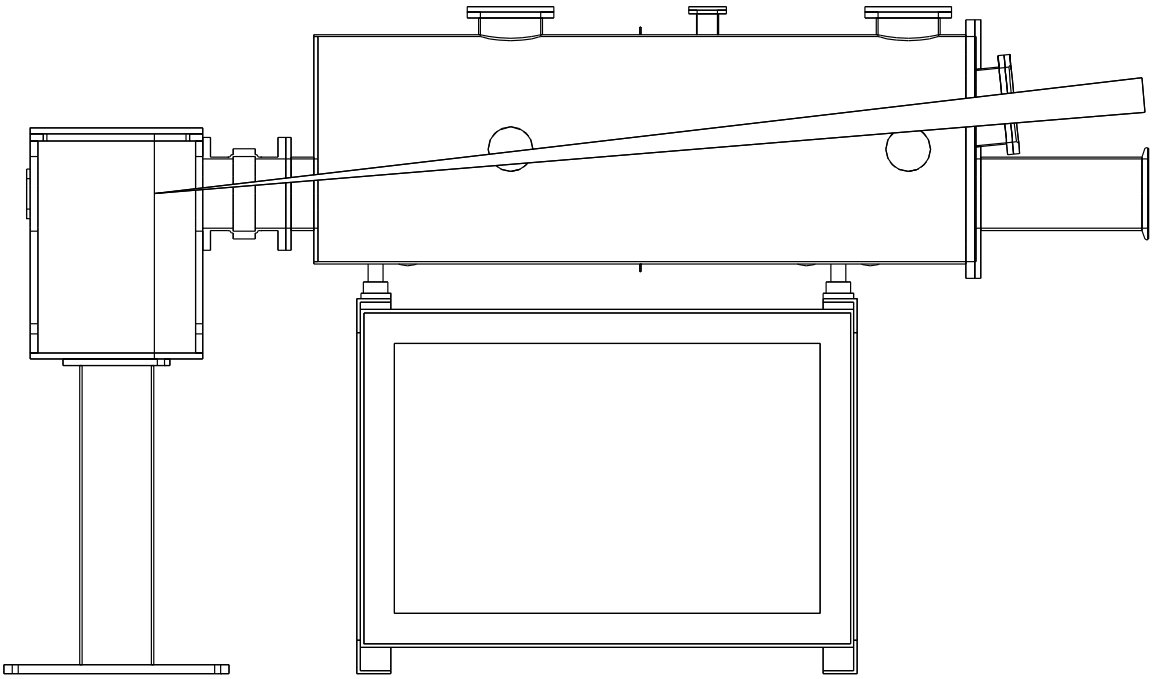

Figure A.2: *Side view of the the target station and the wide tube. The target station and the tube are cut along the proton beam. The secondary beam is shown.*

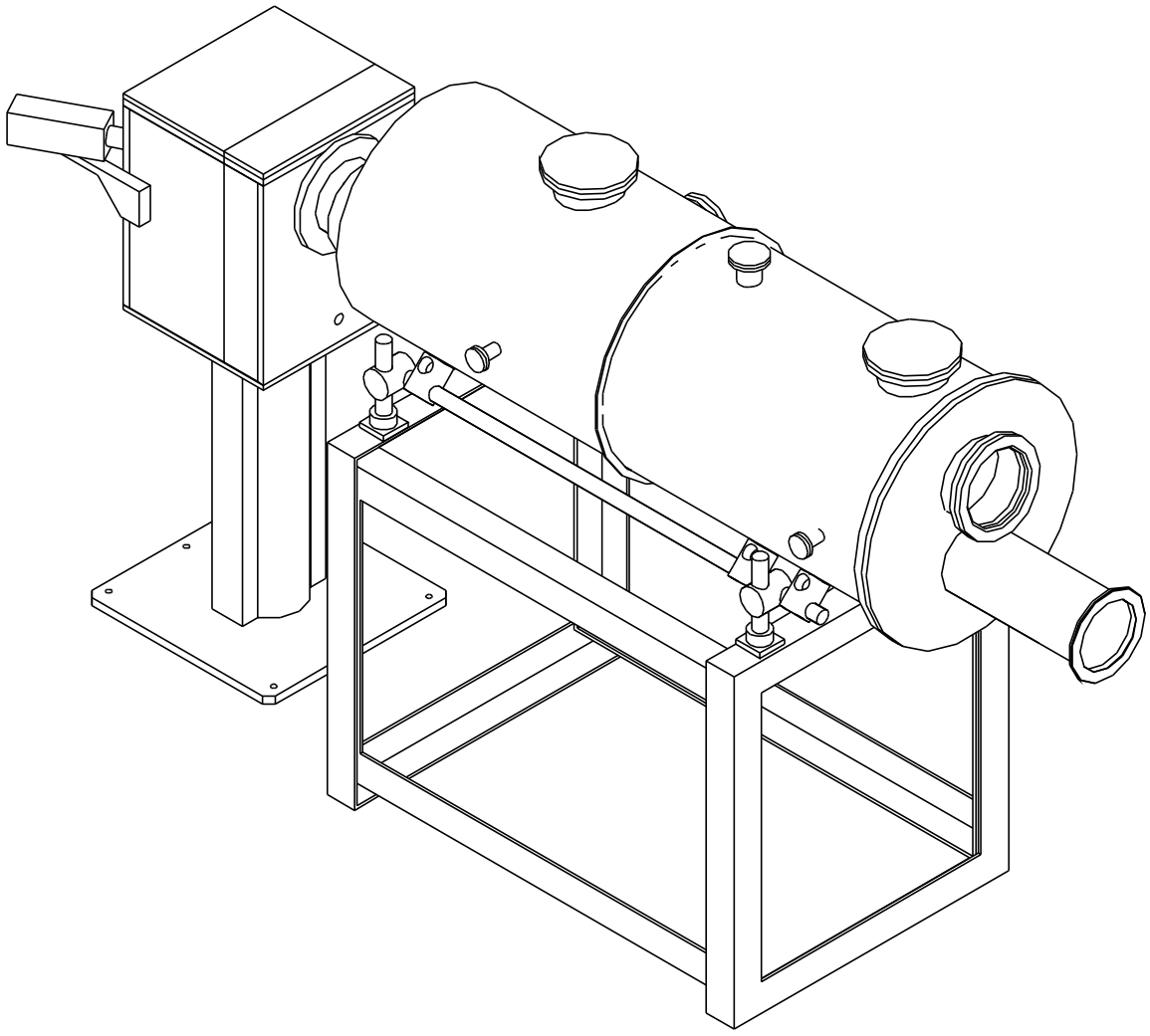

Figure A.3: *Isometrical view of the target station and the wide tube. The exit window for the secondary particles is made of mylar. Downstream of the exit window there is a place for the upstream detectors (MSGC, SFD and IH).*

A.2 New shielding near the target station

Instead of the wide tube we plan to install a shielding (shielding 1) with collimators for the proton and secondary beams. Side and isometric views of the target station and the shielding 1 are shown in Figs. A.4, A.5 and A.6. Simulation shows that after installation of the shielding 1 the counting rates of upstream and downstream detectors will be suppressed by $\sim$1.8 times. The internal dimensions of this part of the proton tube is 80×45 mm^2 (W$\times$H). For comparison, the proton tube main internal diameter is 185 mm. Decreasing of the internal dimensions of the proton tube in the vicinity of the shielding 1 will not increase a background due the beam-wall interactions, because such a collimator was already installed in the shielding 2 with the positive effect: counting rates of the downstream detectors were decreased by two times.

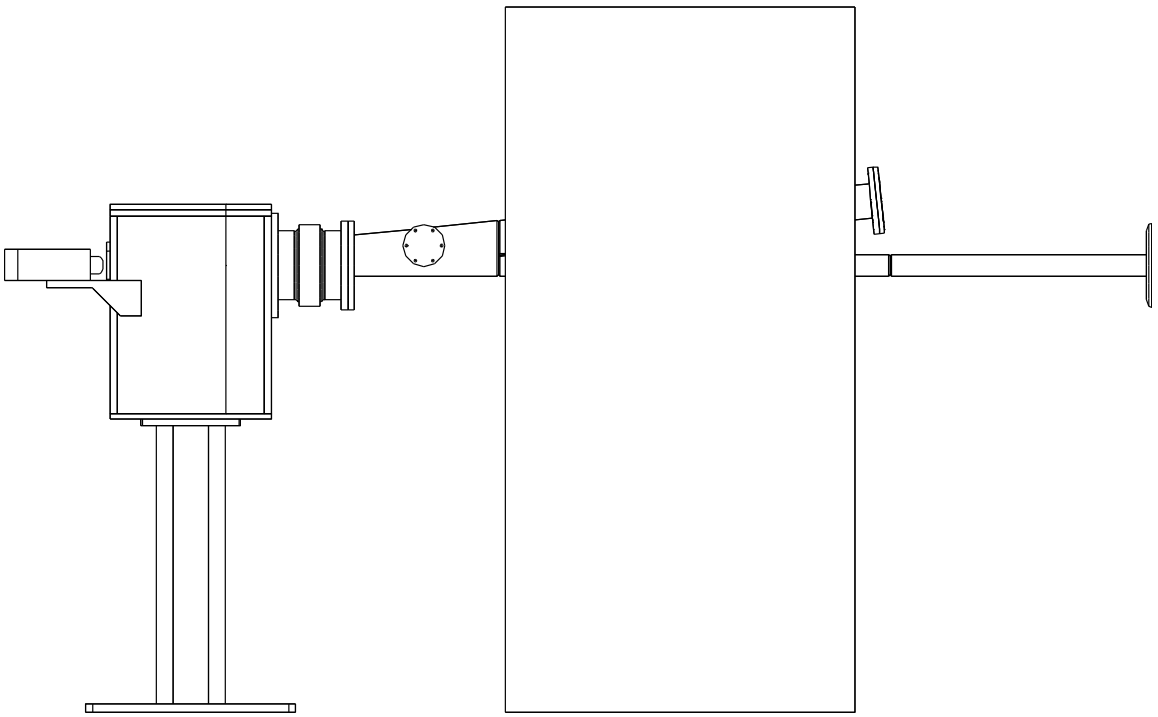

Figure A.4: *Side view of the target station and the shielding 1. The shielding thickness equals to 1 m of iron. Between the target station and the shielding an access into vacuum is shown (circle) for the permanent magnet installation.*

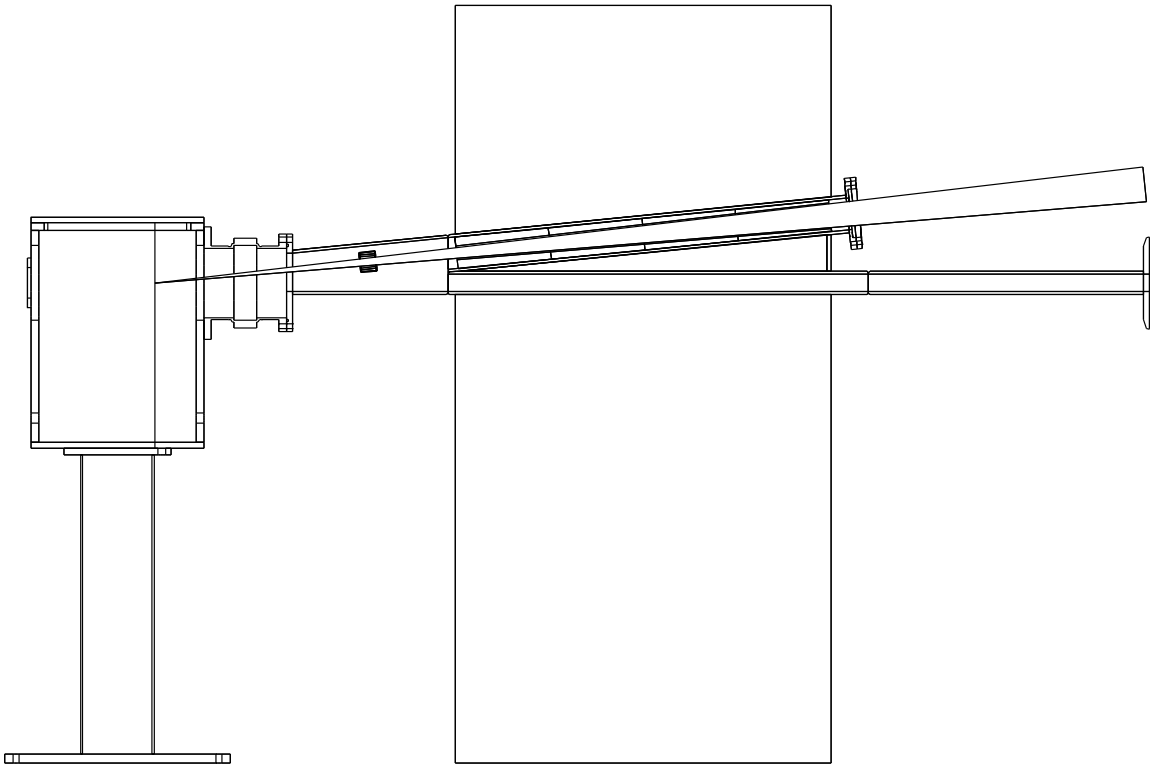

Figure A.5: *Side view of the target station and the shielding 1. The target station, the shielding and the rectangle vacuum tubes (initial part of the secondary particle channel and part of the proton tube) are cut along the proton beam. The secondary beam and a collimator for the secondary beam are shown. The small permanent magnet is visible in vacuum between the target station and the shielding.*

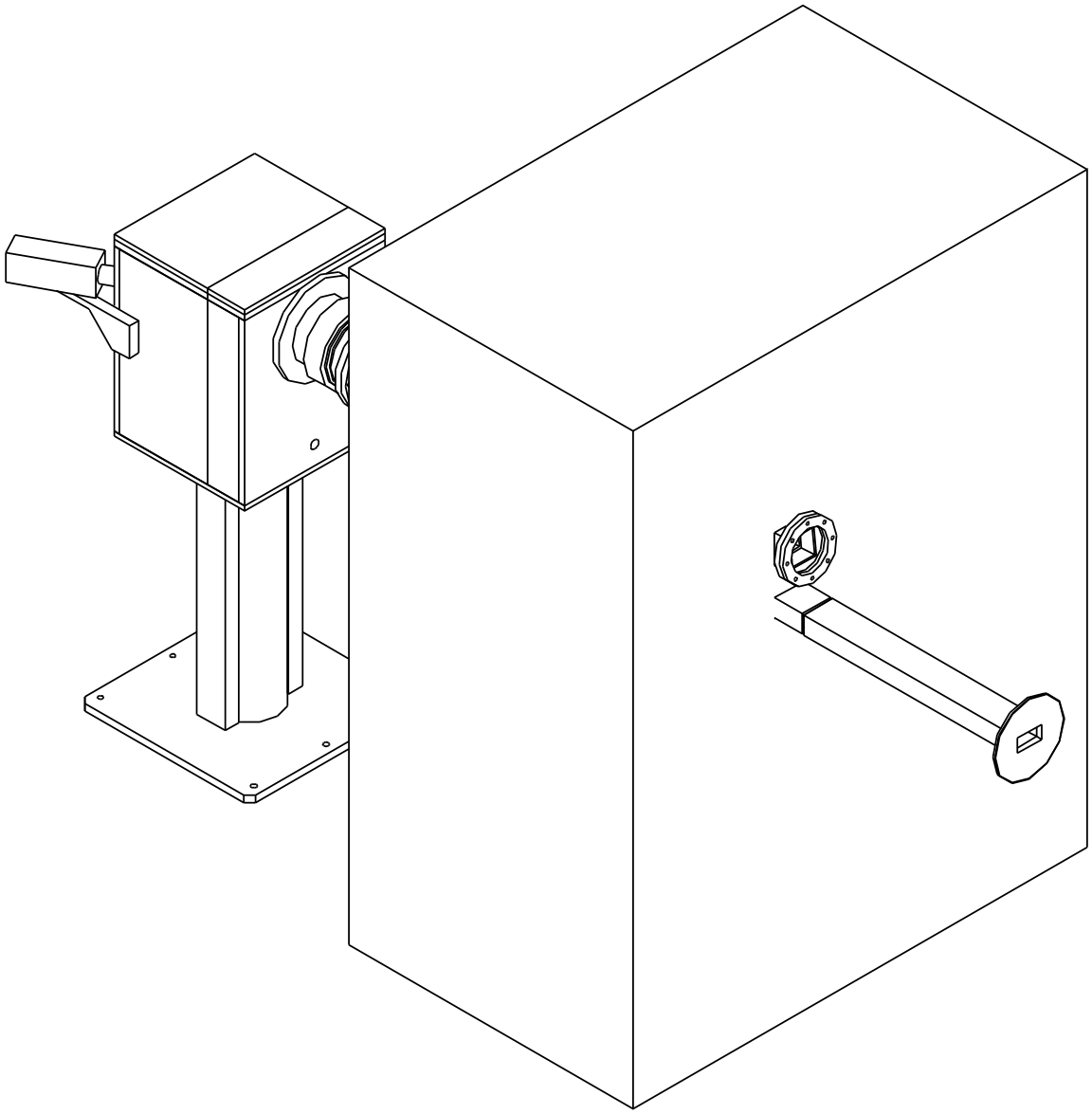

Figure A.6: *Isometric view of the target station and the shielding 1. The exit window for the secondary particles is made of mylar. Downstream of the exit window there is a place for the upstream detectors (MDC, SFD and IH)*

A.3 Sumulation of counting rates without and with the new shielding

Simulation has been done with help of GEANT-DIRAC simulation program of v2.63 [ZREL03]. Modified Fitiof.6 [UZHI96] code has been used as a generator of the interactions in the target. The particles from the target whose tracks belong to the solid angle of the setup channel with momentum $p \geq 1.2$ GeV/c were considered as "useful" events. The other particles were considered as "background" events.

Quantitative results for the counting rates for the present setup and for the setup with the new shielding are shown in the Tables A.1 and A.2. The Tables present counting rates and rates of "useful" particles together with rates of "background" particles and the background percentage for the Ionisation Hodoscope (IH), Verical Hodoscope in the left arm (VHL) and for the particles and the background percentage for the Ionisation Hodoscope (IH), Verical Hodoscope in the right arm (VHR) of the spectrometer. All rates are normalized on 1 interaction in the target. Precision of the results is better than 1 of last figure after decimal point. Dead times of the detectors were taken into account: 30 ns for IH and 80 ns for VH.

In the Table A.3 the control ratios for Monte Carlo and experiment are presented. In the Table A.4 the reduction of counting rates with the additional shielding relatively to the existing setup are presented. In average the detector counting rates will reduce by factror of $\sim$1.8.

For comparison purposes in the Tables A.5 and A.6 similar results are presented, but the dead times were not taken into consideration.

In the Figs. A.7 and A.8 the forward parts of the existing and new setups are shown together with tracks from 2 events from the target.

Table A.1: *Simulated counting rates for the present setup*

Detector	Counting Rates	Useful Particles	Background Particles	Background, %
IH	0.084	0.013	0.071	84%
VHL	0.023	0.004	0.019	82%
VHR	0.017	0.002	0.015	88%

Table A.2: *Simulated counting rates for the setup with the additional shielding*

Detector	Counting Rates	Useful Particles	Background Particles	Background, %
IH	0.045	0.013	0.033	72%
VHL	0.014	0.004	0.010	73%
VHR	0.009	0.002	0.007	77%

Table A.3: *Ratio of counting rates for monte-carlo and experiment*

Detector	Monte-Carlo/Experiment
IH	1.66
VHL	1.68
VHR	1.87

Table A.4: *Reduction of counting rates in case of the setup with the additional shielding*

Detector	Percentage
IH	45%
VHL	38%
VHR	50%

Table A.5: *Simulated counting rates for the existing setup. Dead times were not taken into consideration.*

Detector	Counting Rates	Useful Particles	Background Particles	Background, %
IH1	0.087	0.013	0.074	85%
VHL	0.031	0.004	0.027	87%
VHR	0.022	0.002	0.020	91%

Table A.6: *Simulated counting rates for the setup with the additional shielding. Dead times were not taken into consideration.*

Detector	Counting Rates	Useful Particles	Background Particles	Background, %
IH1	0.047	0.013	0.034	73%
VHL	0.019	0.004	0.016	81%
VHR	0.012	0.002	0.010	84%

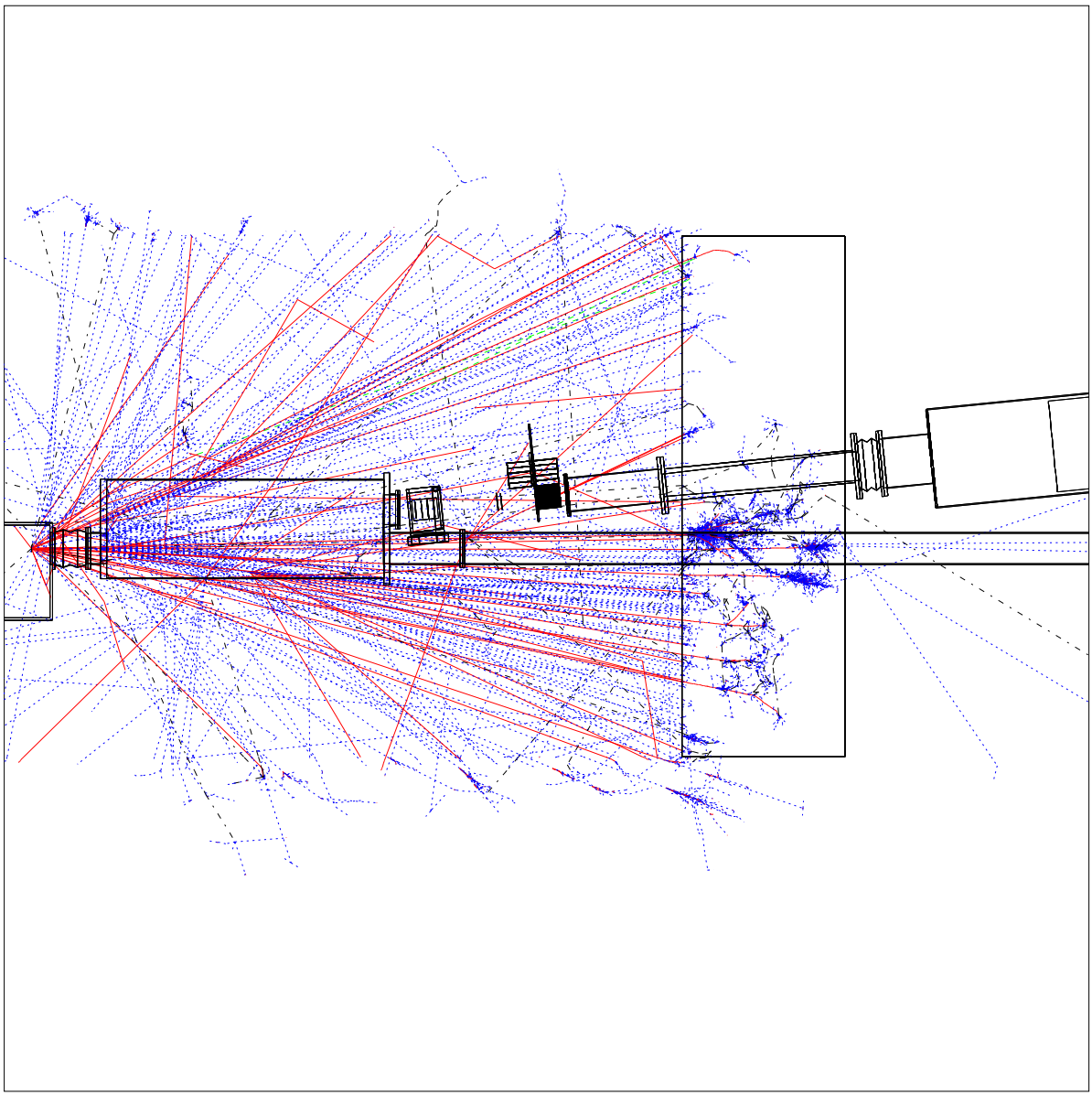

Figure A.7: *Forward part of the existing setup with tracks from 2 events from the target*

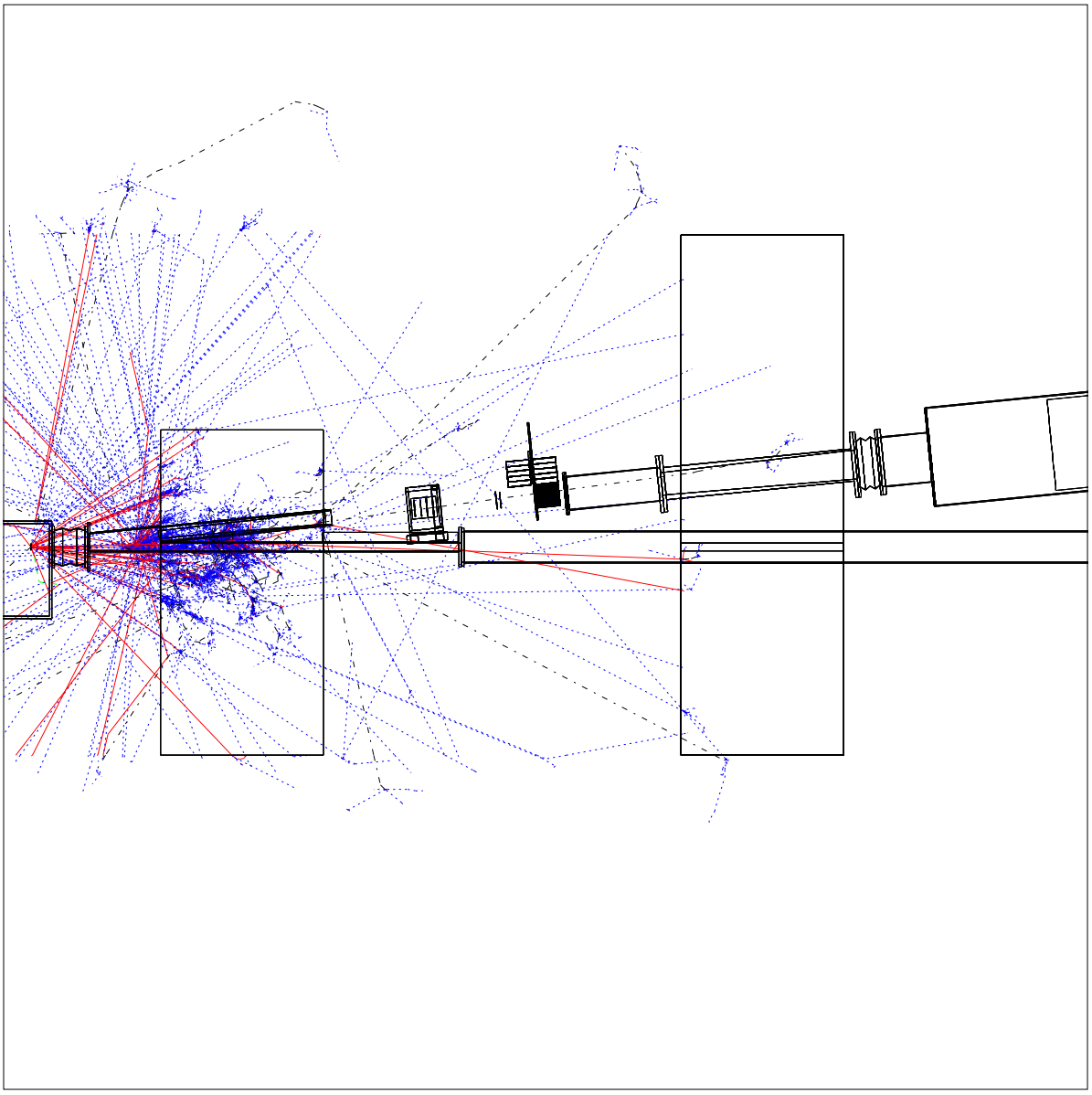

Figure A.8: *Forward part of the setup the additional shielding with tracks from 2 event from the target*

Appendix B

Permanent magnet

B.1 Permanent magnet purpose

In the present setup we have some problems with measurement of the opening angle of two tracks that hit the same fiber of the SFD. A way to overcome this problem is the installation of a small permanent magnet (PMG) close to the target to recover the close track separation [CHIB01].

PMG with BL=0.01 Tm deflects charged particles with a 3 GeV/c momentum by 1 mrad. This deflection corresponds to displacement at SFD of ± 2.35 mm. It means that the magnet separates π^+ and π^- with the transverse component of the relative momentum in the $\pi^+\pi^-$ c.m.s. $Q_x = 0$ into the distance of 4.7 mm at SFD. The region $Q_x \sim 0$ is most important because the pairs with $Q_x \sim 0$ are most likely coming from $A_{2\pi}$.

In reality the $A_{2\pi}$ breaks up mainly to π^+ and π^- with relative momentum $Q_x < 3$ MeV/c. The most likely momentum of the pions from $A_{2\pi}$ is around 2 GeV/c. The 2 GeV/c paricle displacement caused by PMG at the SFD is by 1.5 times larger than at 3 GeV/c. Therefore the separation of 2 GeV/c π^+ and π^- is easier than of 3 GeV/c pions.

B.2 Permanent magnet dimensions

Views of the permanent magnet are shown in Fig. B.1. The size of the PMG is $150 \times 40 \times 50$ mm^3 (W$\times$L$\times$H) with the weight of 1 kg. The permanent magnet poles are made of Nd-Fe-B which is the strongest type of permanent magnet. The pole size is $70 \times 40 \times 5$ mm^3 (W$\times$L$\times$H). The two poles are set with the gap of 30 mm at the soft iron yoke. The wide pole pieces give the uniform magnetic field in transverse direction.

B.3 Measurement of the magnetic field

The vertical component of magnetic field was measured with a Hand-held Gauss/Tesla Meter model 4048 produced by F.W.Bell Co. Ltd. For the measurement a transverse Hall probe, Model T-4048-001, was utilized.

The Hall probe was calibrated by NMR which has a ppm precision. The Hall probe shows constantly 4.7% higher values than NMR one in the wide range from 700 to 8000 Gauss. After the calibration the field precision becomes under 0.5%.

The PMG is designed to have the integral magnetic field BL=0.01 Tm along z axis which is 0.5% of the main spectrometer magnet (BL=2.2 Tm). The measurement shows BL=0.0108 Tm at the horizontal plane. The 8% higher value does not change the performance so much.

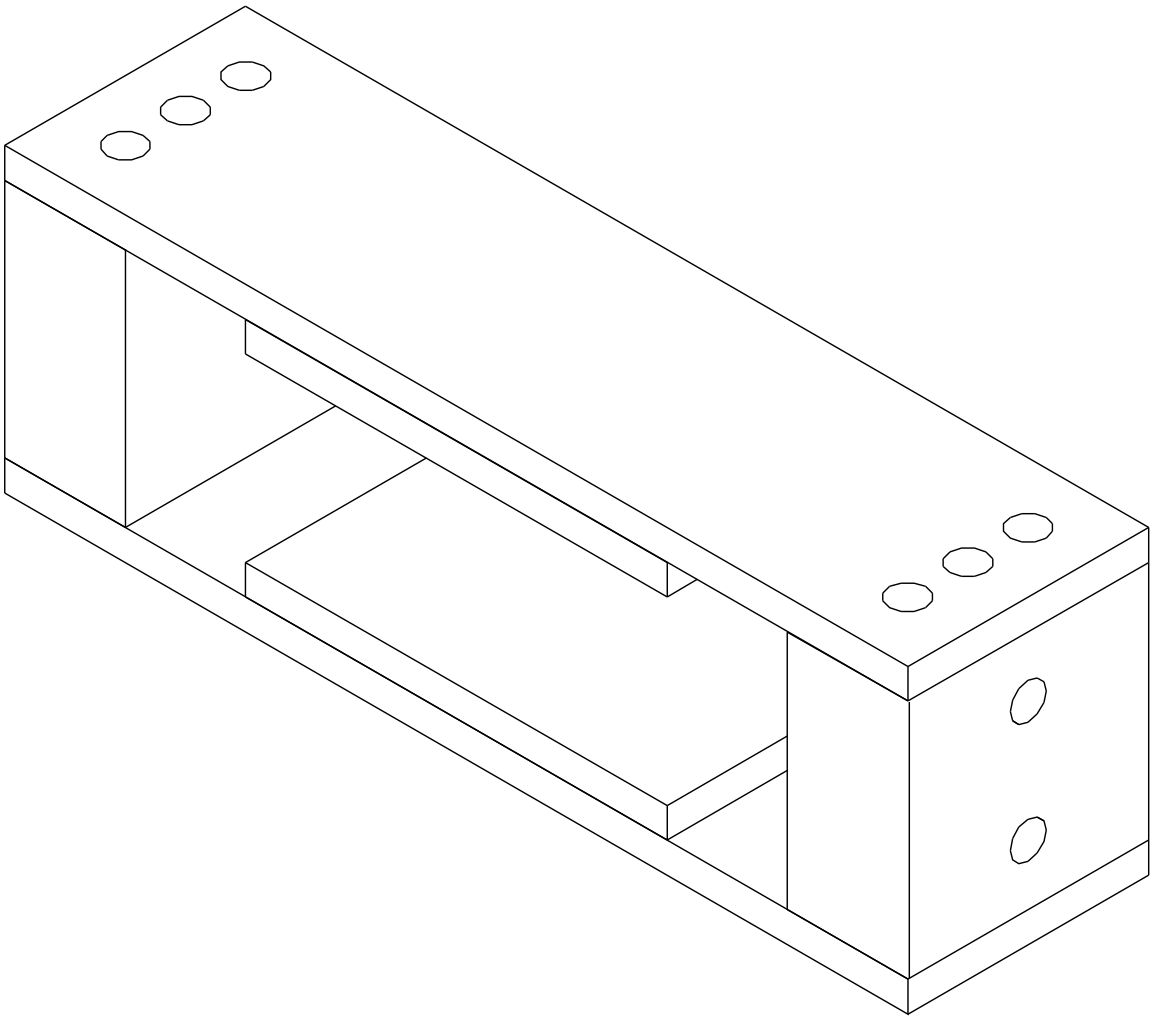

Figure B.1: *Isometric view of the permanent magnet.*

Analysis shows that we can take the box approximation with the constant field strength of B=0.27 T and the length of 40 mm. At the outside region of the box the field considered to be zero.

B.4 Installation

PMG will be installed on the distance of 550 mm (front face) from the target. Therefore the distance from the target to the PMG center is 570 mm. The distance from the target to the SFD plane is 2920 mm. Distance between PMG and SFD is 2350 mm. The profile of the secondary particles to be analyzed is around 20×20 mm^2 at 550 mm from the target.

PMG will be installed in vacuum between the target station and the shielding, see Appendix A. Installation of the permanent magnet is shown in Figs. B.2 and B.3. The secondary particles go across the gap between the two magnet pole pieces.

The angle between the secondary particle channel and the primary proton beam is 5.7° (0.1 rad). The distance from the PMG center to the proton beam is 55 mm at 550 mm from the target. The primary proton beam passes through with the clearance of 30 mm under the yoke of the magnet to avoid background generation by the halo of the proton beam.

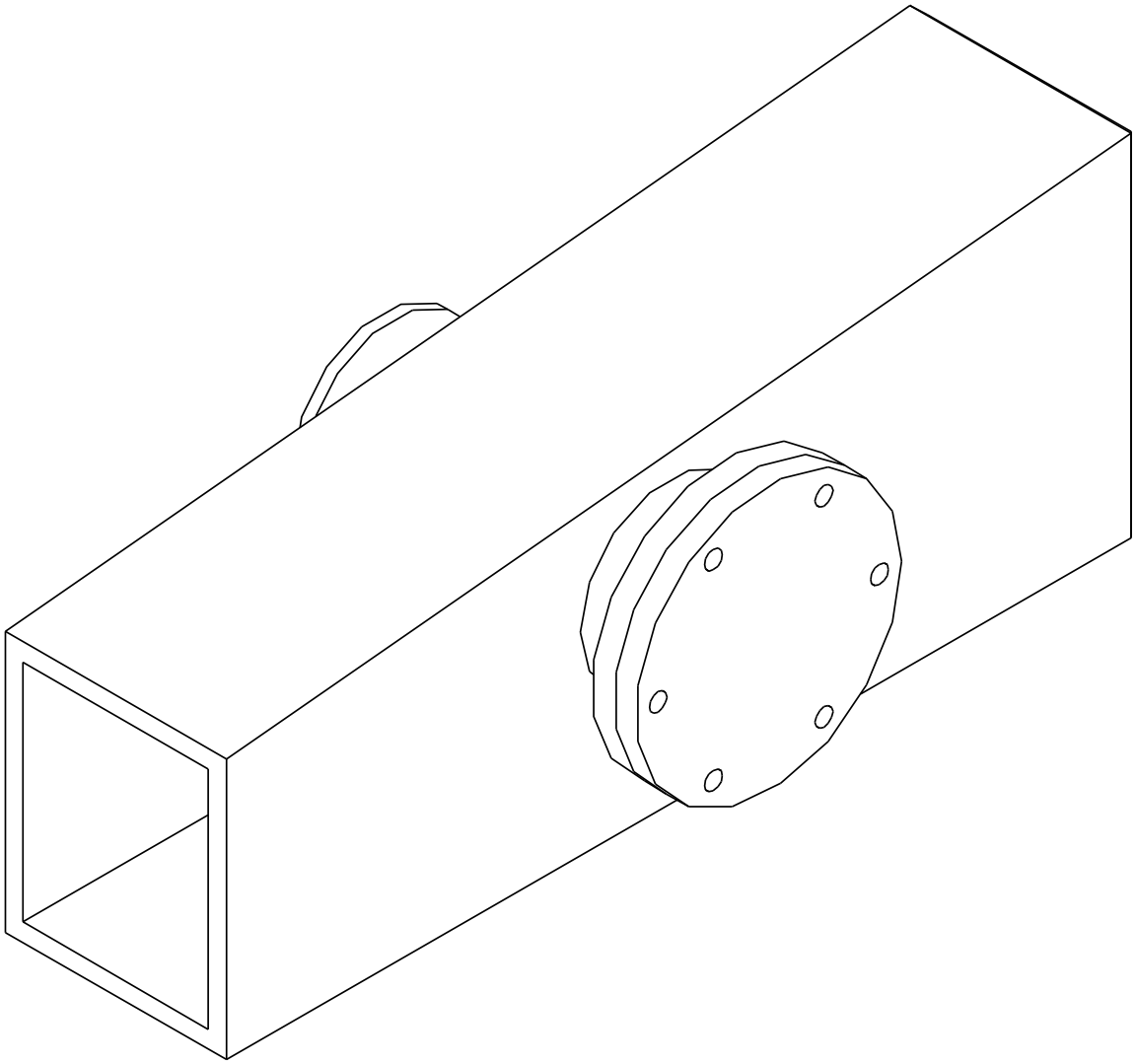

Figure B.2: *Permanent magnet installation in the vacuum channel. The common for the secondary and proton beams vacuum section placed between the target station and the shielding is shown. The permanent magnet is located inside this section.*

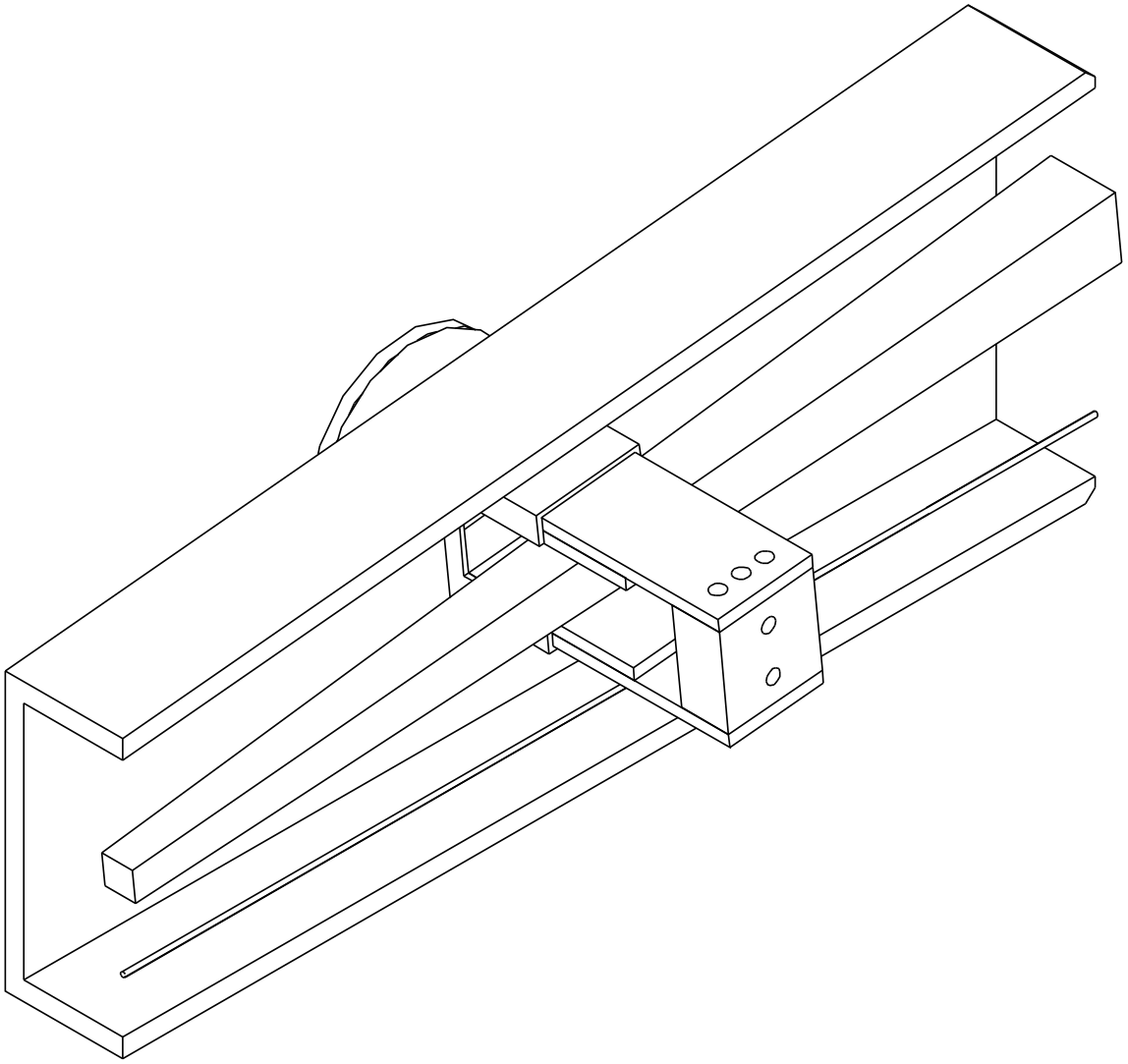

Figure B.3: *Permanent magnet installation in the vacuum channel. The vacuum channel is cut along the proton beam. The secondary and proton beams are shown.*

Appendix C

Micro Drift Chambers

C.1 Microdrift chamber purpose

Drift chambers play a very important role in the present DIRAC experiment. They provide track reconstruction with a high efficiency and with high spatial resolution. Rigid mechanical design, rather simple production technology, nice features of read-out electronics make the drift chamber technique also attractive for particle tracking between the target and the magnet.

The distinctive property of "atomic" pairs is the passage of two charged particles at a rather small relative distance while detected upstream of the magnet. Therefore, upstream coordinate detectors have to detect tracks with high spatial resolution and at the same time to resolve nearby tracks.

In the following we describe the design of Micro Drift Chambers, which combines high space and time characteristics with relatively high double track resolution. And we plan to implement this detector in the upstream setup region (Figs. C.1 and C.2).

The MDC is a new detector with a small cell size (2.54×2 mm^2) and with high coordinate precision replacing the MSGC. The MDC measure particle coordinates using 18 identical planes: X, Y and U with 32 wires in each plane. The sensitive area of MDC is close to $80 \times 80\,$mm^2, the space resolution for single hits is about 25 μm and the efficiency per plane is close to 100%. The MDC will be installed behind the first shielding wall.

C.2 Drift chamber cell

Let us consider how particles are detected in a drift chamber cell. In case of one particle, primary ionisation electrons drift to an anode wire and initiate the avalanche process. This avalanche occupies part of the anode wire ("dead zone") and inhibits the detection of another particle close-by in space. An additional limitation arises from read-out electronics. Even if two particles are detected on the anode wire itself, a later signal may not be accepted by the multi-hit TDC due to a finite double-hit resolution. These limitations are fatal only in case of a single plane chamber. An additional plane, shifted by half a cell width, eliminates not only a left-right ambiguity, but also the double track resolution problem (fig. C.3). If two tracks cross one cell, one particle is detected by the first plane and the other by the second plane.

In the same figure (fig. C.3) a schematic layout of a double plane chamber is presented. Each plane consists of 32 cells. The cell size is 3×2 mm^2 was used in the GARFIELD simulation.

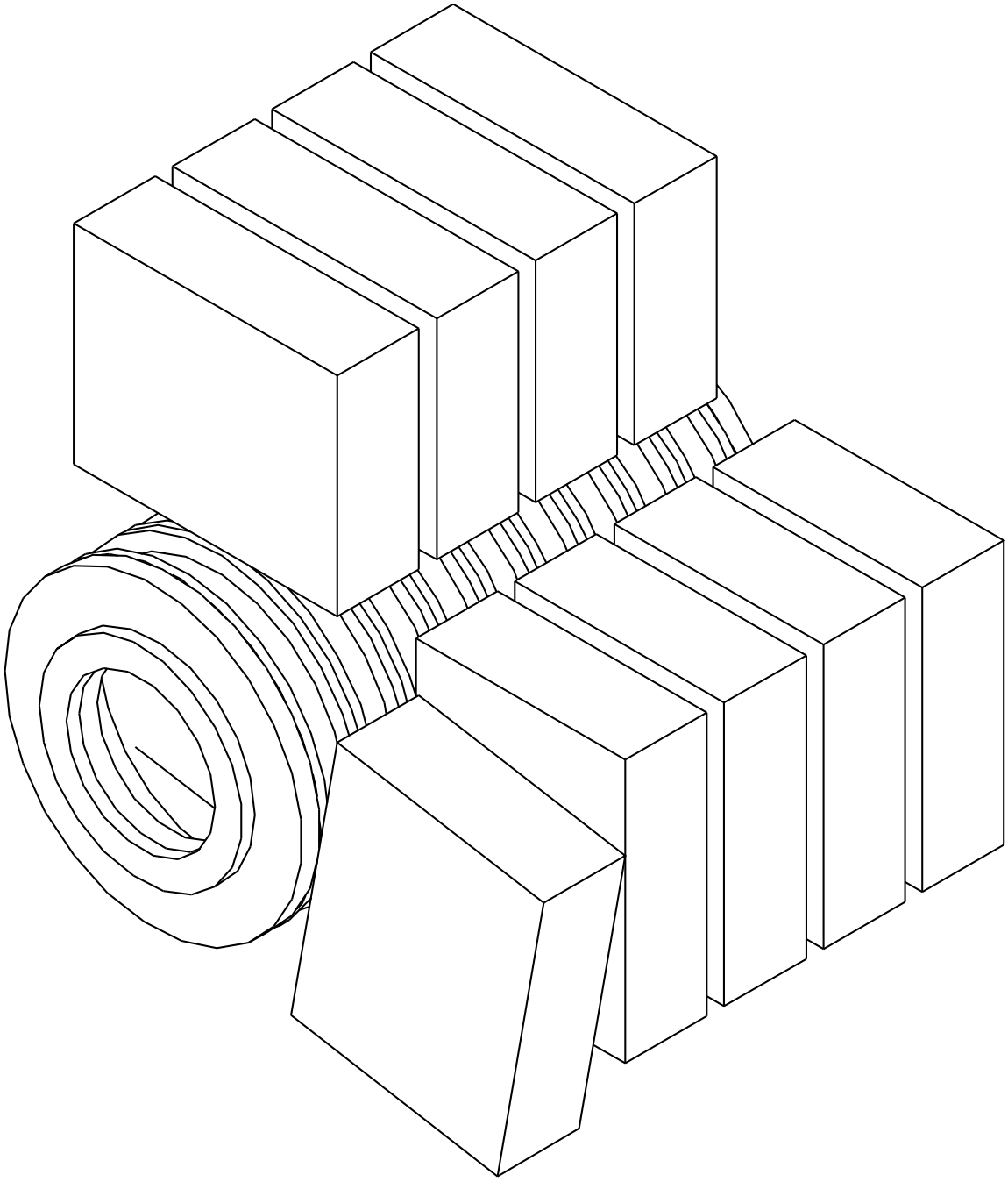

Figure C.1: *Microdrift chambers with electronics.*

C.3 Operation mode

The chamber will operate with the gas mixture $\mathrm{Ar}(0.33) + i\mathrm{C_4H_{10}}(0.66) + \mathrm{H_2O}(0.01)$. This will permit to use a slightly modified read-out electronics, which has demonstrated perfect operating features.

Drift parameters, time and space resolution of the chamber have been investigated with help of the GARFIELD simulation package, and the counting rate capability has been estimated from our "dead zone" measurement.

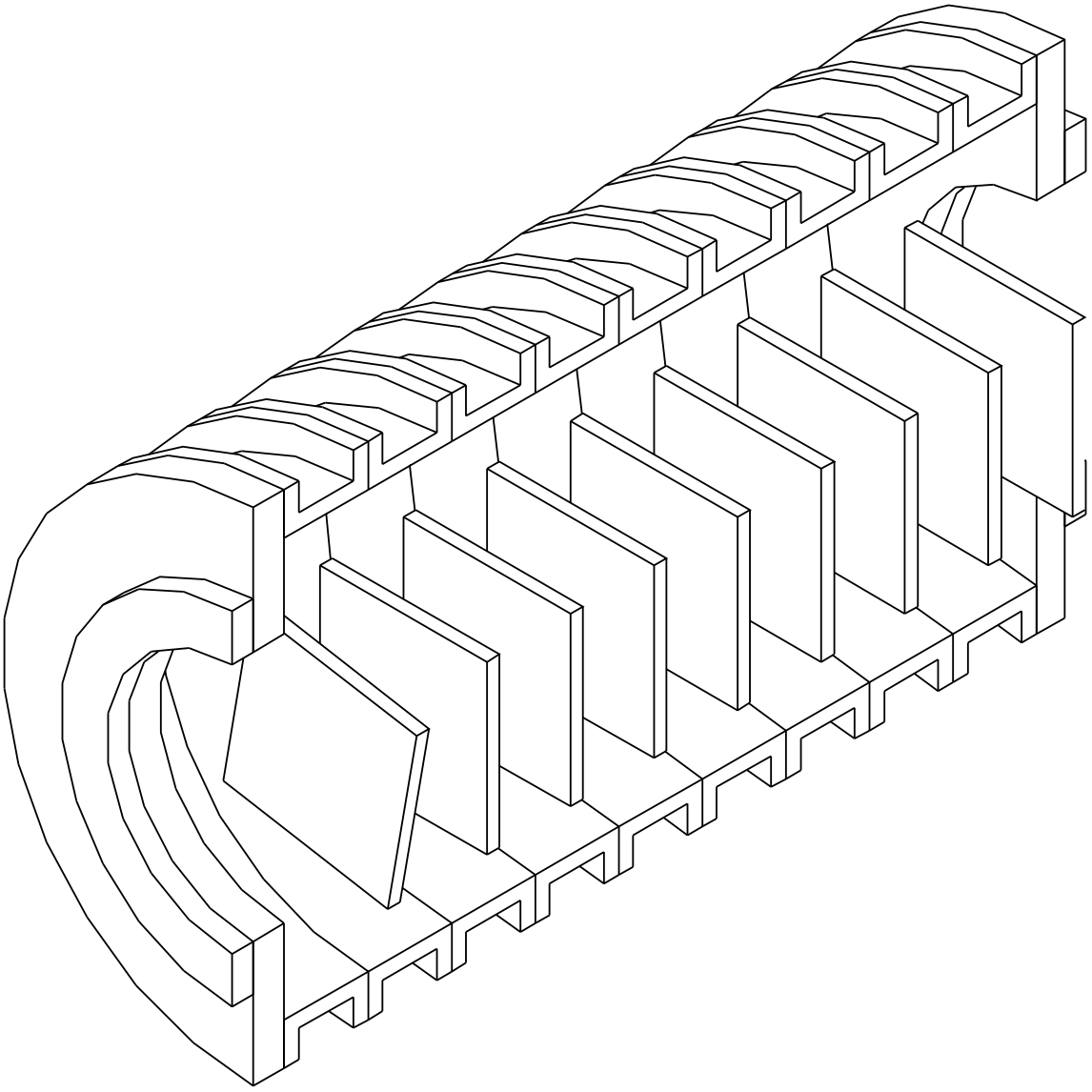

Figure C.2: *Microdrift chambers. The housing of MDC is cut.*

Drift times (T_{dr}) and spreads of arrival time (σ_t) as a function of drift distance are shown in fig. C.4. The drift time T_{dr} exhibits rather linear dependence, that is very convenient for track reconstruction procedures. The maximum drift time is 26 ns. The σ_t value never exceeds 0.5 ns, thus the spatial resolution is better then 30 μm.

C.4 Microdrift chamber performance

The double track resolution of the double plane chamber is illustrated in fig. C.5. The histograms correspond to two tracks separated by 100 μm in space. The left histogram corresponds to tracks detected by the first plane, and the right one to tracks detected by the second plane. The TDC bin width, of 0.5 ns, has been taken into account.

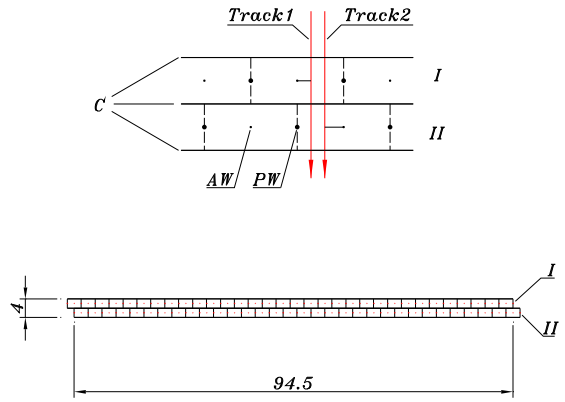

Figure C.3: *Schematic layout of a double-plane drift chamber: AW — anode wires,* $50\ \mu m$ *in diameter; PW — potential wires,* $100\ \mu m$ *in diameter; C — cathode, Mylar foil,* $20\ \mu m$ *thick. Sizes are measured in mm.*

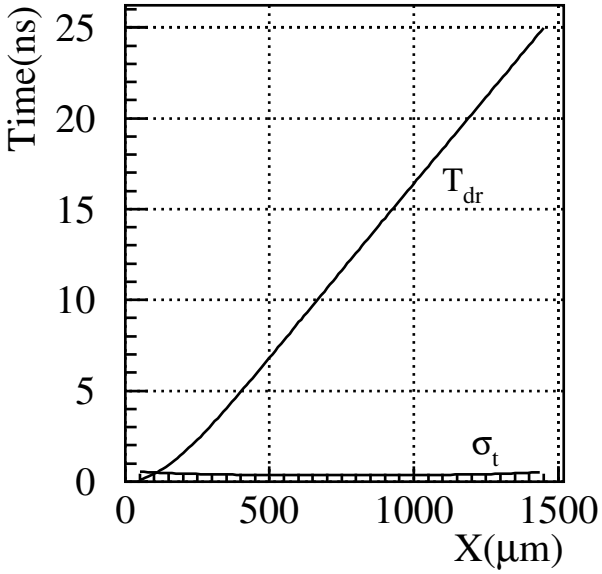

Figure C.4: *Time features of the drift chamber simulated with help of the GARFIELD package. Gas mixture is* $\mathrm{Ar}(0.33) + i\mathrm{C_4H_{10}}(0.66) + \mathrm{H_2O}(0.01)$.

C.5 Radioactive source and beam test of the microdrift chambers

Full scale prototype was extensively tested with Sr90-source. This test confirmed the main features predicted by the GARFIELD simulation.

For the beam test the prototype was placed in the left arm of the DIRAC spectrometer. Off-line MDC data processing gave efficiency estimation more than 99% and spatial resolution 22 ± 4 μm. In 2003 the

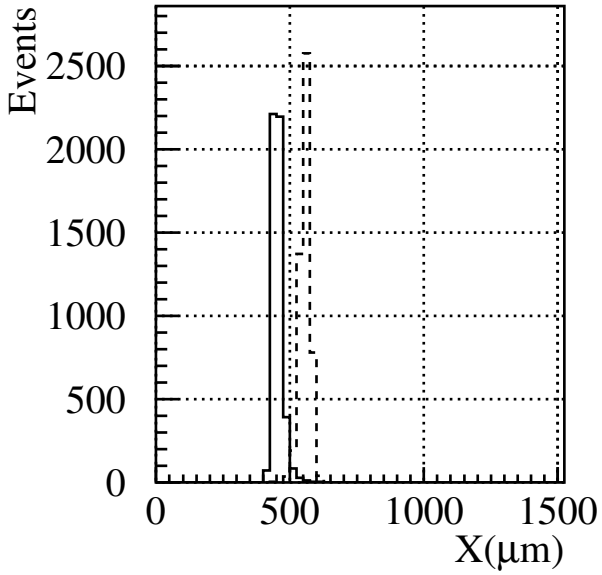

Figure C.5: *The double track resolution of the double-plane drift chamber. The solid histogram corresponds to track position* 450 μ*m and the dashed one to* 550 μ*m with respect to the anode wire.*

beam thest of the full detector placed in upstream region of the setup was carried out. More than 100 million events were collected. Data processing of this information is in progress.

To optimize MDC performance for the future experiment some additional beam test is needed in 2004.

C.6 Summary

The most important features of the detector are:

1. Spatial accuracy $\sigma < 30$ μm, (22 ± 4 μm from the beam test);
2. Double track resolution < 200 μm;
3. One plane efficiency at beam intensity $I = 2 \cdot 10^{11}$ protons per spill, due to the "dead zone" $> 98\%$ ($> 99\%$ from the beam test);
4. Low multiple scattering: total detector thickness $< 5 \cdot 10^{-3}$ X_0;
5. Time resolution $\sigma < 1$ ns;
6. Low track multiplicity < 4 tracks;
7. Small readout time < 3 μs.

Appendix D

Scintillation Fiber Detector

D.1 New readout electronics

The Peak-Sensing Discriminators presently employed for SFD have initially been designed for triggering in order to detect pairs of tracks which are space-wise and time-wise very close. The front-end electronics based on this discriminator, together with LeCroy 3377 TDC provided a real time digitization of multi-tracks separated by a minimum distance corresponding to the pitch of fiber arrays, typically 0.5 mm. In application of this circuit in DIRAC experiment, it has been revealed that SFD is also very powerful as a tracking device. The peak-sensing algorithm tends to reduce the counting efficiency for pairs of hits on adjacent channels, as the signals on each channel kill each other. This is not a problem when the detector is used only for triggering, but annoying if it is used for tracking.

In order to remove this inconvenience we have designed a new electronics providing the amplitude information of all the anode output channels together with the timing information. It consists of an individual discriminator, ADC and multihit-TDC for each channel.

Compared to the present electronics, we can expect a better performance in the following three aspects:

1. High detection efficiency thanks to the direct application of threshold without subtraction of amplitude in adjacent anodes. Assuming that the number of photoelectron per track is ~ 10, it is possible to realize a detection efficiency close to 98% with adequate adjustment of threshold in individual channels.

2. For the same reason as above mentioned we can expect also the same detection efficiency for correlated events in adjacent bins as for separate hits. This advantage will allow to obtain the Δx distribution of double-hit events without bias.

3. Using the ADC information on all the anode amplitudes, it would be possible to improve also the time resolution of SFD, using the ADC information for the correction of the walk in the leading-edge discriminator. Following the results obtained with a similar type of SFD for COMPASS Experiment we expect a time resolution of ~ 500 ps with the aid of such an off-line treatment of pulse amplitudes.

Prototype of the new electronics is presently under construction, and will be tested, in combination with new SFD, this summer on test beam at CERN.

This electronics can be used for the readout of many kinds of multi-channel detectors used in a high counting-rate environment.

D.2 High Resolution SFD

As a technical challenge to a very high space resolution comparable to those obtained with other technology, such as Si-detector, Micro-Strip-Gas-Chamber and so on, we have realized new SFD using finer fibers of 0.28 mm in diameter. After successful tests of the prototypes in 2002, two planes of the detector have been realized.

The mechanical features of the detector are as follows:

Number of planes:	2
Size of sensitive area:	50×50 mm^2
SciFi used:	KURARAY SCSF-78, 0.28 mm ø.
Number of SciFi layer/bundle:	7
Thickness of the bundles:	$\sim$3 mm (1% X_0)
Fiber pitch:	0.205 mm
Number of channels:	240(X) + 240(Y)
Number of PSPM(H6568):	15(X) + 15(Y)

The mechanical structure is also very compact as shown in Fig.D.1

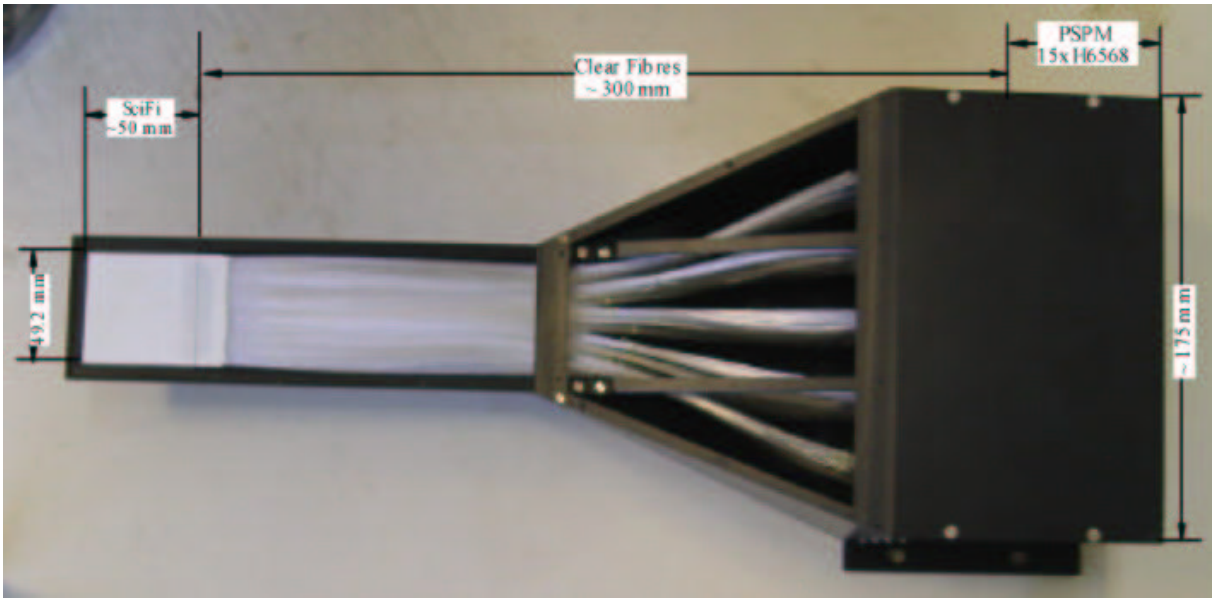

Figure D.1: *High resolution hodoscope with 0.205 mm pitch*

These hodoscopes have been tested in 2003 on T11 beam. Some typical results are:

Detection efficiency:	98%
Number of photoelectrons/hit:	10
Space resolution:	60 microns (σ)
Two-hit resolution:	0.2 mm
Time resolution:	0.6 ns

Fig.D.2a presents the correlation of hit positions separately obtained by the two planes precisely overlapped with fibers aligned in the same direction. Fig.D.2b is an event distribution as a function of the difference of the hit positions observed by these planes. The events are almost confined inside a single channel of 0.205 mm width. The space resolution is therefore estimated to be $\sigma \sim 2.04/\sqrt{12} \approx$ 60 microns.

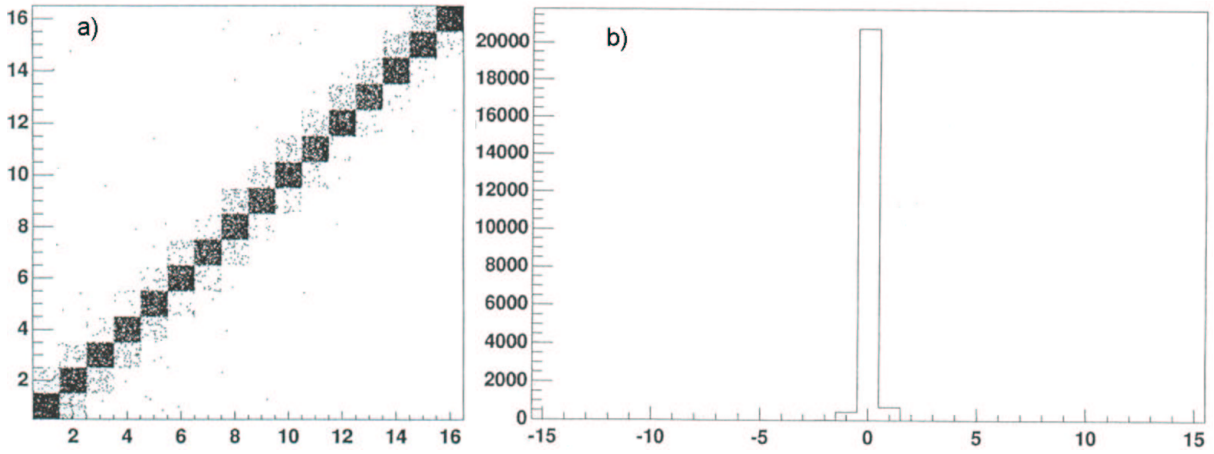

Figure D.2: *a) Correlation of hit position obtained in A and B hodoscopes (1 bin on X and Y is 0.205 mm); b) Difference of hit position obtained in A and B hodoscopes (1 bin on X is 0.205 mm)*

Such an excellent result in the space- and time-resolution allows us to foresee an upgrade of the present SFD (10×10 cm^2) to provide the more than 2 times better space resolution with about 2 times less fiber-array thickness.

A tentative study is also under way to construct the "topological trigger" device by using high-resolution hodoscopes in combination with the small magnet (see sect.9.3.3 and appendix B) placed near the production target. The magnet allows to separate confused double tracks in space at the level of SFD. Therefore, one can clearly recognize events with correlated tracks even at $\Delta X = 0$.

We consider also that such a high-performance SFD will be a unique detector capable to realize a precise topological trigger which needs simultaneously high space- and time-resolution to select events from the long-lived atom breakup.

Appendix E

Silicon detector

E.1 Introduction

Silicon detectors have been widely used for:

1. Precise energy measurement at low energies usually without fine segmentation;
2. dE/dx measurement with medium segmentation;
3. Precise tracking with fine segmentation.

The 6-inch technology now available allows the construction of a $10 \times 10\,\mathrm{cm}^2$ detector using a single silicon wafer. A good solution would be a $300\ \mu$m thick microstrip silicon detector [BACH99] with a pitch between $100\ \mu$m and $200\ \mu$m.

Considering a typical strip capacitance of 1 pF/cm, in a 10 cm detector with standard electronics (ENC $\sim$ 1800e) a signal to noise ratio of 15, an efficiency around 99% is achievable [CERN00].

The existing radiation hard technology allows the use of silicon detectors in extremely irradiated conditions ($>$ 1 Mrad/year in LHC), thus ensuring a long operation ($>$ 10 years) in the less stringent conditions of DIRAC experiment.

The silicon strip detector should have clear advantage such as absence of gaps, etc. compared with plastic scintillator hodoscopes, as far as the electronic noise could be suppressed low enough.

E.2 Silicon detector development

A silicon strip detector [KOBA02] is under developing for the DIRAC experiment with the following goal:

1. A sensitive area of 50–100 cm^2;
2. Segmentation to 0.5–2 mm width in readout;
3. Shaping amplifier output with the peaking time of 40–60 ns with its peak well within 70-80 ns after the particle penetrating the silicon detector;
4. The readout electronics should keep linearity for the high beam intensity up to 10 MHz over the whole silicon plane.

As a first step toward the goal, a silicon strip detector with a sensive area of 63.5$\times$63.5 mm^2 and readout pitch of 2 mm was developed. The preamplifier has a dynamic range large enough to keep the good linearity at 10 MHz per silicon plane. The shaping amplifier output has a FWHM of $\sim$70 ns with

the peaking time of 40–50 ns. The pulse height resolution required in DIRAC should be as good as 10–15%.

It was employed a commercially available single-sided silicon strip detector of p-side readout (Hamamatsu S6933) with a sensitive area of 63.5×63.5 mm^2 and a thickness of 300 μm.

Adjacent 80 strips (2 mm in total width) were ganged to one readout pad (one readout strip). Each readout channel corresponds to an active area of 63.5×2 mm^2 on the silicon, having a bulk capacitance of 43 pF at the full depletion. The silicon board was connected to preamplifier boards (with 16 channels per board) with 20 cm long flat cables. A hybrid preamplifier CS517 was developed.

E.3 Silicon detector main specifications

Silicon main specifications are as follows:

1. Strip pich=25 μm;
2. Strip width=12 μm;
3. Full depletion voltage $V_{fd} = 80$ V;
4. Breakdown voltage=100 V;
5. Total leakage current=2000 nA max. at V_{fd};
6. Bias resistance=12-15 MΩ per 25 μm strip;
7. Coupling capacitance=75 pF;
8. Breakdown of coupling capacitor=20 V.

E.4 Beam test

The beam test was carried out with a $\pi^-/\mu^-/e^-$ beam in the momentum range of 100–230 MeV/c at the π/μ channel of the KEK Proton Synchrotron. The beam separation was carried out by measuring the time of flight between two scintillation counters.

The pulse height resolution (1σ) as good as 9% could be easily obtained for m.i.p. if preamplifier is be placed at a distance of 20 cm from the silicon board.

Appendix F

Simulation of K^+ from $A_{\pi K}$ detected by the DIRAC setup

F.1 Introduction

F.1.1 Simulation purpose

The present DIRAC setup is dedicated to detect $\pi^+\pi^-$ pairs with small relative momenta. For the the continuation of $A_{2\pi}$ lifetime measurement and for observation and lifetime measurement of $A_{\pi K}$ we are planning to update the DIRAC experimental setup retaining symmetric geometry. In the symmetric geometry we will detect simultaneously πK "atomic" pairs of both signs with acceptable efficiency.

Contrary to $\pi\pi$ pairs the π and K mesons from $A_{\pi K}$ breakup have momenta that differ by a factor $\sim$ 3.5. Only $A_{\pi K}$ with momenta higher than $\sim$5.0 GeV/c breakup into detectable πK pairs, namely pairs entering the apparatus acceptance. The kaons have momentuma between 3.9 GeV/c and 8.9 GeV/c whereas the pions from $A_{\pi K}$ pairs have momentum range between 1.1 and 2.5 GeV/c.

In order to detect π^+K^- "atomic" pairs one needs to discriminate pions from kaons in the negative arm. The detection of π^-K^+ pairs is somehow more complex because in this case, in addition to π^+, a large admixture of protons is also expected.

The present setup has to be upgraded in order to detect πK pairs from $A_{\pi K}$. Two aerogel Cherenkov counters will be installed in the left arm of the downstream detectors for kaon and proton separation. New gas Cherenkov detectors will be installed in the both arms of the spectrometer for pion and kaon separation. These counters will be filled by sulfur hexafluoride (SF_6) or by perfluorobutane (C_4F_{10}). The existing gas Cherenkov counters filled by nitrogen (N_2) after a modification will be still in use for electron suppression.

In order to choose the transverse dimensions of the all Cherenkov counters, the number of aerogel Cherenkov counters and their indices of refraction the dedicated simulation of positive kaons from $A_{\pi K}$ breakup detected by the DIRAC setup was performed (see Chapter 2). The simulation was accomplished by the new method. In the previous method the atom yield was estimated on the base of single inclusive cross-sections of positive and negative particles. Now the atom yield is estimated using directly double inclusive cross-section (pairs from the same stars with small relative momenta in the pair c.m. system). Of course, the kaons and pions should be detected in coincidence. In figures below with more details than in Chapter 2 the different distributions of positive kaons are shown. The K^- distributions from $A_{\pi^+K^-}$ are analogous.

We use the coordinate system for the left (positive) arm:
Z — along the centers of the downstream detectors.
X — horizontal coordinate, positive direction is to outside of the proton beam.
Y — vertical coordinate, positive direction from down to up.

F.2 K^+ momentum distributions

F.2.1 K^+ momentum distribution

The momentum distribution of kaons is shown in Fig. F.1. The momentum range of kaons detected is $3.9 \div 8.9$ GeV/c. The most probably value is 4.7 GeV/c, mean value is 5.5 GeV/c. Integral is $5.21 \cdot 10^{-11}$. The integral is normalised on the one p-Ni interaction. Angular aperture of the secondary particle channel, pion and kaon decays up to the gas Cherenkov counters and the pion and kaon detection by the Drift Chambers are taken into account.

F.2.2 K^+ momentum — X-coordinate plot

The momentum distributions of kaons depending on X-coordinate at DC2, DC3, DC4 and Ch are shown in Fig. F.2. The main conclusion is: the kaons detected by the DC's and Ch at some X-coordinate are usualy mixed in the wide momentum range. The exception is at small values of X (nearest to the detector center). In the Table the boundaries of X-coordinates and ΔX intervals at DC2, DC3, DC4 and Ch for the detected kaons are shown.

Detector	X_{min}, cm	X_{max}, cm	Δ, cm
DC2	-17	-40	23
DC3	-25	-56	31
DC4	-32	-64	32
Ch	-42	-95	53

F.3 K^+ space distributions

F.3.1 K^+ X-distributions

The kaon distributions along X axes in the four positions (DC2, DC3, DC4, and the front of the existing gas Cherenkov counter) are shown in Fig. F.3. Boundary coordinates and dimensions of the kaon beam are shown in the Table.

Detector	X_{min}, cm	X_{max}, cm	Δ, cm
DC2	-17	-40	23
DC3	-25	-56	31
DC4	-32	-64	32
Ch	-42	-95	53

So if the two aerogel Cherenkov counters will be placed in front of DC3 and DC4 then their horizontal dimensions should be 30 cm. If the front side of the new gas Cherenkov counter is coincides with the front side of the existing gas Cherenkov counter then its entrance window horizontal dimension is 50 cm.

F.3.2 K^+ Y-distributions

The kaon distributions along Y axis in the four positions (DC2, DC3, DC4, front of the existing gas Cherenkov counter) are shown in Fig. F.4. Boundary coordinates and dimensions of the kaon beam are shown in the Table.

Detector	Y_{min}, cm	Y_{max}, cm	Δ, cm
DC2	-18	+18	36
DC3	-19	+19	38
DC4	-20	+20	40
Ch	-22	+22	44

So if the two aerogel Cherenkov counters will be placed in front of DC3 and DC4 then their vertical dimensions should be 40 cm. If the front side of the new gas Cherenkov counter is coincides with the front side of the existing gas Cherenkov counter then its entrance window vertical dimension is 44 cm.

F.3.3 K^+ X, Y two dimensional distributions

The two dimensional plots in the planes X, Y in the four positions (DC2, DC3, DC4, front of the existing gas Cherenkov counter) are shown in Fig. F.5. Boundary X and Y coordinates and dimensions of the kaon beam are shown in the Table.

Detector	X_{min}, cm	X_{max}, cm	ΔX, cm	Y_{min}, cm	Y_{max}, cm	ΔY, cm
DC2	-17	-40	23	-18	+18	36
DC3	-25	-56	31	-19	+19	38
DC4	-32	-64	32	-20	+20	40
Ch	-42	-95	53	-22	+22	44

F.4 Kaon momentum distributions in ΔX intervals

F.4.1 Kaon momentum distributions in the DC2 ΔX intervals

The kaon momentum distributions in the four ΔX intervals in the DC2 position are shown in Fig. F.6. The coordinates and momentum intervals of the kaon beam are shown in the Table.

Detector	X_{min}, cm	X_{max}, cm	ΔX, cm	p_{min}, GeV/c	p_{max}, GeV/c	$I \times 10^{-12}$
DC2	-40	-34	6	4.0	9.0	21.4
DC2	-34	-28	6	4.0	8.0	17.5
DC2	-28	-22	6	3.7	6.0	10.5
DC2	-22	-16	6	3.7	4.8	2.8

F.4.2 Kaon momentum distributions in the DC3 ΔX intervals

The kaon momentum distributions in the four ΔX intervals in the DC3 position are shown in Fig. F.7. The coordinate and momentum intervals of the kaon beam are shown in the Table.

Detector	X_{min}, cm	X_{max}, cm	ΔX, cm	p_{min}, GeV/c	p_{max}, GeV/c	$I \times 10^{-12}$
DC3	-56	-48	8	4.0	9.0	18.5
DC3	-48	-40	8	4.0	8.5	18.3
DC3	-40	-32	8	4.0	6.2	11.6
DC3	-32	-24	8	3.7	4.8	3.7

F.4.3 Kaon momentum distributions in the DC4 ΔX intervals

The kaon momentum distributions in the four ΔX intervals in the DC4 position are shown in Fig. F.8. Coordinate and momentum intervals of the kaon beam are shown in the Table.

Detector	X_{min}, cm	X_{max}, cm	ΔX, cm	p_{min}, GeV/c	p_{max}, GeV/c	$I \times 10^{-12}$
DC4	-64	-56	8	4.2	9.0	19.6
DC4	-56	-48	8	4.0	7.5	17.5
DC4	-48	-40	8	4.0	6.0	11.0
DC4	-40	-32	8	3.7	4.8	3.9

F.4.4 Kaon momentum distributions in the Ch ΔX intervals

The kaon momentum distributions in the four ΔX intervals in the Ch front position are shown in Fig. F.9. Coordinate and momentum intervals of the kaon beam are shown in the Table.

Detector	X_{min}, cm	X_{max}, cm	ΔX, cm	p_{min}, GeV/c	p_{max}, GeV/c	$I \times 10^{-12}$
Ch	-100	-85	15	5.3	9.0	2.9
Ch	-85	-70	15	4.2	9.0	24.3
Ch	-70	-55	15	4.0	7.0	19.5
Ch	-55	-40	15	3.8	5.0	5.3

F.5 Kaon momentum — X correlations

F.5.1 Kaon momentum — X correlations, DC2 position

Kaon momentum — X correlations in the DC2 position are shown in Fig. F.10 and in the Table.

Detector	p_{min}, GeV/c	p_{max}, GeV/c	X_{min}, cm	X_{max}, cm	ΔX, cm	$I \times 10^{-12}$
DC2	4.0	4.5	-15.5	-40.0	24.5	12.3
DC2	4.5	5.0	-20.5	-40.0	19.5	13.2
DC2	5.0	5.5	-24.0	-40.0	16.0	9.3
DC2	5.5	6.0	-26.5	-40.0	13.5	6.3
DC2	6.0	6.5	-28.5	-40.0	11.5	4.2
DC2	6.5	7.0	-30.5	-40.0	9.5	6.8

F.5.2 Kaon momentum — X correlations, DC3 position

Kaon momentum — X correlations in the DC3 position are shown in Fig. F.11 and in the Table.

Detector	p_{min}, GeV/c	p_{max}, GeV/c	X_{min}, cm	X_{max}, cm	ΔX, cm	$I \times 10^{-12}$
DC3	4.0	4.5	-23.0	-56.0	33.0	10.1
DC3	4.5	5.0	-29.0	-56.0	27.0	13.3
DC3	5.0	5.5	-33.0	-56.0	23.0	9.7
DC3	5.5	6.0	-36.0	-56.0	20.0	6.7
DC3	6.0	6.5	-39.0	-56.0	17.0	4.5
DC3	6.5	7.0	-41.0	-56.0	15.0	7.9

F.5.3 Kaon momentum — X correlations, DC4 position

Kaon momentum — X correlations in the DC4 position are shown in Fig. F.12 and in the Table.

Detector	p_{min}, GeV/c	p_{max}, GeV/c	X$_{min}$, cm	X$_{max}$, cm	ΔX, cm	$I \times 10^{-12}$
DC4	4.0	4.5	-30.0	-64.0	34.0	11.5
DC4	4.5	5.0	-37.0	-64.0	27.0	14.1
DC4	5.0	5.5	-42.0	-64.5	22.0	9.8
DC4	5.5	6.0	-46.0	-64.0	18.0	6.5
DC4	6.0	6.5	-49.0	-64.5	15.0	4.2
DC4	6.5	7.0	-52.0	-64.0	12.0	6.0

F.5.4 Kaon momentum — X correlations, Ch position

Kaon momentum — X correlations in the Ch front position are shown in Fig. F.13 and in the Table.

Detector	p_{min}, GeV/c	p_{max}, GeV/c	X$_{min}$, cm	X$_{max}$, cm	ΔX, cm	$I \times 10^{-12}$
Ch	4.0	4.5	-40.0	-80.0	40.0	9.6
Ch	4.5	5.0	-49.0	-83.0	34.0	12.4
Ch	5.0	5.5	-55.0	-86.0	31.0	9.3
Ch	5.5	6.0	-60.0	-88.0	28.0	6.7
Ch	6.0	6.5	-64.0	-89.0	25.0	4.7
Ch	6.5	7.0	-67.0	-96.0	29.0	9.4

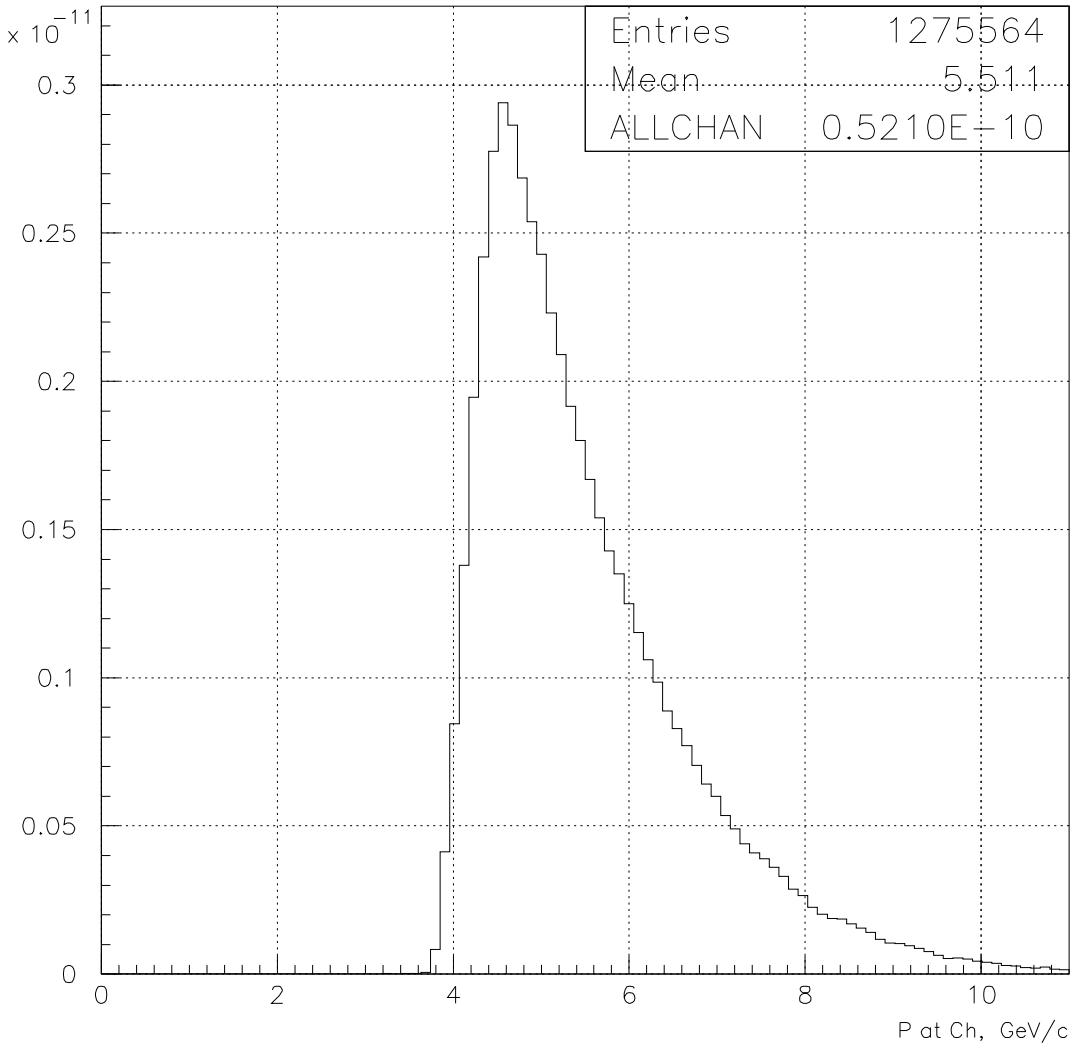

Figure F.1: *Momentum distribution of K^+ mesons from $A_{\pi K}$ breakup detected by the setup.*

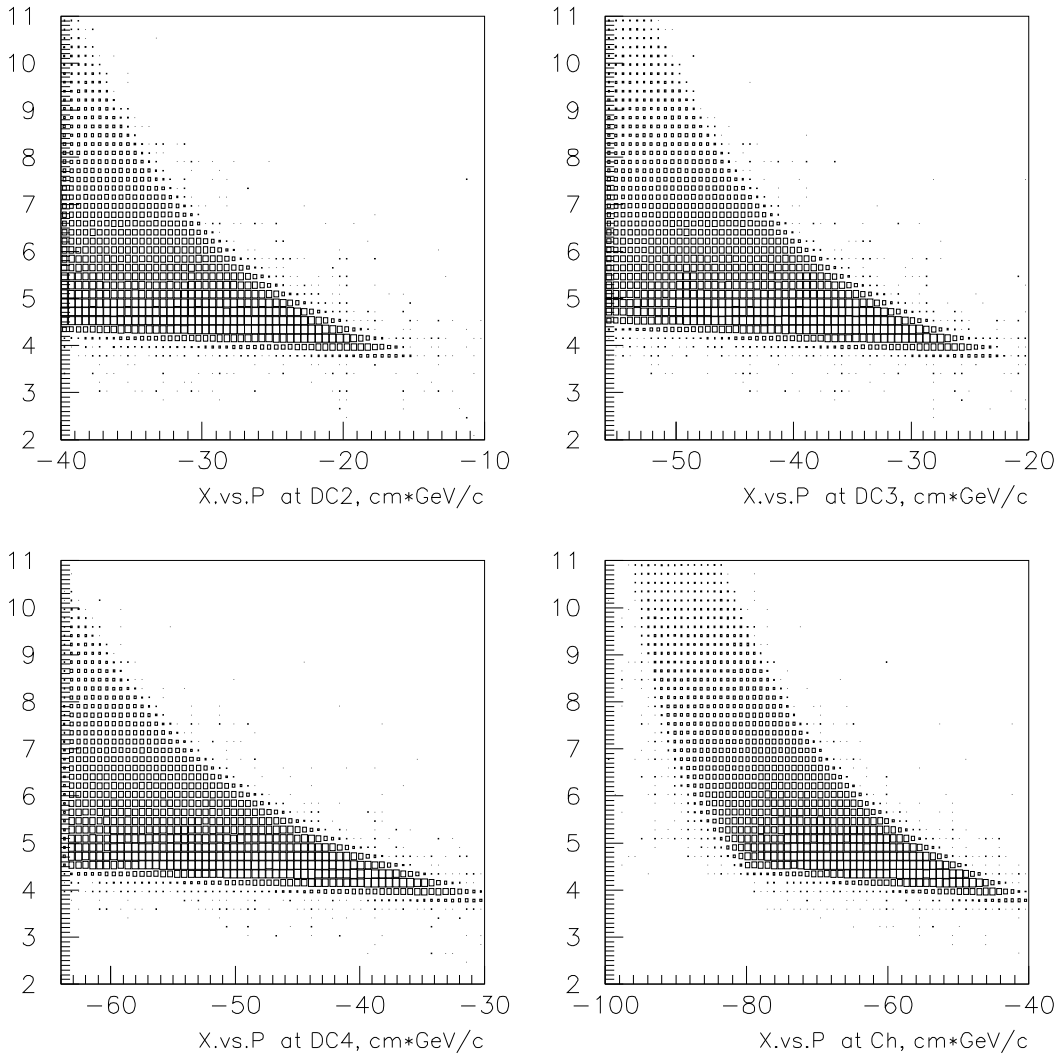

Figure F.2: *Momentum — X-coordinate plots at DC2, DC3, DC4 and Ch of K^+ mesons from $A_{\pi K}$ breakup detected by the setup.*

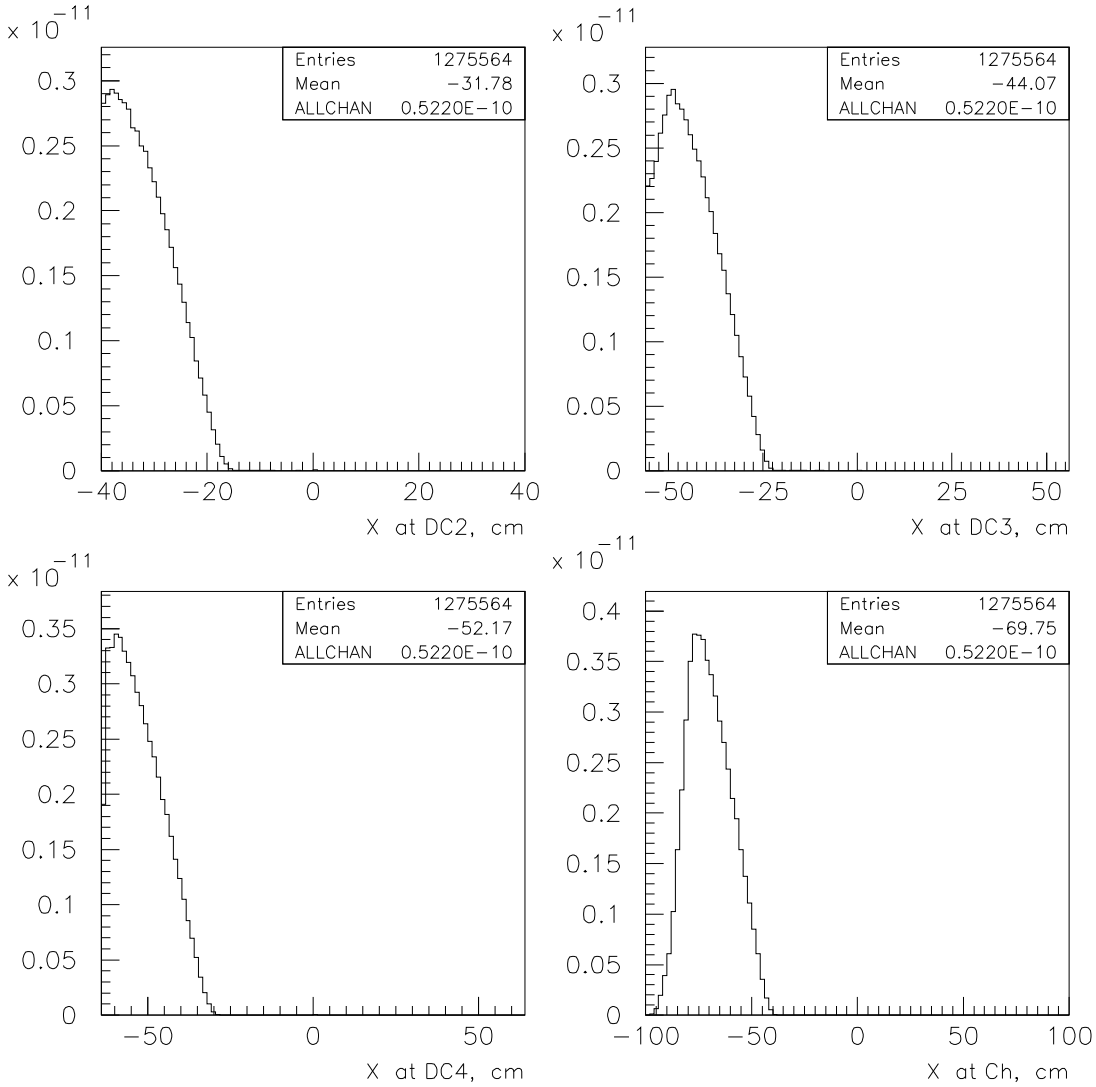

Figure F.3: *Kaon distributions along X axis in the four positions (DC2, DC3, DC4, front of the existing gas Cherenkov counter).*

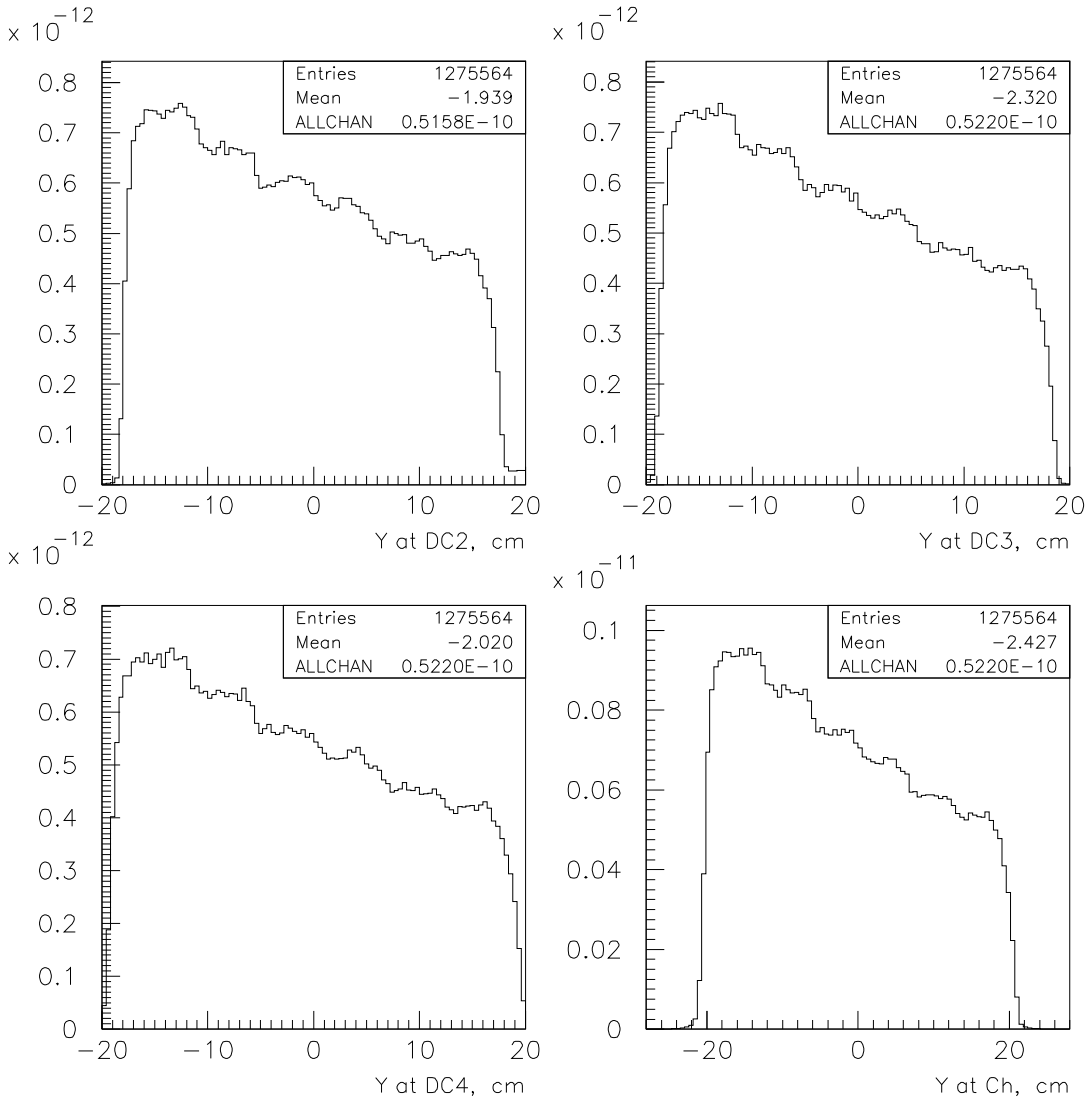

Figure F.4: *Kaon distributions along Y axis in the four positions (DC2, DC3, DC4, front of the existing gas Cherenkov counter).*

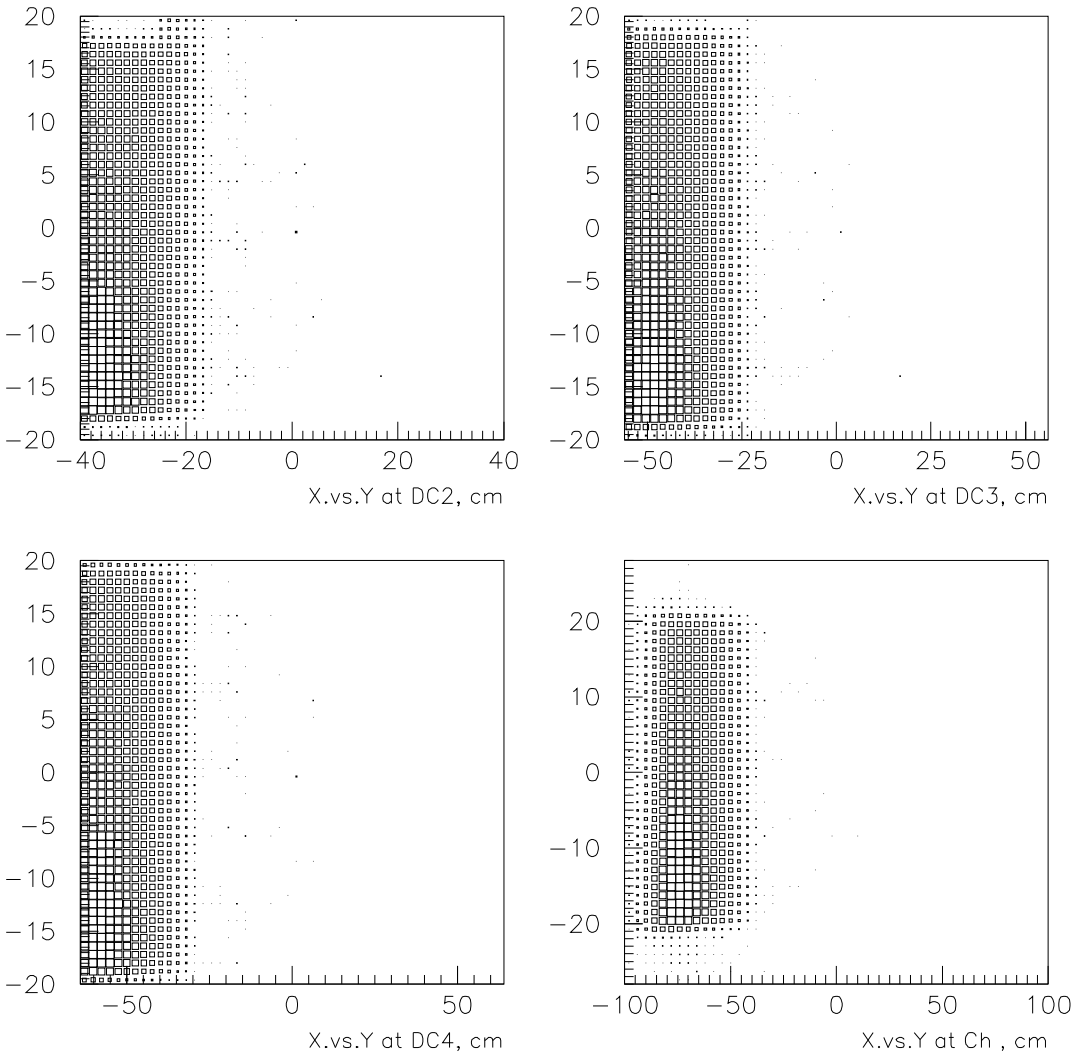

Figure F.5: *Kaon X,Y two dimensional distributions in the four positions (DC2, DC3, DC4, front of the existing gas Cherenkov counter).*

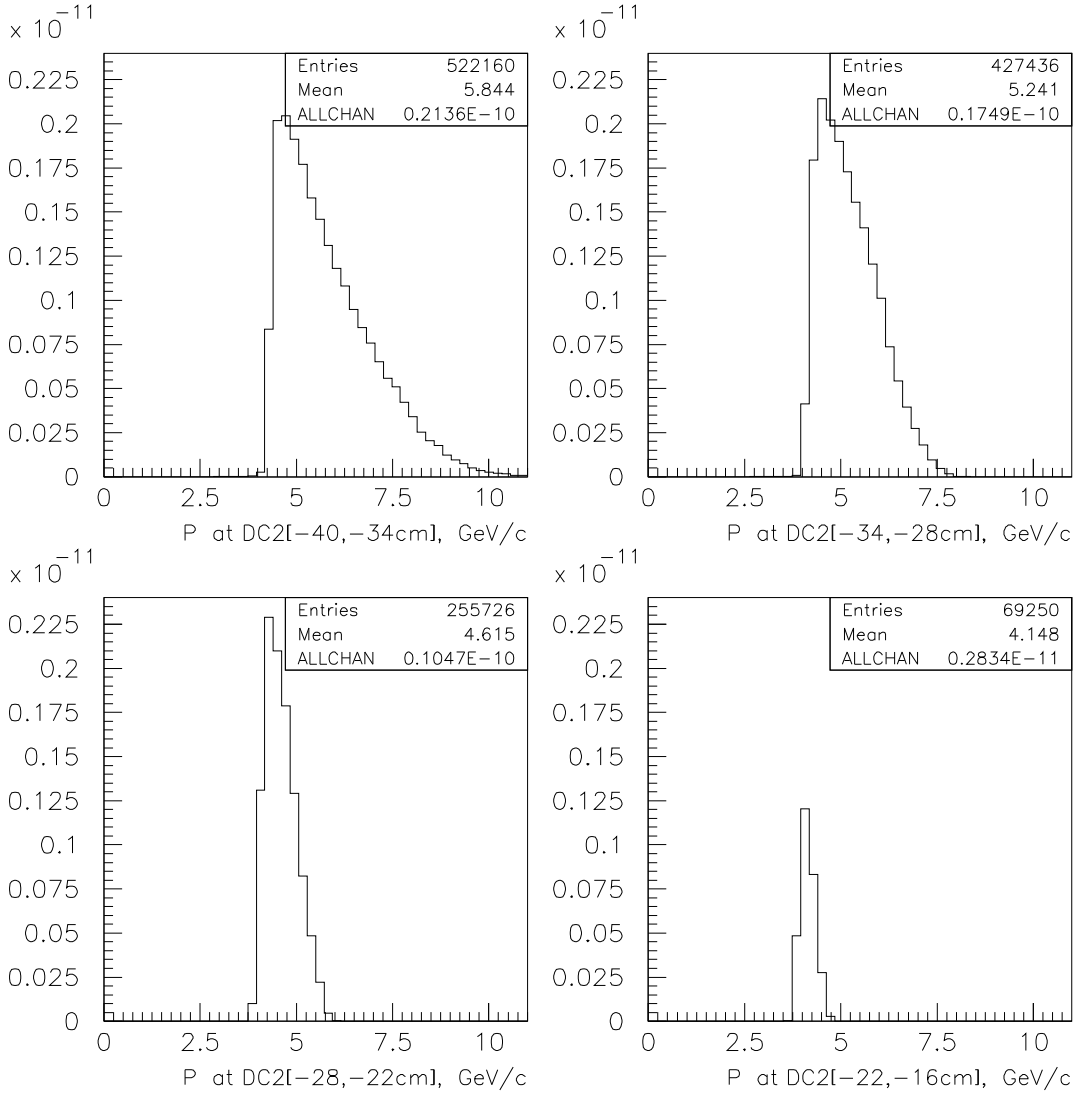

Figure F.6: *Kaon momentum distributions in the four ΔX intervals in the DC2 position.*

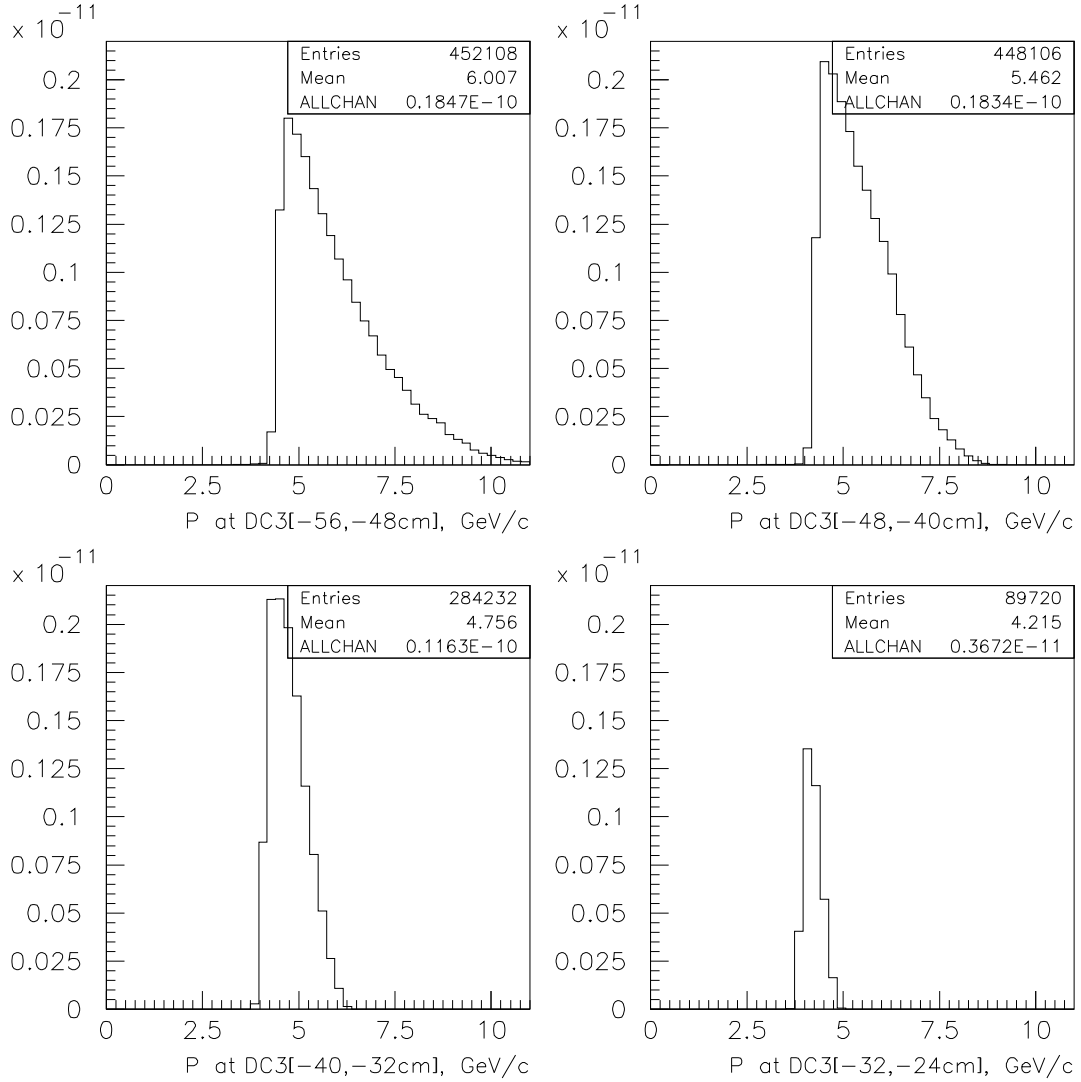

Figure F.7: *Kaon momentum distributions in the four ΔX intervals in the DC3 position.*

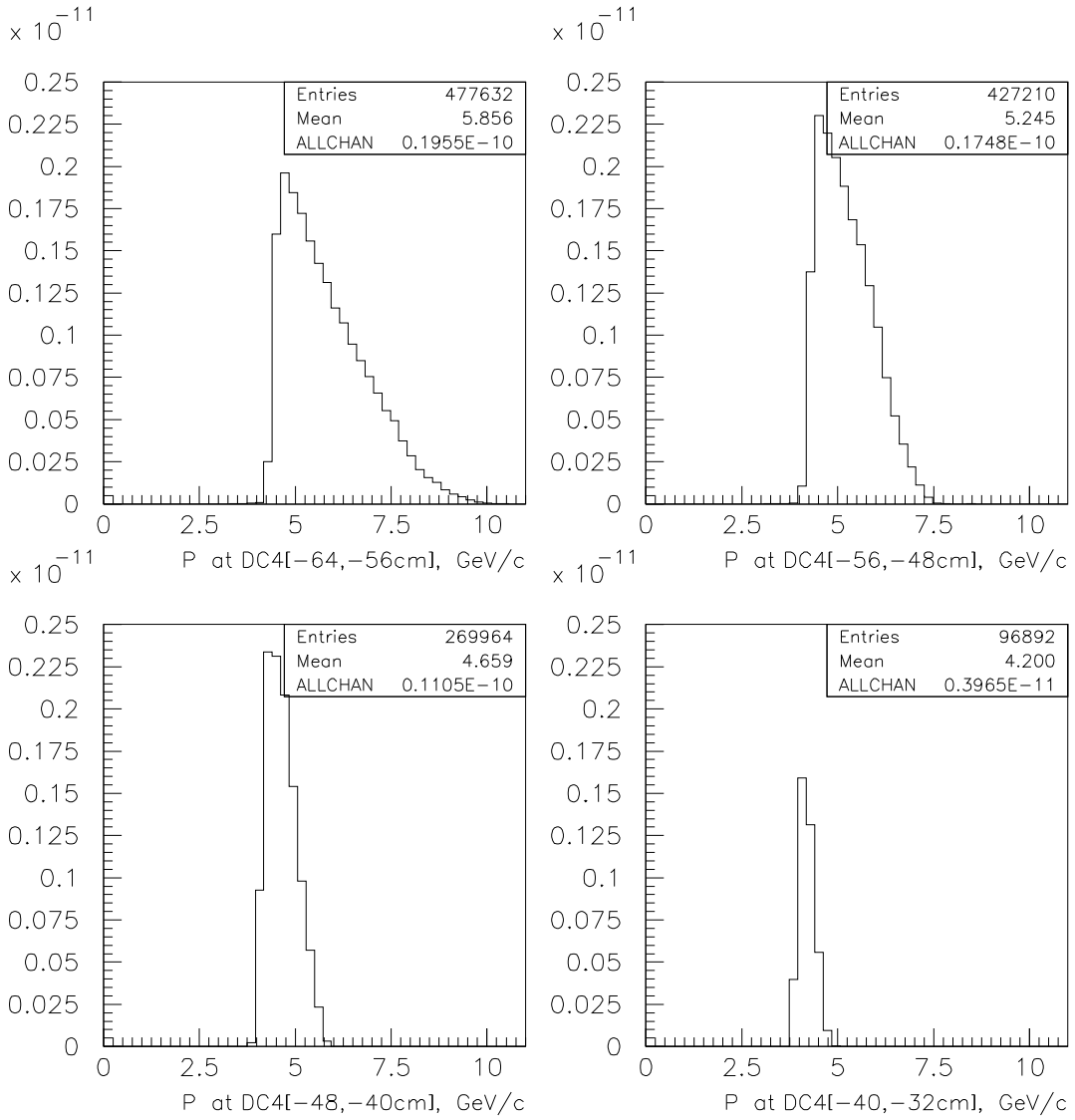

Figure F.8: *Kaon momentum distributions in the four ΔX intervals in the DC4 position.*

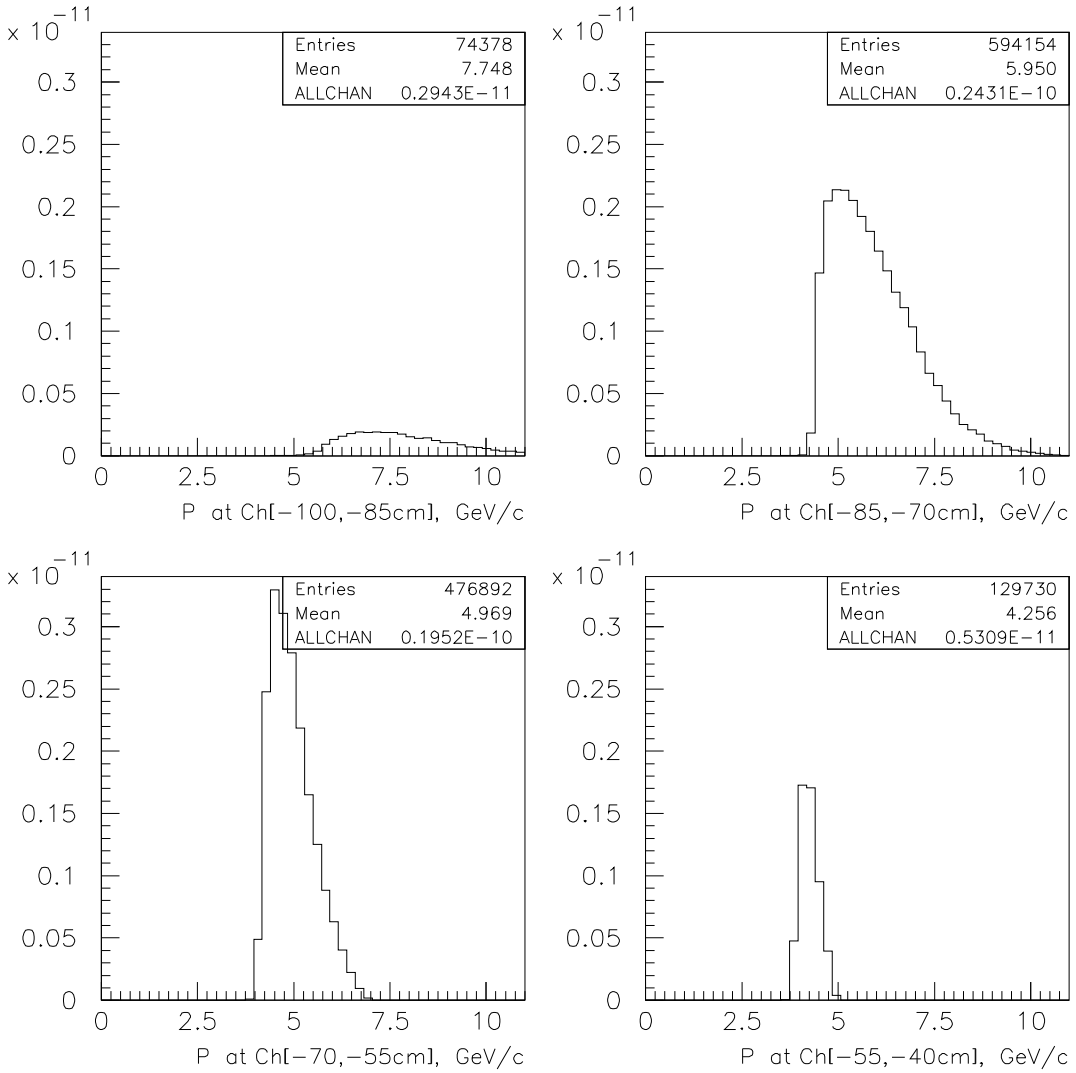

Figure F.9: *Kaon momentum distributions in the four ΔX intervals in the Ch front position.*

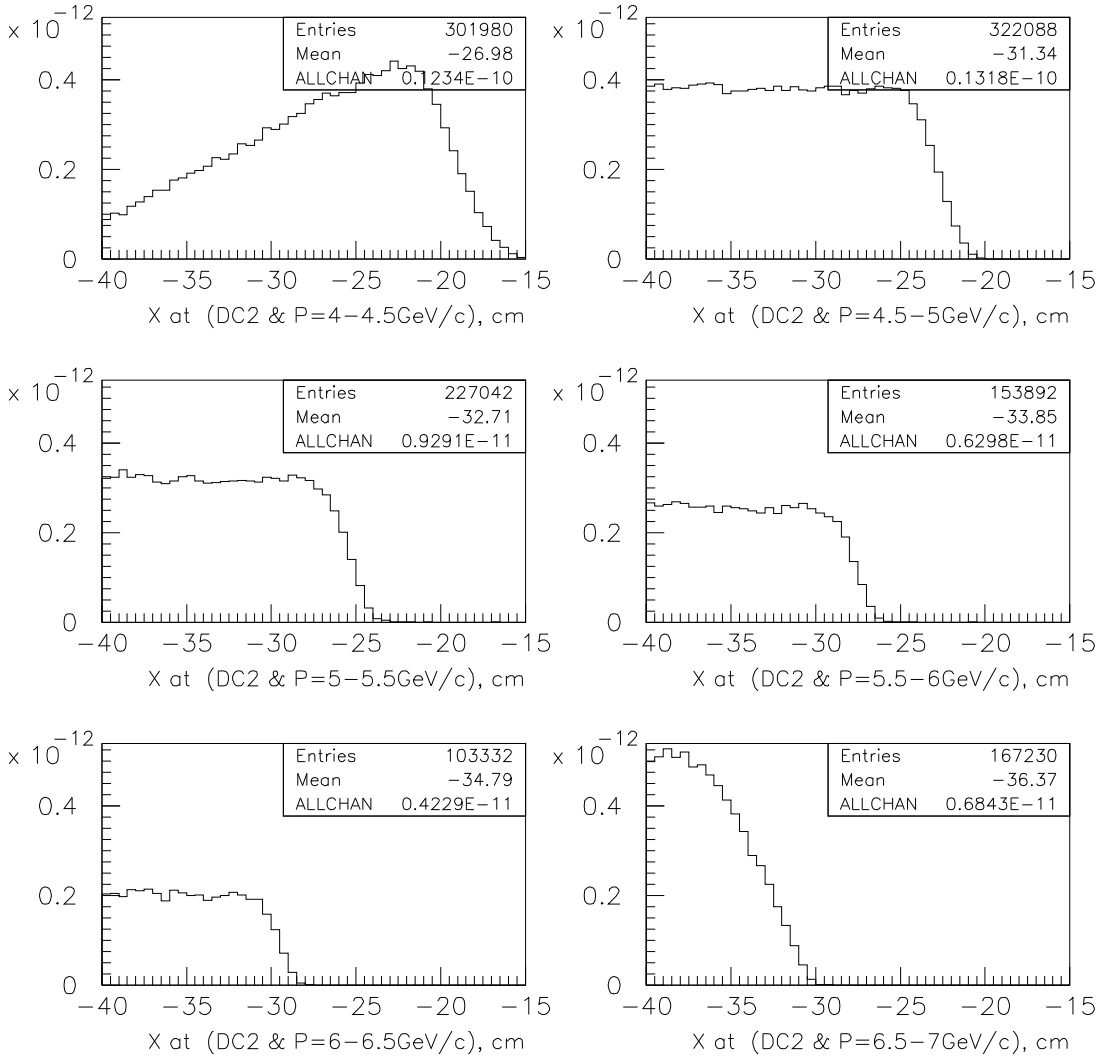

Figure F.10: *Kaon momentum — X correlations in the DC2 position.*

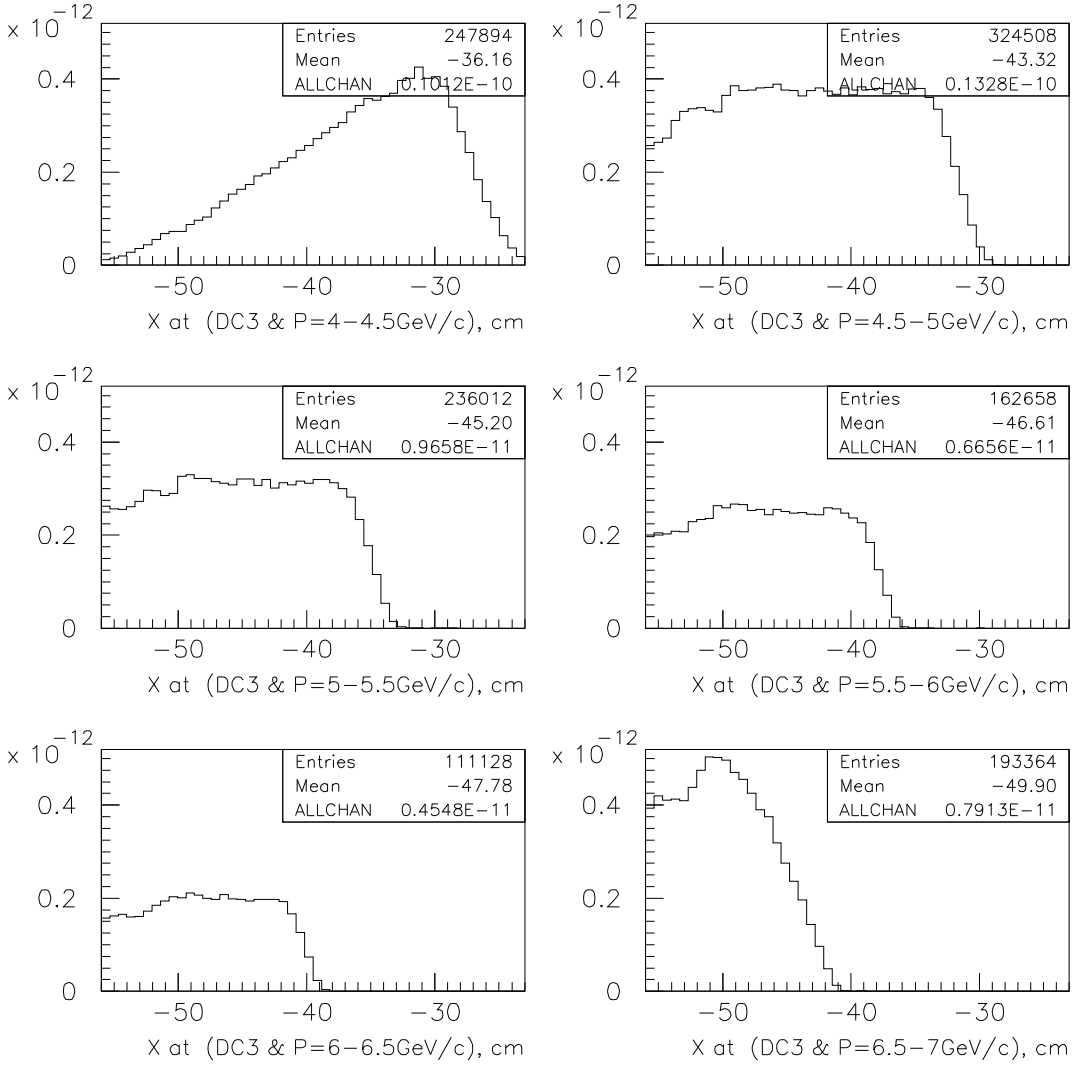

Figure F.11: *Kaon momentum — X correlations in the DC3 position.*

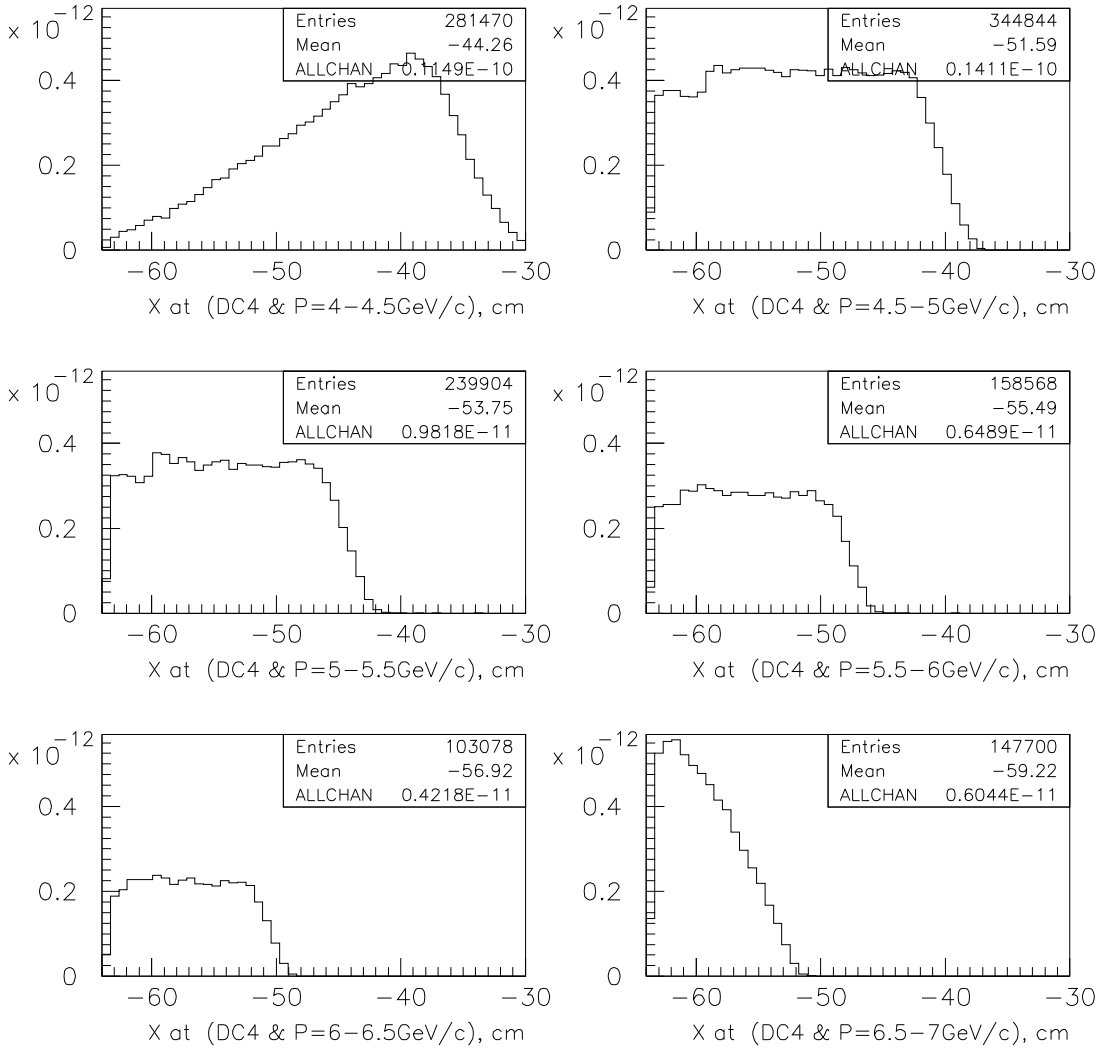

Figure F.12: *Kaon momentum — X correlations in the DC4 position.*

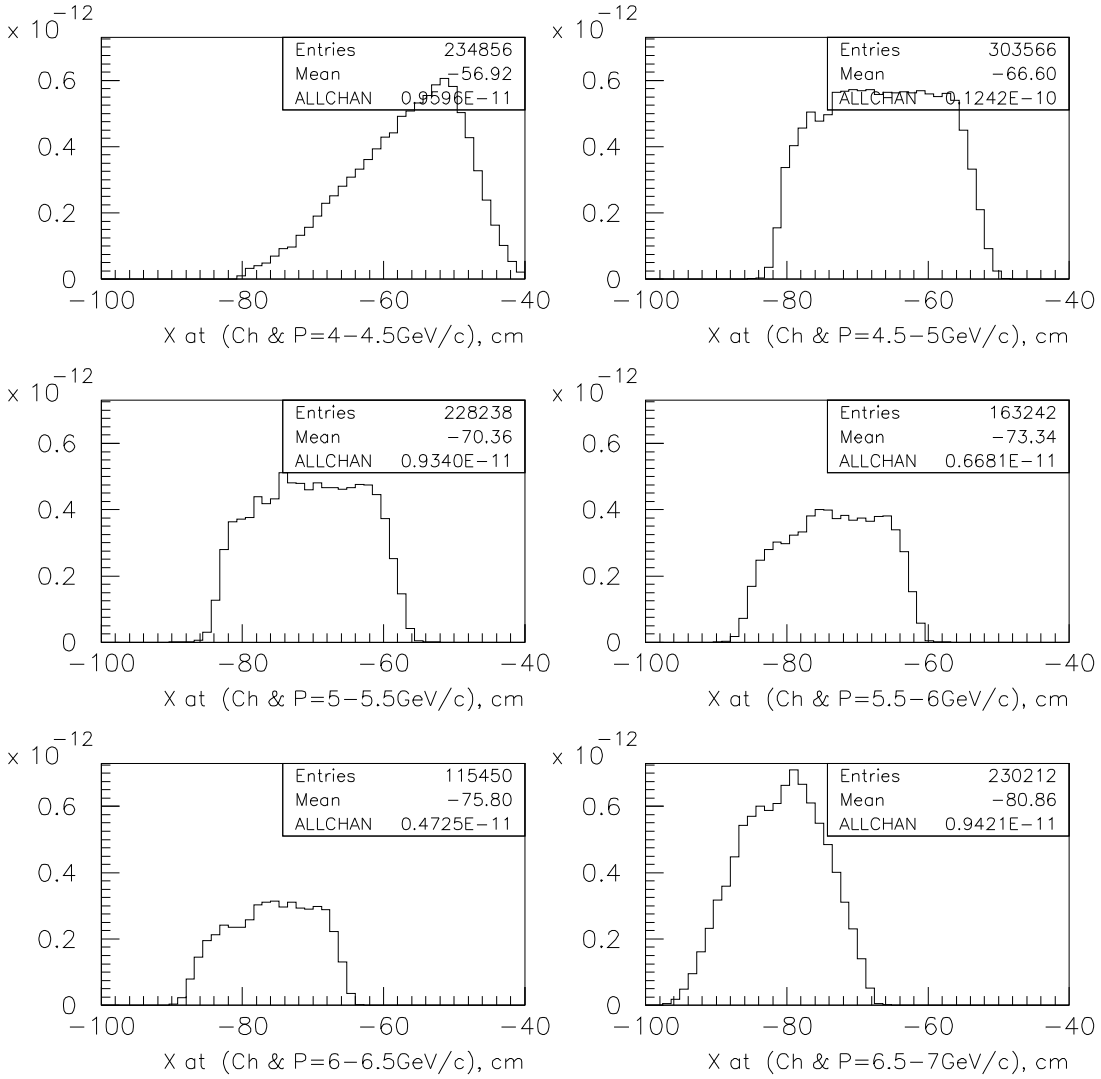

Figure F.13: *Kaon momentum — X correlations in the Ch front position.*

Appendix G

Cherenkov radiation: formulae, tables

G.1 Atom and particle momentum range in the DIRAC setup

G.1.1 $\pi^+\pi^-$ atoms

$\pi^+\pi^-$ atom dynamic range: $2.6 \div 8.6$ GeV/c.
π^+ (π^-) dynamic range: $1.3 \div 4.3$ GeV/c.

G.1.2 π^+K^- and π^-K^+ atoms

π^+K^- (π^-K^+) atom dynamic range: $5.0 \div 11.4$ GeV/c.
π^+ (π^-) dynamic range: $1.1 \div 2.5$ GeV/c.
K^+ (K^-) dynamic range: $3.9 \div 8.9$ GeV/c.

G.2 Units, masses, momenta of particles and atoms

G.2.1 Units, particle masses

m in GeV, E in GeV, p in GeV/c.
$m_e = 0.000511$.
$m_\pi = 0.13957018$.
$m_K = 0.493677$.
$m_p = 0.938271998$.

G.2.2 $\pi\pi$ atoms

$p_\pi = p_A/2$.
$p_A = 2p_\pi$.

G.2.3 πK atoms

$p_\pi = p_A m_\pi/(m_\pi + m_K) = p_A \cdot 0.22040395$.
$p_K = p_A m_K/(m_\pi + m_K) = p_A \cdot 0.779596049$.
$p_A = p_\pi(m_\pi + m_K)/m_\pi = p_\pi \cdot 4.537123$.
$p_A = p_K(m_\pi + m_K)/m_K = p_K \cdot 1.282716$.

G.2.4 Kp atoms

$p_K = p_A m_K/(m_K + m_p) = p_A \cdot 0.344758787.$
$p_p = p_A m_p/(m_K + m_p) = p_A \cdot 0.6552411212.$
$p_A = p_K(m_K + m_p)/m_K = p_K \cdot 2.900579.$
$p_A = p_p(m_K + m_p)/m_p = p_p \cdot 1.526156.$

G.3 Cherenkov radiation

G.3.1 Emission angle, maximum angle

$\cos\theta = 1/(\beta n).$
$\theta_{max} = \arccos(1/n).$

G.3.2 Threshold β, γ, p, E, n values

$\beta_{thr} = 1/n.$
$\gamma_{thr} = n/(n^2-1)^{1/2}.$
$p_{thr} = m/(n^2-1)^{1/2}.$
$E_{thr} = mn/(n^2-1)^{1/2}.$
$n_{thr} = E/p.$

G.3.3 Number of photons per cm

$N_\gamma = k(1 - 1/n^2\beta^2).$
$N_\gamma = k \cdot \sin^2\theta.$
$N_\gamma^{max} = k(1 - 1/n^2).$
$k = 370 \div 490.$

G.3.4 Number of photoelectrons

Gas counters:
$n_{pe} = N_0 L(1 - 1/n^2\beta^2)$
N_0 in cm^{-1} — figure of merit.
$N_0 = 60 - 90 - 130$ cm^{-1}.
Aerogel counters.
$N_0 = 35$ cm^{-1} for thickness 5 mm.
$N_0 = 25$ cm^{-1} for thickness 10 mm.
$N_0 = 20$ cm^{-1} for thickness 15 mm.

G.4 Tables

G.4.1 Table: atom momenta (p_A) and p_π, p_K, p_p momenta in atoms

p_A	$p_\pi^{A2\pi}$	$p_\pi^{A\pi K}$	$p_K^{A\pi K}$	p_K^{AKp}	p_p^{AKp}
2.5	1.25	0.551	1.949	0.862	1.638
3.0	1.50	0.661	2.339	1.034	1.966
3.5	1.75	0.771	2.729	1.207	2.293
4.0	2.00	0.882	3.118	1.379	2.621
4.5	2.25	0.992	3.508	1.551	2.949
5.0	2.50	1.102	3.898	1.724	3.276
5.5	2.75	1.212	4.288	1.896	3.604
6.0	3.00	1.322	4.678	2.069	3.931
6.5	3.25	1.433	5.067	2.241	4.259
7.0	3.50	1.543	5.457	2.413	4.587
7.5	3.75	1.653	5.847	2.586	4.914
8.0	4.00	1.763	6.237	2.759	5.242
8.5	4.25	1.873	6.627	2.930	5.570
9.0	4.50	1.984	7.016	3.103	5.897
9.5	4.75	2.094	7.406	3.275	6.225
10.0	5.00	2.204	7.796	3.448	6.552
10.5	5.25	2.314	8.186	3.620	6.880
11.0	5.50	2.424	8.576	3.792	7.208
11.5	5.75	2.535	8.965	3.965	7.535

G.4.2 Table: particle momenta (p) and β_π, β_K, β_p

p	β_π	β_K	β_p
1.0	0.99040011	0.89668358	0.72925623
1.5	0.99569905	0.94987769	0.84780214
2.0	0.99757388	0.97086040	0.90532459
2.5	0.99844525	0.98105494	0.93623409
3.0	0.99891954	0.98672910	0.95441003
3.5	0.99920585	0.99019838	0.96589478
4.0	0.99939181	0.99246976	0.97357455
4.5	0.99951936	0.99403608	0.97894687
5.0	0.99961063	0.99516101	0.98284469
5.5	0.99967817	0.99599580	0.98575879
6.0	0.99972956	0.99663213	0.98799264
6.5	0.99976955	0.99712819	0.98974164
7.0	0.99980128	0.99752233	0.99113605
7.5	0.99982689	0.99784064	0.99226530
8.0	0.99984785	0.99810138	0.99319238
8.5	0.99986522	0.99831763	0.99396270
9.0	0.99987977	0.99849896	0.99460961

G.4.3 Table: particle momenta (p) and n_{thr} for π, K, p

p	n^{π}_{thr}	n^{K}_{thr}	n^{p}_{thr}
1.0	1.009693	1.115221	1.371260
1.5	1.004320	1.052767	1.179520
2.0	1.002432	1.030014	1.104576
2.5	1.001557	1.019311	1.068109
3.0	1.001082	1.013449	1.047768
3.5	1.000795	1.009899	1.035309
4.0	1.000609	1.007587	1.027143
4.5	1.000481	1.006000	1.021506
5.0	1.000390	1.004863	1.017455
5.5	1.000322	1.004020	1.030612
6.0	1.000271	1.003379	1.012154
6.5	1.000231	1.002880	1.010365
7.0	1.000199	1.002484	1.008943
7.5	1.000173	1.002164	1.007795
8.0	1.000152	1.001902	1.006854
8.5	1.000135	1.001685	1.006074
9.0	1.000120	1.001503	1.005420

G.4.4 Table: refractive index (n) and β_{thr}, θ°_{max}, $1 - 1/n^2$

n	β_{thr}	θ°_{max}	$1 - 1/n^2$
Gases			
1.0003	0.99970090	1.4033	0.00060
1.0004	0.99960016	1.6203	0.00080
1.0005	0.99950025	1.8115	0.00100
1.0006	0.99940036	1.9843	0.00120
1.0007	0.99930049	2.1432	0.00140
1.0008	0.99920064	2.2911	0.00160
1.0009	0.99910081	2.4300	0.00180
1.0010	0.99900100	2.5613	0.00200
1.0011	0.99890121	2.6862	0.00220
1.0012	0.99880144	2.8055	0.00240
1.0013	0.99870169	2.9199	0.00259
1.0014	0.99860196	3.0300	0.00279
1.0015	0.99850225	3.1363	0.00299
Aerogel			
1.0080	0.99206349	7.2234	0.01581
1.0090	0.99108028	7.6584	0.01776
1.0100	0.99009901	8.0693	0.01970
1.0150	0.98522167	9.8625	0.02934
1.0200	0.98039216	11.3648	0.03883
1.0250	0.97560976	12.6804	0.04819
1.0300	0.97087379	13.8624	0.05740

Appendix H

Aerogel Cherenkov counters

H.1 Aerogel Cherenkov counters purpose

The detection of $\pi^- K^+$ pairs is more complex task in comparison with $\pi^+ K^-$ because in this case in addition to π^+ a large admixture of protons to positive kaons is also expected.

To discriminate kaons from protons in the kinematic range of accepted $A_{\pi K}$ we plan to install two aerogel threshold Cherenkov counters in the positive (left) arm of the spectrometer.

H.2 Aerogel counter design and installation

The transverse dimensions of the aerogel counters 300×400 mm^2 (W$\times$H) will be sufficient to intersect all trajectories of K^+ from $A_{\pi K}$ breakup. The thickness of the aerogel radiator is 90 mm. The more thick radiators have no advantages because the optical transmittance length is rather small (25$\div$50 mm). The longitudinal dimension of the boxes containing aerogel tiles is 200$\div$250 mm. This space will be needed for light collection (mirror or diffuse). The each module is viewed by four 5-inches photomultipliers (Hamamatsu R1587) attached to the top and bottom sides.

More difficult task is to choose the refractive indices of the aerogel tiles. The best refractive index for our conditions would be n=1.01 because in the full momentum interval kaons are detected and practically all protons are under the threshold (see Tables below). But number of photoelectrons is small. If we would use two aerogel counters with n=0.01 in "or" logic this variant may be acceptable.

The second variant is to use two aerogel counters with n=1.014 with "or" logic and with an analysis of the amplitude information. Of course it is possible to use two counters with different n for low and high momenta. It is important to find out a method of increasing of light collection efficiency.

The two Aerogel Cherenkov counters are shown in Fig. H.1. The aerogel detectors will be placed in front of the third (DC3) and the fourth (DC4) drift chamber modules. Their position between the drift chambers is shown in Fig. H.2.

H.3 Beam test of the DIRAC aerogel counter prototype

The small size aerogel counter was manufactured and tested at the beam in order to estimate the number of photoelectrons. Aeogel tiles of high qualite were manufactured in Boreskov Institute of Cathalysis (Novosibirsk). The aerogel radiator of 50 mm thick is composed from two tiles with dimensions of $160\times160\times25$ mm^3. Aerogel refractive index is n=1.008.

Aerogel is wrapped with 3 layers of high reflective material TETRATEX (250 μm thick film). Cherenkov light is detected by two photomultipliers 5 in. Hamamatsu R1587 with UV glass window. There were studied diffuse and mirror light collection.

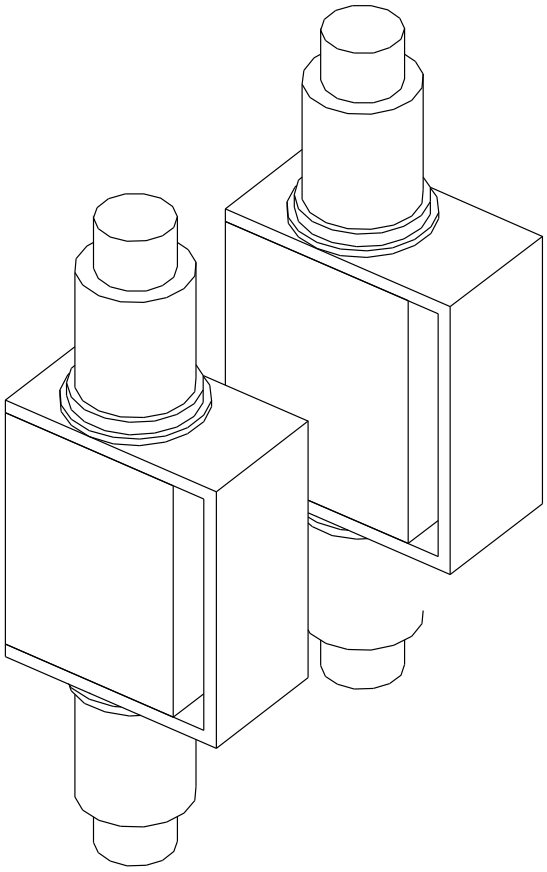

Figure H.1: *Aerogel Cherenkov counters.*

In 2002 the counter was investigated at the CERN PS T11 test beam with the momentum of 3.6 GeV/c (88% of pions and 12% of electrons). The number of photoelectrons detected with diffuse light collection was $\sim$5, with mirror collection was $\sim$10.

In the Table below (n=1.008) the number of photoelectrons is calculated using counter [LAGA01] with a diffuse light collection. The number of photoelectrons in the Table is $\sim$2 times less than obtained with the tested small aerogel counter. The explanation of this descripancy is:
1. The counter [LAGA01] was large and aerogel in it had the short transmission length, about 25 mm.
2. The tested counter was small and in this aerogel the trasmission length was big, about 50 mm.

H.4 Aerogel

Next we mention some aerogel properties and methods of light collection in aerogel counters. Then we estimate the light collection efficiency in aerogel counters using prototype. After that we add the tables with the estimated (using prototype) the number of photoelectrons depending on particle momentum and aerogel refraction index for aerogel of 90 mm thick.

The main drawback of aerogel is a poor optical transmittance, and consequently the number of photoelectrons detected is usually small. So it is necessary to be carefull when choosing a production facility.

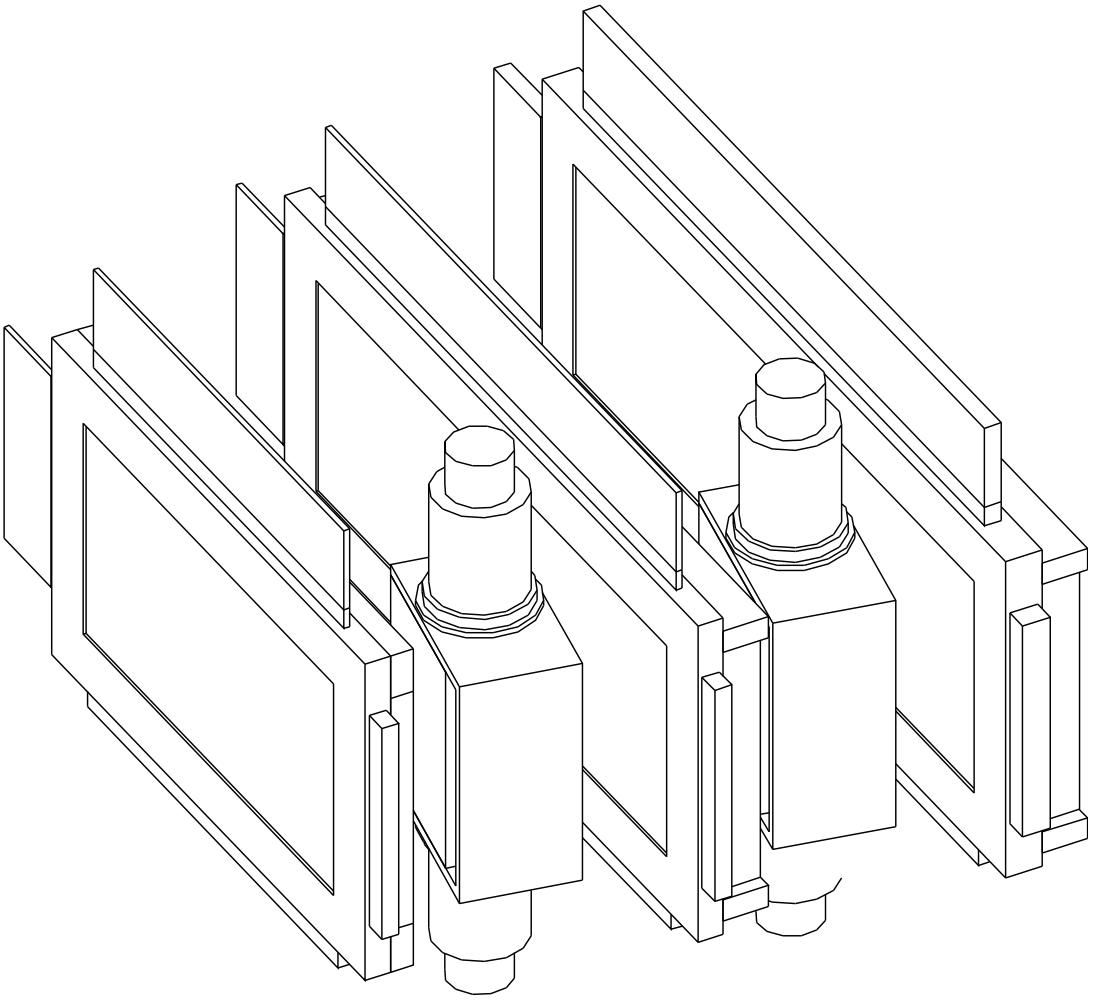

Figure H.2: *Aerogel Cherenkov counters between drift chambers.*

H.4.1 Production

Aerogel tiles are avalaible from Matsushita Electric Works, Ltd., Chiba University, KEK BELEE PID group, Facility at Mohri Ol Mill Co., Ltd. (Japan), Boreskov Institute of Catalysis and Budker Institute of Nuclear Physics (Novosibirsk), Joint Institute for Nuclear research (Dubna), Lawrence National Laboratory, Lockheed Corporation, Jet Propulsion Laboratory, and may be from Airglass Co. (Sweden). Depending on technology the hydrophobic or hydrophilic aerogel is produced. Hydrophobic aerogel keeps transparency for years. Hydrophilic aerogel requires a backing procedure.

H.4.2 Physical properties

Aerogel is chemically identical to quartz. With 3% of water the calculations below are give: $Z/A = 0.50093$, nuclear collision length is 66.3 g/cm^2, nuclear interaction length is 96.9 g/cm^2, $dE/dx = 1.71$ MeV/g·cm^2, radiation length is $X_0 = 27.25$ g/cm^2.

H.4.3 Refractive index

The aerogel refractive index is proportional to density: n= $1 + 0.21\rho$, where ρ is the density in g/cm^3. Lower densities are as 20 mg/cm^3. 100 mg/cm^3 corresponds to n=1.021. Refractive index can be measured by optical devices.

Threshold behavior allows also to measure refractive indices of aerogels with high precision. For that it is necessary to measure the dependence of N_{pe} from particle momentum. N_{pe} is a linear function of $1/p^2$.

H.4.4 Transmittance

The limiting processes to the Cherenkov photon detection are the Rayleigh scattering ($L_{sc} \sim \lambda^4$) and the absorption ($L_{abs} \sim \lambda^2$). Optical transmittance accounts for residual light from aerogel in the forward direction. This is combined processes of absorption, scattering and reflection. Transmission length strongly depends on the wavelength and increases with increasing photon wavelengths. Most of the Rayleigh scattered photons have nearly the same direction as the beam. Scattering (transmittance) length is usually $L_{sc} = 25 - 50$ mm at 400 nm. Absorption length is $L_{abs} \sim 1$ m at 400 nm. So $L_{sc} \ll L_{abs}$. Because of light scattering it is impossible to increase the photoelectron number by increasing the aerogel thickness. The N_{pe} saturates at 7–15 cm depending on the aerogel transparency.

Baking [LAGA01] (if aerogel is hydrophilic) considerably improves the transmittance for all photon wavelengths. Baking procedure (to remove water) is 3 h ramp up to 500°C, 12 h at 500°C, 3 h rump down room temperature. After baking the transmittance increases. Improvement estimted is 53% for aerogel 9 cm thick. Experimental value is 58%.

H.4.5 Light collection

For light collection in aerogel counters the mirror or diffuse reflections are used. Sometimes mirror collection is better, sometimes diffuse one. The diffusion geometry usually requires larger aerogel volumes to get the same performance as mirror detectors. The best light collection may be with mirrors and with good geometry like in gas Cherenkov counters ("long" counters) where the light collection is usually good.

The number of photoelectrons is equal to $n_{pe} = N_0 L(1 - 1/\mathrm{n}^2\beta^2)$, where n is refractive index, β is particle velocity, L is radiator length in cm, N_0 is figure of merit in cm^{-1}. For aerogel counters the figute of merit is $N_0 = 35$ cm^{-1} for thickness 5 mm, $N_0 = 25$ cm^{-1} for thickness 10 mm, $N_0 = 20$ cm^{-1} for thickness 15 mm. From simulation it is follows that figure of merit for new aerogel is attainable ∼45 and pracically can be independent of aerogel thickness.

H.4.6 Aerogel and gas combination

The combination of aerogel with a heavy gas (C_4F_{10}) in a dual radiator RICH makes it possible to cover the entire kinematic range of HERMES for hadron energies from 2 to 16 GeV (refractive indices 1.03 and 1.0014 for aerogel and C_4F_{10}, respectively).

RICH detectors have advantage over threshold detectors. In the both types of detectors the number of photoelectrons the same if the light collection the same, and the ring radius in RICH detectors is proportional to the signal amplitude in threshold detectors, but resolution in radius is much better than in amplitude.

H.5 Calibration: N_γ to n_{pe}

H.5.1 Prototype

We used the aerogel Cherenkov counter [LAGA01] with diffuse light collection as prototype to estimate the efficiecy of light collection. Aerogel dimensions are $50 \times 51 \times 9$ cm^3, with n=1.025. Aerogel was baked at 500°. Aerogel tiles are kept in position by a mesh of thin nylon wires. Aerogel is stored in CO_2. Internal surfaces are covered with a white millipore paper. Light was collected with 6 PMs of 5 in. BURLE 8854 Quantacon with quantum efficiency of 20%. The detecter was tested at the 5 GeV/c multiparticle beam at CERN PS at T10 beam. The numbers of photoelectrons detected are $n_{pe} = 13.3$ for e, $n_{pe} = 8.7$ for π and $n_{pe} = 3.1$ for p.

H.5.2 Number of photons from e

For $\beta = 1$, $\theta = 12.68^\circ$, $N_\gamma = 490 \cdot 9 \cdot (1 - 1/\mathrm{n}^2) = 490 \cdot 9 \cdot 0.0482 = 213$, $n_{pe} = 42.6$ at $\varepsilon = 1$, $n_{pe}^{exp} = 13.3$ for e, $\varepsilon = 0.31$.

H.5.3 Number of photons from π

For $\beta = 0.99961063$, $\theta = 12.58^\circ$, $N_\gamma = 490 \cdot 9 \cdot (1 - 1/\mathrm{n}^2\beta^2) = 490 \cdot 9 \cdot 0.0474 = 209$, $n_{pe} = 41.8$ at $\varepsilon = 1$, $n_{pe} = 8.7$ for π, $\varepsilon = 0.21$.

H.5.4 Number of photons from p

For $\beta = 0.98284469$, $\theta = 6.96^\circ$, $N_\gamma = 490 \cdot 9 \cdot (1 - 1/\mathrm{n}^2\beta^2) = 490 \cdot 9 \cdot 0.0147 = 64.8$, $n_{pe} = 13.0$ at $\varepsilon = 1$, $n_{pe} = 3.1$ for p. $\varepsilon = 0.24$. So the average collection efficiency is $\varepsilon = (0.31 + 0.21 + 0.24)/3 = 0.25$. Average $n_{pe}/N_\gamma = 0.2 \cdot 0.25 = 0.05$.

H.6 Tables: n_{pe} for 9 cm thick aerogel detector

n=1.008

p	n_{pe}^{e}	n_{pe}^{π}	n_{pe}^{K}	n_{pe}^{p}
4.0	3.49	3.22	0.18	
4.5	3.49	3.28	0.87	
5.0	3.49	3.32	1.37	
5.5	3.49	3.35	1.74	
6.0	3.49	3.37	2.02	
6.5	3.49	3.39	2.23	
7.0	3.49	3.40	2.41	
7.5	3.49	3.41	2.55	0.09
8.0	3.49	3.42	2.66	0.50
8.5	3.49	3.43	2.75	0.84
9.0	3.49	3.43	2.83	1.12

n=1.010

p	n_{pe}^{e}	n_{pe}^{π}	n_{pe}^{K}	n_{pe}^{p}
4.0	4.34	4.08	1.05	
4.5	4.34	4.14	1.74	
5.0	4.34	4.18	2.24	
5.5	4.34	4.21	2.60	
6.0	4.34	4.23	2.88	
6.5	4.34	4.25	3.10	
7.0	4.34	4.26	3.27	0.46
7.5	4.34	4.27	3.41	0.96
8.0	4.34	4.28	3.52	1.37
8.5	4.34	4.29	3.62	1.71
9.0	4.34	4.29	3.69	2.00

n=1.012

p	n_{pe}^{e}	n_{pe}^{π}	n_{pe}^{K}	n_{pe}^{p}
4.0	5.20	4.94	1.92	
4.5	5.20	4.99	2.61	
5.0	5.20	5.03	3.10	
5.5	5.20	5.06	3.46	
6.0	5.20	5.08	3.74	
6.5	5.20	5.10	3.96	
7.0	5.20	5.11	4.13	1.33
7.5	5.20	5.12	4.27	1.83
8.0	5.20	5.13	4.38	2.24
8.5	5.20	5.14	4.47	2.57
9.0	5.20	5.15	4.55	2.83

n=1.014

p	n_{pe}^{e}	n_{pe}^{π}	n_{pe}^{K}	n_{pe}^{p}
4.0	6.05	5.79	2.78	
4.5	6.05	5.84	3.47	
5.0	6.05	5.88	3.96	
5.5	6.05	5.91	4.32	
6.0	6.05	5.93	4.59	0.80
6.5	6.05	5.95	4.81	1.58
7.0	6.05	5.96	4.98	2.19
7.5	6.05	5.97	5.12	2.69
8.0	6.05	5.98	5.23	3.10
8.5	6.05	5.99	5.32	3.43
9.0	6.05	6.00	5.40	3.72

n=1.016

p	n_{pe}^{e}	n_{pe}^{π}	n_{pe}^{K}	n_{pe}^{p}
4.0	6.89	6.63	3.64	
4.5	6.89	6.68	4.32	
5.0	6.89	6.72	4.81	
5.5	6.89	6.75	5.17	0.67
6.0	6.89	6.77	5.44	1.67
6.5	6.89	6.79	5.66	2.44
7.0	6.89	6.81	5.83	3.05
7.5	6.89	6.82	5.96	3.55
8.0	6.89	6.83	6.08	3.95
8.5	6.89	6.83	6.17	4.29
9.0	6.89	6.84	6.25	4.57

n=1.018

p	n_{pe}^{e}	n_{pe}^{π}	n_{pe}^{K}	n_{pe}^{p}
4.0	7.73	7.47	4.49	
4.5	7.73	7.52	5.17	
5.0	7.73	7.56	5.65	0.24
5.5	7.73	7.59	6.01	1.54
6.0	7.73	7.61	6.29	2.53
6.5	7.73	7.63	6.50	3.30
7.0	7.73	7.64	6.67	3.91
7.5	7.73	7.66	6.81	4.40
8.0	7.73	7.66	6.92	4.80
8.5	7.73	7.67	7.01	5.14
9.0	7.73	7.68	7.09	5.42

n=1.020

p	n_{pe}^{e}	n_{pe}^{π}	n_{pe}^{K}	n_{pe}^{p}
4.0	8.56	8.30	5.33	
4.5	8.56	8.36	6.01	
5.0	8.56	8.40	6.50	1.10
5.5	8.56	8.43	6.85	2.39
6.0	8.56	8.45	7.13	3.38
6.5	8.56	8.46	7.34	4.15
7.0	8.56	8.48	7.51	4.75
7.5	8.56	8.49	7.64	5.25
8.0	8.56	8.50	7.76	5.65
8.5	8.56	8.51	7.85	5.98
9.0	8.56	8.51	7.92	6.26

n=1.022

p	n_{pe}^{e}	n_{pe}^{π}	n_{pe}^{K}	n_{pe}^{p}
4.0	9.39	9.13	6.18	
4.5	9.39	9.19	6.85	0.21
5.0	9.39	9.23	7.33	1.96
5.5	9.39	9.26	7.69	3.25
6.0	9.39	9.27	7.96	4.23
6.5	9.39	9.29	8.17	4.99
7.0	9.39	9.31	8.34	5.60
7.5	9.39	9.32	8.48	6.09
8.0	9.39	9.33	8.59	6.49
8.5	9.39	9.33	8.68	6.82
9.0	9.39	9.34	8.76	7.10

n=1.024

p	n_{pe}^{e}	n_{pe}^{π}	n_{pe}^{K}	n_{pe}^{p}
4.0	10.21	9.96	7.01	
4.5	10.21	10.01	7.68	1.07
5.0	10.21	10.05	8.16	2.81
5.5	10.21	10.08	8.52	4.09
6.0	10.21	10.10	8.79	5.07
6.5	10.21	10.12	9.00	5.83
7.0	10.21	10.13	9.17	6.44
7.5	10.21	10.14	9.30	6.92
8.0	10.21	10.15	9.41	7.32
8.5	10.21	10.16	9.51	7.65
9.0	10.21	10.16	9.58	7.93

n=1.026

p	n_{pe}^{e}	n_{pe}^{π}	n_{pe}^{K}	n_{pe}^{p}
4.0	11.03	10.78	7.84	
4.5	11.03	10.83	8.51	1.93
5.0	11.03	10.87	8.99	3.66
5.5	11.03	10.90	9.35	4.94
6.0	11.03	10.92	9.62	5.91
6.5	11.03	10.94	9.83	6.67
7.0	11.03	10.95	9.99	7.27
7.5	11.03	10.96	10.13	7.76
8.0	11.03	10.97	10.24	8.15
8.5	11.03	10.98	10.33	8.48
9.0	11.03	10.98	10.40	8.76

n=1.028

p	n_{pe}^{e}	n_{pe}^{π}	n_{pe}^{K}	n_{pe}^{p}
4.0	11.85	11.59	8.67	0.37
4.5	11.85	11.65	9.34	2.78
5.0	11.85	11.69	9.81	4.50
5.5	11.85	11.71	10.17	5.78
6.0	11.85	11.74	10.44	6.75
6.5	11.85	11.75	10.64	7.50
7.0	11.85	11.77	10.81	8.10
7.5	11.85	11.78	10.94	8.58
8.0	11.85	11.78	11.05	8.98
8.5	11.85	11.79	11.14	9.31
9.0	11.85	11.80	11.22	9.58

n=1.030

p	n_{pe}^{e}	n_{pe}^{π}	n_{pe}^{K}	n_{pe}^{p}
4.0	12.66	12.40	9.49	1.22
4.5	12.66	12.46	10.16	3.62
5.0	12.66	12.50	10.63	5.33
5.5	12.66	12.52	10.98	6.61
6.0	12.66	12.55	11.25	7.54
6.5	12.66	12.56	11.46	8.33
7.0	12.66	12.57	11.62	8.92
7.5	12.66	12.59	11.76	9.40
8.0	12.66	12.59	11.87	9.78
8.5	12.66	12.60	11.96	10.13
9.0	12.66	12.61	12.03	10.40

Appendix I

Existing gas Cherenkov counters modified

I.1 Existing gas Cherenkov counters

In the experiment planned for the detection of $A_{2\pi}$, $A_{\pi^+K^-}$ and $A_{\pi^-K^+}$ we have to separate electrons, pions and kaons in the right arm, and positrons, pions, kaons and protons in the left arm of the spectrometer.

To suppress electrons and positrons we use the gas Cherenkov counters filled with nitrogen (N_2). The existing gas Cherenkov counters are shown in Fig. I.1

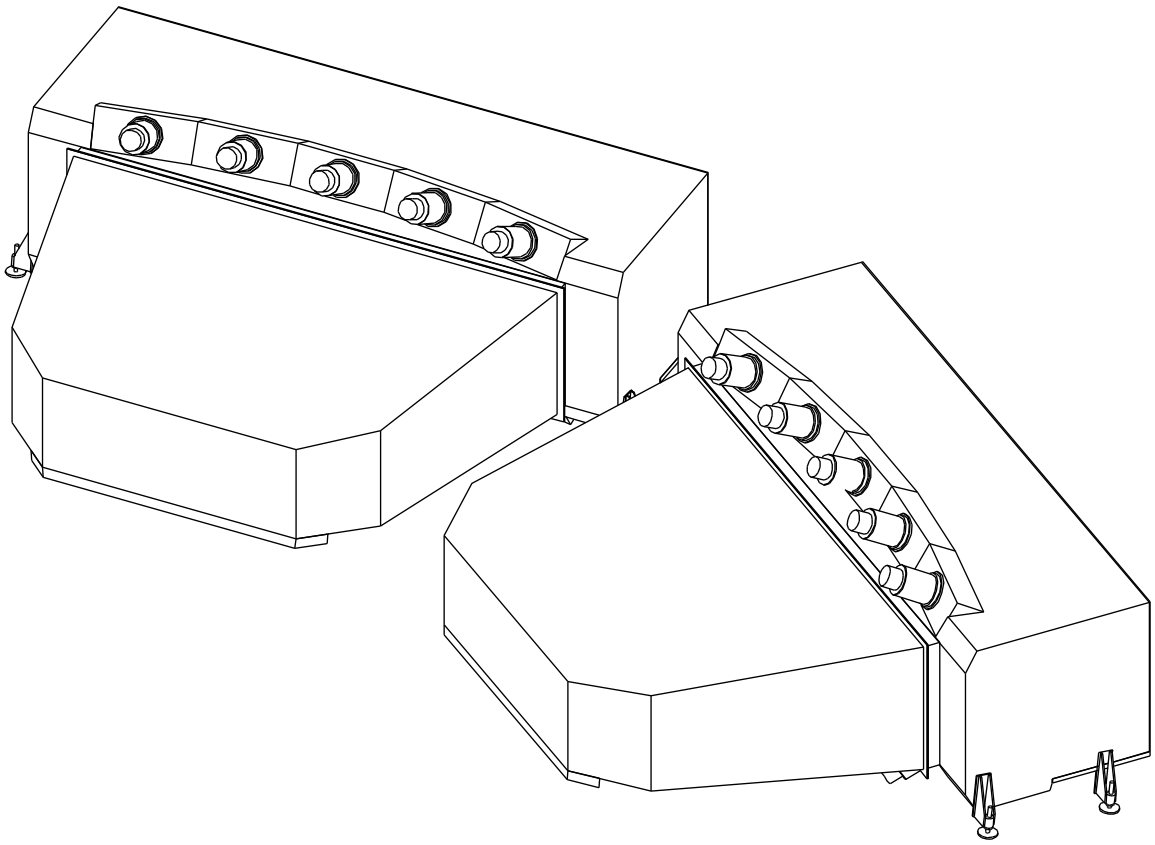

Figure I.1: *Existing gas Cherenkov counters filled with N_2*

The two present Cherenkov counters are used at first trigger level for rejecting e^+ and e^-. The counters have a total length of 285 cm, and the radiator length is 250-260 cm. Their entrance windows have dimensions 143×56 cm^2 and the exit ones 336×96 cm^2. The gas radiator used is nitrogen (N_2) at normal temperature and pressure.

Each counter is provided with 20 mirrors, and 10 photomultipliers on two rows. The Cherenkov light reflected by a pair of adjacent mirrors is focused onto the same PM (Hamamatsu R1587 with UV-glass window). Mirrors are spherically formed rectangles, with average dimensions 30×35 cm^2 and 6 mm thick.

The average number of photoelectrons for particles with $\beta = 1$ is over 16. Both counters have an efficiency $> 99.8\%$ at the detection threshold of 5 p.e., and the pion contamination above the detection threshold is less than 1.5%. Such contamination arises from pions with momenta above the Cherenkov threshold and from accidental coincidences occurring within the gate window.

I.1.1 Properties of nitrogen

Nitrogen is a gas at normal atmospheric conditions, colorless, odorless, tasteless, nonflammable, physiologically inert, nontoxic. One liter of liquid N_2 liberates 691 liters of gas (expanded to 15°C). It is shipped as a liquefied gas under its own vapor pressure. Molecular weight (g·mole^{-1}) is 28.0134, gas density at S.T.P. (kg·m^{-3}) is 1.25053.

I.1.2 Index of refraction, transparency, scintillations

At 20°C and 1013 mbar the index of refraction is n=1.0002824. The maximum Cherenkov emission angle is 1.39°. N_2 is known to have excellent transparency to light with wavelength above 190 nm [GARW71]. Number of scintillation light quanta emitted into the full solid angle in the S11 spectral range from 1 cm path of m.i.p. at 20°C and 1013 mbar is $2.7 \cdot 10^{-1}$.

I.2 Modification of the present gas Cherenkov counters

These counters should be modified to clear a space for gas Cherenkov counters dedicated for pion and kaon separaion. To separate pions and kaons of both signes we plan to implement small gas Cherenkov counters filled with a heavy gas (SF_6 or C_4F_{10}).

There are two possibilities:

— Parts of the both counters nearest to the beam axis are removed along the half of the radiator lenght leaving part of N_2 radiator to detect high energetic electrons.

— Parts of the both counters nearest to the beam axis are removed along the full radiator lenght. This is the case if the contamination of high energetic electrons (positrons) is small and unimportant.

The first version is shown in Fig. I.2, the second one in Fig. I.3.

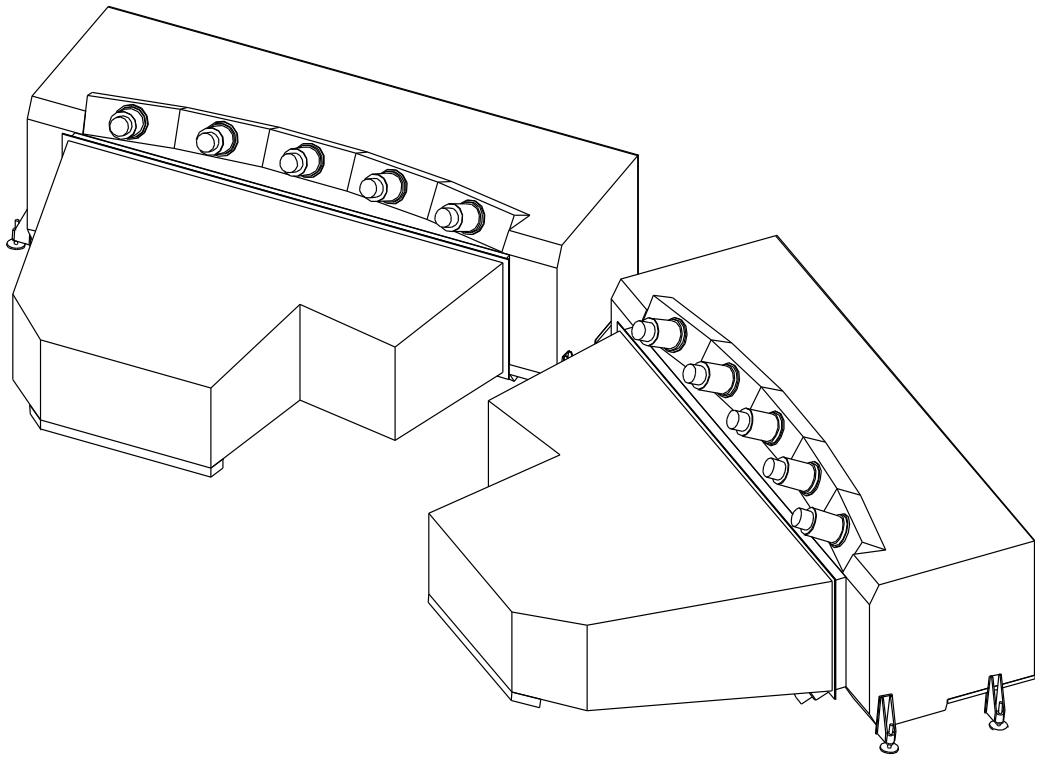

Figure I.2: *First version of the modified existing Cherenkov counters.*

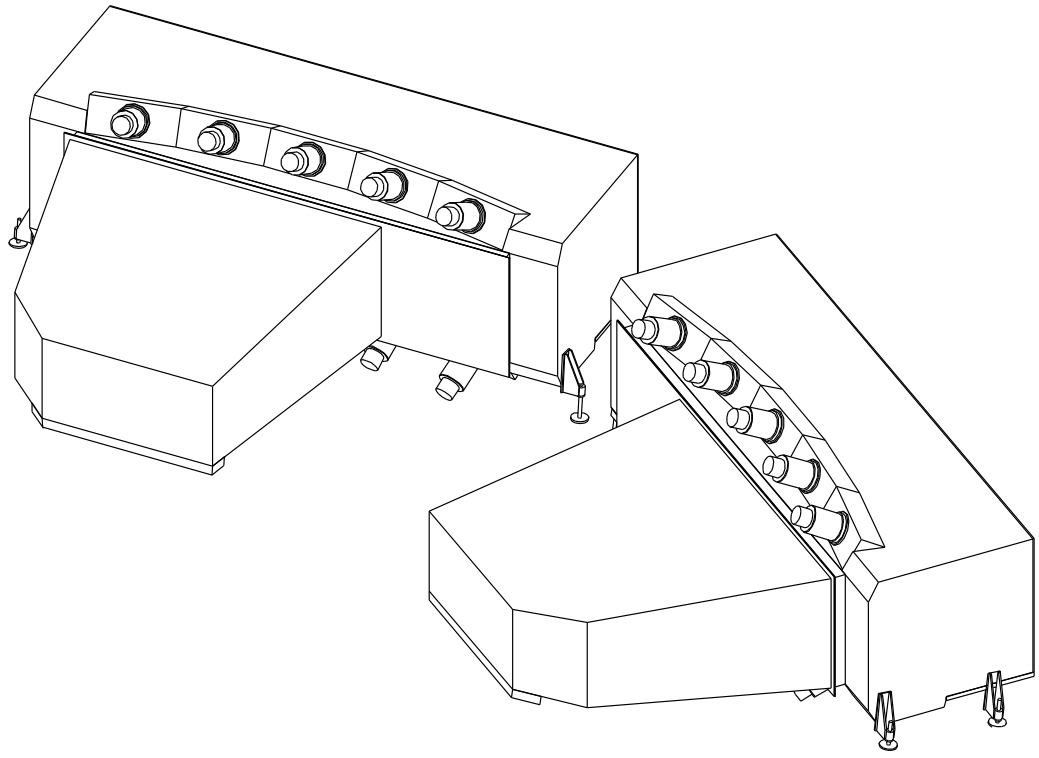

Figure I.3: *Second version of the modified existing Cherenkov counters.*

Appendix J

New gas Cherenkov counters

J.1 New gas Cherenkov counters purpose

In the experiment planned for the detection of $A_{2\pi}$, $A_{\pi^+K^-}$ and $A_{\pi^-K^+}$ we have to separate electrons, pions and kaons in the right arm, and positrons, pions, kaons and protons in the left arm of the spectrometer.

To suppress electrons and positrons we will use the existing gas Cherenkov counters filled with nitrogen (N_2). But these counters should be modified to clear a space for gas Cherenkov counters dedicated for pion and kaon separaion.

To separate pions and kaons of both signs we plan to implement small gas Cherenkov counters filled with a heavy gas (SF_6 or C_4F_{10}).

J.2 Sulfur hexafluoride (SF_6) as Cherenkov radiator

A suitable radiator for the new Cherenkov counter is sulfur hexafluoride (SF_6) gas, which has an index of refraction n=1.00072 and corresponding threshold on pion and kaon momenta at $\sim$ 3.7 GeV/c and $\sim$ 13.0 GeV/c, respectively. It allows to discriminate electrons, muons and pions from kaons because only e, μ and π are produce Cherenkov light in SF_6 in the appropriate momentum range (3.9$\div$8.9 GeV/c).

The maximum Cherenkov emission angle is 2.17° to be compared with 1.39° for N_2. Since the optics of the counter is optimised to focus light emitted at a maximum Cherenkov angle of 1.39° we expect a partial loss of Cherenkov photons falling outside the mirror acceptance. This loss does, however, correspond to a negligible loss of efficiency since the expected light yield in SF_6 is larger than in N_2, for the same radiator path length.

We have performed a simulation of the detector response to pions with momenta from 3.9 to 7.8 GeV/c traversing the ~ 2.8 m long SF_6 gas radiator. With the present optical arrangement of the mirrors and photomultipliers, and with a detection threshold set at 5 p.e. level, the pion detection efficiency is 99.3%, to be compared to a positron detection efficiency of 99.6% for the counter on the positive arm filled with N_2 gas.

J.2.1 Properties of sulfur hexafluoride

Sulfur hexafluoride is a gas in normal atmospheric conditions (15°C, 760 mm Hg), practically nontoxic, nonflammable in air, inert, noncorrosive, thermally stable up to 800°C, previously used as radiator. Molecular weight is 146.05 g·mole^{-1}. Prize: 68 kg — 2500$.

J.2.2 Refractive index, transparency, scintillations

Refractive index of SF_6 at 20°C and 1013 mbar is n=1.000719.

SF_6 is known to have excellent transparency to light with wavelength above 190 nm [GARW71], comparable to that of N_2.

Number of scintillation light quanta emitted into the full solid angle in the S11 spectral range from 1 cm path of m.i.p. at 20°C and 1013 mbar: $4.1 \cdot 10^{-2}$. Scintillation intensity 6.6 times less than in nitrogen [HEIN76].

J.3 Perfluorobutane (C_4F_{10}) as Cherenkov radiator

We consider also the option with gas C_4F_{10} at atmospheric pressure as a radiator with a high refraction index (n=1.0014) in the new Cherenkov counters for pion and kaon discrimination. This radiator is suitable to discriminate pions from kaons in the kinematic range of accepted $A_{\pi K}$ since the threshold is 2.6 GeV/c and 9.3 GeV/c for pions and kaons, respectively. With C_4F_{10} the separation will be improved even further in comparison with SF_6.

J.3.1 Properties of perfluorobutane

Perfluorobutane, also known as decafluorobutane, is a gas in normal atmospheric conditions (15°C, 760 mm Hg), colorless, odorless, nontoxic, nonflammable in air, thermally stable and chemically inert, environmentally safe, can be operated at room temperature, and has a well-understood behaviour from previous experiments. However, mixtures with flammable gases may, if ignited, lead to its decomposition with the liberation of toxic components. In other respects, save for flammability, it resembles its hydrocarbon counterpart, butane. The most abundant form resulting from commercial production is the n-isomer, a completely fluorinated linear carbon chain.

Formula: C_4F_{10} or CF_3 — CF_2 — CF_2 — CF_3.
Molecular weight (g·mole^{-1}): 238.028.
Boiling point (°C): -1.7, -1.9, -2.
Liquid density (kg·m^{-3}): 1594.
Gas density (kg·m^{-3}): 11.21.
1 liter of liquid liberates 158 liters of gas (expanded to 15°C, 1 bar).

J.3.2 Refractive index, optical properties

Refractive index of C_4F_{10} is n=1.001415 at 1 atm, 300 K at 300 nm. Threshold $\gamma = 18.3$, $\theta_{max} = 55.6$ mrad, threshold for kaons is 9.0 GeV/c.

C_4F_{10} has low chromatic dispersion (chromatic aberrations) combined with a transmission cutoff that almost matches that of the quartz windows. It is completely transparent (if pure) at wave lengths down to 160 nm.

J.3.3 Delivery

C_4F_{10} is shipped as a liquefied gas under its own vapor pressure:
— Commercial brands carry the designation 610 (old).
— 3M Co. St.Paul, MN 55144, USA, product code DP L-12321.
— PCR, Inc.: Gainesville, FL 32602, USA.
— Cost 930 CHF/m^3.

J.4 Versions of new gas counters

The two options of the new Cherenkov counter are shown in Figs. J.1 (short counter) and J.2 (long counter).

All gas Cherenkov counters are shown in Figs. J.3 (with short counters) and in Fig. J.4 (with long counters).

Of couse the option is possible with four short counters when the first pair can work with aerogel with good optics for light collection, and second pair of counters with a heavy gas (Fig. J.5).

Finally the all Cherenkov counters (with aerogel and gases) are shown in Fig. J.6.

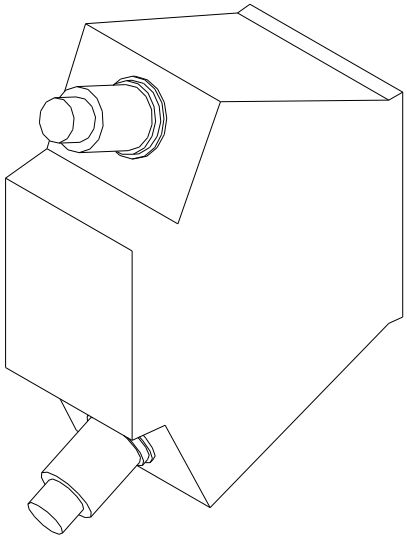

Figure J.1: *Short version of the new gas Cherenkov counter.*

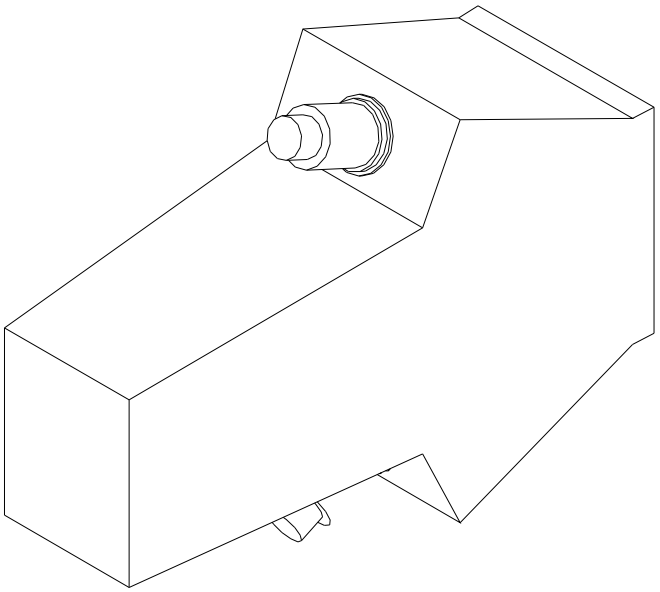

Figure J.2: *Long version of the new gas Cherenkov counter.*

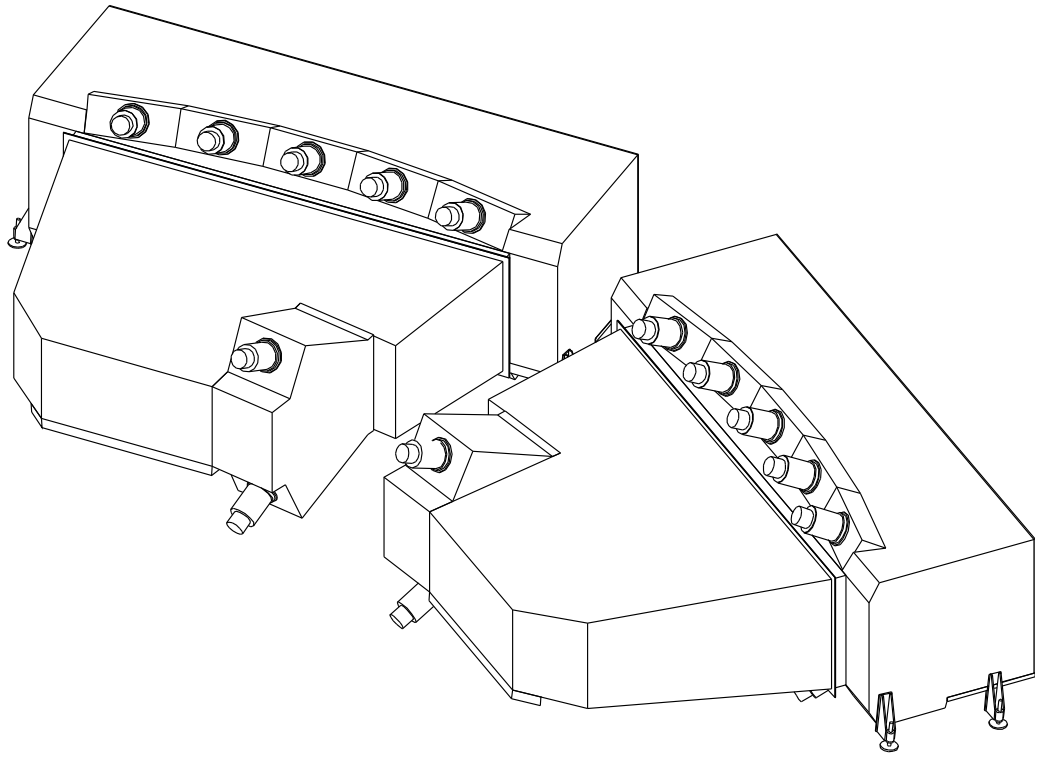

Figure J.3: *All gas Cherenkov counters. Counters with a heavy gas are short*

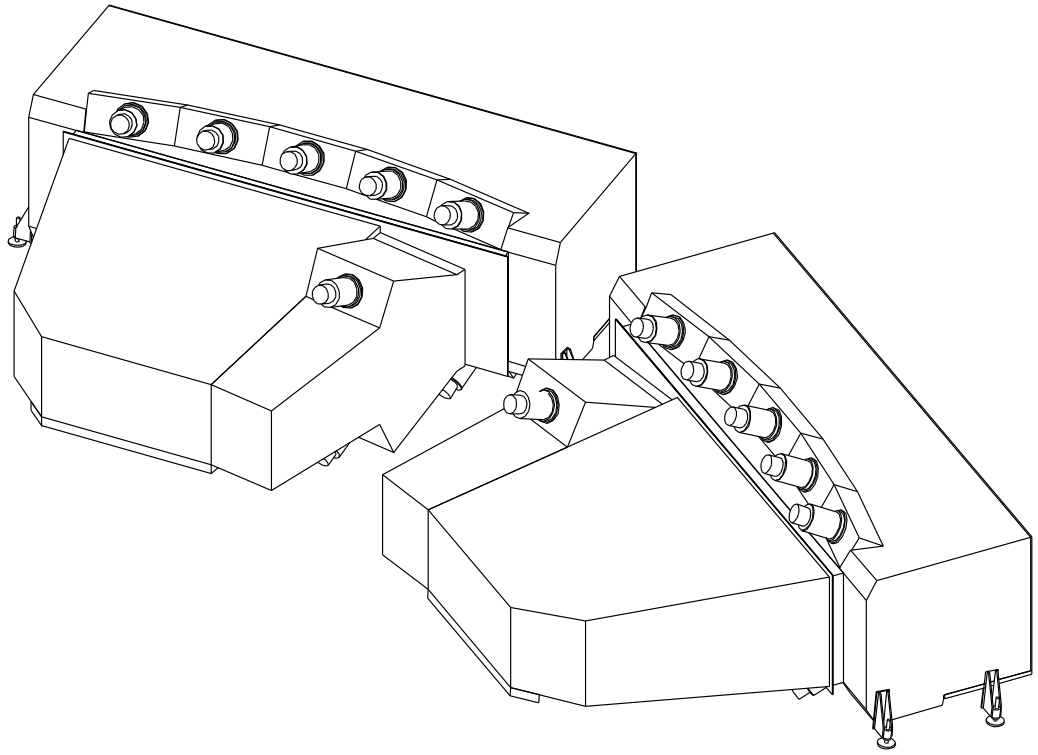

Figure J.4: *All gas Cherenkov counters. Counters with a heavy gas are long.*

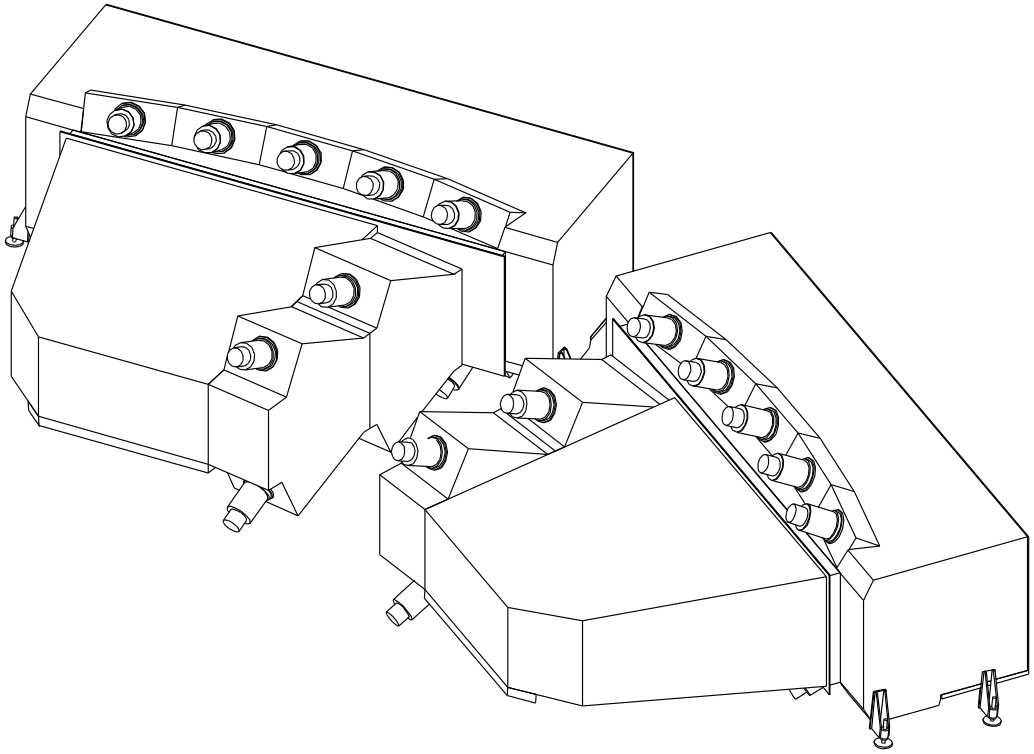

Figure J.5: *All gas Cherenkov counters. Counters with a heavy gas are short. The first pair of the short counters can be used with aerogel as radiator, the second pair with a heavy gas*

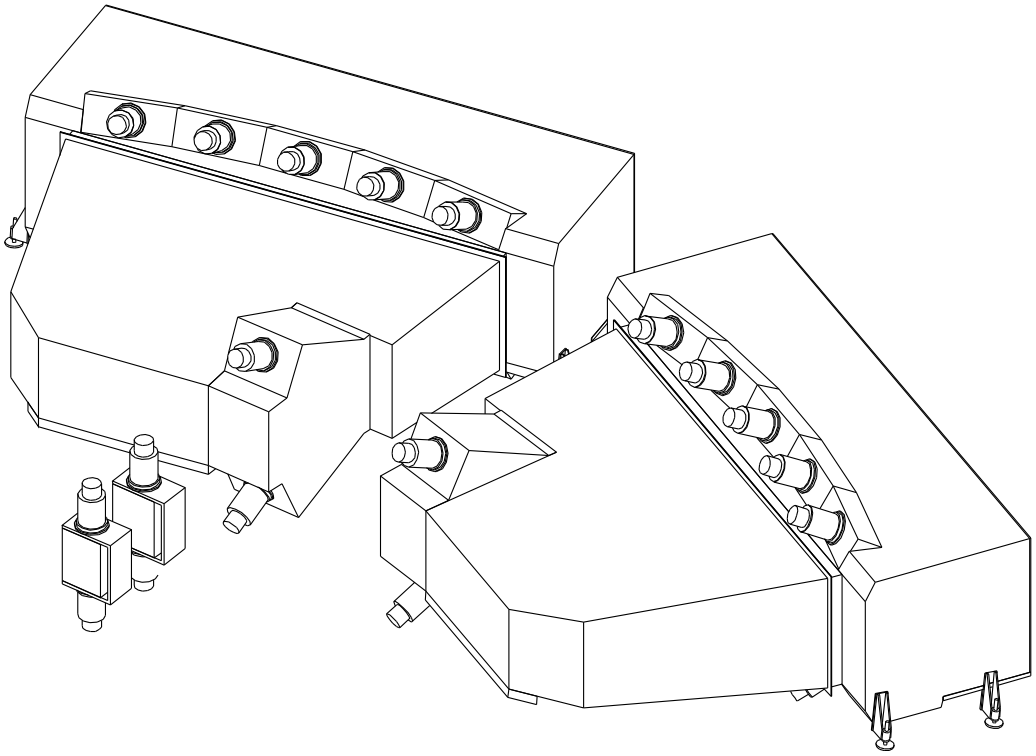

Figure J.6: *All aerogel and gas Cherenkov counters. Counters with a heavy gas are short.*

J.5 Beam test of the prototype counter with SF_6

In 2001 the existing gas Cherenkov countes were filled with SF_6 (instead of N_2) and were tested in the real coditions of the DIRAC. In reality the counters were filled by the mixture: 90% SF_6 + 10% N_2 with n=1.00067. For the pure SF_6 n=1.00072. The fourth level trigger hardware processor was reloaded in order to detect K^+K^- pairs from ϕ decay. The both $e^\pm$ and $\pi^\pm$ in DIRAC conditions are above threshold in SF_6 and $K^\pm$ are under threshold. So it was possible to eliminate $e^\pm$ and $\pi^\pm$. The rest events are mostly K^+K^- pairs.

The data were taken during 15 hours. The ϕ signal was clearly extracted with $M = 1019.4 \pm 0.6$ MeV and $\Gamma = 3.33 \pm 1.02$ MeV, see Fig. J.7. The numbers of photoelectrons predicted and estimated from the experiment are shown in the Table. In the last column the photoelectron number is estimated for pure SF_6 on the base of the experiment (previous column) and the refractive indices of the mixed and pure gas. This result is in agreement with the estimations in the Table below calculated for pure SF_6.

Particle	p, GeV/c	n_{pe}^{th}, mixture	n_{pe}^{exp}, mixture	n_{pe}, pure SF_6
$\pi^\pm$	4.3÷5.0	12	10	12
$\pi^\pm$	5.0÷6.0	16	15	17
$\pi^\pm$	6.0÷7.0	21	20	22
$e^\pm$	$>$ threshold	33	28	30

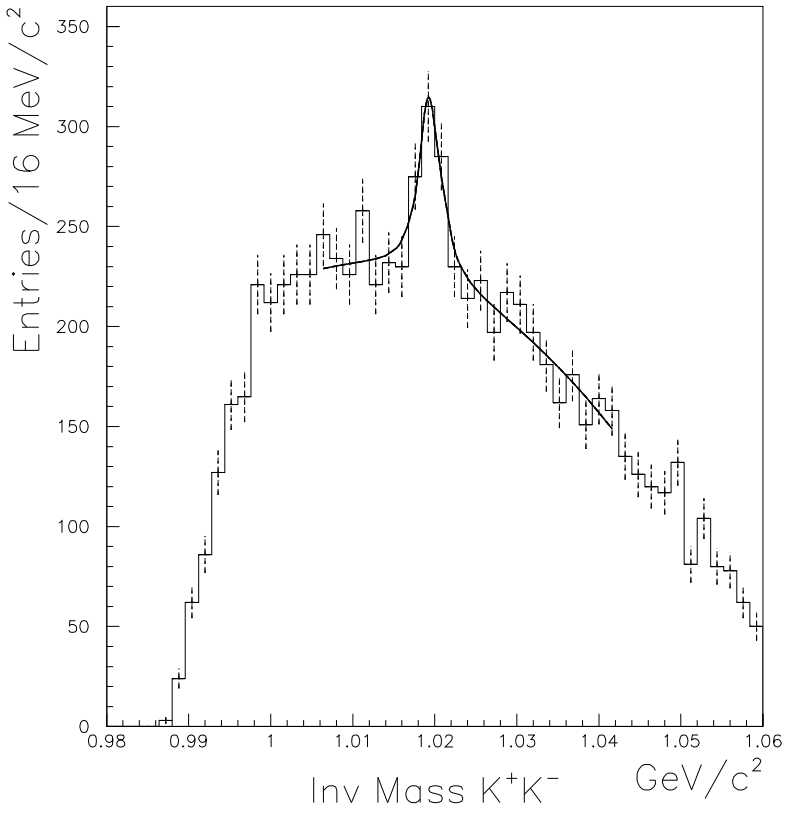

Figure J.7: $\phi \to K^+K^-$ decay signal extracted using the particle identification with the Cherenkov counter filled with the heavy gas.

J.6 Tables: πK atoms, n_{pe}^{π} in SF_6 and C_4F_{10}

In the two tables below the number of photoelectrons from pions n_{pe}^{π} is esimated at conditions: π momentum is equal to K momentum from $A_{\pi K}$. This means the number of photoelectrons from background pions with the same momentum as the kaon momentum. The radiator length the same as in the present gas Cherenkov counters filled with N_2, but the radiators in calculations are SF_6 and C_4F_{10}. The full length of the present counters is 280 cm, and active length of the radiator is 250-260 cm (up to the mirrors).

Comments to the tables: $p_{A\pi K}$ — in GeV/c, $p_\pi = p_A m_\pi/(m_\pi + m_K)$, $p_K = p_A m_K/(m_\pi + m_K)$, β_A — β of πK atoms, β_π — β of π with the same momentum as K, θ_K — angle of Cherenkov light for K, θ_π — angle of Cherenkov light for π with $p_\pi = p_K$, N_{pe}^{π} — number of photoelectrons for π with $p_\pi = p_K$.

J.6.1 π^+K^- atoms, Cherenkov counter with SF_6

$p_{\pi K}$	p_π	p_K	β_A	$\beta_\pi, p_\pi = p_K$	θ_K	θ_π	N_{pe}^{π}
5.0	1.10	3.90	0.9920751	0.9993602	—	0.71	4.0
5.5	1.21	4.29	0.9934369	0.9994739	—	1.12	9.9
6.0	1.32	4.68	0.9944765	0.9995647	—	1.36	14.6
6.5	1.43	5.07	0.9952878	0.9996193	—	1.49	17.5
7.0	1.54	5.46	0.9959330	0.9996667	—	1.59	19.9
7.5	1.65	5.85	0.9964544	0.9997228	—	1.70	22.8
8.0	1.76	6.24	0.9968817	0.9997448	—	1.74	23.8
8.5	1.87	6.63	0.9972363	0.9997773	—	1.80	25.5
9.0	1.98	7.02	0.9975338	0.9998064	—	1.86	27.2
9.5	2.09	7.41	0.9977857	0.9998235	—	1.89	28.2
10.0	2.20	7.80	0.9980009	0.9998399	—	1.91	28.7

J.6.2 π^+K^- atoms, Cherenkov counter with C_4F_{10}

$p_{\pi K}$	p_π	p_K	β_A	$\beta_\pi, p_\pi = p_K$	θ_K	θ_π	N_{pe}^{π}
5.0	1.10	3.90	0.9920751	0.9993602	—	2.23	38.5
5.5	1.21	4.29	0.9934369	0.9994739	—	2.39	44.4
6.0	1.32	4.68	0.9944765	0.9995647	—	2.51	49.0
6.5	1.43	5.07	0.9952878	0.9996193	—	2.59	52.0
7.0	1.54	5.46	0.9959330	0.9996667	—	2.64	54.1
7.5	1.65	5.85	0.9964544	0.9997228	—	2.71	57.1
8.0	1.76	6.24	0.9968817	0.9997448	—	2.74	58.4
8.5	1.87	6.63	0.9972363	0.9997773	—	2.78	59.9
9.0	1.98	7.02	0.9975338	0.9998064	—	2.81	61.2
9.5	2.09	7.41	0.9977857	0.9998235	—	2.83	62.2
10.0	2.20	7.80	0.9980009	0.9998399	—	2.85	63.0

J.7 Tables: dependence of n_{pe} from partille type and momenum

For normalisation we use the experimental results obtained with the DIRAC gas Cherenkov counters filled with nitrogen (N_2), n=1.000296, $\theta = 1.39^\circ$ for electrons. $Npe = 15$ at passage of relativistic electrons through N_2 radiator. The photoelectron number is proportional to $\sin^2\theta$. $\sin^2(1.39) = 0.000588$ corresponds to 15 photoelectrons. N_{pe} — number of photoelectrons for pions: $15 \cdot \sin^2\theta/0.000588$.

Number of photoelectrons with SF_6, radiator length the same, n=1.000719, $\theta = 2.17^\circ$ for electrons, $\sin^2 2.17^\circ = 0.00143$. $N_{pe} = 15 \cdot 143/58.8 = 36.5$ for electrons, if the light collection is the same as for nitrogen.

Number of photoelectrons with C_4F_{10}, radiator length the same, n=1.001400, $\theta = 3.03^\circ$ for electrons, $\sin^2 3.03^\circ = 0.002794$. $N_{pe} = 15 \cdot 279.4/58.8 = 73.1$ – number of photoelectrons for electrons, if the light collection is the same as for nitrogen.

Now we estimate figure of merit N_0. $N_{pe}^{max} = N_0 \cdot L_{rad} \cdot (1 - 1/n^2)$. L_{rad} — radiator length, 250 cm. $N_{pe}^{max} = N_0 \cdot 250 \cdot 0.0005797 = 15$. $N_0 = 104$. This is a good value comparable with the best published results.

In the tables below a bit different number of photoelectrons for N_2 is used. Protons and kaons are under threshold in these gases for the momentum range 2–9 GeV/c.

n=1.00029, N_2

p	n_{pe}^e	n_{pe}^π
2.0	14.20	
2.5	14.20	
3.0	14.20	
3.5	14.20	
4.0	14.20	
4.5	14.20	
5.0	14.20	
5.5	14.20	
6.0	14.20	0.95
6.5	14.20	2.91
7.0	14.20	4.47
7.5	14.20	5.72
8.0	14.20	6.75
8.5	14.20	7.60
9.0	14.20	8.31

n=1.00072, SF_6

p	n_{pe}^e	n_{pe}^π
2.0	35.24	
2.5	35.24	
3.0	35.24	
3.5	35.24	
4.0	35.24	5.46
4.5	35.24	11.71
5.0	35.24	16.18
5.5	35.24	19.49
6.0	35.24	22.00
6.5	35.24	23.96
7.0	35.24	25.52
7.5	35.24	26.77
8.0	35.24	27.80
8.5	35.24	28.65
9.0	35.24	29.36

n=1.0014, C_4F_{10}

p	n_{pe}^e	n_{pe}^π
2.0	68.46	
2.5	68.46	
3.0	68.46	15.58
3.5	68.46	29.61
4.0	68.46	38.71
4.5	68.46	44.95
5.0	68.46	49.42
5.5	68.46	52.72
6.0	68.46	55.24
6.5	68.46	57.19
7.0	68.46	58.74
7.5	68.46	60.00
8.0	68.46	61.02
8.5	68.46	61.87
9.0	68.46	62.58

Bibliography

[ACHA02] P. Achard *et al.*(L3), Phys. Lett., B540 (2002) 185.

[ADAM03] C. Adams *et al.*(STAR), Phys. Rev. Lett., 91 (2003) 262301.

[ADDE00] B. Adeva, *et al.*, CERN/SPSC 2000-032, SPSC/P284 Add.1, 17 August 2000.

[ADEV95] B. Adeva, *et al.*, CERN/SPSLC 95–1, SPSLC/P 284, Geneva 1995; http://cern.ch/dirac.

[ADEV02] B. Adeva *et al.*, Nucl. Instr. Meth. A491 (2002) 41.

[ADEV03] B. Adeva, *et al.*, NIM A515 (2003) 467-49.

[ADEV03] B. Adeva *et al.*, Nucl. Instr. Meth. A515 (2003) 467.

[ADEV03] B. Adeva, A. Romero and O. Vazquez Doce, DIRAC note 03-08.

[AFAN91] L. G. Afanasyev, JINR E2-91-578, Dubna, 1991;
JINR B1-2-91-572, Dubna, 1991.

[AFAN93] L.G. Afanasyev *et al.*, Phys. Lett. B308 (1993) 200.

[AFAN93A] L. G. Afanasyev, A. V. Tarasov, JINR E4-93-293, Dubna, 1993.

[AFAN94] L. G. Afanasyev *et al.*, Phys. Lett. 338B (1994) 478.

[AFAN96] L.G. Afanasyev and A.V. Tarasov, Yad.Fiz. 59 (1996) 2212; (Phys. At. Nucl. 59 (1996) 2130).

[AFAN96B] L.G. Afanasyev *et al.*, Communication JINR P1-97-306, Dubna, 1997.

[AFAN97] L. G. Afanasyev, O. Voskresenskaya and V. Yazkov, JINR preprint, P1-97-306, Dubna, 1997.

[AFAN97A] L. G. Afanasyev, "Observation of $\pi^+\pi^-$ atom", PhD thesis, JINR, Dubna, 1997.

[AFAN99] L. Afanasyev, A. Tarasov and O. Voskresenskaya, J.Phys. G25 (1999) B7-B10.

[AFAN99A] L. G. Afanasyev and O. Voskresenskaya, Phys. Lett. B453 (1999) 302.

[AFAN00] L. G. Afanasyev and S. Santamarina, DIRAC note 00-04

[AFAN02] L. Afanasyev, A. Tarasov and O. Voskresenskaya, Phys.Rev.D 65 (2002) 096001, hep-ph/0109208.

[AFAN021] L. Afanasyev, M. Gallas, V. Karpukhin, A. Kulikov, Nucl. Instr. Meth. A479 (2002) 407.

[AFAN02M] L. Afanasyev *et al.*, Nucl. Instr. Meth. A491 (2002) 376.

[AGGA00] M. Aggarwal *et al.*(WA98), Phys. Rev. Lett., 85 (2000) 2895.

[AGUI73] M.Aguilar-Benitez *et al.*, Phys. Rev. Lett. 30 (1973) 672.

[AMIR99] I. Amirkhanov *et al.*, Phys. Lett. 452 (1999) 155.

[ANTI71] P. Antich *et al.*, Nucl. Phys. B29 (1971) 305.

[AOKI99] S. Aoki *et al.*, hep-lat/9911025.

[ARIAN] Analysis software package for DIRAC, unpublished.

[AUST83] G.J.M.Austen, J.J. de Swart, Phys.Rev.Lett. 50 (1983) 2039.

[BACH99] N. Bacchetta *et al.*, Nucl. Instr. and Meth. A426 (1999) 16.

[BAKE75] S. L. Baker *et al.*, Nucl. Phys. B99 (1975) 211.

[BAKE99] N. van Bakel *et al.*, Snowmass 1999, "Electronics for LHC experiments", 167.

[BAKK70] A. M. Bakker *et al.*, Nucl. Phys. B24 (1970) 211.

[BALD76] R. Baldi *et al.*, Phys.Letters 63B (1976) 344.

[BALD78] R. Baldi *et al.*, Nucl. Phys. B134 (1978) 365.

[BARK03] A.R. Barker, H. Huang, P.A.Toale, and J. Engle, Phys. Rev. D**67**, 033008.

[BAYE69] V. N. Bayer and V. S. Fadin, Zh. Eksp. Teor. Fiz. 57 (1969) 225;
Sov. Phys. JETP 30 (1970) 120.

[BAUE99] C. Bauer *et al.*, Snowmass 1999, "Electronics for LHC experiments", 508.

[BEAR99] I.G. Bearden *et al.*(NA44), Phys. Lett., B455 (1999) 77.

[BERN91] V. Bernard, N. Kaiser and U. Meissner, Phys. Rev. D43 (1991) 2757;
V. Bernard, N. Kaiser and U. Meissner, Nucl. Phys. B357 (1991) 129.

[BIJN96] J. Bijnens *et al.*, Phys. Lett. B374 (1996) 210.

[BIJN97] J. Bijnens *et al.*, Nucl. Phys. B508 (1997) 263; (hep-ph/9707291).

[BILE69] S.M. Bilenky *et al.*, Yad. Phys. 10 (1969) 812; (Sov. J. Nucl. Phys. 10 (1969) 469).

[BING72] H. H. Bingham *et al.*, Nucl. Phys. B41(1972) 1.

[BOAL86] D.H. Boal and J.C. Shillcock, *Phys. Rev.* C33, 549 (1986); D.H. Boal, C.-K. Gelbke and B.K. Jennings, *Rev. Mod. Phys.* 62, 553 (1990).

[BRAG99] M. Bragadireanu *et al.*, Nucl. Instr. Meth. A426 (1999) 254.

[BRAN77] G. W. Brandenburg *et al.*, not published, (1977).

[BREK01] V. Brekhovskikh and M. V. Gallas, DIRAC note 2001-02

[BRES99] A. Bressan *et al.*, Nucl. Instr. and Meth. A425 (1999) 254

[BUTT03] P. Buttiker, S. Descotes-Genon and B. Moussallam, arXiv:hep-ph/0310045.

[BUTT03B] P.Büttiker, S.Descotes-Genon and B.Moussallam, arXiv: hep-ph/0310283.

[CERN00] CERN/LHCC 2000-016 CMS TDR 5 Addendum 1, 21 Feb. 2000.

[CHIB01] M. Chiba, A. Kuptsov and K. Okada, DIRAC Note 2001-06, CERN, 2001.

[CHLI75] P. V. Chliapnikov *et al.*, Phys.Letters 55B (1975) 237.

[CHO70] Y. Cho *et al.*, Phys Lett. 32B (1970) 409.

[CHPT] For recent reviews on CHPT see:
H. Leutwyler, [LEUT93];
U. G. Meißner, Rep. Prog. Phys. 56 (1993) 903;
A. Pich, Lectures given at the V Mexican School of Particles and Fields, Guanajuato, México, December 1992,
preprint CERN-Th.6978/93 (hep-ph/9308351);
G. Ecker, Chiral perturbation theory, in: Quantitative Particle Physics: Cargèse 1992, Eds. M. Lévy *et al.*, Plenum Publ. Co. (New York, 1993);
J. F. Donoghue, E. Golowich. and B. R. Holstein, "Dynamics of the Standard Model" (1992), Cambridge University Press, Cambridge.

[COLA00] G. Colangelo, J. Gasser and H. Leutwyler, Phys. Lett. B 488 (2000) 261, hep-ph/0007112.

[COLA01A] G. Colangelo, J. Gasser and H. Leutwyler, Phys. Rev. Lett. 86 (2001) 5008.

[COLA01B] G. Colangelo, J. Gasser and H. Leutwyler, Nucl. Phys. B603 (2001) 125.

[CSOR96] T. Csörgö, B. Lorstadt and J. Zimanyi, Z. Phys., C71 (1996) 491.

[DEBA69] W. De Baere *et al.*, Nucl. Phys. B14 (1969) 425.

[DENI87] K. G. Denisenko and S. Mrowczynsky, Phys.Rev. D36 (1987) 1529.

[DESC00] S. Descotes and J. Stern, hep-ph/0007082.

[DESC03] S. Descotes *et al.*, LPT-ORSAY/03-82, ECT*-03-06, IPNO DR 03-09; hep-ph/03111202.

[DESE54] S. Deser *et al.*, Phys. Rev. 96 (1954) 774.

[DULI83] L. S. Dulian and A. M. Kotsinian, Yad.Fiz. 37 (1983) 137; (Sov. J. Nucl. Phys. 37 (1983) 78).

[DUNW77] W. M. Dunwoodie *et al.*, not published, (1977).

[EFIM86] G. V. Efimov, M. A. Ivanov and V. E. Lyubovitskij, Yad. Fiz. 44 (1986) 460; Sov. J. Nucl. Phys. 44 (1986) 296.

[EFIM87] G. V. Efimov, M. A. Ivanov and V. E. Lyubovitskij, Pis'ma Zh. Exp. Teor. Fiz. 45 (1987) 526.

[EFIM02] G.V. Efimov, M.A. Ivanov and V.E. Lyubovitskij, Yad. Fiz. 44 (1986) 460; (Sov. J. Nucl. Phys. 44 (1986) 296.

[EICH72] T. Eichten and D. Haidt, Nucl. Phys. B44 (1972) 333.

[EIRA00] D.Eiras and J.Soto, Phys.Lett. B491 (2000) 101; hep-ph/0005066.

[ESTA78] P. Estabrooks *et al.*, Preprint SLAC-PUB-1886 and Nucl. Phys. B133 (1978) 490.

[FERR97] O.Ferrando and J.-Y.Hemery, CERN-PS Division, PS/CA/Note 97-16.

[FIRE72] A. Firestone *et al.*, Phys.Rev. D5 (1972) 2188.

[FOX74] G. C. Fox and M. L. Griss, Nucl. Phys. B80 (1974) 403.

[FOWL77] G.N. Fowler and R.M. Weiner, Phys. Lett., B70, (1977); Phys. Rev., D17 (1978) 3118.

[FRIN02] M. Frink, B. Kubis, U.-G. Meissner, Eur.Phys.J.C25 (2002) 259; hep-ph/0203193.

[FUCH91] M. H. Fuchs, H. Sazdjian and J. Stern, Phys. Lett. B269 (1991) 183.

[FUKU95] M. Fukugita *et al.*, Phys. Rev. D52 (1995) 3003.

[GALL99] A. Gall, J. Gasser, V. E. Lyubovitskij and A. Rusetsky, Phys. Lett. B462 (1999) 335.

[GALL02] M. Gallas, Nucl. Instr. Meth. A481 (2002) 222.

[GARW71] E. L. Garwin and A. Roder, Nucl. Instr. and Meth. 93 (1971) 593.

[GASH98] A. Gashi *et al.*, Nucl. Phys. A628 (1998) 101.

[GASH02] A. Gashi *et al.*, Nucl. Phys. A699 (2002) 732.

[GASS83] J. Gasser and H. Leutwyler, Phys.Lett. B125 (1983) 325;
ibid Nucl. Phys. B250 465, 517, 539.

[GASS84] J. Gasser and H. Leutwyler, Annals Phys. 158 (1984) 142.

[GASS99] J. Gasser, V. E. Lyubovitskij and A. G. Rusetsky, Phys. Lett. B471 (1999) 244.

[GASS00] J. Gasser and A. G. Rusetsky private comunication.

[GASS01] J. Gasser *et al.*, Phys.Rev. D64 (2001) 016008; hep-ph/0103157.

[GEANT] GEANT3 for DIRAC, version 2.63, unpublished.

[GELL68] M. Gell-Mann, R. J. Oakes and B.'Renner, Phys. Rev. 175 (1968) 2195.

[GLAS68] S. Glashow and S. Weinberg, Phys. Rev. Lett. 20 (1968) 224.

[GMIT86] M. Gmitro *et al.*, *Czech. J. Phys.* B36, 1281 (1986).

[GOLD60] G. Goldhaber *et al.*, *Phys. Rev.* 120, 300 (1960).

[GOME97] F. Gómez *et al.*, Nucl. Instr. and Meth. A384 (1997) 351.

[GOR68] M. Gell-Mann, R.J. Oakes and B. Renner, Phys. Rev. 175 (1968) 2195.

[GORC96] O. E. Gorchakov *et al.*, Yad. Fiz. 59 (1996) 2015; (Phys. At. Nucl. 59 (1996) 1942).

[GORC99] O. E. Gorchakov, A. V. Kuptsov, L. L. Nemenov, D. Y. Riabkov, preprint, JINR E1-99-134, Dubna 1999.

[GORC00] O. E. Gorchakov *et al.*, Yad. Fiz. 63 (2000) 1936; (Phys. At. Nucl. 63 (2000) 1847).

[GRAE77] H. Graessler *et al.*, Nucl. Phys. B125 (1977) 189.

[GRIS82] V. G. Grishin "Inclusive processes in hadron interaction at high energy", Energoizdat, Moscow 1982, 131.

[GUIL79] M. Gyulassy, S.K. Kauffmann and L.W. Wilson, Phys. Rev., C20 (1979) 2267.

[HALA99] Z. Halabuka *et al.*, Nucl. Phys. 554 (1999) 86.

[HART94] E. Hartouni *et al.*, Phys. Rev. Lett. 72 (1994) 1322.

[HEIM00] T.A. Heim *et al.*, J. Phys. B33 (2000) 3583.

[HEIM01] T. A. Heim *et al.*, J. Phys. B34 (2001) 3763.

[HEIN76] J. Heintze *et al.*, Nucl. Instr. and Meth. 138 (1976) 641.

[HEIN97] U. Heinz and Q.H. Zhang, Phys. Rev., C56 (1997) 426.

[HORI93] R. Horisberger and D. Pitzl, Nucl. Instr. and Meth. A326 (1993) 92.

[HUBB75] J. H. Hubbel *et al.*, J. Phys. Chem. Ref. Data 4 (1975) 71.

[HUBB79] J. H. Hubbel, I. Overbo, J. Phys. Chem. Ref. Data 8 (1979) 9.

[IVAN98] M.A. Ivanov *et al.*Phys. Rev. D58 (1998) 094024.

[IVAN99] M. A. Ivanov, V. E. Lyubovitskij, E. Z. Lipartia and A. G. Rusetsky, Phys. Rev. D58 (1998) 0094024.

[IVAN99A] D. Yu. Ivanov and L. Szymanowski, Eur.Phys. J. A5 (1999) 117.

[JALL98] H. Jallouli and H. Sazdjian, Phys. Rev. D58 (1998) 014011; Erratum: ibid., D58 (1998) 099901.

[JALL99] H. Jallouli and H. Sazdjian, Phys. Rev. D58 (1998) 014011; 099901(E).

[JOHA78] N. Johannesson and G. Nilsson, Nuovo Cimento 43A (1978) 376.

[JONE99] L. L. Jones *et al.*, Snowmass 1999, "Electronics for LHC experiments", 162.

[JONG73] B. Jongejans *et al.*, Nucl. Phys. B67 (1973) 381.

[KALM79] P. Maybeck, Stochastic Models, Estimation and Control, Volume 1. Academic Press, New York (1979).

[KARA80] A. Karabarbouris and G. Shaw, Journal of Phys. G6 (1980) 583.

[KARI79] A. Karimhodjaev and R. N. Faustov, Yad. Fiz. 29 (1979) 463; Sov.J.NuclPhys. 29 (1979) 232.

[KARI86] A. Karimhodjaev and R. N. Faustov, JINR, P2-86-142, Dubna, 1986.

[KARP03] V. Karpukhin *et al.*, Nucl. Instr. Meth. A512 (2003) 578.

[KIRS71] A. R. Kirschbaum *et al.*, Phys.Rev. D4 (1971) 3254.

[KNEC93] M. Knecht 28th Rencontre de Moriond : QCD and High-energy Hadronic Interactions - Particle Physics Meetings, Les Arcs, France, 20–27 Mar 1993 / Ed. by J. Tran Thanh Van. - Ed. Frontieres, Gif-sur-Yvette, (1993) 187.

[KNEC93A] M. Knecht *et al.*, Phys. Lett. B313 (1993) 229.

[KNEC95] M. Knecht *et al.*, Nucl. Phys. B457 (1995) 513.

[KOBA02] M. Kobayashi *et al.*, Nucl. Instr. and Meth. A487 (2002) 353.

[KOKK01] P.Kokkas, M.Steinacher, L.Tauscher, S.Vlachos., NIM A471 (2001) 358.

[KOON77] S.E. Koonin, *Phys. Lett.* B70, 43 (1977); M. Gyulassy, S.K. Kauffmann and L.W. Wilson, *Phys. Rev.* C20, 2267 (1979).

[KOPY72] G.I. Kopylov and M.I. Podgoretsky, *Sov. J. Nucl. Phys.* 15, 219 (1972); M.I. Podgoretsky, *Sov. J. Part. Nucl.* 20, 266 (1989).

[KROL55] N.M. Kroll and W. Wada, Phys. Rev. 98, 1355 (1955).

[KUBI01] B. Kubis, U.-G. Meißner, Phys.Lett. B529 (2002) 69; hep-ph/0112154;
B. Kubis, U.-G. Meißner, Nucl.Phys. A699 (2002) 709; hep-ph/0107199.

[KULI03] A. Kulikov and M. Zhabitsky, DIRAC internal note 2003-05.

[LAGA01] L.Lagamba *et al.*, NIM A471 (2001) 325.

[LANA01] A. Lanaro, DIRAC note 2001-01.

[LANA02] A.Lanaro, DIRAC Note 2002-02.

[LANG77] C. B. Lang, Nuovo Cimento 41A (1977) 73.

[LANG78] C. B. Lang, Fortschrinder für Physik, 26 (1978) 509.

[LAUS75] P. Lauscher *et al.*, Nucl. Phys. B86 (1975) 189.

[LEDN79] R. Lednicky and M.I. Podgoretsky, Yad. Fiz., 30 (1979) 837.

[LEDN82] R. Lednicky and V.L. Lyuboshitz, Sov. J. Nucl. Phys. 35, 770 (1982); Proc. CORINNE 90, Nantes, France, 1990 (ed. D. Ardouin, World Sci., 1990) p. 42.

[LEDN83] R. Lednicky, V.L. Lyuboshitz and M.I. Podgoretsky, Yad. Fiz., 38 (1983) 251.

[LEDN92] R. Lednicky and T.B. Progulova, Z. Phys., C55 (1992) 295.

[LEDN96] R. Lednicky *et al.*, *Phys. Lett.* B373, 30 (1996).

[LEDN99] R. Lednicky, NA49 Note number 210 (1999); nucl-th/0112011.

[LEDN04] R. Lednicky, nucl-th/0305027, to appear in Phys. At. Nucl. 67, 71 (2004).

[LEUT93] H. Leutwyler, Proc. XXVI Int. Conf. on High Energy Physics, Dallas, 1992, edited by J. R. Sanford, IAP Conf. Proc. N.272 (AIP New York 1993) 185.

[LEUT94] H. Leutwyler, Ann. Phys. 235 (1994) 165; (hep-ph/9311274).

[LING73] D. Linglin *et al.*, Nucl. Phys B55 (1973) 408; Nucl. Phys. B57 (1973) 64.

[LYUB88] V.L. Lyuboshitz, *Sov. J. Nucl. Phys.* 48, 956 (1988).

[LYUB91] V.L. Lyuboshitz, Yad. Fiz., 53 (1991) 823.

[LUBO97] V. E. Lyubovitskij, E. Z. Lipartia and A. G. Rusetsky, Pis'ma Zh. Exp. Teor. Fiz 66 (1997) 747.

[MART78] A. D. Martin *et al.*, Nucl. Phys. B134 (1978) 392.

[MATI74] M. J. Matison *et al.*, Phys. Rev. D9 (1974) 1872.

[MERC71] R. Mercer *et al.*, Nucl. Phys. B32 (1971) 381.

[MERC97] S.P. Merkuriev, Theor. Math. Phys., 32 (1997) 680;
M. Brauner *et al.*, J. Phys., B22 (1989) 2265;
B.Erazmus *et al.*, Nucl. Phys., A583 (1995) 395;
L. Martin *et al.*, Nucl. Phys., A604 (1996) 69;
R. Lednicky, Nukleonika, 43 (1998) 345;
E.O. Alt *et al.*, Phys. Lett., B458 (1999) 407.

[MOLI47] G. Moliere, Z. Naturforsch. 2A (1947) 3.

[MOOR95] U. Moor, G. Rasche and W. S. Woolcock, Nucl. Phys. A587 (1995) 747.

[MROW86] S. Mrówczyński, Phys. Rev. A33 (1986) 1549, S. Mrówczyński, Phys. Rev. D36 (1987) 1520, K. G. Denisenko and S. Mrówczyński, ibid. D36 (1987) 1529.

[MROW87] S. Mrowczynski, Phys. Rev. D36 (1987) 1520.

[MROW92] S. Mrowczynski, *Phys. Lett. B* 277, 43 (1992); *ibid.* 308, 216 (1993).

[NAGE79] See compilation of Nagels M.M. *et al.*, Nucl. Phys. 147 (1979) 189, and references mentioned therein.

[NEHM02] A. Nehme, Eur.Phys.J. C23 (2002) 707; hep-ph/0111212;
A. Nehme, P. Talavera, Phys.Rev. D65 (2002) 054023; hep-ph/0107299.

[NEME85] L. L. Nemenov, Yad. Fiz 41 (1985) 980; Sov. J. Nucl. Phys. 41 (1985) 629.

[NEME01] L. L. Nemenov and V. D. Ovsyannikov, Phys. Lett. B514 (2001) 247.

[NEME01] L.L. Nemenov and V.D. Ovsiannikov, Phys. Lett. B514 (2001) 247.

[NEME02] L. L. Nemenov, V. D. Ovsyannikov and E. V. Chaplygin, Nucl. Phys. A 710 (2002) 303.

[NEME02] L.L. Nemenov, V.D. Ovsyannikov, E.V. Chaplygin, Nucl. Phys. A710 (2002) 303.

[NILS87] B. Nilsson-Almquist, E. Stenlund, Com. Phys. Comm. 43 (1987) 387.

[OLSH00] V. G. Olshevsky, S. V. Trusov, JINR E10-2000-150, Dubna, 2000.

[OLSH00A] V. G. Olshevsky, S. V. Trusov, DIRAC internal note 00-06.

[OLSH01] V.G.Olshevsky, S.V.Trusov, Nucl. Instr. Meth. A 469 (2001) 216.

[PDG002] K. Hagiwara *et al.*(PDG), Phys. Rev. D66 (2002) 010001.

[PENT96] M. Pentia *et al.*, Nucl. Instr. Meth. A369 (1996) 101, M. Pentia and S. Constantinescu, DIRAC note 01-04.

[PISL01] S. Pislak *et al.*, Phys. Rev. Lett. 87 (2001) 221801.

[PISL03] S. Pislak *et al.*, Phys.Rev. D67 (2003) 072004; hep-ex/0301040.

[PLAN59] R. Plano, A. Prodell, N. Samios, M. Schwartz, and J. Steinberger, Phys. Rev. Lett. 3, 525 (1959).

[ROES99] A. Roessl, Nucl. Phys. B555 (1999) 507; (hep-ph/9904230).

[ROSS77] L. Rosselet *et al.*, Phys. Rev. D15 (1977) 547.

[RUSETS] A.Rusetsky, private communication.

[SAKH48] A. D. Sakharov, Zh. Eksp. Teor. Fiz. 18 (1948) 631.

[SALV87] F. Salvat *et al.*, Phys. Rev. A36 (1987) 467.

[SAMI62] N.P. Samios, R. Plano, A. Prodell, M. Schwartz, and J. Steinberger, Phys. Rev. 126, 1844 (1962).

[SANT03] C. Santamarina and Ch. P. Schuetz, DIRAC note 2003-09.

[SANT03] C. Santamarina *et al.*, J. Phys. B36 (2003) 4273.

[SATO81] H. Sato and K. Yazaki, *Phys. Lett. B* 98, 153 (1981).

[SAZD00] H. Sazdjian, hep-ph/0004226.

[SCHE99] R. Scheibl and U. Heinz, *Phys. Rev. C* 59, 1585 (1999).

[SCHU02] M. Schumann *et al.*, J. Phys. B35 (2002) 2683.

[SCHU02B] Ch. P. Schuetz and L. Tauscher, DIRAC note 02-01, Ch. P. Schuetz and L. Tauscher, DIRAC note 03-06.

[SCHW04] J. Schweizer, to be submitted to Phys. Lett.; arXiv:hep-ph/0401048.

[SJOS87] T. Sjöstrand, M. Bengtsson, Com. Phys. Comm. 43 (1987) 367.

[SPIR77] M. Spiro *et al.*, Saclay preprint DPhPE 77/05 (1977).

[STER93] J. Stern, H.Sazjian and N.H. Fuchs, Phys. Rev. D47 (1993) 3814.

[SUMI99] T. Sumiyoshi *et al.*, Nucl. Instr. and Meth. A433 (1999) 385.

[TARA91] A. V. Tarasov and I. U. Christova, JINR P2-91-10, Dubna, 1991.

[TARA91] A. V. Tarasov and I.U. Khristova, JINR-P2-91-10, Dubna 1991.

[TRIP68] T. G. Trippe, Phys. Lett. 28B (1968) 143.

[URET61] J. Uretsky and J. Palfrey, Phys. Rev. 121 (1961) 1798.

[URIB94] J. Uribe *et al.*, Phys. Rev. D49 (1994) 4373.

[UZHI96] V.V. Uzhinskii: Modified code FRITIOF. User's Guide. JINR Comm., 1996, E2-96-192

[VLAC00] S. Vlachos, DIRAC note 2000-13.

[VLAC03] S. Vlachos, DIRAC note 2003-04.

[VOSK98] O. O. Voskresenskaya, S.R. Gevorkyan and A.V. Tarasov, Phys. At. Nucl. 61 (1998) 1517.

[WEIN66] S. Weinberg, Phys. Rev. Lett. 17 (1966) 616.

[WEIN68] S. Weinberg, Phys. Rev. 166 (1968) 1568.

[WEIN79] S. Weinberg, Physica 96A (1979) 327.

[WEIN79] S. Weinberg, Physica A96 (1979) 327, J. Gasser and H. Leutwyler, Phys. Lett. B125 (1983) 325 and Nucl. Phys. B250 465, 517, 539.

[YUTA71] H. Yuta *et al.*, Phys. Rev. Lett. 26 (1971) 1502.

[ZREL03] P.Zrelov, V.Yazkov. The GEANT - DIRAC simulation program Version 2.63. http://zrelov.home.cern.ch/zrelov/dirac/montecarlo/instruction/instruct26.html.